Characterization of the Geothermal Resource at Clarke Lake Field Northeast British Columbia

By

Evan Renaud

A thesis submitted in partial fulfillment of the requirements for the degree of

Master of Science

Department of Earth and Atmospheric Sciences
University of Alberta

Abstract

Clarke Lake is a depleted gas field developed in carbonate platform deposits of the Slave Point Formation (Middle Devonian) in northeastern British Columbia, Canada. It displays anomalously high reservoir temperature and strong water drive, making it a candidate for repurposing as a source of geothermal power. Porous and permeable reservoir near the platform margin developed through the hydrothermal alteration of host limestone to dolomite. A geothermal resource requires permeable reservoir rock that allows for flow rates that can sustain economic electricity generation. A depositional model in provides a basis for mapping the dolomite reservoir, and thus, permeability. Porosity and permeability measurements can be incorporated in a comprehensive suite of flow simulations to test how reinjected water affects geothermal power production.

Nine depositional facies and two diagenetic facies are identified, the former based on bioclast assemblages, rock types, texture and composition and the latter based on rock fabric and the degree of alteration to dolomite. Deposition of these facies occurred within lagoonal, reef-flat and foreslope settings associated with a rimmed carbonate platform. Dolomitized lagoon, reef flat, reef margin and shoal lithologies show enhanced porosity and permeability due to dissolution of stromatoporoid bioclasts, forming mouldic and vuggy porosity. Diagenetic facies show high permeability but reduced porosity as a result of precipitation of porosity-occluding dolomite, fluorite, and sulphide minerals. High quality reservoir zones occur primarily at the reef margin, caused by fabric-selective hydrothermal alteration of carbonate sediments near the contact with shales of the Horn River and Muskwa formations.

Correlation of core descriptions and wireline log data allow the Slave Point Formation to be separated into successions that influenced dolomitization: an initial shoal unit, S1, three subsequent reef units, R1, R2, R3, and terminal shoal units of D1, D2 and D3. Shoal units were deposited in the transgressive systems tracts, whereas reef growth units were deposited in the highstand systems tracts. An initial transgression deposited shoals of the S1 unit across the carbonate platform.

As the rate of relative sea level rise waned, a well-defined reef margin developed at the platform edge, which influenced depositional energy across the platform top and allowed deposition of reef units (R1, R2, and R3). A subsequent transgression began to drown the reef, during which spatially restricted shoals, D1, D2 and D3, were deposited near the reef margin before the rate of relative sea level rise outpaced the rate of deposition.

We assessed the viability of geothermal energy production by simulating the water temperatures in production scenarios that use different operation conditions, well configurations and grid sizes, and by applying a Monte Carlo approach to different porosity and permeability realizations. Both an injection-production well doublet and an array of 4 injection and 8 production wells were simulated. Temperature drops at production wells result from a migration of an injected cold water plume and are most strongly related to flow rate. Varying flow rates result in a temperature drop that ranges from 0.47 to 5.6 °C. Simulations using progressively finer grids predict longer thermal breakthrough time compared to coarser grids, while coarser grids predict greater temperature drops at the production well.

The impact of thermal breakthrough at a geothermal production well is a reduction of the power potential. Reduced power potentials using doublet production-injection scenarios are 465 kWe at 25 kg/s flow rates and 930 kWe at 50 kg/s flow rates, compared to baseline results (that assume no thermal breakthrough) of 511 kWe and 1036 kWe, respectively . The four injection-eight production well scenarios estimate a power production of 3456 kWe at 200 kg/s flow rates, compared to a baseline result of 4085 kWe without thermal breakthrough.

Preface

This thesis was undertaken to test the viability of repurposing the Clarke Lake field into a source of geothermal power by analyzing the geological properties of the reservoir and applying those properties to a flow model. The geothermal potential of the Clarke Lake reservoir and other sedimentary reservoirs in the Western Canadian Sedimentary Basin has been recognized by previous researchers (Johnstone, 1982; Arianpoo, 2009; Walsh, 2013; Weides & Majorowicz, 2014; Palmer-Wilson et al., 2018). The sedimentology and sequence stratigraphy of the Slave Point Formation, along with numerical models for thermal breakthrough presented in this study, advance our knowledge on geothermal resource development in hot, sedimentary reservoirs.

The depositional model and petrophysical analysis of reservoir rock in this study delineate the vertical and lateral extent and variation of the dolomite reservoir and identify prospective locations for geothermal well doublet and four injection-eight production well layouts. Numerical modelling of thermal breakthrough using hydrothermal dolomite petrophysical properties provides a relevant case study on low-enthalpy, carbonate-hosted geothermal systems and helps quantify reductions of power potential from temperature drops at the production well.

The thesis is divided into two main chapters. Chapter 1 is a reservoir study that examines depositional and diagenetic facies of the Slave Point Formation. Core sampling and description was done at the BCOGC Core Facility in Fort St. John, British Columbia and at the University of Alberta in Edmonton. A version of Chapter 1 will be submitted to the CSPG Bulletin as Renaud, E., Weissenberger, J.W., Harris, N.B., and Banks, J., 2020a. Geothermal resource characterization of the Middle Devonian Slave Point Formation at Clarke Lake field, Fort Nelson, British Columbia, Canada. Renaud, E was responsible for data collection and manuscript composition, Weissenberger, J.W, Harris, N.B and Banks, J assisted in data collection and contributed to manuscript edits.

Chapter 2 includes a group of flow simulations that uses petrophysical properties inputs from described facies presented in Chapter 1 to investigate the effect of thermal breakthrough in a

hydrothermal dolomite reservoir. A version of Chapter 2 will be submitted to Geothermics as Renaud, E., Banks, J., Harris, N.B., Weissenberger, J.W., and Wilson, B., 2020b. Simulating thermal breakthrough in a heterogeneous hydrothermal dolomite reservoir. Renaud, E was responsible for data collection and manuscript composition, J, Banks and Harris, N.B were responsible for data collection and manuscript edits. Weissenberger, J.W was responsible for manuscript edits. Wilson, B provided the cloud transformation workflow for generating simulation inputs.

Chapter 3 presents conclusions for both Chapters 1 and 2. Renaud, E was responsible for manuscript composition, Harris, N.B. and Weissenberger, J.W provided manuscript edits.

Acknowledgments

As a part of the University of Alberta's Future Energy Systems research initiative, this research was possible in part thanks to funding from the Canada First Research Excellence Fund.

Many individuals throughout my project work offered guidance in a technical and professional capacity, which helped me to better develop my ideas and become a more critically sound scientist. Firstly, I would like to thank my supervisor Dr. Nicholas Harris, along with Dr. John Weissenberger and Dr. Jonathan Banks for their guidance throughout my research project. Thank you to Brandon Wilson and Dr. Arif Rabbani for assisting in developing the inputs for the Monte Carlo simulations. The exceptional assistance with core handling provided by Sung-Eun Kim at the BCOGC Core Facility in Fort St. John was greatly appreciated. Thank you to Mark Labbe for providing sampling tools and outstanding lab services at the University of Alberta. A special thank you to my family for their support.

Table of Contents

Figures

List of tables

Chapter 1: Reservoir geology of the Slave Point Formation

1.1 Introduction

Clarke Lake is a mature gas field situated approximately 10 km southeast of Fort Nelson, B.C., Canada (Fig. 1.1). The discovery well, Prophet River No. 1, was drilled in the winter of 1957 as a joint venture between Western Natural Gas Company, El Paso Natural Gas Company, Hudson's Bay Oil and Gas Company Limited and Union Oil Company of California (Gray and Kassube, 1963). A prolific Devonian gas pool, Clarke Lake has produced over 52 x 10^9 m^3 (1.83 TCF) of gas, and 49 x 10^9 m^3 (308126 MMbbl) of water since going on stream in January of 1961 (British Columbia Oil and Gas Commission, 2019). Clarke Lake field has largely been depleted of gas and is losing economic value, which affects stakeholders such as field operators and the residents of the Fort Nelson area. The recognition of an anomalously high geothermal gradient and a strong water drive within the permeable hydrothermal dolomite reservoir has led to an interest in repurposing the gas field as a source of geothermal power (Petro-Canada Oil and Gas, 2009; Weides and Majorowicz, 2014).

The geothermal potential at Clarke Lake has been investigated by Johnstone (1982), Arianpoo (2009), and Walsh and Grasby (2013). Geological studies detailing the reservoir characteristics, sedimentology and diagenesis of the Slave Point Formation at Clarke Lake field have also been completed (Gray and Kassube, 1963; Lonnee and Machel, 2006). The current study advances earlier work by associating depositional and diagenetic features with petrophysical and geothermal properties and placing these in a detailed spatial context.

Critical elements of economically viable low-enthalpy geothermal resources within sedimentary reservoirs are high formation fluid temperatures and high flow rates (Walsh and Grasby, 2013; Weides and Majorowicz, 2014). Required temperatures vary with usage: 100 – 210°C for electricity production, > 70°C district heating, and > 50 °C for warm water provision. Elevated formation temperatures, a strong water drive and permeable reservoir rock at Clarke Lake satisfy these requirements.

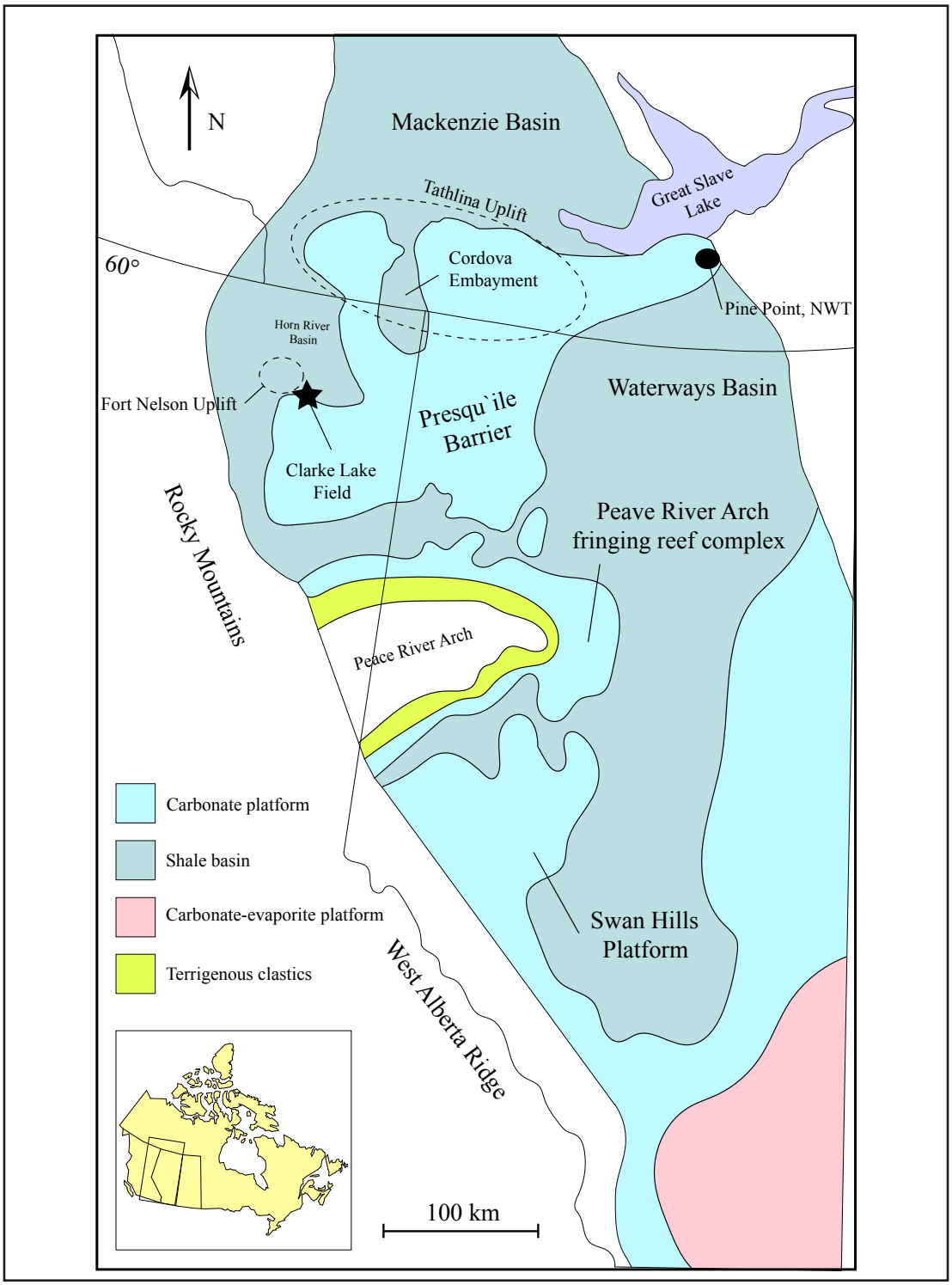

Figure 1.1: Location of Clarke Lake field on the Presqu'ile Barrier, and Middle Devonian paleogeography of the Western Canadian Sedimentary Basin. Major Clarke Lake time-equivalent carbonate build-ups include the Swan Hills platform and the Peace River Arch fringing reef complex. The Peace River Arch and the West Alberta Ridge were two land masses that persisted through the Middle Devonian and were surrounded by reef growth (Modified from Yose et al., 2001 and Turner et al., 2003).

Weides and Majorowicz (2014) mapped heat flow (mW/m^2) and the geothermal gradient (°C/km) throughout the Western Canadian Sedimentary Basin to locate potential geothermal pools that meet the temperature requirement. They found a geothermal gradient of 50 – 55°C/km at the Clarke Lake field corresponding to reservoir temperatures of 110 - 123°C, and concluded that potential for electricity production exists.

A strong water drive was identified in an experiment conducted by Petro-Canada Oil and Gas, who investigated the viability of liberating trapped gas within the Clarke Lake field by depressurizing the reservoir. To accomplish this, they produced formation water at high rates (between 2100 and 2800 m^3/day) from January 1st, 2007 to December 29th, 2008, employing two wells as water producers and two wells as water disposal wells. Six remaining wells were designated as gas lift wells. Water-gas ratio plots showed that no gas had been liberated as a result of depressurization. Water rates at one water producer well peaked at 1800 m^3/day while the gas-to-water ratio remained stable at 3 m^3 gas / m^3 water (Petro-Canada Oil and Gas, 2009). Petro-Canada speculated that they would need at least a 1 MPa drop in reservoir pressure to access the trapped gas but at the end of the experiment found that reservoir pressure dropped by only 100 KPa. This unexpectedly low pressure drop was a result of a strong water drive.

Walsh and Grasby (2013) recognized that Clarke Lake may be a strong candidate for geothermal power generation due to this favorable combination of high water deliervability, high permeabilities associated with hydrothermal dolomite and high reservoir temperatures shown by well data. Using a USGS model to estimate thermal energy (Brook, 1978), Walsh and Grasby (2013) estimated the total recoverable thermal energy from the field to be 10.1×10^{14} kJ (with a standard deviation of 3.2×10^{14} kJ), approximately the same energy as available in 165 million barrels of oil. With existing binary geothermal plant technology, five wells at Clarke Lake field should have the capability of producing 6-7.5 MW of electricity. The field-wide total electricity generation potential is estimated to be 34 MW.

The unique temperature anomaly and strong water drive present at Clarke Lake field offers a test case on the applicability of geothermal exploration within sedimentary reservoirs. As a new en-

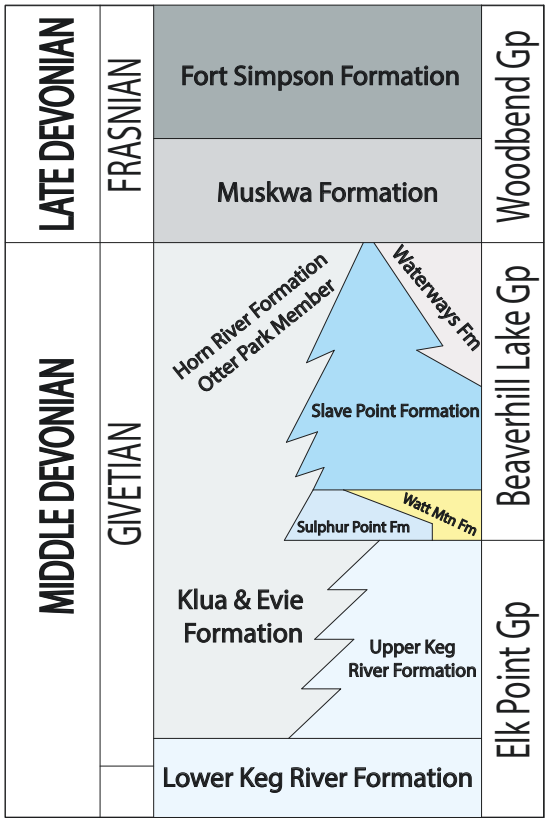

Figure 1.2: Stratigraphic column showing carbonate formations that compose the Presqu'ile Barrier.

ergy venture and departure from typical geothermal plays, the success of Clarke Lake field as a geothermal power source has implications for expanding our knowledge within the renewable energy sector.

1.2 Geologic Background

1.2.1 Geological History

The Slave Point Formation, along with the Lower Keg River, Upper Keg River, Sulphur Point and Watt Mountain formations comprise a large Middle Devonian barrier reef complex referred to as the Presqu'ile Barrier (Fig. 1.1, 1.2). Deposition of the barrier began at the end of the Eifelian and persisted until the end of the Givetian. It extends roughly 600 km long from the subsurface near the Rocky Mountains of northeast B.C. to the outcrop edge at Pine Point, Northwest Territories, and the width ranges from 20 to 100 km. The barrier divides the Horn River and Mackenzie shale basins to the north from the Waterways shale basin, Peace River Arch fringing reef complex and the Swan Hills reef complex to the south (Fig. 1.1, 1.2).

In the Devonian, the Presqu'ile Barrier was located at approximately 5° south of the paleoequator within a shallow epicontinental sea favourable for carbonate deposition (Witzke and Heckel, 1988).The oldest Devonian strata unconformably overlie Precambrian or lower Paleozoic rocks and were deposited within basins adjacent to paleohighlands that include the Tathlina Highland, Fort Nelson Uplift, Western Alberta Ridge and the Peace River Arch (O'Connell et al., 1990). The Tathlina Highland and Fort Nelson Uplift were structural features that existed before deposition of the Presqui'le Barrier and were the loci of reef growth, strongly influencing the stratigraphy and depositional patterns of the Presqu'ile Barrier (Hriskevich, 1967; Meijer Drees, 1994). After a major transgression onto the paleohighlands in the late Eifelian, a continent-wide, regres-

sive carbonate platform comprising deposits of the Lower Keg River Member developed (Meijer Drees, 1994; Morrow et al., 2002). Upper Keg River Formation reefs grew on top of the Lower Keg River and restricted seawater circulation to the south, allowing for widespread deposition of evaporites (Muskeg and Prairie Evaporite formations; Qing and Mountjoy, 1994; Potma et al., 2001).

In the late Givetian, a rapid sea level rise terminated most reef growth within the Presqu'ile Barrier. Horn River Formation shales and aggradational deposits of the Sulphur Point Formation reflect this final transgression before deposition of the upper Givetian to Frasnian second-order sequence (Fig. 1.3; Potma et al., 2001). The upper Givetian to Frasnian sequence can be subdivided into at least nine third-order sequences; the Slave Point Formation deposited within the first third-order sequence, termed the Beaverhill Lake Sequence 1. The lowstand portion of Beaverhill Lake Group (and beginning of the Givetian-Frasnian sequence) is first represented by the thin shale of the Watt Mountain Formation; this unit gradually decreases in thickness northward from the platform interior to the Presqu'ile Barrier, where it is absent (Meijer Drees, 1988). The shale sits unconformably above the Sulphur Point Formation and the contact has been interpreted as an erosional and/or transgressive event (Meijer Drees, 1988; Potma et al., 2001; Lonnee and Machel, 2006).

As conditions favourable for carbonate deposition persisted into the Late Devonian, aggradational patch reefs of the Slave Point Formation continued to develop on the Presqu'ile Barrier (Potma et al., 2001). These reefs backstepped as sea level rose until, much like the underlying Keg River, they drowned when reef growth failed to keep up with sea-level rise. This major Late Devonian sea-level rise resulted in a thick package of Muskwa and Fort Simpson formation shales on top of the reef complex, which provided a regional seal for many Devonian oil and gas plays in Alberta and B.C. (Fig. 1.3; Morrow et al., 2002).

1.2.2 WCSB Devonian Reservoirs

Clarke Lake field is one of many prolific Devonian hydrocarbon reservoirs within the Western Canadian Sedimentary Basin. Devonian reservoirs contain 55 % of conventional oil and 27 % of

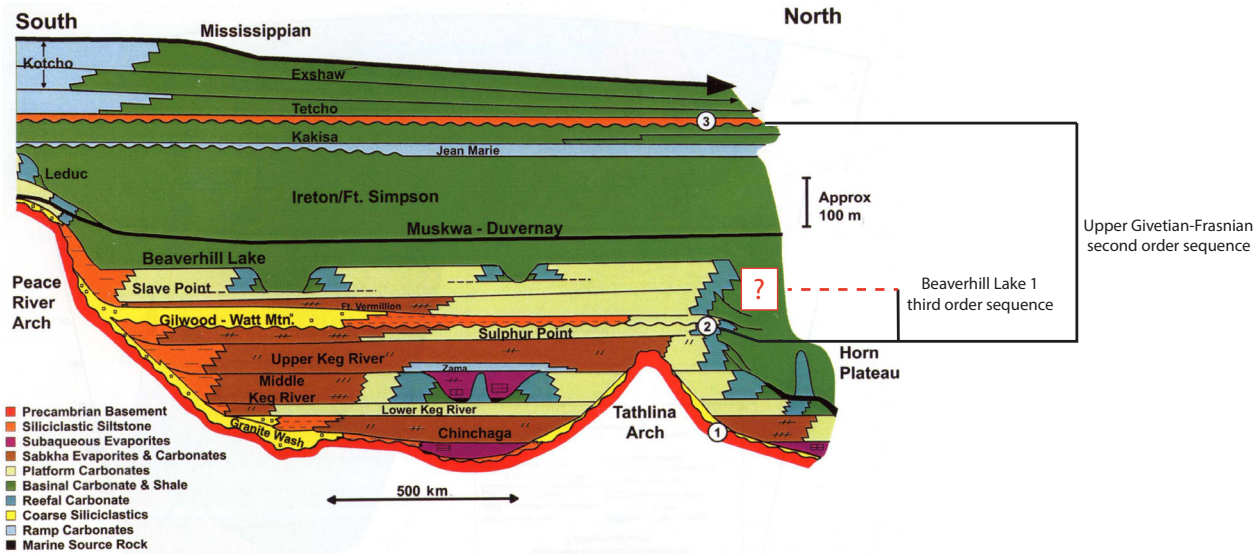

Figure 1.3: Eifelian to Famennian stratigraphy of Alberta, British Columbia and Northwest Territories, showing the second and third order depositional sequences that the Slave Point Formation was deposited within (Modified from Weissenberger & Potma., 2001).

gas reserves in Western Canada (Fowler et al., 2001). Dolomitization has been shown to be an important factor in the distribution of reserves. Hutton (1994) compared two Middle Devonian fields in Alberta, Hamburg and Shekilie, and concluded that reservoirs without a dolomitic over-print have up to 80% lower volumetric storage capacity than dolomitized reservoirs of similar size. Davies and Smith (2006) estimated that of the 105 TCF of gas within dolomite reservoirs of Alberta and British Columbia, 30 TCF are within Devonian and Mississippian reservoirs that show a hydrothermal dolomite association. Fields in the Slave Point and Keg River formations on the Presqu'ile Barrier reef edge and platform or as isolated reefs in northeast British Columbia, such as Clarke Lake, July Lake, Helmet, Adsett, Yoyo and Peggo are hosted within hydrothermal dolomite reservoirs (Geological Survey of Canada, 1993; Morrow et al., 2002; Davies and Smith, 2006).

1.3 Data Set and Methods

Twenty cores from wells within Clarke Lake field and eight more cores from outside the field were provided by the BC Oil and Gas Commission Core Research Facility, and described in this study. Descriptions were produced at a scale of 1:50, noting the lithology, bioclast assemblage, pore types, and sedimentary structures observed. Dunham's (1962) carbonate classification was

used to identify facies and facies associations. The eight cores from outside of Clarke Lake field were limestone and offer a better understanding of well-log response to specific facies and the depositional fabrics that are obscured within the dolomite body (Fig. 1.4; Table 1.1).

Thin-section petrographic analysis was completed on 50 thin sections in order to assess microscopic porosity and permeability development in representative samples from all depositional and diagenetic facies encountered at Clarke Lake. Particular attention was given to the dolomitized reservoir facies, but limestone samples were also taken to investigate reservoir potential. Half of each thin section was exposed to a dilute-acid Alizarin-red-S and potassium ferricyanide solution to reveal calcite and ferroan dolomite. Thin sections were photographed using a Nikon Super Coolscan 5000 ED scanner. Dolomite crystals were classified using Gregg and Sibley's (1984) and Sibley and Gregg's (1987) dolomite textural classification system.

Logs for 28 wells were taken from the GeoScout database and compared to rock descriptions in

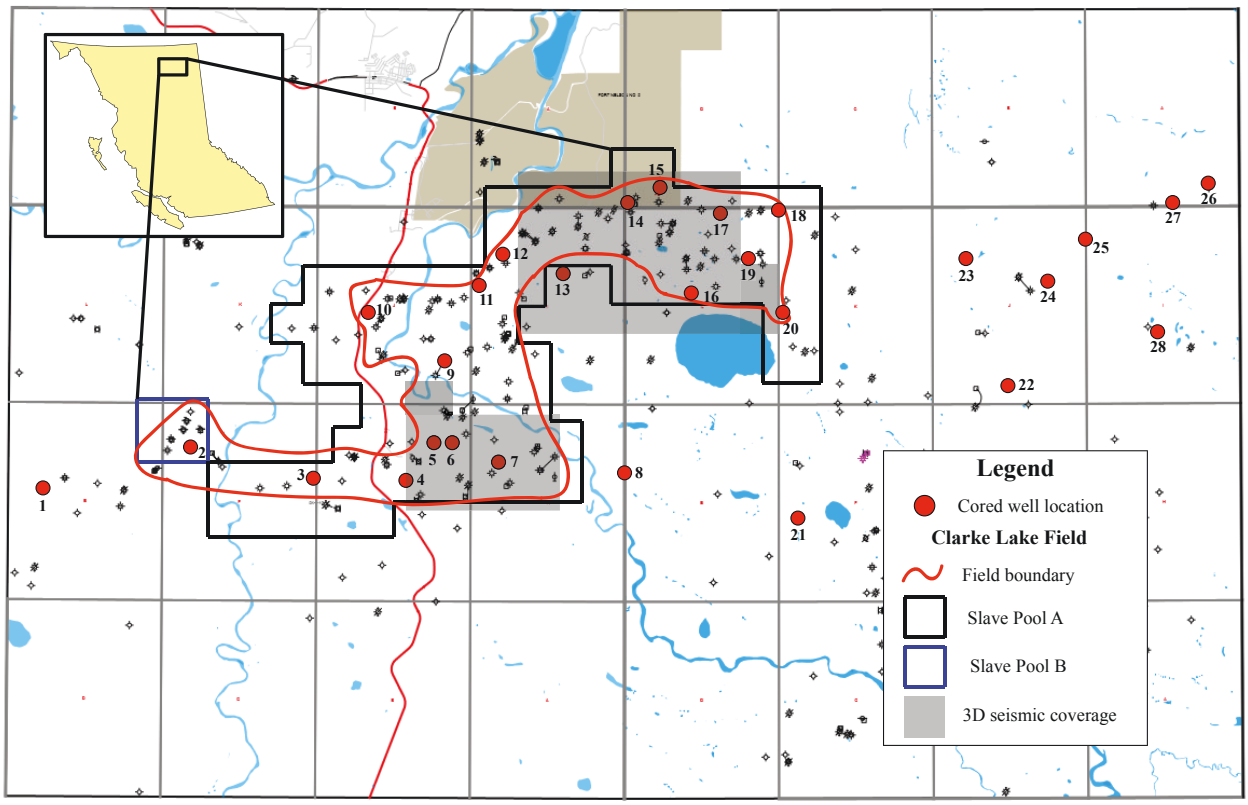

Figure 1.4: Locations of described core, 3D seismic coverage and the field boundary are shown. Slave Pool A is the main pool, while Slave Pool B is minor and is located in the southwest portion of the field boundary.

Map #	Well name	Well location
1	CANLIN MILO C- 058-E/094-J-10	200/c-058-E 094-J-10/00
2	CHEVRON MILO D- 079-F/094-J-10	200/d-079-F 094-J-10/00
3	CANLIN ET AL CLARKE A-061-F/094-J-10	200/a-061-F 094-J-10/00
4	CANLIN ET AL CLARKE A-065-G/094-J-10	200/a-065-G 094-J-10/00
5	CANLIN CLARKE A- 083-G/094-J-10	200/a-083-G 094-J-10/00
6	CANLIN CLARKE D- 072-G/094-J-10	200/d-072-G 094-J-10/00
7	CANLIN CLARKE D- 069-H/094-J-10	200/d-069-H 094-J-10/00
8	BA SHELL KLUA C- 070-E/094-J-09	200/c-070-E 094-J-09/00
9	CANLIN ET AL HZ CLARKE B-022-J/094-J-10	200/b-022-J 094-J-10/00
10	CANLIN CLARKE C- 047-J/094-J-10	200/c-047-J 094-J-10/00
11	CANLIN ET AL CLARKE B-070-I/094-J-10	200/b-070-I 094-J-10/00
12	CANLIN ET AL CLARKE C-078-I/094-J-10	200/c-078-I 094-J-10/00
13	CVE ENERGY CLARKE LAKE C-064-I/094-J-10	200/c-064-I 094-J-10/00
14	CANLIN CLARKE B- 010-D/094-J-16	200/b-010-D 094-J-16/00
15	CANLIN CLARKE B-A018-D/094-J-16	200/c-008-D 094-J-16/00
16	CANLIN CLARKE C- 056-L/094-J-09	200/c-056-L 094-J-09/00
17	CANLIN CLARKE C- 094-L/094-J-09	200/c-094-L 094-J-09/00
18	CANLIN CLARKE D- 091-L/094-J-09	200/d-091-L 094-J-09/00
19	CANLIN CLARKE B- 072-L/094-J-09	200/b-072-L 094-J-09/00
20	CANLIN CLARKE C- 050-K/094-J-09	200/c-050-K 094-J-09/00
21	BA SHELL KLUA B- 049-F/094-J-09	200/b-049-F 094-J-09/00
22	CNRL KLUA D- 006-J/094-J-09	200/d-006-J 094-J-09/00
23	CANLIN CLARKE B- 078-J/094-J-09	200/b-078-J 094-J-09/00
24	CHINOOK ET AL HOFFARD A-063-J/094-J-09	200/a-063-J 094-J-09/00
25	CHINOOK ET AL HOFFARD A-081-J/094-J-09	200/a-081-J 094-J-09/00
26	SRL HOFFARD B- 006-A/094-J-16	200/b-006-A 094-J-16/00
27	BP ENERGY GROUP CLARKE A-005-A/094-J-16	200/a-005-A 094-J-16/00
28	CNRL HOFFARD D- 036-I/094-J-09	200/d-036-I 094-J-09/00

Table 1.1: Name and location of cored wells.

order to identify common log responses representive of specific depositional or diagenetic facies. These log signatures provide a methodology for interpretation of facies where only well logs were available. Well-top data for 308 wells were available and used to construct structural maps of the Slave Point Formation.

Five 3D seismic cubes were provided by Canlin Energy and used to interpret the top of the Slave Point Formation in the northeast and southwest portions of the field. Velocity models were built in order to convert and correlate the seismic data with core and wireline log data by tying applicable wells to seismic data using compressional sonic log data. Synthetic seismic traces were created and shifted to produce an accurate time-depth relationship that allows stratigraphic and seismic horizons to be correlated. Check-shot survey and vertical seismic profile data were not available for this study.

We applied a facies model based on core descriptions within stratigraphic cross-sections to build a depositional model of the Slave Point Formation at Clarke Lake field, from which we delineated the most porous and permeable zones. All stratigraphic cross-sections were built using the Watt Mountain Formation as a datum. The top of the Slave Point Formation was picked (constrained by 3D seismic data) as well as internal flooding surfaces, which formed the basis of our static geomodels.

Porosity and permeability data were correlated to depositional and diagenetic facies to build reservoir models. A total of 256 porosity and permeability analyses for samples from the Slave Point Formation were available through the GeoScout database, including analyses both of small plugs and full cores taken the Slave Point Formation. An additional 62 porosity and permeability small plug analyses were completed for this study at AGAT Laboratories. The samples were selected within specific depositional facies and limestone or dolomite sections. Porosity was found by measuring the bulk density of samples using calipers, and the grain density was measured by a porosimeter using Boyle's Law. Permeability was measured with a steady-state permeameter. We transformed the geomodel into a geocellular model, allowing us to populate a grid with porosity and permeability. All data were viewed and interpreted using Petrel 2017 software.

1.4 Results

1.4.1 Facies

Four facies associations can be distinguished in the Slave Point Formation at Clarke Lake field. Facies Associations 1 to 3 consist of limestone with preserved depositional character, partially dolomitized carbonate rock in which depositional features are discernible, or are completely dolomitized carbonate rock with remnant depositional textures. Facies Association 4 consists of breccia and gray matrix dolomite formed in a diagenetic event that destroyed all original depositional character.

The extent of dolomitization has a direct effect on the quality of lithofacies interpretation. Because of this, careful attention was given to the size and shape of mouldic pores in completely dolomitized rocks, which generally represent the pre-alteration bioclast assemblage and depositional facies. Depositional facies were classified based on bioclast type, abundance and size; additional features noted include the presence of dolomite or limestone, sedimentary structures, texture and pore types. Diagenetic facies were classified based on pore types and the dominance of breccia or gray matrix dolomite.

1.4.2 Facies Descriptions (Depositional)

Facies Association 1

Facies within this association are commonly composed of mudstone, wackestone or packstone, and generally show relatively small, non-robust bioclasts. *Amphipora,* of the *Stromatoporoidea* subclass, is common in all.

1A: *Stachyodes* **/ Nodular Stromatoporoid / Coral Wackestone to Packstone**

Facies 1A consists of abundant *Stachyodes* of the *Stromatoporoidea* subclass, nodular stromatoporoids and coral bioclasts (Fig. 1.5A, 1.5B) in a wackestone to packstone matrix. *Amphipora* bioclasts also occur in this facies. The matrix is mainly composed of micrite and skeletal fragments with scattered calcispheres, ostracods and peloids. Fracturing of bioclasts is common.

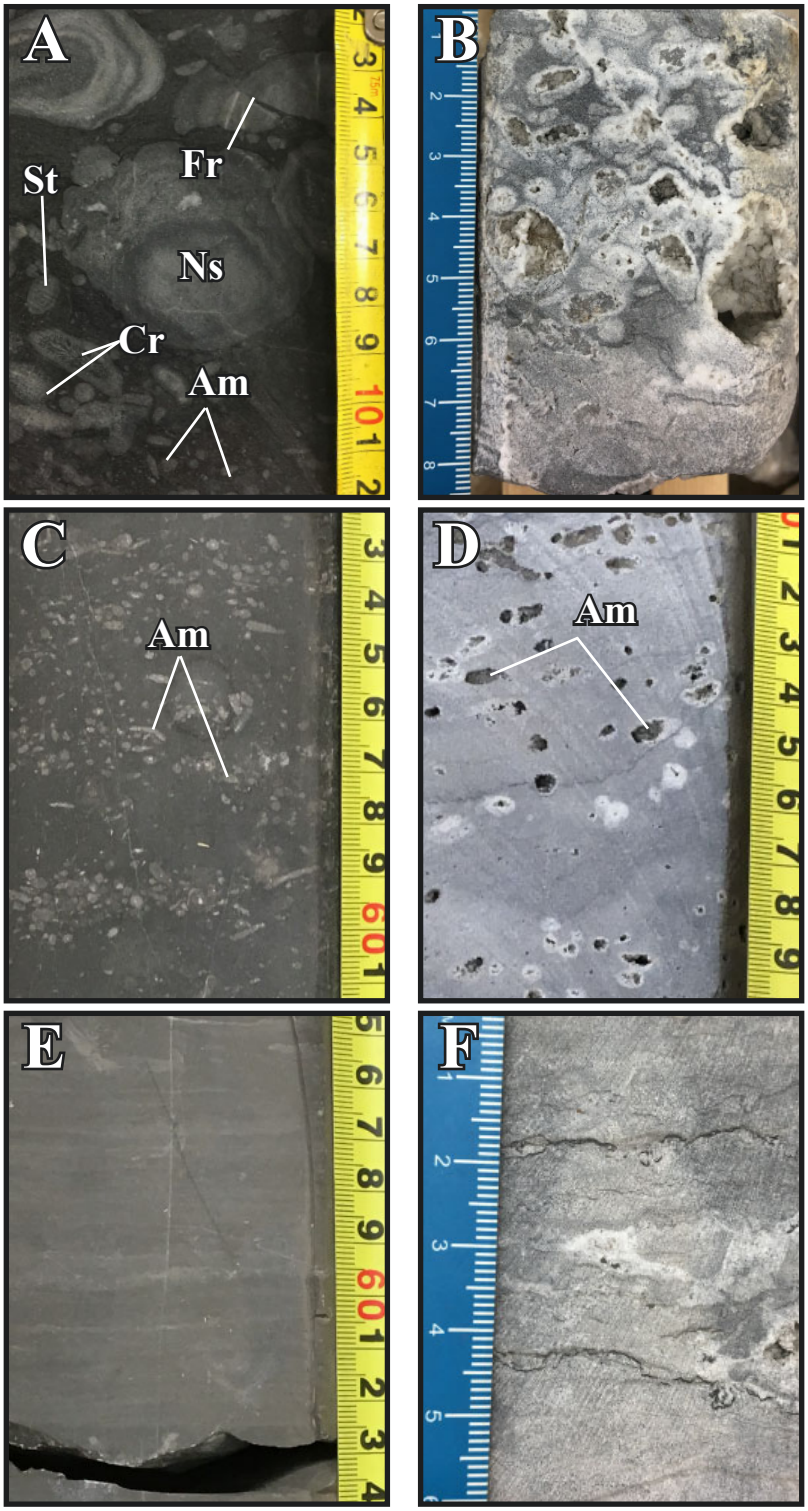

Figure 1.5: Facies Association 1. (A) Limestone Facies 1A showing a wackestone with nodular stromatoporoids (Ns), corals (Cr), *Stachyodes* (St), and *Amphipora* (Am) and a fractured nodular stromatoporoid (Fr). (B) Dolomitized Facies 1A showing leached bioclasts varying in size. (C) Limestone Facies 1B showing *Amphipora* wackestone and packstone. (D) Dolomitized Facies 1B showing leached *Amphipora* bioclasts (Am). (E) Limestone Facies 1C showing weak lamination. (F) Dolomitized Facies 1C showing minor amounts of porosity.

Packstone intervals vary from 10 cm to 20 cm in thickness, whereas wackestone intervals are usually thicker, locally exceeding 2 m, and share a gradational contact with packstone intervals.

Bioclasts within wackestone intervals lack any obvious sorting, but are deposited irregularly throughout. Bioclast assemblages vary, with some sections being predominantly composed of *Stachyodes* and coral and some dominantly composed of larger nodular stromatoporoids.

1B: ***Amphipora*** **Wackestone to Grainstone**

The primary constituent of Facies 1B is small (1 – 4 mm) *Amphipora* bioclasts (Fig. 1.5C, 1.5D), with minor *Stachyodes*, nodular stromatoporoids and corals. A matrix is composed mainly of peloids, micrite and skeletal fragments with scattered calcispheres and ostracods. Bioclasts are generally smaller in this facies than in Facies 1A. This facies shows minor intervals composed of 2 – 4 cm nodular stromatoporoid wackstones with scattered *Amphipora*. Some nodular stromatoporoids encrust coral bioclasts. Stylolites exist throughout, commonly occurring between intervals with higher concentrations of *Amphipora* and underlying sections with nodular stromatoporoid and scattered *Amphipora* sections; they vary in amplitude from 1 - 10 cm. Fractured

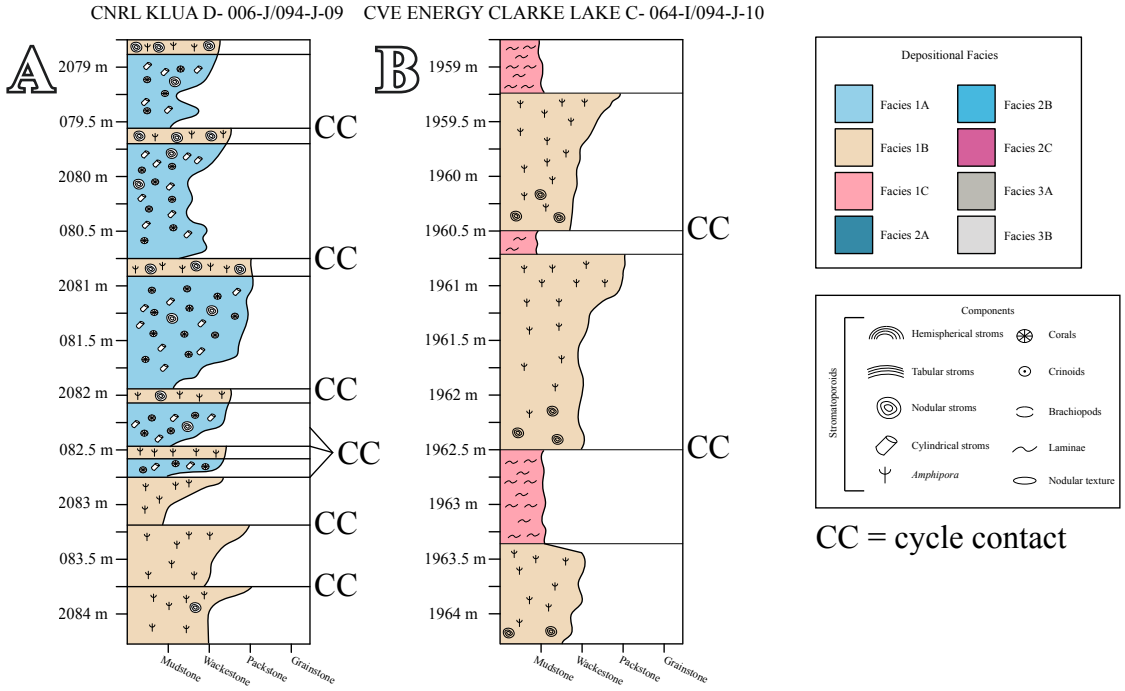

Figure 1.6: Facies Association 1 stacking patterns. (A) The typical stacking pattern shown between Facies 1B and Facies 1A. (B) The typical stacking pattern shown between Facies 1B and Facies 1C.

grains and rip-up clasts are present, but rare.

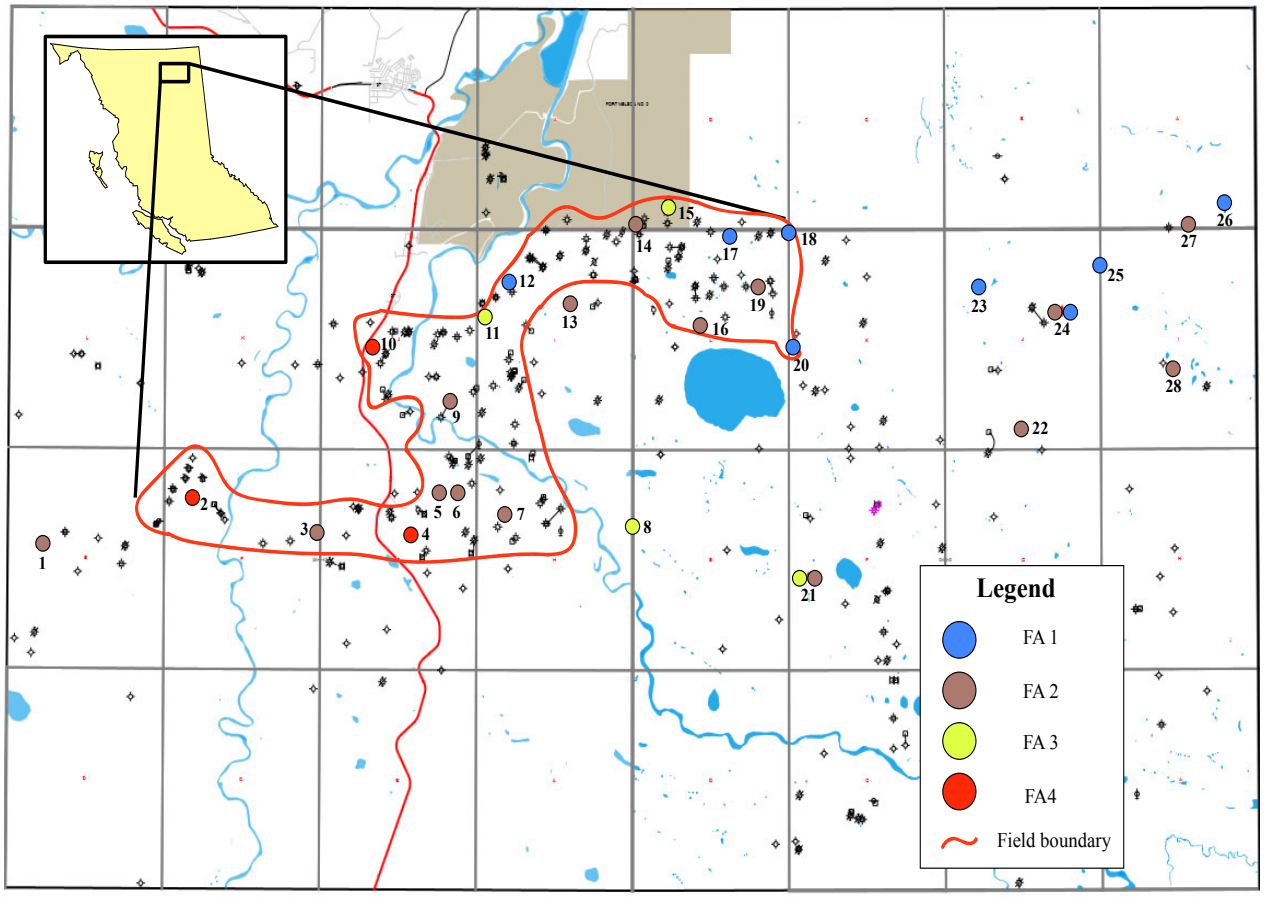

Figure 1.7: Location of core showing facies associations. Numbered core showing two circles denotes cores showing two facies associations.

1C: Brown / Gray Lime Mudstone

Facies 1C consists of gray or brown mudstone composed mainly of peloids and micrite with scattered skeletal fragments, ranging from well-laminated to unlaminated (Fig. 1.5E, 1.5F). Bioclasts are generally absent where the rock is well laminated, whereas weakly laminated to unlaminated sections show minor occurrences of *Amphipora* and ostracods. Organic-rich laminae were also observed in some of the sections. Differentiating between dolomitized mudstone deposits of Facies 1C and dolomitized nodular wackestones and *Amphipora* wackestone sections of Facies 1B is locally difficult because both facies conatin small intervals devoid of bioclasts, and the matrix minerals are completely replaced by gray matrix dolomite.

1D: *Stachyodes* **/ Coral Wackestone to Packstone**

This facies is mainly composed of *Stachyodes* and coral bioclasts with minor lamellar stromatoporoid intervals. Thin (~ 2 cm) intervals showing crinoid ossicles are present throughout. *Stachyodes* show a digitate form, and vary from 1 - 6 cm in length. A matrix is composed of micritic mudstone. Broken bioclasts are common throughout this facies. Laminar stromatoporoids are mostly concentrated within thin (1-5 cm) packstone intervals and are more rarely seen in ~ 3 cm grainstone intervals. This facies forms a minor component of Facies Association 1.

Stratigraphic Relationships within FA 1

Two shallowing-upward profiles are seen in FA1. In the first, a 0.5 -1 m interval of Facies 1A occurs above a gradational contact, which gradually becomes more abundant in nodular stromatoporoids, corals and *Stachyodes* before gradationally transitioning into a small (10 - 20 cm) layer of Facies 1B (Fig. 1.6A). The second pattern shows a sharp to gradational contact underlying a 1 – 1.75 m wackestone to packstone interval of Facies 1B, which gradationally to sharply underlies a 0.25 – 0.75 m interval of Facies 1C (Fig. 1.6B). This same pattern is observed with smaller intervals of Facies 1B (1 - 4 cm) that are organic-rich. Less commonly, Facies 1C is absent from the stacking pattern and a sharp contact underlies Facies 1B wackstone, which gradationally transitions into Facies 1B packstone (or more rarely, grainstone). Facies 3A and 3B (described below) gradationally underlie crinoidal wackstone and mudstone of Facies 1D. These stacking patterns reflect cyclicity, which will be discussed below.

Facies 1A was identified in cores along the north edge of the field (Fig. 1.7; cores 3, 6 and 14), within the field (core 7), and east of the field boundary (cores 22 and 24). Facies 1B is present throughout the field (in cores 1, 3, 5, 6, 9, 13, 16, 19, 21) and east of the field boundary (cores 22, 24, 27 and 28). Facies 1C is present throughout the field (cores 6, 13, 16) and east of the field boundary (cores 22 and 28). Facies 1D is present in one core, south of the field boundary (core 21).

Facies Association 2

This facies association typically occurs as packstones or grainstones composed of relatively large, robust forms of stromatoporoids, the most common being *Stachyodes*. The bioclast assemblage is the most diverse of the facies associations.

2A: Massive Stromatoporoid Boundstone

Facies 2A is represented by laterally continuous intervals of predominantly large hemispherical or massive stromatoporoids (Fig. 1.8A, 1.8B). Intervals of this facies are up to 50 cm thick in core and comprises a minor part of Facies Association 2. Observation of this facies within dolomitized sections is difficult but possible due to selective dolomite replacement of the stromatoporoid fabric (Fig 1.7B), especially in partially dolomitized sections.

2B: *Stachyodes* **Wackestone to Grainstone**

Facies 2B represents the majority of Facies Association 2 and is composed mostly of *Stachyodes* stromatoporoids (Fig. 1.8C, 1.8D). The matrix consists of brown wackestone to grainstone with skeletal fragments (up to 3 cm in length), crinoids and brachiopod fragments. Minor bioclasts are diverse and include *Amphipora*, crinoids, tabular stromatoporoids, hemispherical stromatoporoids and corals. Facies 2B locally shows a distinct black colour due to hydrothermally altered components that obscure depositional fabrics.

2C: Tabular Stromatoporoid Wackestone to Grainstone

Facies 2C is dominated by tabular stromatoporoids and *Stachyodes*. Minor bioclasts include corals, crinoids and gastropods. The matrix is a dark gray skeletal mudstone to wackestone. This facies is a minor component of Facies Association 2, typically forming intervals only ~10 cm thick, but locally thicker (5 m grainstone intervals).

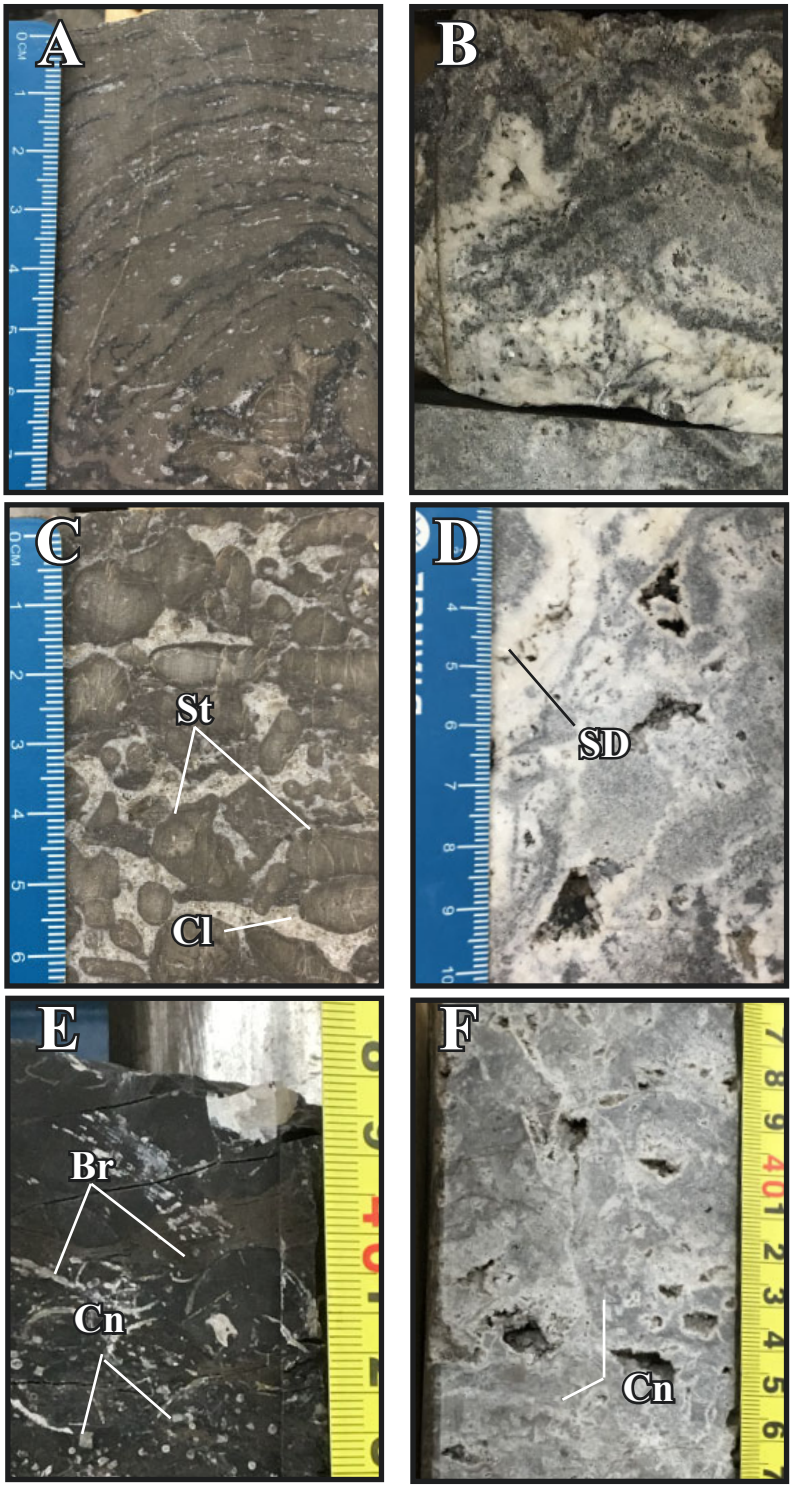

Figure 1.8: Facies Association 2 and 3. (A) Limestone Facies 2A showing a hemispherical stromatoporoid boundstone. (B) Dolomitized Facies 2A showing relict hemispherical stromatoporoids. (C) Limestone Facies 2B showing *Stachyodes* (St) packstone with interparticle calcite cement (Cl). (D) Dolomitized Facies 2B with vuggy porosity and coarse saddle dolomite crystals (SD). (E) Limestone Facies 3A wackestone with crinoids (Cn) and brachiopod shell fragments (Br). (F) Dolomitized Facies 3A showing vuggy porosity and crinoid bioclasts replaced by dolomite (Cn).

Facies Association 3

This facies association is composed of mudstone or wackestone with relatively low diversity and concentrations of bioclasts. Crinoids and brachiopods make up the majority of the observed bioclasts.

3A: Crinoidal Wackestone

Facies 3A is a dark gray/black wackestone with crinoids, skeletal fragments and large (up to 3.5 cm) brachiopod shells and shell fragments (Fig. 1.8E, 1.8F). There are also minor occurrences of *Stachyodes* bioclasts. The matrix is dark gray/black lime mudstone, displaying some soft sediment deformation. Pyrite mineralization occurs throughout limestone and dolomite cored intervals.

3B: Crinoidal Mudstone

Facies 3B is a dark gray/black lime mudstone with lower bioclast density than Facies 3A (Fig 1.10A, 1.10B). Minor crinoid ossicles, skeletal fragments and rare brachiopod shells constitute the bioclast assemblage. Some intervals are completely devoid of bioclasts. Replacement of bioclasts by silica and calcite is present. Facies 3B intervals are thicker than Facies 3A, typically 0.9 to 2 m.

Stratigraphic relationships within FA 3

The typical stacking pattern shows a 0.9 – 2 m thick interval of Facies 3B, which sharply underlies small (7 - 20 cm), cemented layers of Facies 3A (Fig. 1.9B). Facies 3B also shares a sharp contact showing rip up clasts with overlying Facies 1B deposits. Finally, Facies 4B shows a gradational to sharp contact with overlying Facies 1D. These stacking patterns reflect cyclicity and are discussed in detail below. These facies are present in cores south of the field (cores 8 and 21) and within the top 30 meters of the Slave Point Formation within wells close to the north boundary of the field (cores 11 and 15) (Fig. 1.7).

Stratigraphic relationships within FA 2

Facies Association 2 usually shows an amalgamated nature with no distinct pattern in facies stacking. Facies 2A and 2B locally occur in stratigraphic association, where 0.5 – 0.75 m intervals of *Stachyodes* grainstone or packstone of Facies 2B sharply overlie and underlie ~ 0.25 m sections of Facies 2A (Fig. 1.9A). A gradational or sharp contact occurs below ~ 0.75 m thick laminar stromatoporoid wackestone of Facies 2C before grading upward into *Stachyodes* packstone or grainstone of Facies 2B (Fig. 1.8). In one core, a 30 cm section of fissile shale sharply overlies Facies 2B deposits. The amalgamated and poorly cyclic nature of these deposits will be discussed below.

Cores showing Facies Association 2 are located along the northern edge of the field boundary (Fig. 1.7; cores 12, 17, 18), the eastern edge of the field (core 20) and east of the field boundary (cores 23, 24, 25 and 26).

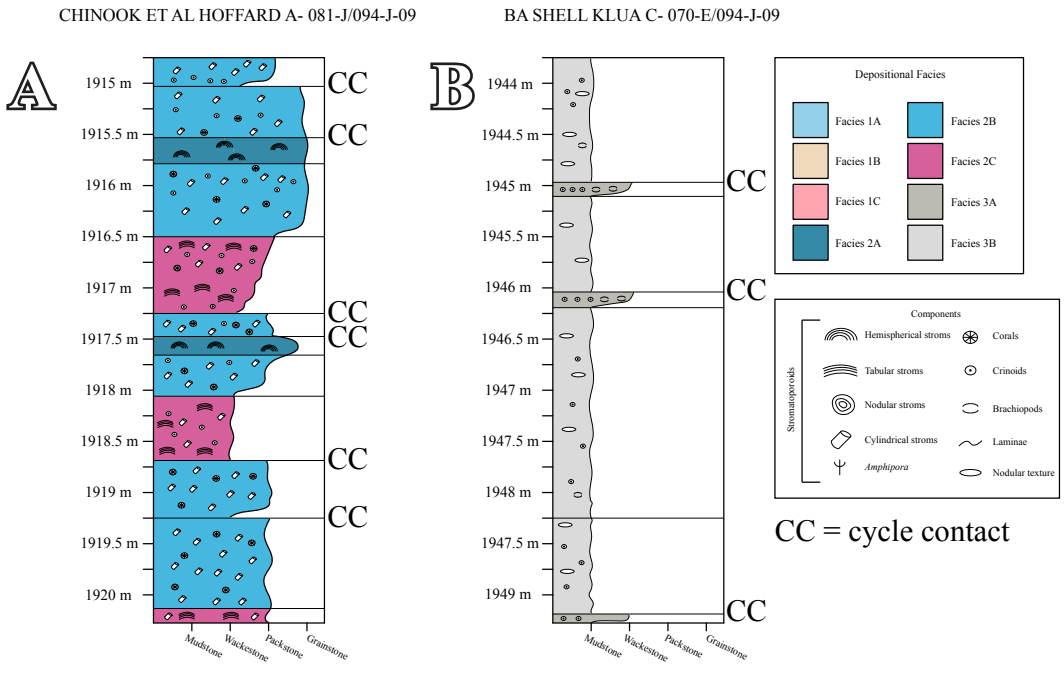

Figure 1.9: Facies Association 2 and 3 stacking patterns. (A) The typical stacking pattern shown between Facies 2A, 2B and 2C. (B) The typical stacking pattern between Facies 3A and Facies 3B.

1.4.3 Facies Descriptions (Diagenetic)

Facies Association 4

This facies association includes altered rock that is predominantly composed of saddle or gray matrix dolomite. Depositional features in are completely overprinted and remnant bioclasts are not observable.

4A: Breccia

Facies 4A is breccia with rounded to angular clasts that vary in length (1 – 5 cm). Angular clasts are composed of mudstone, gray matrix dolomite or saddle dolomite and are separated by saddle dolomite veins or gray matrix dolomite (Fig. 1.10C, 1.10D) Rounded clasts are cut by large saddle dolomite veins (Fig. 1.9E). Fractures are common throughout and show no preferential orientation. White saddle dolomite forms a significant portion of this facies, locally comprising 100% of cored intervals. Fluorite mineralization is prevalent throughout this facies, present as an alteration product of dolomite. Sulphide mineralization is present with higher concentrations toward the stratigraphically lower portion of cored intervals. Facies 4A is found in the southwest and west area of the field (in cores 2, 4 and 10) (Fig. 1.7).

4B: Gray Matrix Dolomite

Facies 4B represents sections of rock where depositional character has been entirely destroyed and replaced with gray matrix dolomite with minor saddle dolomite (Fig. 1.10F) and is differentiated from Facies 4A by the absence of significant quantities of saddle dolomite and brecciated clasts. Saddle dolomite in this facies primarily occurs as partial infill within vugs. Stylolites and subvertical to subhorizontal fractures are common. Bioclasts are rare but can be identified from the size and shape of mouldic pores that have been filled by dolomite. Ghosts of clasts are commonly visible throughout this facies. Facies 4A and 4B occur in distinct intervals of variable thickness. Facies 4B is found in the southwest area of the field (in cores 2 and 4) (Fig. 1.7).

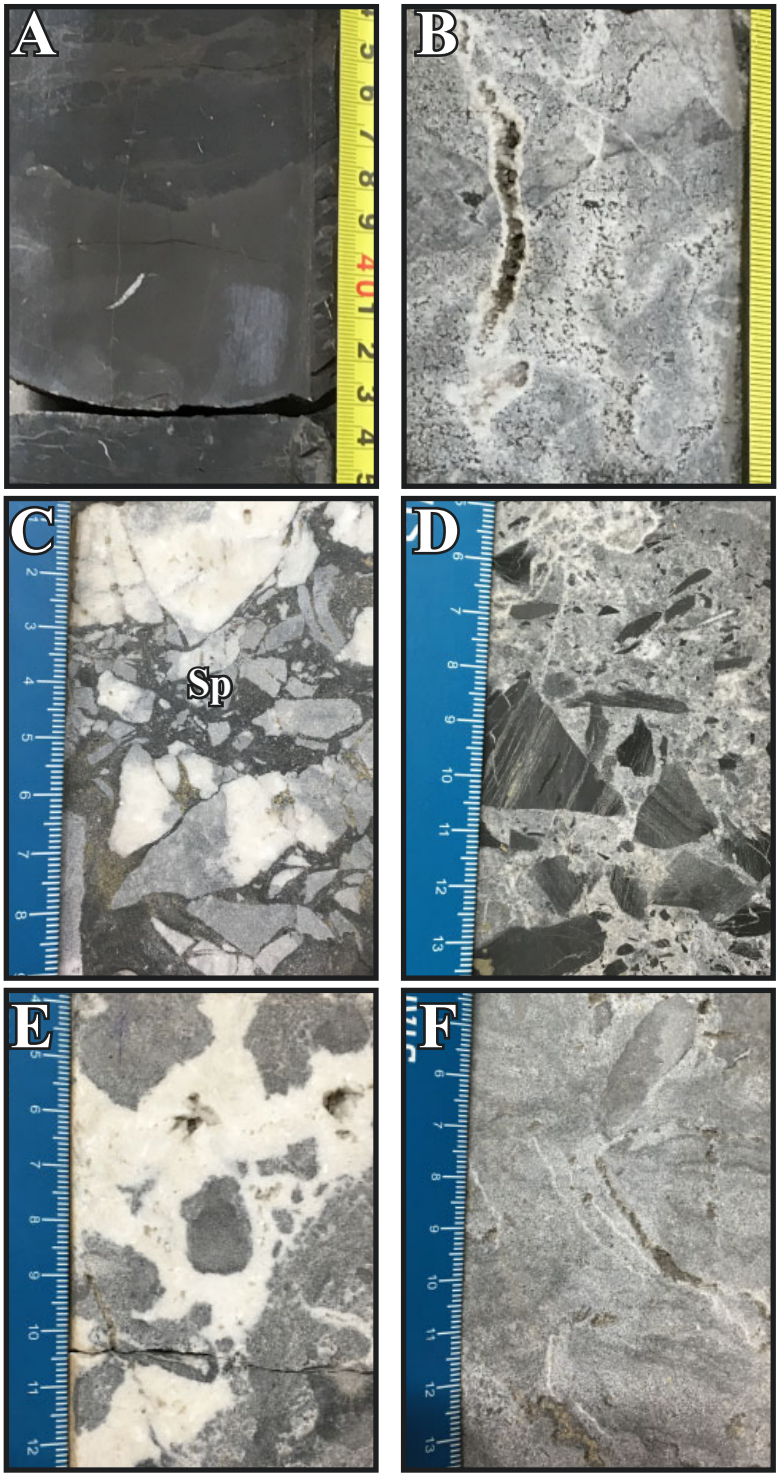

Figure 1.10: Facies Association 3 and 4. (A) Limestone of Facies 3B showing nodular mudstone that is largely devoid of bioclasts. (B) Dolomitized Facies 3B showing a large fracture. (C) Facies 4A breccia with angular clasts composed of GMD and SD. Sulpide mineralization (Sp) is present in the dark coloured matrix. (D) Facies 4A breccia with angular clasts composed of laminated mudstone. (E) Facies 4A breccia showing rounded clasts of GMD within a coarse white saddle dolomite matrix. (F) Facies 4B gray matrix dolomite.

1.4.4 Diagenesis and Pore Systems

The effect of diagenesis on the Slave Point Formation is observed throughout most of the dolomitized and limestone facies. The most common diagenetic features in limestone facies are coarse crystalline calcite cementation of interparticle and intraparticle pores and stylolite development. In dolomite facies, two main dolomite types were recognized: gray matrix dolomite and saddle dolomite. Gray matrix dolomite is composed of relatively fine, closely packed anhedral dolomite crystals with curved, lobate, serrated or irregular boundaries (nonplanar-a), whereas saddle dolomite is composed of coarse, saddle dolomite crystals. Subhedral to anhedral crystals with straight boundaries (planar-s) and euhedral crystals lining pores and vugs (planar-c) form a minor component of observed dolomite. Fluorite is identified in dolomitized facies and is relatively abundant in Facies Association 2 (where it composes 90% of the observable mineral assemblages individual thin sections) and is less abundant in other facies associations. Sulphide mineralization occurs in Facies Association 4. Limestone, dolomite and mixed lithology facies show fracturing, but fracturing density is highest in dolomite. Stylolites are common throughout dolomitized and mixed lithology facies.

Dolomite Porosity

Significant secondary porosity observed in dolomite facies is attributed to diagenetic alteration of the host limestone. Intercrystalline pores are rare in dolomite facies, which are mostly occluded by dolomite, fluorite or pyrobitumen. Fracture porosity is most commonly observed in Facies Association 4 (but present within all facies), where it is partially to fully cemented by dolomite or fluorite and sometimes lined or occluded by pyrobitumen (Fig. 1.11A, 1.11B). The dominant pore types in dolomitized and partially dolomitized intervals are mouldic and vuggy. Mouldic and vuggy pores are cemented by coarse, nonplanar-a, planar-s or saddle dolomite crystals or partially cemented by planar-c or saddle dolomite crystals (Fig. 1.11C, 1.11D, 1.11E). Planar-s crystals are often seen as cement within ghosts of bioclasts. Facies associations 1 and 3 generally show a higher proportion of mouldic pores and less cement fill compared to facies associations 2 and 4, which show predominantly vuggy pores that are almost completely filled by relatively coarse saddle or planar-c dolomite crystals.

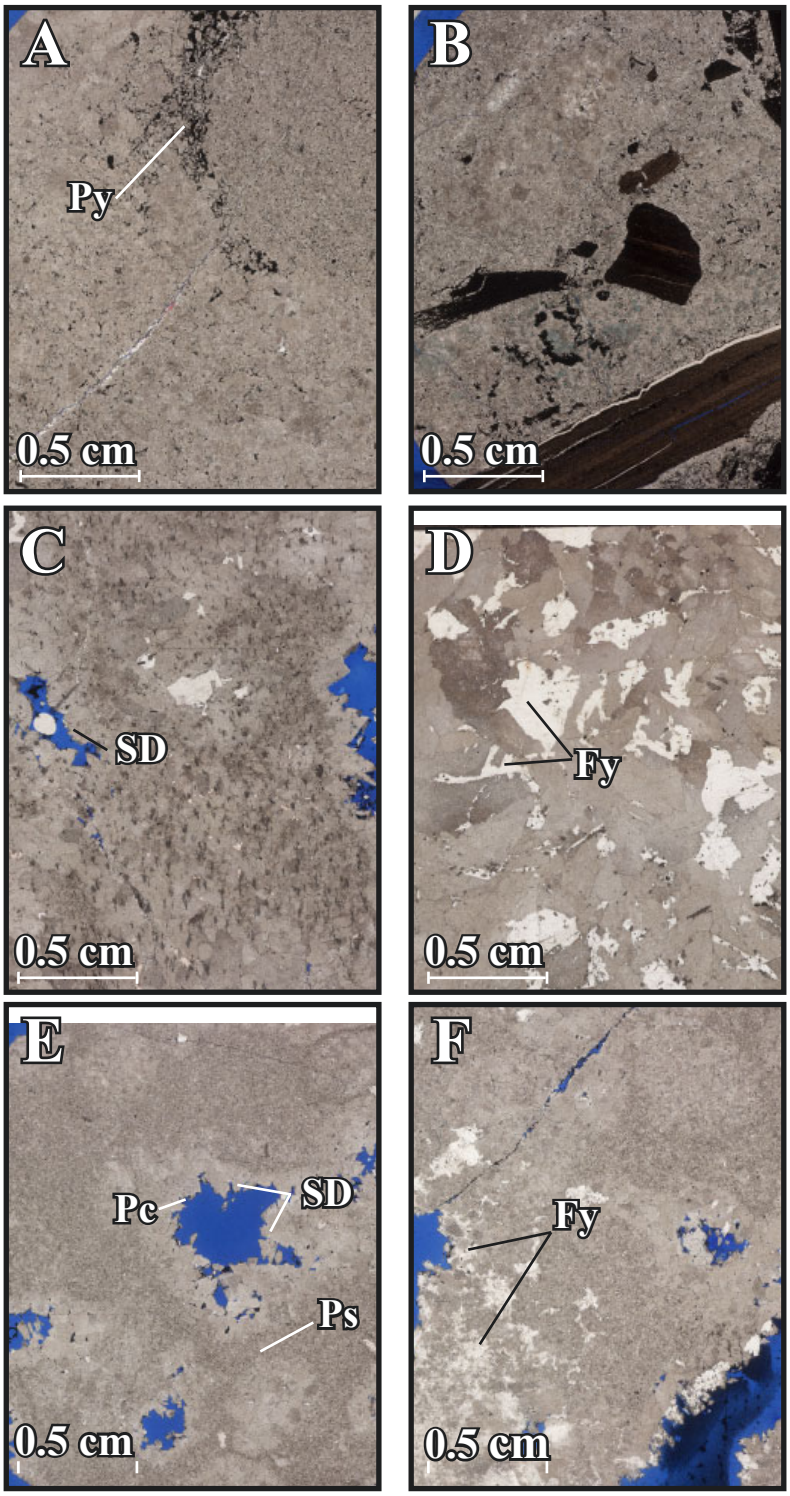

Figure 1.11: Pore types in thin section. (A) Fracture porosity present in Facies Association 4 and minor pyrobitumen (Py) occluding intercrystalline porosity. (B) Mudstone clasts with fractures cemented by dolomite and fluorite. (C) Vuggy porosity that is partially cemented by planar-c or saddle dolomite crystals. (D) Coarse saddle dolomite crystals with fluorite mineralization (Fy). (E) Mouldic porosity partially cemented by planar-c (Pc) or saddle dolomite (SD) crystals or fully cemented by planar-s (Ps) dolomite crystals. (F) Mouldic and fracture porosity with fluorite.

Mixed Dolomite/Limestone Porosity

Mixed lithology intervals are rare, and calcite makes up at most 5 % of the total observable minerals in thin section. Since the dolomite fraction in these samples is 95 %, the pore system parallels that observed in dolomite intervals. In such intervals, vuggy and mouldic porosity is the most significant, and fracture or intercrystalline pores are less common.

Limestone Porosity

Primary porosity in limestone intervals is poorly developed and restricted to interparticle and intraparticle pores. These pores are almost always cemented by calcite except in rare occurrences, where there is visible interparticle porosity. Interparticle porosity is more evident in Facies Association 2, where the grainstone matrix is completely cemented by fine calcite crystals. In facies associations 1 and 3, intraparticle pores are common within the central canals of stromatoporoids or within coral bioclasts, but are cemented by coarse calcite crystals.

1.4.5 Well-Log Character of Depositional Facies

Identification of facies from well logs is difficult, partly due to poor core recovery (leading to inaccuracy in matching core features to well logs) and also because the available well logs do not readily show depositional variation observed in core. However, some relationships viewed in core can be interpreted in the gamma ray log. The common cycle of *Amphipora* wackestone, packstone and grainstone of Facies 1B and mudstone of Facies 1C can be seen in the gamma ray log response, where Facies 1C layers are indicated by subtly higher gamma ray responses (Fig. 1.12A and 1.12B). Facies 2A and 2B deposits show the lowest gamma ray response, the cleanest intervals reading 2.85 API. This relationship can be seen in Figure 1.12C, where a gamma ray response of 3.7 API associated with Facies 2B sharply underlies a shale bed with a response of 37.6 API.

1.4.6 Well-Log Character of Dolomite

The photoelectric log effectively distinguishes dolomite from limestone, yielding values of ~3.0

barns/electron for dolomite and ~5.0 barns/electron for limestone. Increases in resistivity, density porosity, sonic two-way travel time and decreases in porosity/neutron counts also indicate transitions from dolomite to limestone (Fig 1.13). Extremely high PE log responses of 6 – 17 barns/electron may be associated with sulphide and fluorite mineralization, which is present in Facies Association 4.

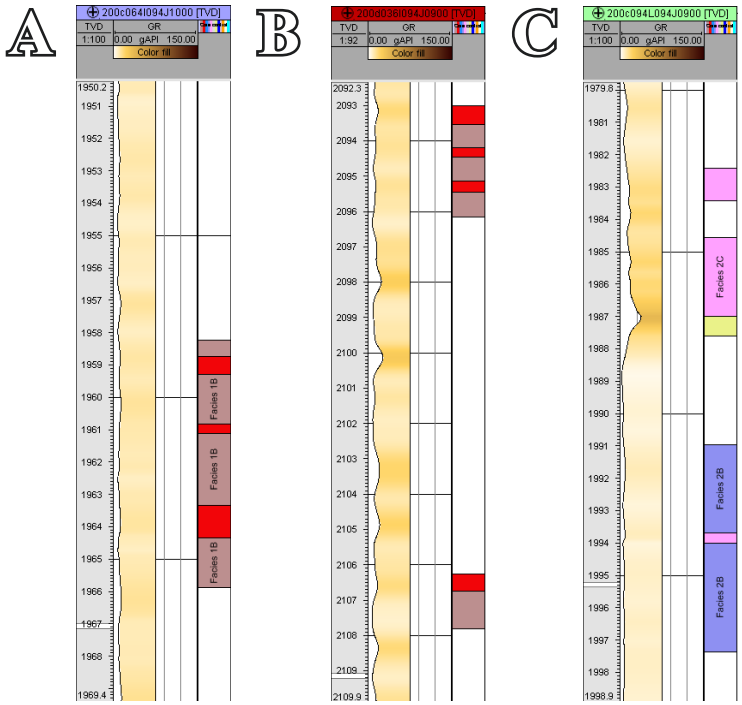

Figure 1.12: Facies interpreted from gamma ray log. (A, B) The typical stacking pattern between Facies 1B and 1C is shown by the gamma ray log, where Facies 1C shows slightly higher gamma ray response compared to Facies 1B, which shows slightly lower gamma ray response. (C) Facies Association 2 deposits over top of Facies 1A is shown by a decrease in the overall gamma ray response after transitioning from Facies 1A into Facies 2C.

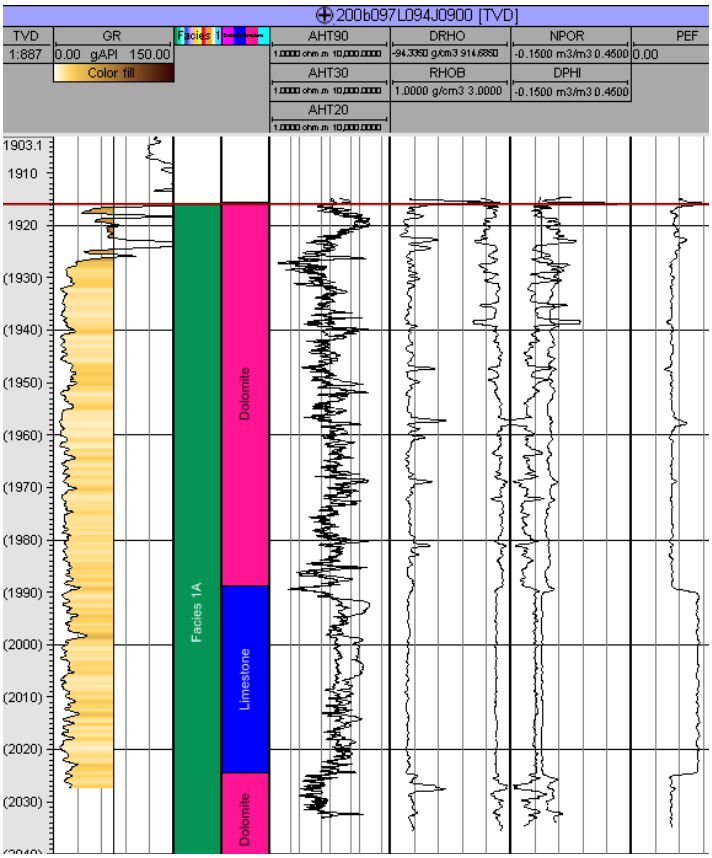

Figure 1.13: Typical well log responses that differentiate dolomite and limestone intervals.

1.4.7 Controls on Petrophysical Properties

Sampling for routine core analysis was focused on a comparison of dolomite and limestone intervals. Facies 1D, 2B and 2C were not sampled because they were not dolomitized or because they comprised insignificant portions of the described core. Limestone cored intervals of Facies Association 3 showed no visible porosity and contained 95 – 100 % mud and were also not sampled.

Petrophysical readings are clearly controlled by lithology (Fig. 1.14). Limestone samples generally have both low porosity and permeability, while dolomite and dolomite-limestone mixed samples show higher porosity and permeability. Mean values are plotted using log values on the y-axis. Porosity and permeability mean values for limestone are 2.5 % and 0.7 md, respectively. Mean values for dolomite are 6.4 % and 104 md and for mixed lithologies are 8.4 % and 81 md.

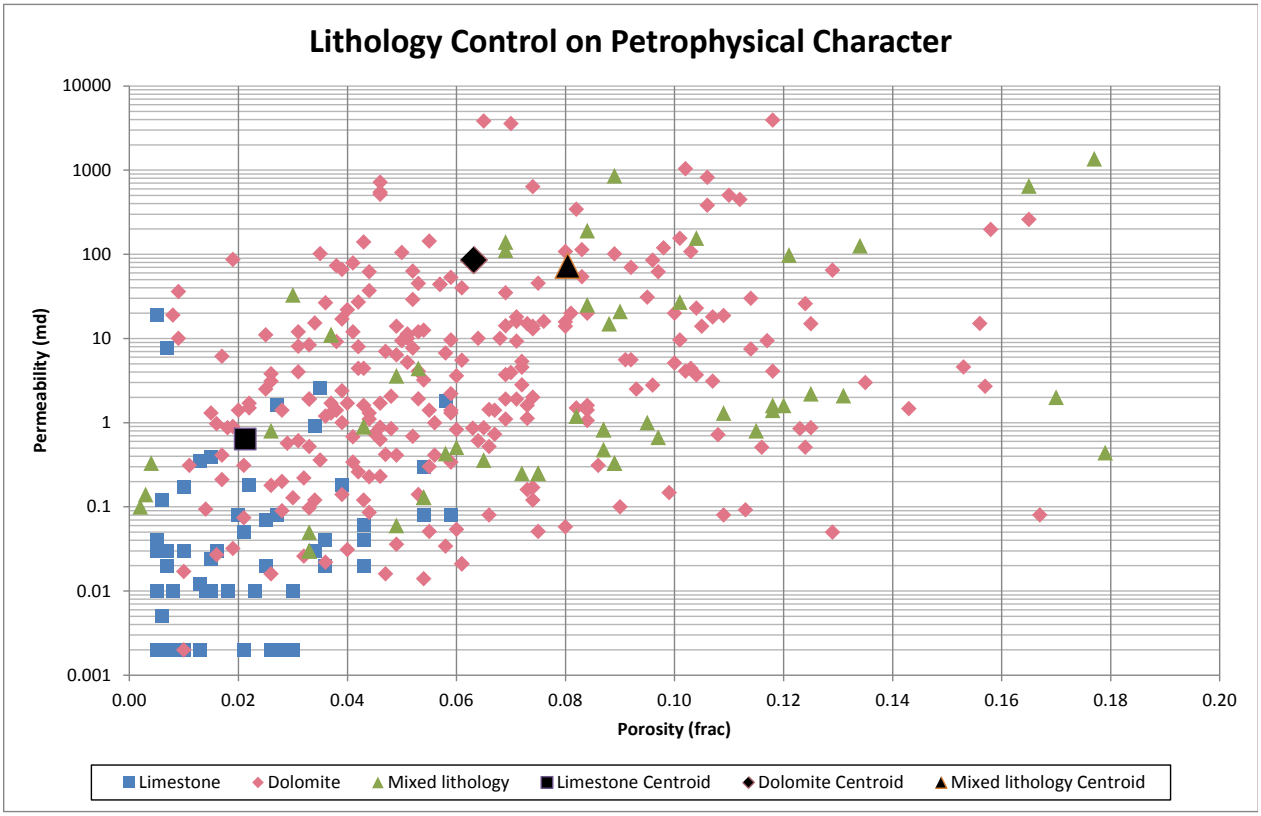

Figure 1.14: Petrophysical data points showing porosity and permeability for dolomite samples (pink diamond), limestone (blue square), or mixed lithology (green triangle).

Lithofacies also exert a control on petrophysical properties, although this is less pronounced than lithology. Facies associations 1 and 3 are characterized by relatively high porosities and low permeabilities (Fig. 1.15A; 1.15B; 1.15C; 1.15E), whereas facies associations 2 and 4 are characterized by relatively high permeabilities and low porosities (Fig. 1.15D; 1.15F; 1.15G). Porosity and permeability mean values for dolomite samples of Facies Association 1 are 7.3 % and 43 md, respectively, compared to 6.4 % and 56 md in Facies Association 2, 10.3 % and 72 md for Facies Association 3 and 4.9 % and 175 md for Facies Association 4.Facies 1A and 1B are more porous and permeable than Facies 1C. Facies 4A and 4B both show low porosity, but Facies 4A is more permeable than Facies 4B. Average porosity and permeability are shown in Table 1.2.

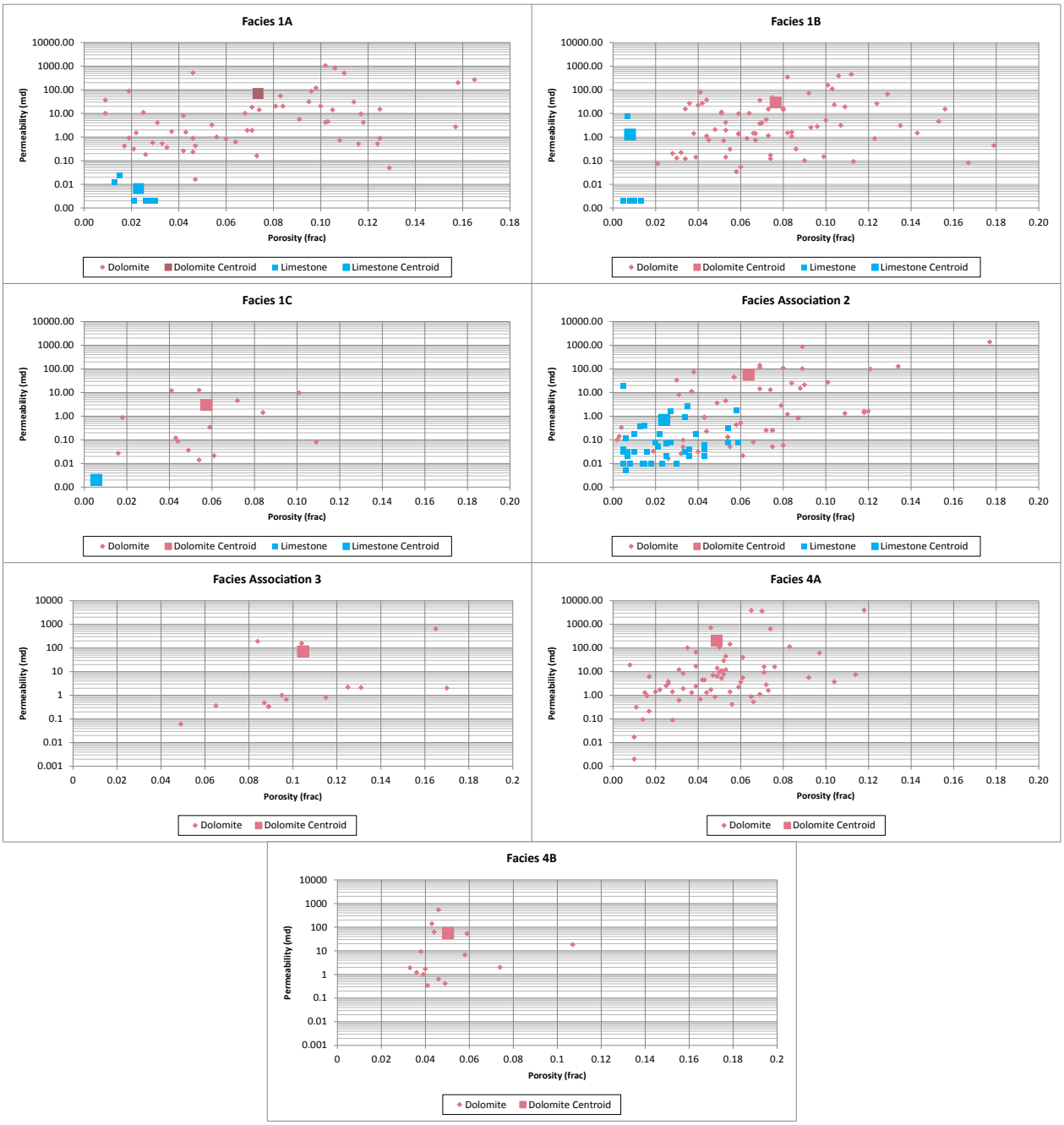

Figure 1.15: Petrophysical data points showing porosity and permeability for samples taken from depositional and diagenetic facies. Pink data points indicate dolomite samples, whereas blue data points indicate limestone samples.

Facies	Average porosity (%)	Average permeability (md)
Facies 1A	7.3	69
Facies 1B	7.6	29
Facies 1C	6	3
Facies Association 2	6.4	56
Facies Association 3	10.4	72
Facies 4A	4.9	204
Facies 4B	5	57

Table 1.2: Average porosity and permeability for Facies and Facies Associations.

1.4.8 Seismic Reflection Characteristics

Seismic data were used to map the top of the Slave Point Formation, specifically delineating the reef transition from platform to foreslope in the field (Fig. 1.16). Also of note were small (~ 1.3 km diameter), subrounded troughs in the reef interior that show a maximum of 75 m in relief (measured from the trough bottom to the top of Slave Point Formation) within the northeast and southwest portions of the field. Topographically high locations elongated parallel to the reef margin that are ~ 0.75 km in width and up to ~ 4 km in length within the northeast and southwest portion of the field were also observed (Fig. 1.16).

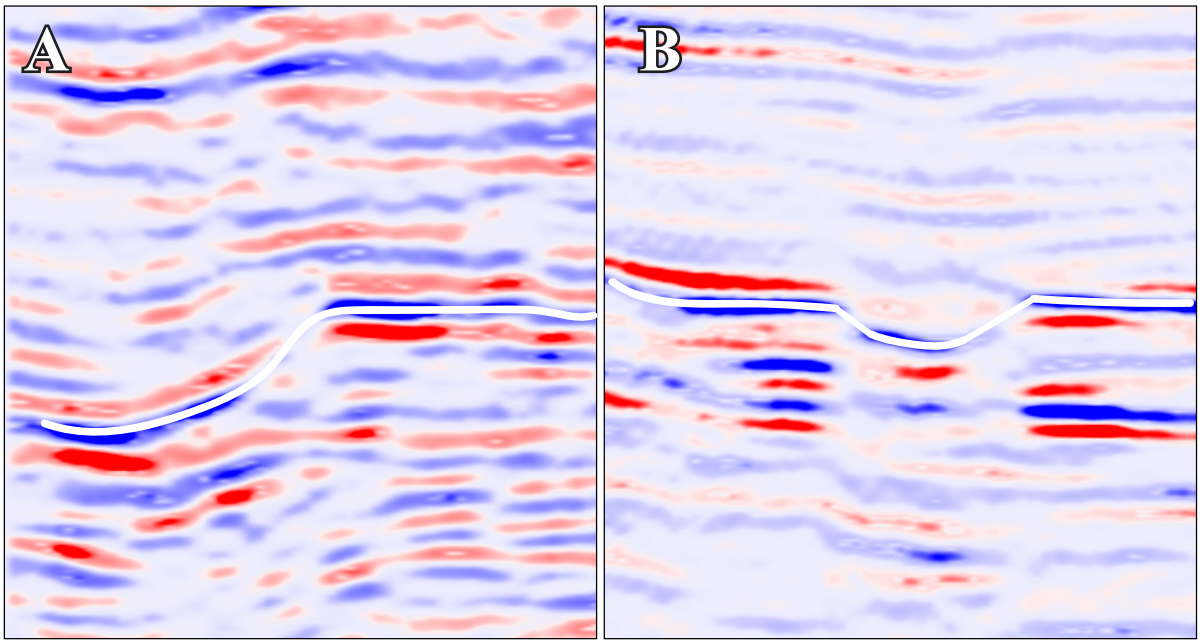

Figure 1.16: (A) A seismic horizon (highlighted in white) that shows a transition from a flat surface into a slope, resembling a platform to foreslope transition. (B) A seismic horizon (highlighted in white) that shows localized vertical displacement (right).

1.5 Discussion

1.5.1 Depositional Facies Interpretation

We apply the depositional model of a rimmed carbonate platform and an unrimmed carbonate platform to the Slave Point Formation sediments at Clarke Lake field. The rimmed carbonate depositional model follows Wendte's (1992) model for the Swan Hills Formation at Judy Creek field, Alberta, which shares markedly similar depositional facies to Clarke Lake (Fig. 1.17). The model depicts a relatively low-energy reef interior comprising lagoonal and tidal deposits and a higher energy platform margin with reef flat deposits. Beyond the reef margin is the upper slope with high energy deposits, whereas further down the slope are increasingly lower-energy deposits in a basinal depositional setting. Where this model is not applicable, we apply the depositional model of an unrimmed carbonate platform (Cutler, 1983).

Dunham and Crawford (1983) noted the consistency in the description of Devonian facies across the world, and many reservoir studies in Alberta and British Columbia reflect this consistency. In general, facies at Clarke Lake are similar to facies at Gift Lake, Slave, Golden, Evi, Otter, Seal, Norman Wells, Cranberry and Judy Creek fields (Wong and Oldershaw, 1980; Dunham and Crawford, 1983; Craig, 1987; Gosselin and Smith, 1988; Tooth and Davies, 1988; Wendte, 1992; Muir et al., 1995; White, 1995; Bernstein and Stoakes, 1996; Yose et al., 2001; Sack, 2002).

Depositional patterns at Clarke Lake field were strongly influenced by differing rates of accommodation creation during Slave Point Formation deposition. Facies stacking patterns, stratigraphic surfaces and lateral relationships between facies can be explained by increases and decreases in relative sea level, which foster the cyclicity observed at reservoir and sequence level scales. Depositional styles associated with highstand systems tracts and transgressive systems tracts are observed in Slave Point Formation sediments. These systems tracts are used to describe styles of deposition during relative sea-level rise and fall (Catuneanu et al., 2009). Subaerial exposure surfaces and significant basinward shifts of sedimentation were not observed, and we therefore concluded that there was no record of lowstand systems tract deposition. Cycles at Clarke Lake

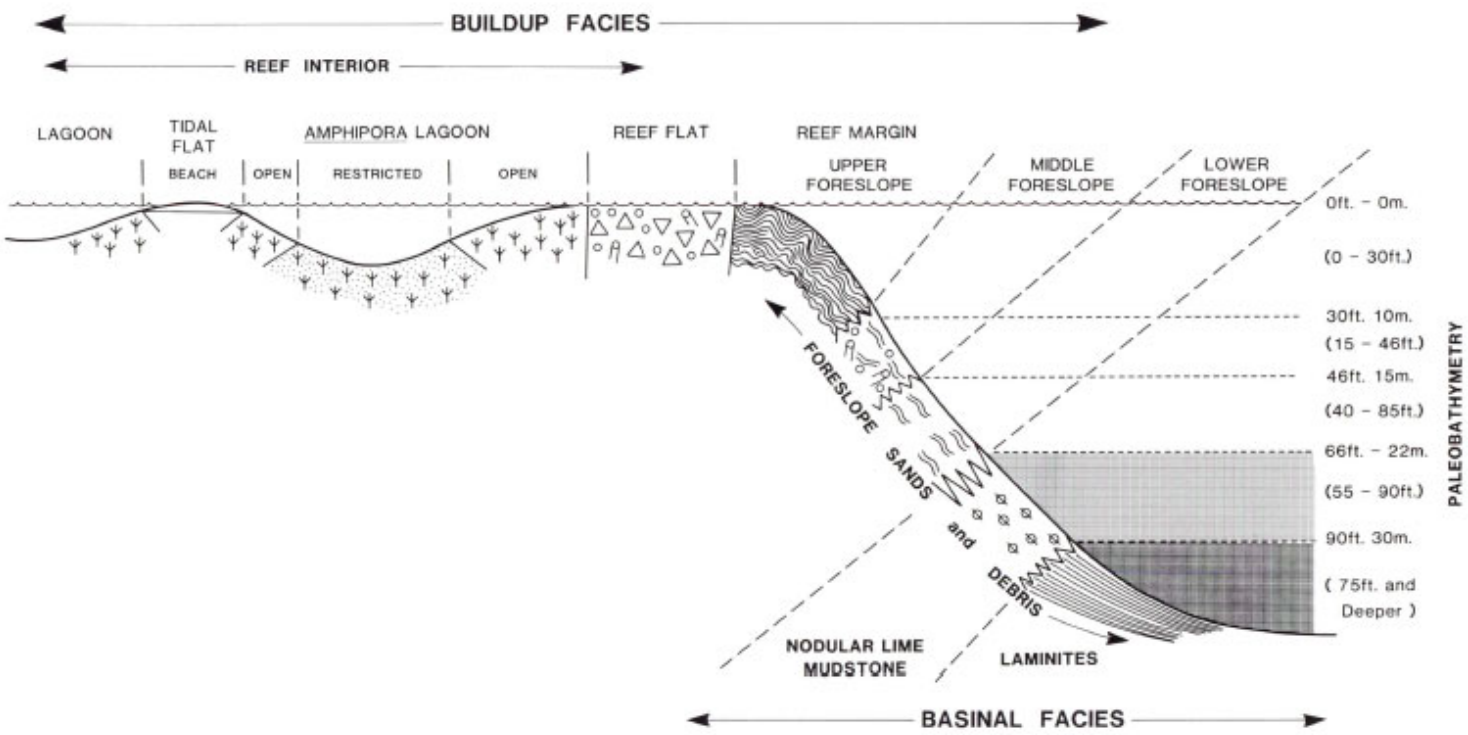

Figure 1.17: Wendte's (1992) depositional model for the Swan Hills Formation at Judy Creek field.

are divided using terminology proposed by Kerans (1991) and Kerans and Kempter (2002). This hierarchy uses cycles (which combine to form cycle sets), high-frequency sequences and composite sequences, which roughly represent fifth-order, fourth-order and third-order cycles, respectively. Cycles observed in the Slave Point Formation core at Clarke Lake correspond to fifth-order depositional cycles, which are typically the highest resolution cycles that can be interpreted.

1.5.2 Rimmed Carbonate Platform Deposition

Highstand Systems Tracts

Highstand systems tract deposits are identified by strong differentiation of facies across the platform top and well developed cycles in the reef interior (Fig. 1.18). Deposition occurred when the rate of sedimentation outpaced accommodation. Reef interior deposition occurred in reef flat, lagoonal and tidal flat depositional environments; this succession describes a transect from platform margin to center. Platform margin deposition occurred in upper and middle foreslope environments, which represent progressively deeper water and lower energy settings.

Reef Interior Deposition

Tidal Flat

In Facies 1C, poorly developed laminae, very low bioclast diversities and concentrations, and high mud content are interpreted to indicate deposition in a poorly circulated, low energy, tidal

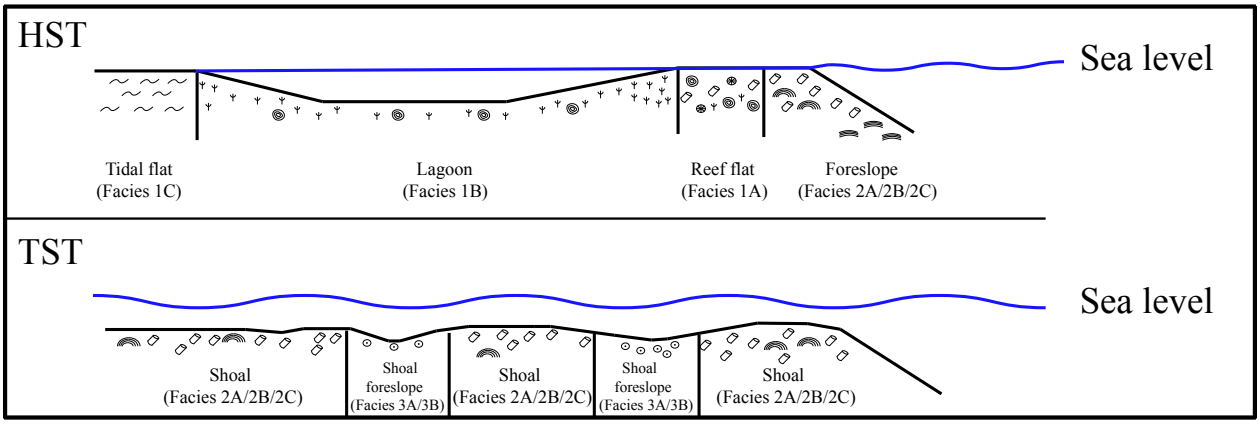

Figure 1.18: Graphic showing the idealized difference between depositional patterns of the highstand systems tract and the transgressive systems tract

flat environment. Minor *Amphipora* represent local shallow subtidal to intertidal deposits. Elsewhere, where *Amphipora* are absent, water levels may have been even shallower, i.e. a supratidal environment. Thicker successions of Facies 1C occurred in shallower, lower energy areas of the reef interior where tidal islands developed.

Lagoon

Low bioclast concentration and diversity, a predominance of smaller, millimeter-scale *Amphipora* and high mud content in Facies 1B suggests deposition in a low energy, lagoon setting. The local presence of *Amphipora* grainstone is indicative of higher depositional energy in restricted areas of the lagoon. Cored intervals showing higher proportions of nodular stromatoporoids and a smaller proportion of *Amphipora* represent deposition in a restricted in an open or deeper lagoon; these transition upward to increased abundance of *Amphipora* resulting from aggradation of the sea bed to sea level.

Reef Flat

Larger *Amphipora*, *Stachyodes* and nodular stromatoporoids of Facies 1A are indicative of deposition within the reef flat. Fracturing of bioclasts implies reworking by wave action above fair weather wave base. The lack of well-developed bedding implies periodic storm deposition, where bioclasts were transported from the reef margin to the reef flat forming packstone and grainstone during turbulent storm conditions and wackestone intervals were deposited during relatively quiescent depositional periods.

Reef Margin Deposition

Lower to Upper Foreslope

Upper foreslope deposition of Facies 2A and 2B is characterized by a diverse, abundant and robust bioclast assemblage deposited within a high energy, well oxygenated and shallow water setting. Intervals with hemispherical and tabular stromatoporoids from Facies 2A, rather than Facies 2B, with an abundance of *Stachyodes* bioclasts represent upper foreslope deposition. The presence of crinoids in the matrix implies normal salinity and/or proximity to the open basin. This

facies was deposited on the upper foreslope at the reef margin and above fair-weather wave base.

Lower to middle foreslope deposition of Facies 2C is indicated by lower bioclast diversities, tabular stromatoporoids and crinoids, and increased mud content, which together indicate deposition in a lower energy, and deeper water environment. Tabular stromatoporoid boundstones were likely deposited on the middle foreslope where wave energy was relatively higher.

Transgressive Systems Tracts

Transgressive systems tracts are identified by the lack of facies differentiation across the platform top (Fig. 1.18) and poorly developed cycles. This represents deposition when the rate of accommodation outpaced the rate of sedimentation. The resulting lack of a well-developed reef margin allowed open marine circulation with similar energy levels to extend across the platform. High-energy shoals and shoal foreslope deposits were deposited throughout the transgressive phase.

Shoal and Shoal Foreslope

Core intervals interpreted to be shoal deposits in the upper Slave Point Formation show the same lithofacies as intervals interpreted to be foreslope deposits in the lower part of the formation. Lower in the formation these facies are distinguished by a well-developed, time-equivalent reef interior. Cylindrical stromatoporoid grainstones and packstones were deposited in a relatively shallow, higher energy shoal environment compared to tabular stromatoporoid wackestones and packstones, which were deposited in a deeper, lower energy shoal environment. Facies interpreted to be deposits on the shoal foreslope are composed of crinoid wackestones and were deposited on the peripheral edge of shoals within relatively deep water.

The similarity between foreslope and shoal sediments may reflect the fact that the reef at Clarke Lake field was a ‘stratigraphic reef’ (Dunham, 1970), where organisms provided the bulk of the deposited sediment, but lacked the rigid, wave-resistant, topographic feature erected by sediment-binding organisms. Thick or well-developed sections of stromatoporoid boundstone, which occur on the upper foreslope at Judy Creek field (Wendte, 1992), reflecting a rigid, wave-resistant

topographic feature are not observed at Clarke Lake.

Cyclicity on a rimmed platform due to relative sea level changes

Sediment responses to sea level fluctuation differ between the reef margin and interior. Within the interior, the transition from lagoonal *Amphipora* deposits to laminated tidal-flat deposits reflects diminishing relative sea level rise, as the platform aggraded, and a shift from subtidal lagoon deposition to supratidal/intertidal tidal flat deposition (Fig. 1.19A). Lagoonal deposits deposited over tidal flat deposits represent abrupt flooding events and a shift from supratidal/intertidal to subtidal deposition. Transitions from reef flat to lagoonal deposits reflect aggradation and shift from deeper reef flat deposition to shallower lagoonal deposition (Fig 1.19B). Conversely, the contact between lagoon and overlying reef flat deposits corresponds to a flooding event and a shift from shallow lagoon deposition to deeper reef flat deposition.

At the reef margin, cycles are expressed by upward transitions from tabular stromatoporoid wackestones to *Stachyodes* grainstone and stromatoporoid boundstone deposits; these represent decreasing relative sea level and a shift from lower and middle foreslope to upper foreslope settings (Fig. 1.19C). Cycles are capped by sharp transitions from upper foreslope deposits to overlying lower or middle foreslope deposits that represent flooding events. However, cycles within foreslope deposits themselves are typically amalgamated or poorly developed and difficult to define. In this environment, rises in sea level are defined by transitions from grainstones or packstones to muddier wackestone intervals.

Evidence for backstepping of the reef can be observed in core. In the CNRL Klua D-006-J/094-J-09 core (core 22; Fig. 1.4), a thick interval of lagoonal to reef-flat cycle sets overlies a thick succession of lagoonal to tidal cycle sets, representing a transition upward from tidal flat depositional environment into a reef flat environment, thus a back-step on the reef. In the Chinook et al Hoffard A- 063-J/094-J-09 core (core 24; Fig. 1.4), a large interval of reef margin cycle sets stratigraphically overlies intervals of Facies Association 1 cycle sets representing a transition from reef flat deposition into a middle foreslope depositional environment, also a back-step of the reef.

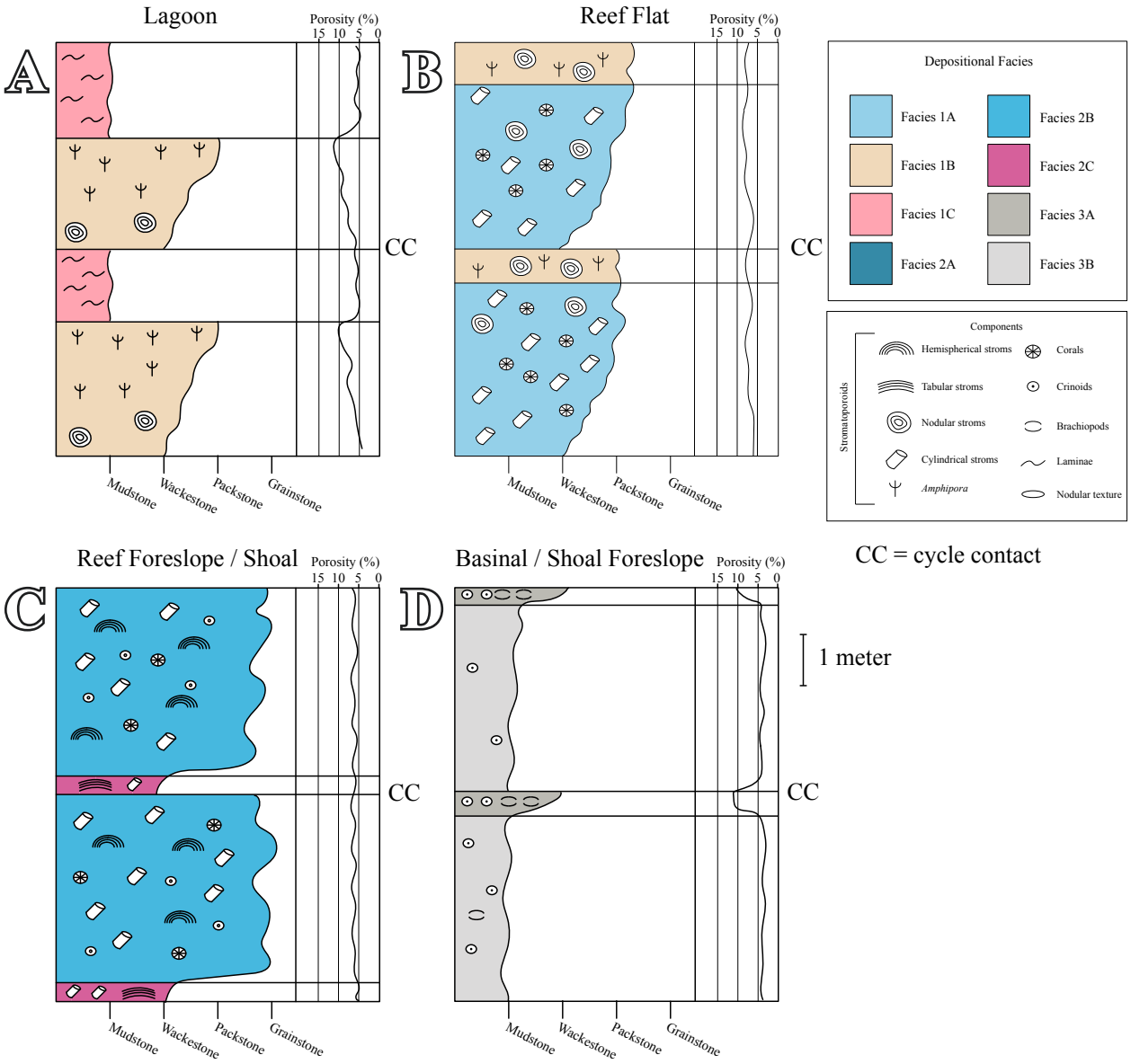

Figure 1.19: Common depositional cycles and their control on porosity development.

1.5.3 Carbonate Platform Deposition

Deposits south of the reef interior more closely resemble platform sediments of the Upper Devonian Grosmont Formation (Cutler, 1983; Fig. 1.20), rather than the Wendte (1999) model for a rimmed carbonate platform. Davies (1999) also noted that deposition south of the reef interior was ‘ramp-like’ in character. Conceivably, the platform became shallower moving further

south past locations where open platform deposition occurred. Platform sedimentation occurred throughout Slave Point Formation deposition, although variations in accommodation rate are difficult to determine due to poor core control.

Open Platform

Facies 1D dominates the open platform deposits, displaying a high mud content with a relatively diverse bioclast assemblage with intervals of lamellar stromatoporoids indicating slow sedimentation rates and low wave energy (Kershaw, 1998; Wendte, 2009). These indicate a low-energy, open marine depositional setting. Thin intervals of abraded crinoid ossicles, and abraded cylindrical stromatoporoid reflect intermittent storm deposition.

Deep Platform

Deep platform deposits include Facies 3A, which exhibits abundant crinoids with minor brachiopod shells/shell fragments in a muddy matrix, indicating a deeper water setting between storm and fair weather wave base. Layers of increased bioclast concentrations were deposited as a result of turbulent storm events, after which mud was settled out of suspension (Lonnee and Machel, 2006). Nodular textures are the result of early cementation, accentuated by compaction (Wendte, 1992). Facies 3B displays lower bioclast concentrations and increased mud content than Facies 3A. The latter is interpreted to have been deposited in slightly deeper water and less oxy-

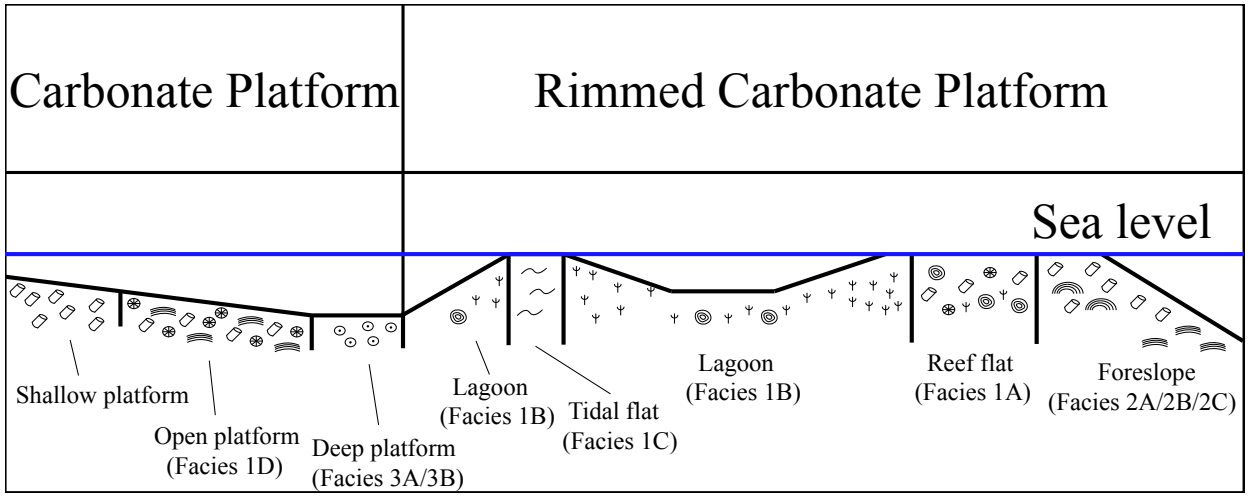

Figure 1.20: Graphic showing depositional model that includes carbonate platform deposition south of the rimmed carbonate platform.

genated conditions on the platform, where in-situ fauna were sparse to absent.

Cyclicity on a platform due to relative sea level changes

Cycles are represented in platform deposits by upward transition from deep platform mudstones to deep platform wackestones that represent aggradation and a decrease in accommodation (Fig. 1.19D). Deep platform mudstones deposited over deep platform wackestones indicate flooding events and a transition to a deeper- water depositional setting. Intervals of deep platform deposits grading upward into open platform deposits represent aggradation during a relative sea level rise.

1.5.4 Depositional Model

A detailed sequence-stratigraphic framework for the Slave Point Formation in the region has not been established to date. As mentioned above, Weissenberger and Potma (2001; Figure 1.3 herein) placed the Slave Point into the transgressive portion of a major, second-order depositional sequence. The exact correlation of the Clarke Lake Slave Point strata to their (Potma et al., 2001) third-order depositional sequences is uncertain.

However, comparing the Clarke Lake area to central Alberta, the Slave Point Formation is thicker than the entire Beaverhill Lake Group (e.g. Potma et al. Figure 3). Also, the Muskwa/ Duvernay formations (representing the second-order maximum transgression) lie immediately, or almost immediately, above both the Slave Point in northeast British Columbia and the Beaverhill Lake in Alberta. It is therefore possible that the Slave Point of this study is equivalent to most or all of the Beaverhill Lake Group and hence to the three third- order sequences of Potma et al. (2001). Greater certainty in correlation will require further regional stratigraphic and biostratigraphic work.

In the absence of a regional sequence stratigraphic framework, the Slave Point Formation is, for the purposes of this study, divided into units corresponding to high-frequency sequences or composite sequences (Kerans, 1991; Kerans and Kempter, 2002): in ascending order, an initial shoal unit, S1, three reef-building units, R1, R2, and R3 and three drowning shoal units, D1, D2 and D3 (Fig. 1.21, 1.22, 1.23). These are either fourth- or third-order packages, representing hundreds

of thousands to a million years in duration. The contacts between these units correspond to rapid rises in the relative sea level and shifts in depositional patterns across the reef. In some cases, these rises in sea level resulted in the cessation of shallow water deposition at some locations on the reef, while shallow water deposition kept pace with sea level rise in other localities.

The erosional unconformity at the base of the Watt Mountain Formation represents the base of the second-order depositional sequence and the Beaverhill Lake 1. For this study, the Watt Mountain Formation is used as a stratigraphic datum as it is interpreted to have been a relatively flat surface during Slave Point Formation deposition. The deposition of S1 above the Watt Mountain Formation represents the first unit of the Beaverhill Lake 1. The S1 unit was deposited during a time of increasing accommodation space, where relative sea-level rise outpaced sedimentation rates. Open marine conditions existed across the platform, in which amalgamated cylindrical stromatoporoid packstone to grainstone was deposited. Isolated shoals coalesced toward the top of the S1 unit, a feature seen in other Devonian fields (Bernstein and Stoakes, 1996; Yose et al., 2001). The S1 unit averages approximately 35 m in thickness, compared to an average platform thickness of about 30 m that developed along the West Alberta Ridge representing the entire Beaverhill Lake 1. Carbonate platform deposits in the eastern portion of the basin were 5 – 10 m thinner (Potma et al., 2001).

The R1, R2 and R3 units represent individual sequences and highstand systems tract deposition, where there was decreasing accommodation space from the rate of sedimentation outpacing relative sea-level rise. These units are similar to Upper Beaverhill Lake 1 units in Western Alberta, which show *Amphipora* floatstones in platform interiors and stromatoporoid grainstones and boundstones on platform margins (Potma et al., 2001). Deposition was characterized by well-defined platform margins, strong differentiation of facies tracts and wave energies across the bank top, and the development of distinct shoaling-upward stacking patterns within the reef interior.

The contact separating the R3 and the D1 units marks the onset of a transgression during which cylindrical stromatoporoid shoals developed across the platform. Deposition occurred during a time of decreasing accommodation space due to relative sea-level rise outpacing sedimentation

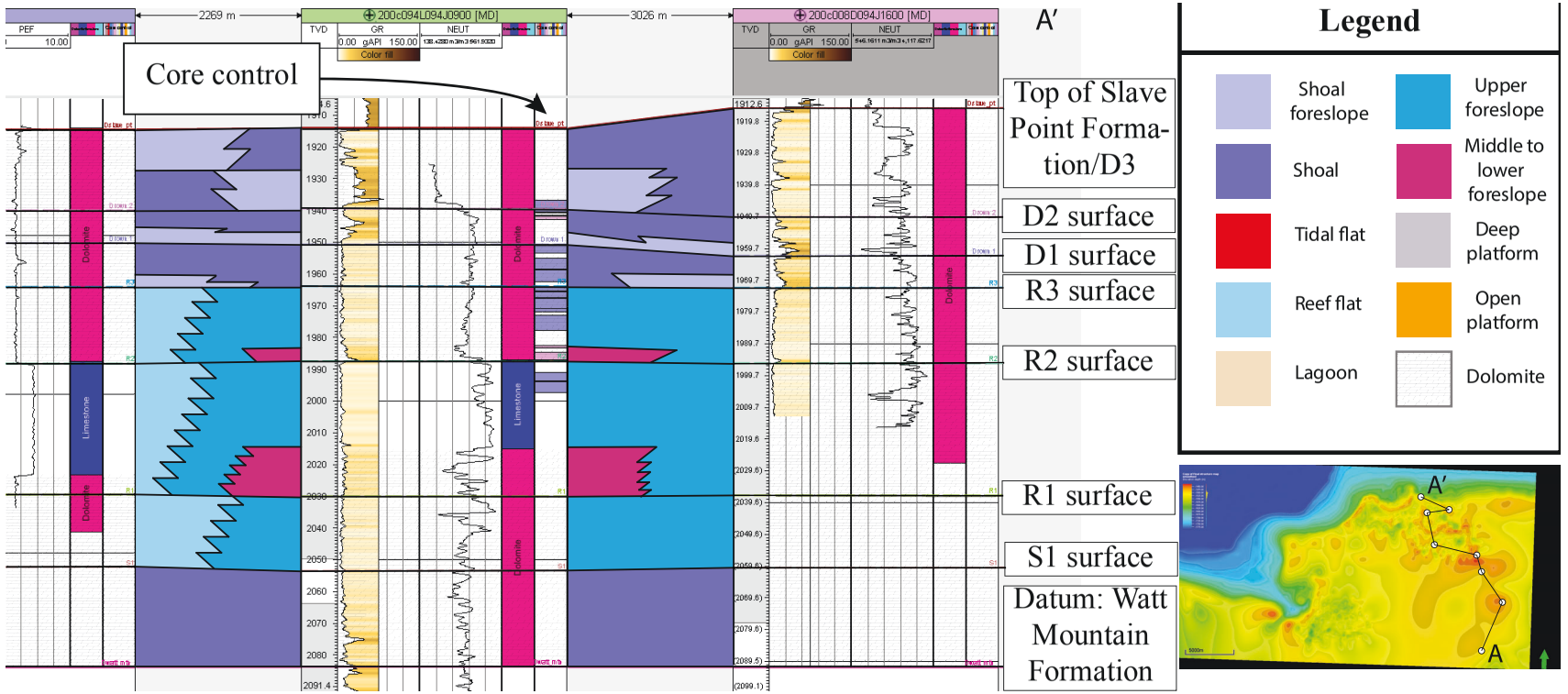

Figure 1.21: Stratigraphic cross-section 1 of 3, showing the extent of dolomite and the internal facies architecture of the Clarke Lake reef.

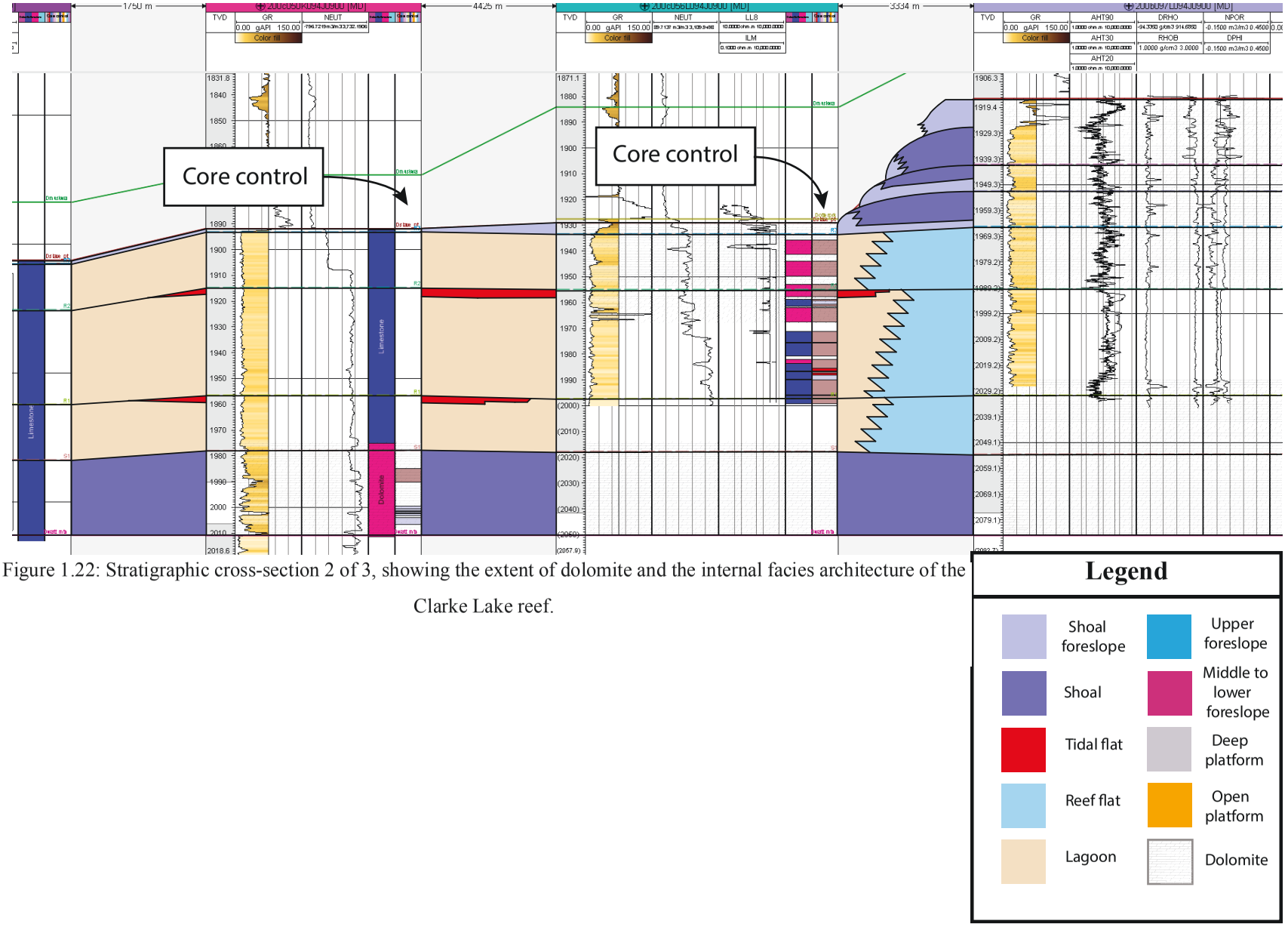

Figure 1.22: Stratigraphic cross-section 2 of 3, showing the extent of dolomite and the internal facies architecture of the Clarke Lake reef.

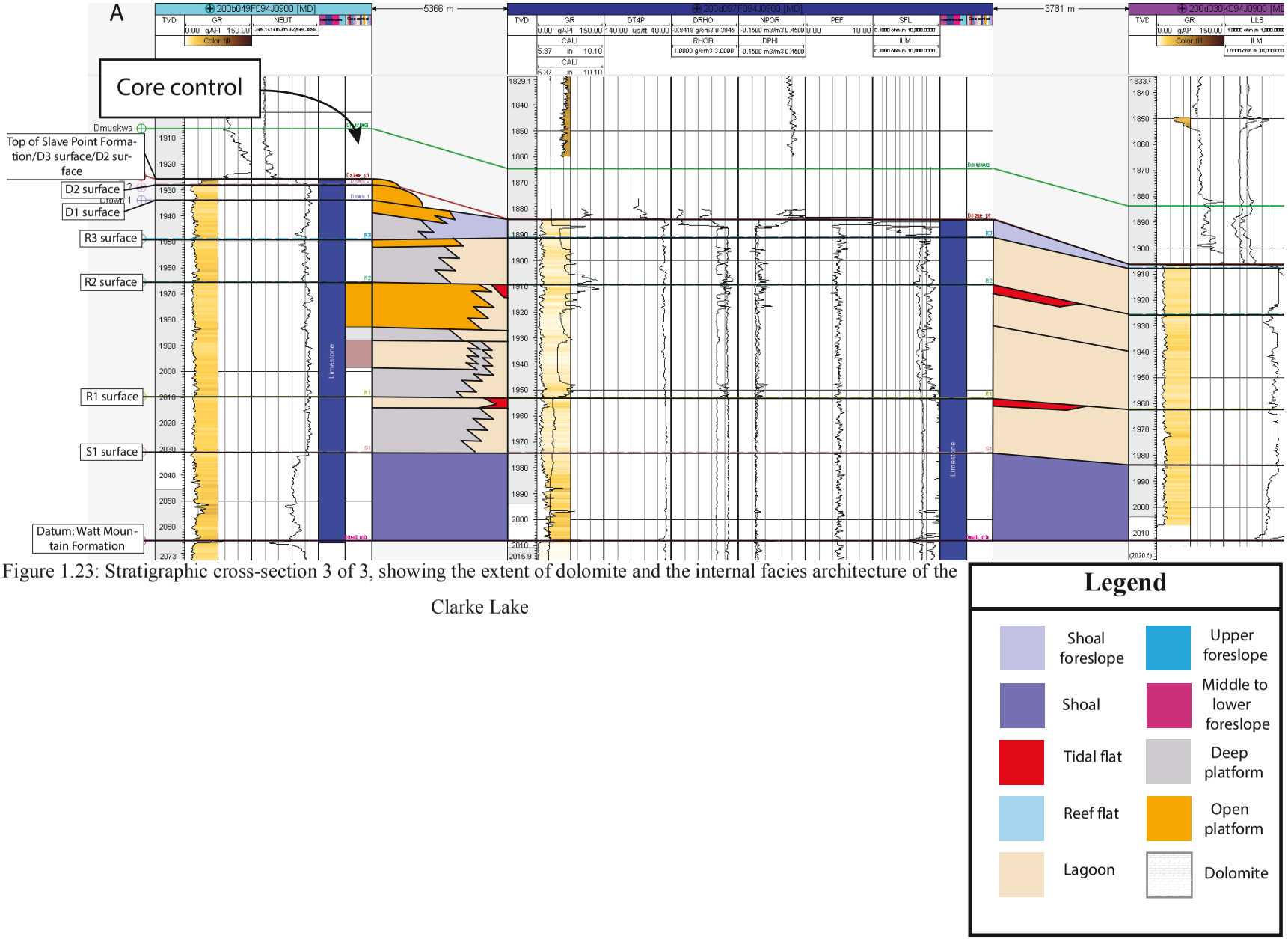

Figure 1.23: Stratigraphic cross-section 3 of 3, showing the extent of dolomite and the internal facies architecture of the Clarke Lake

rates. Similar to the S1 unit, a well-developed reef margin was absent at this time; thus, there was little differentiation of depositional energy across the platform top, and the deposits lack definitive cycle boundaries. Shoal deposition within the reef interior proximal to the margin ceased by the end of the D1 interval and shoal deposition halted completely, except near the reef margin, by the start of the D3 interval. Shoal deposition at Clarke Lake field persisted until the rate of accommodation increase outpaced carbonate deposition, resulting in deposition of the Muskwa Formation shales above the shallow water D1, D2, and D3 shoals.

1.5.5 Hydrothermal Dolomite in the Slave Point Formation

Saddle dolomite at the Clarke Lake field is interpreted to be of hydrothermal origin based on several diagnostic features observed in core and thin section:

1. The presence of curved, coarse, saddle dolomite crystals filling or partially infilling vugs, molds, fractures (Sun, 1995; Davies and Smith, 2006).

2. The presence of fluorite, sulphide mineralization and pyrobitumen, which are common in hydrothermal dolomites in Mississippi Valley - type lead-zinc sulphide deposits. Sulphides in particular have been shown to be directly associated with hydrothermal dolomite fabrics (Sun, 1995; Nadjiwon, 2001; Davies and Smith, 2006).

3. The brecciated nature of the dolomite, forms through a process called hydrofracturing, wherein the mechanical effect of the dolomitizing fluid in a differential stress regime results in solution-collapse (Phillips, 1972). Solution collapse allowed mudstone from the overlying Muskwa Formation to infiltrate the Slave Point Formation from above (Park and Jones 1985).

Gray matrix dolomite crystals may be emplaced hydrothermally or geothermally (in thermal equilibrium with the surrounding rock) (Lonnee and Machel, 2006); however, we lack the temperature data to resolve these models. Matrix dolomitization is pervasive, likely due to significant microporosity of the limestone precursor, high surface area to volume ratio and the presence of abundant nucleation sites within fine grained carbonate sediment (Sun, 1995).

The model proposed for dolomitization at the Clarke Lake field is long-distance lateral fluid flow (Lonnee and Machel, 2006). Halite brines sourced from evaporites near the Peace River Arch to the south moved northward and down dip through the Lower Keg River Formation until reaching a permeability barrier composed of Horn River Group shale where the brine was forced upward into the Upper Keg River, Sulphur Point and Slave Point formations. Clarke Lake field was dolomitized at the reef margin and within platform interior facies, where brines moved upward through fault conduits then permeated laterally through carrier beds. Interpretations can be made about dolomitizing fluid flow at Clarke Lake, based on the recognition that early, porosity forming dolomite can undergo an increase in volume and lose porosity due to later diagenetic alteration (Warren, 2000). Maximum alteration and lower porosity occurs within the lowermost S1 interval, and throughout the reef margin irrespective of stratigraphic units, implying these areas saw initial lateral and upward movement, respectively, of dolomitizing fluids. Afterward, the fluid moved laterally and invaded the less altered, more porous sediments of the platform interior (reef flat and lagoon).

The development of secondary porosity by dolomitizing fluids depended strongly on the types of bioclasts and depositional characteristics of the original host rock. Thus, mapping of depositional facies is a valuable tool for delineating porosity development in a hydrothermal dolomite reservoir (Davies and Smith, 2006). Dolomitization at the reef margin was controlled, at least partially, by depositional facies, restricted to reef margin and shoal units, because the pre-alteration limestone was composed of upper foreslope or shoal sediments that had higher primary porosity and permeability. In reef flat and lagoonal facies, alteration was not complete, which resulted in pervasive matrix dolomitization, but preserved depositional fabrics and pores unfilled by dolomite.

1.5.6 Diagenetic Controls on Reservoir Properties

Dolomite diagenesis is the fundamental control on reservoir character at Clarke Lake. Therefore, understanding field-wide variations in porosity and permeability of the dolomite body is necessary to delineate high quality reservoir zones. Low porosity within diagenetic, reef margin and shoal facies is the result of increased amounts of dolomite precipitation, which occludes porosity.

Permeability is high within the diagenetic facies due to the presence of fractures. Porosity generally increases away from the reef margin into the reef flat and lagoon, likely due to a decrease in dolomite precipitates within pores as seen at the reef margin. Permeability in reef-flat and lagoon facies is reduced due to the lack of the significant fracturing that is seen in shoal, reef margin and diagenetic facies. This results in relatively higher permeability but less porosity near the reef front and relatively high porosity but lower permeability behind the reef front, as observed by

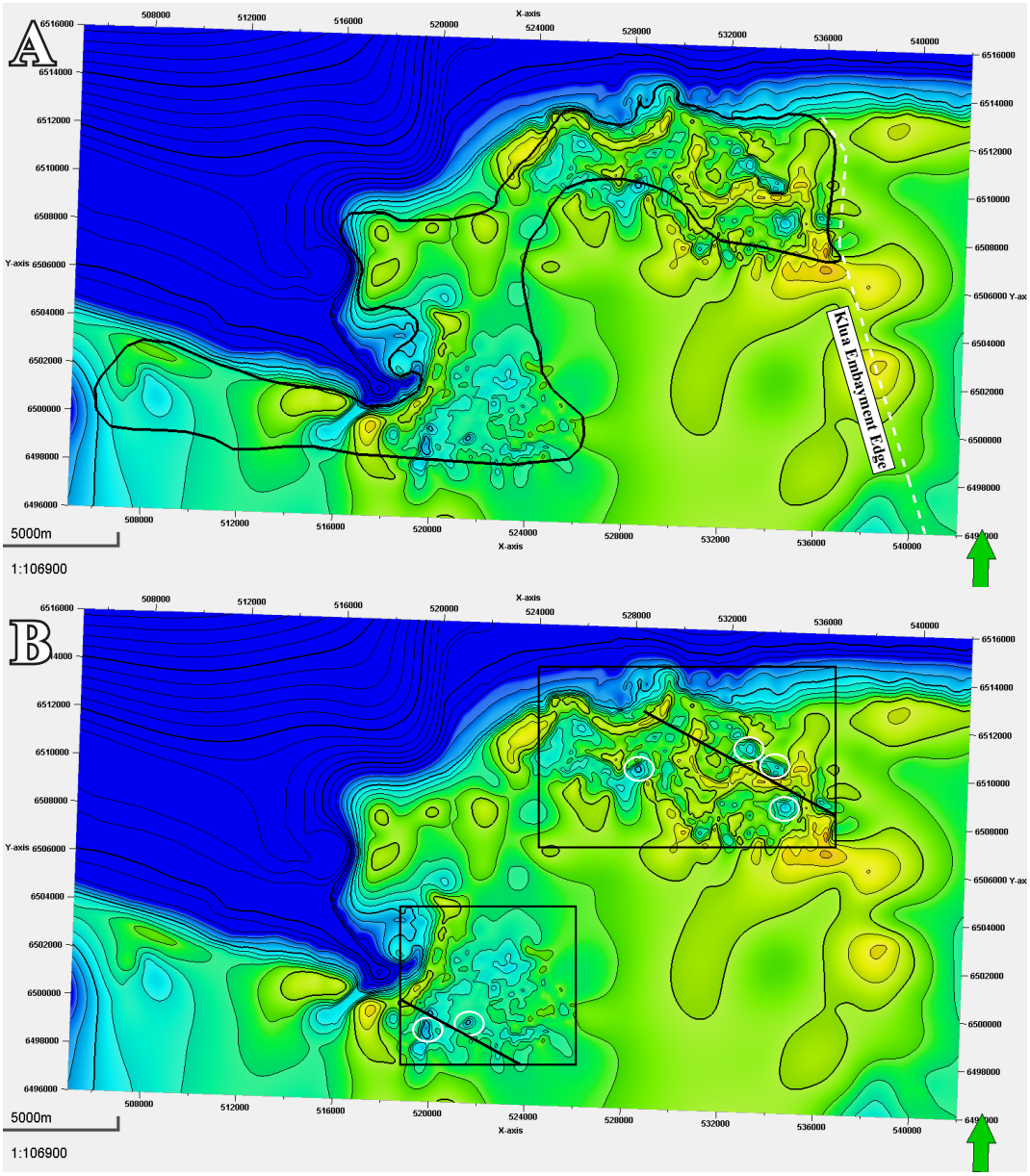

Figure 1.24: (A) Slave Point structural top map showing extent of dolomitization (black line) and the boundary of the Klua Embayment (white line). (B) Slave Point Formation structural top map showing structural sags (white circles) within seismically covered areas (black boxes) and interpreted strike-slip faults (black lines).

Frank and Kassube (1963).

Identifying the transition from non-reservoir limestone to the area of dolomite alteration is crucial in determining the extent of the reservoir. Dolomitization extends at least 5 km into the reef interior within the S1 interval, but upper units (R1, R2, R3) show dolomitization approximately 2 km into reef interior (Fig. 1.24A; 1.25). East of the Canlin Clarke D- 091- L/094-J-09 well, the reef front is unaltered, because the underlying Klua Formation forms an aquiclude, blocking the upward movement of brines (Morrow et al., 2002). Fig. 1.23A shows the extent of alteration at Clarke Lake field and the Klua Embayment edge, where a thick unit of Klua Formation shales onlaps the underlying Keg River Formation, blocking the upward movement of brines. The Watt Mountain Formation, which thickens away from the reef margin, also formed an aquiclude to the upward movement of brines resulting in a reduction of the net reservoir thickness within the reef interior.

1.5.7 Cyclic Controls on Reservoir Properties

Higer order sequences impose the most significant control on reservoir properties, while cycles impose less influence on reservoir properties. In reef foreslope and shoal deposits, reservoir compartmentalization is low and lateral and vertical continuity of reservoir properties are high due to the amalgamation of cycles (Fig. 1.19C). Within reef interior and shoal foreslope facies, however, the development of well-developed depositional cyclicity results in increased reservoir compartmentalization and a decrease in continuity of reservoir properties (Fig. 1.19A; 1.19B). The origin of flooding surfaces within cycles that terminate upward in tidal mudstones may be due to either autocyclic or allocyclic controls (Wong et al., 1980; White, 1995). The lack of obviously correlatable flooding surfaces at Clarke Lake suggests controls by both auto- and allocyclic factors, leading to increased compartmentalization of lagoonal – tidal cycles.

High-frequency or composite sequences at Clarke Lake are separated by boundaries corresponding to major flooding surfaces. These flooding surfaces can be correlated from the reef margin into the reef interior and have a variable impact on reservoir compartmentalization, locally controlling the movement of dolomitizing fluid, and thus, the development of dolomitized reservoir

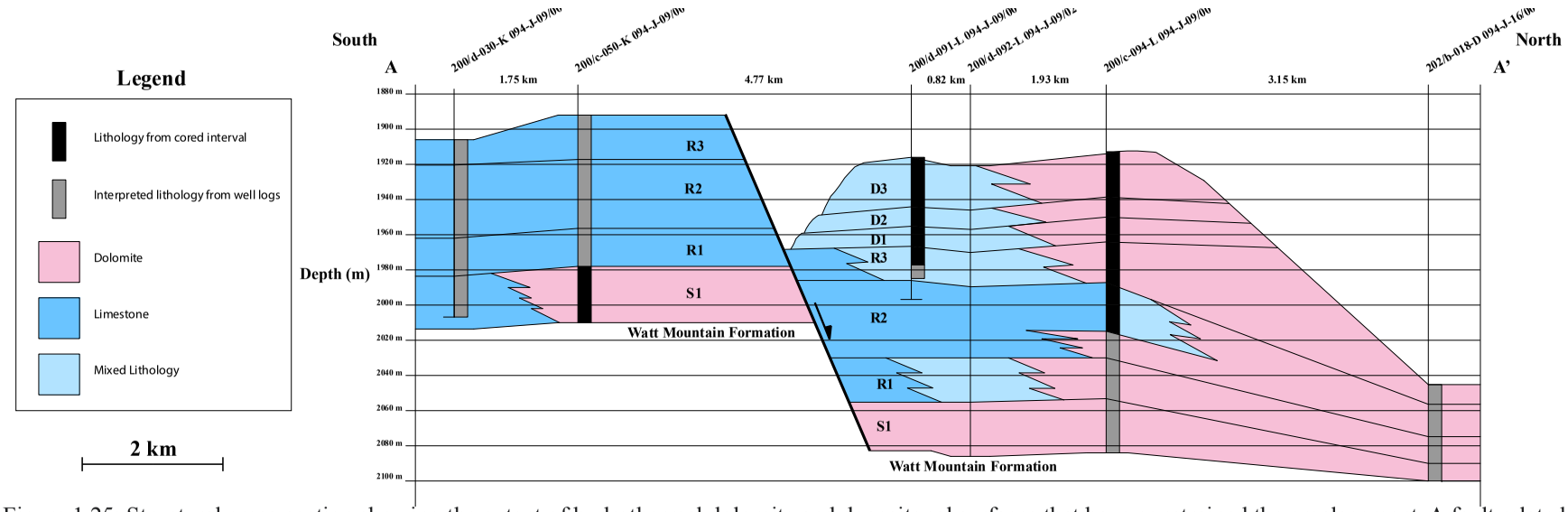

Figure 1.25: Structural cross-section showing the extent of hydrothermal dolomite and depositonal surfaces that have constrained the emplacement. A fault related to compaction of shales where the Slave Point Formation overstepped the Klua Formation.

rock (Fig. 1.20; 1.21; 1.22). Within the reef margin these surfaces exert less control on dolomitization. Instead, dolomitization at the reef margin is primarily controlled by upward movement of brines through depositional facies, the presence of shale permeability barriers or, possibly, the influence of faults.

1.5.8 Reservoir Architecture

Seismic data allow the interpretation of topographical features on the Slave Point Formation surface at Clarke Lake field. Specifically, small (~ 1.3 km), subrounded areas within the reef interior with a maximum of 75 m in relief represent collapse synclines related to dissolution (Fig. 1.24B). Similar hydrothermal sags have been interpreted with seismic data within the Clarke Lake Slave Pool B directly west of the Slave Pool A reef margin (Gorecki et al., 2014). A high concentration of hydrothermal dolomite breccia in core from Canlin et al Clarke A- 065- G/094-J-10, located ~ 1 km from an interpreted collapse syncline, suggests that maximum hydrothermal alteration is associated with these features.

Davies and Smith (2006) emphasizes that faults, fault damage zones and fracture networks are the primary conduits for dolomitizing fluids and the locations of highly permeable hydrothermal dolomite reservoirs. Their recognition can guide exploration for hydrothermal dolomite reservoirs, an approach utilized with success in the discovery of the Ladyfern field along the Hotchkiss Embayment trend in northeast British Columbia and northwest Alberta. The thickest and best reservoir intervals there were directly associated with seismically-resolvable collapse synclines at the intersection of faults (Boreen and Colquhoun, 2001). The fault intersections occur as complex shear faults at oblique angles to a primary deep wrench fault. Interpreted oblique faults at Clarke Lake coincident with collapse synclines are shown in Fig. 1.24B. These faults trend northwest, transecting older, northeast trending wrench faults that are related to the Hay River Shear Zone. Northwest-southeast joint sets identified at Pine Point, NWT are consistent in orientation with faults interpreted at Clarke Lake (Turner and Gal, 2003). Similarly, relationships between hydrothermal alteration and northwest trending faults have been identified in Zama Lake and Rainbow Lake, Alberta (Muir and Dravis, 1992; Lonnee and Al-Aasm, 2000). It is also possible that fluid-conveying faults related to compaction of underlying shale are present, where the Slave

Point Formation oversteps the underlying Klua Formation. (Fig. 1.25). More detailed work with seismic data is needed to resolve the location of these faults.

1.5.9 Flow Units

The thickness and degree of compartmentalization of flow units at Clarke Lake field depends on proximity relative to the reef margin as well as the stratigraphic architecture. Flow units are relatively thin in reef interior deposits, typically 0.5 to 2 m in thickness, associated with the development of depositional cyclicity. Where lower-permeability tidal flat facies are absent above lagoonal facies, improved vertical continuity of reservoir properties may be present. Reef interior flow units are 0.5 to 2 m in thickness with variable compartmentalization and lateral or vertical continuity. Where dolomite enhances porosity and permeability in tidal flat facies, reservoir compartmentalization in lagoon – tidal flat cycles is reduced. Because foreslope and shoal deposits are largely homogeneous, flow units corresponding to high-frequency or composite sequences are thicker, ranging from 11 to 40 m. Vertical continuity is enhanced in some cases since dolomitization has enhanced flow properties across cycle boundaries, but elsewhere, vertical compartmentalization is present where facies changes at cycle boundaries obstructed the vertical movement of dolomitizing fluids.

1.6 Conclusions

This study develops a static reservoir model of the Slave Point Formation at Clarke Lake field, relating depositional and diagenetic facies to porosity and permeability. The depositional model helps to show the impact of depositional facies distribution and depositional cyclicity on dolomite development and the resulting secondary porosity and permeability. Petrophysical properties as well as distribution and character of of flow units presented in this study are essential for selecting locations for production and/or injection wells capable of supplying/sustaining adequate flow rates for geothermal power production.

Slave Point Formation carbonates were deposited during the transgressive portion of a late Givetian-Frasnian second-order sequence and represent the evolution of an aggradational and backstepping carbonate platform and margin (Potma et al., 2001). An initial sequence, associated

with increasing accommodation space and a rapid flooding of the carbonate platform, consists of cylindrical stromatoporoid shoals. Subsequent intervals of reef deposition occurred as the rate of increase in accommodation slowed during the highstand portion of the high-frequency or composite sequence. These intervals are separated by flooding surfaces and show distinct facies differentiation representing foreslope, reef flat, lagoon and tidal flat depositional environments. Deposition of the Slave Point Formation ended with the development of spatially restricted shoals, formed during the transgressive portion of a sequence, where energy differentiation across the platform lessened and the rate of accommodation increased, generating shoal and shoal foreslope deposits.

Diagenetic dolomite is related to enhanced porosity and permeability, and formed the major reservoir body at Clarke Lake field. Parent limestone has been hydrothermally altered, forming fractures, mouldic pores and vugs. Limestone lithologies are considered non-reservoir because primary porosity and permeability is poor, pore space having been occluded by calcite cement. Dolomitized rocks are generally porous and permeable, but, with increased hydrothermal alteration, porosity is reduced by dolomite cement and permeability increases due to fractures. Reservoir continuity is at least partly influenced by depositional cyclicity at different scales, but good-quality reservoir zones exist wherever dolomite occurs. Dolomite within reef margin and reef interior facies has generated the major reservoir body at Clarke Lake field. Internal flooding surfaces affect reservoir continuity in the reef interior but play less of a role at the reef margin, where the Slave Point Formation is completely dolomitized. Wells drilled into recognizable sags identified on seismic data are clearly associated with high productivity due to the occurrence of hydrothermal dolomite (Davies and Smith, 2006); these collapse synclines at Clarke Lake could represent potential locations for geothermal fluid exploitation.

Chapter 2: Simulating Thermal Breakthrough in a Heterogeneous Hydrothermal Dolomite Reservoir

2.1 Introduction

Thermal breakthrough is the migration of cold, reinjected fluids to a geothermal production well. Avoiding breakthrough is critical for geothermal reservoir management. Unanticipated temperature drops in produced fluids can lead to fluid flow rates per unit power that are economically inadequate for electrical power production and to a reduction of Second Law efficiencies to 22 % or lower (Franco & Villani, 2009). Declines in temperature of produced waters can cause plant outputs to run below their design specifications, add costs for makeup wells and require modifications to field operations (Shook, 2001). A geological model that accurately represents reservoir characteristics is essential for optimizing reinjection strategies and avoiding thermal breakthrough (Franco & Vaccaro, 2014). Accurate geological models of sedimentary formations account for the spatial heterogeneity of porosity and permeability in the subsurface and incorporate heterogeneities related to depositional or diagenetic facies (Hamm & Lopez, 2012). Less accurate models fail to reproduce production-well temperature decreases observed in more accurate models. Simulations that incorporate heterogeneity cause the net present value of geothermal doublets to vary up to 40 % and overestimation of doublet (a production and injection well) productive life times (Crooijmans et al., 2016; Willems et al., 2016).

In this study we assess thermal breakthrough at geothermal production wells in a heterogeneous carbonate reservoir, focusing on the Clarke Lake field (Fig. 2.1), a carbonate reservoir in the Western Canada Sedimentary Basin (WCSB). The WCSB is a foreland basin with a rich history of hydrocarbon exploration and production that hosts several potential, low-enthalpy geothermal reservoirs with an estimated total thermal power capacity of ~ 6100 MWt for a 30 – year production period (Banks & Harris, 2018). One such reservoir is Clarke Lake field, a prolific but now depleted producer of natural gas. The reservoir at the Clarke Lake field is hosted within the Slave Point Formation, which is composed of hydrothermally-altered carbonate sediments with significant secondary porosity and enhanced permeability from the recrystallization, replacement, and dissolution of the host limestone.

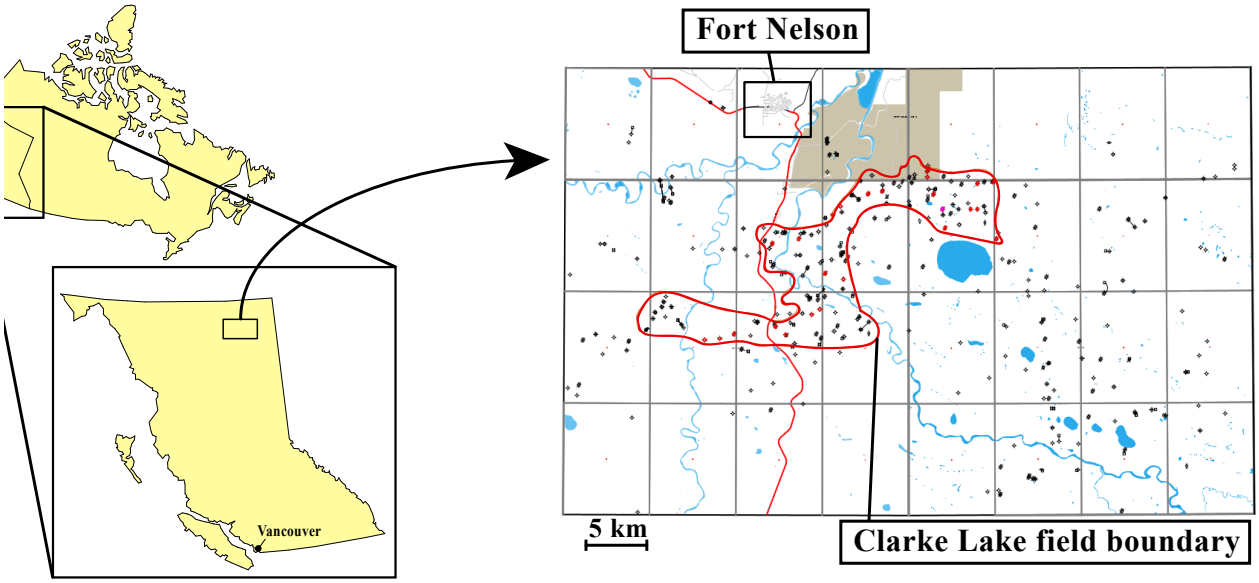

Figure 2.1: Location of Clarke Lake field in northeast British Columbia showing the town of Fort Nelson and the boundary of the field denoted in red.

This study utilizes porosity and permeability measurements from Clarke Lake field in flow simulations to understand how reservoir fluid flow might affect thermal breakthrough over 25 years of production and injection. We apply a Monte Carlo approach to examine how the hydrogeological heterogeneity of a hydrothermal dolomite reservoir affects the ultimate power potential of specific well configurations under a range of operational conditions. The simulation results will help to show whether Clarke Lake field strata can sustain fluid flow for geothermal power production and provide new lessons on low-enthalpy geothermal reservoirs hosted in carbonate formations.

2.1.1 Geological Background

The Slave Point, Lower Keg River, Upper Keg River, Sulphur Point and Watt Mountain formations form a large Middle Devonian barrier reef known as the Presqu'ile Barrier (Lonnee & Machel, 2006). Deposition of the barrier began at the end of the Eifelian (~388 ma), and persisted until the early Frasnian (~383 ma). The barrier extends roughly 600 km from the subsurface near the Rocky Mountains of northeast B.C. to the outcrop edge at Pine Point, Northwest Territories. The width ranges from 20 to 100 km.

In the late Eifelian, a continent-wide carbonate platform comprising deposits of the Lower Keg

River Formation developed in an epicontental sea located approximately 5° south of the paleo-equator (Witzke & Heckel, 1988; Meijer Drees, 1994; Morrow et al., 2002). Upper Keg River Formation reefs grew on top of the Lower Keg River Member and restricted southward circulation of seawater, allowing deposition of the Muskeg and Prairie Evaporite formations to the southeast of the Presqu'ile Barrier (Qing & Mountjoy, 1994; Potma et al., 2001).

A middle Givetian sea-level rise terminated most reef growth within the Presqu'ile Barrier, reflected in deposition of Horn River Group shales and aggradational deposits of the Sulphur Point Formation. Subsequently, thin shale of the Watt Mountain Formation was deposited, unconformably above the Sulphur Point Formation (Drees, 1988; Potma et al., 2001; Lonnee & Machel, 2006). As conditions favourable for carbonate deposition persisted into the Late Devonian, aggradational patch reefs of the Slave Point Formation continued to develop on the Presqu'ile Barrier (Potma et al., 2001). These Slave Point reefs backstepped as sea level rose until they were drowned when reef growth failed to keep up with sea-level rise. This major Late Devonian (~383 ma) sea-level rise resulted in deposition of a thick package of shales of the Muskwa and Fort Simpson formations on top of the reef complex, providing a regional seal for many Devonian oil and gas plays in Alberta and B.C. (Morrow et al., 2002).

The Slave Point Formation strata in the Clarke Lake field reservoir are divided into four facies associations that represent deposition within a rimmed carbonate platform setting, a platform setting and their diagenetic alteration (described in detail in Section 1.5 of Chapter 1). Facies Association 1 includes *Stachyodes* nodular stromatoporoid coral wackestone to packstone (Facies 1A), *Amphipora* wackestone to grainstone (Facies 1B) and brown/gray mudstone (Facies 1C). These facies were deposited, respectively, within the reef flat, lagoon and tidal flat areas of the reef interior. Facies Association 2 includes massive stromatoporoid boundstone (Facies 2A), *Stachyodes* packstone to grainstone (Facies 2B), and tabular stromatoporoid wackestone to grainstone (Facies 2C). Deposition of these facies occurred at the high energy upper foreslope of the platform margin. Facies Association 3 includes crinoidal wackestone (Facies 3A) and crinoidal mudstone (Facies 3B), which were deposited in a basinal setting. Facies Association 4 comprises diagenetic lithologies, limestone rock units that have undergone hydrothermal alteration to dolomite. Dia-

genetic facies predominantly occur within the margin of the reef, near the platform to foreslope transition.

The Clarke Lake field discovery well, Prophet River No. 1, was drilled in the winter of 1957 as a joint venture between Western Natural Gas Company, El Paso Natural Gas Company, Hudson's Bay Oil and Gas Company Limited and Union Oil Company of California (Gray & Kassube, 1963). A prolific Devonian gas producer, the Clarke Lake field has produced over 52 x 10 m^3 (1.83 TCF) of gas, and 49 x 10 m^3 (308126 MMbbl) of water since production began in January of 1961 (British Columbia Oil and Gas Commission, 2019). The long production history of the Clarke Lake field has led to the development to a large subsurface dataset. Currently, the field is losing economic value to stakeholders, including both field operators and the residents of the Fort Nelson area, due to the in situ gas being near depletion.

2.1.2 Geothermal Potential at the Clark Lake field

Repurposing the Clarke Lake field as a geothermal power source suggests the further economic potential of the mature gas field. The geothermal energy at Clarke Lake has been shown to be potentially exploitable as a resource for electricity production (Johnstone, 1982; Arianpoo, 2009; Walsh, 2013; Weides & Majorowicz, 2014; Palmer-Wilson et al., 2018). The field possesses a strong water drive, critical to the production of significant volumes of water. The strong water drive was observed in an experiment conducted by Petro-Canada Oil & Gas, who investigated the viability of liberating trapped gas within the Clarke Lake field (Petro-Canada Oil & Gas, 2009). To accomplish this, they attempted to depressurize the reservoir by producing formation water at high rates (2100 - 2800 m^3/day) between January 1st, 2007 and December 29th, 2008, employing two wells as water producers and two wells as water disposal wells. Six remaining wells were designated as gas-lift wells. Water-gas ratio plots showed that no gas had been liberated as a result of dewatering. Water production rates at one water producer well peaked at 1800 m^3/day while the volumetric gas to water ratio remained stable at ~3. Petro-Canada Oil & Gas speculated that they would need at least a 1 MPa drop in reservoir pressure to access the trapped gas, but at the end of the experiment, reservoir pressure had dropped by only 100 kPa. This unexpectedly low pressure drop was a result of the strong water drive.

Further work using a Monte-Carlo analysis found that Clarke Lake has a mean recoverable thermal energy of 10.1×10^{14} kJ ± 3.2×10^{14} kJ. An estimate of the mean field-wide generation potential using the same Monte-Carlo approach was determined to be 34 MW ± 10.8 MW (Walsh, 2013). Palmer-Wilson et al. (2018) estimated the mode potential to be 63.2 MW. The large discrepancy between estimates is due to different reservoir volumes used in the power potential calculations. Although several researchers have estimated the geothermal potential available at the Clarke Lake field, further work needs to be done to assess whether reservoir-scale permeability and porosity is conducive to a geothermal operation. By simulating the movement of fluid through the Clarke Lake reservoir, we can estimate the impact of thermal breakthrough on power potential. These estimates are compared to previous estimates to better understand the power generation capability of Clarke Lake field.

2.2 Methods and Materials

2.2.1 Methods Overview

Five sets of flow simulations were completed to model the temperature of produced fluid after a 25-year production and injection period, applying rock properties existing at the Clarke Lake reservoir. All simulations were completed using PetraSim. PetraSim is a pre- and post-processor for the TOUGH2 family of codes that allows fluid flow modelling in porous and fractured media (Pruess et al., 1999). The final temperatures at production well cells after a 25-year simulation run were recorded and analyzed to observe the how different porosity/permeability inputs, flow rates, completion lengths and grid sizes affect thermal breakthrough. Flow rates were based on observed upper limits of co-produced fluid rates within the Clarke Lake field (Petro-Canada Oil & Gas, 2009). The thickness of completion zones in production and injection wells were set to 50 m for all simulations except one simulation set using 100 m completions. These lengths were based on net pay thicknesses in the Clarke Lake field, which have a maximum value of 165 m and a mean of 62 m. The first four sets of simulations use grids that were built within the PetraSim software. The fifth set of flow simulations includes a geocellular model of the Clarke Lake field that was constructed in Petrel and then imported into PetraSim. Boundary and initial temperature

conditions were kept constant throughout all simulations. Boundary conditions were set as no-flow. We tested doublet well configurations with 500 m well spacing to ensure adequate pressure communication between production and injection wells. Well configurations using four injection wells and eight production wells (four injection-eight production well configuration) were also tested, with the injection wells located at the corners of a 200 x 200 m square in the center of the model, and the eight production wells spaced in an octagonal pattern 900 m away from the perimeter of the square (Fig. 2.2). The well spacing in these simulations was increased relative to doublet well models to account for higher fluid injection rates.

2.2.2 Data Inputs

Pressure and Temperature

A total of 89 wells penetrate the Slave Point Formation at the Clarke Lake field, of which 23 wells had 43 individual drill stem tests (DSTs). We use reservoir pressure and temperature from the DSTs as data inputs, as shown in Table 2.1. Reservoir pressure is corrected using a Horner plot with shut-in-drill-stem-test pressure data. Temperatures from DSTs are generally reliable and were uncorrected, following Peters and Nelson (2012). We assume minimum, mean and maximum reservoir pressures of 1.8×10^7 Pa, 2.1×10^7 Pa, 2.8×10^7 Pa, respectively and a temperature of 100°C as initial conditions. The Facies 1A simulations were conducted at both minimum and maximum reservoir pressures, whereas the remaining sets of simulations were conducted at mean reservoir pressure.

Porosity and Permeability

Within the Clarke Lake field and the surrounding area, 318 small-plug porosity and permeability analyses from 15 cored wells and porosity well-log data from 4 wells are available, selected to represent specific depositional or diagenetic facies. Facies rock types, bioclast types, depositional environments and petrophysical properties are summarized in Table 2.2.

A geostatistical analysis was conducted on 7 wells where small-plug and well-log porosity/permeability data exist. The location of these wells is shown on a structural map of the Slave

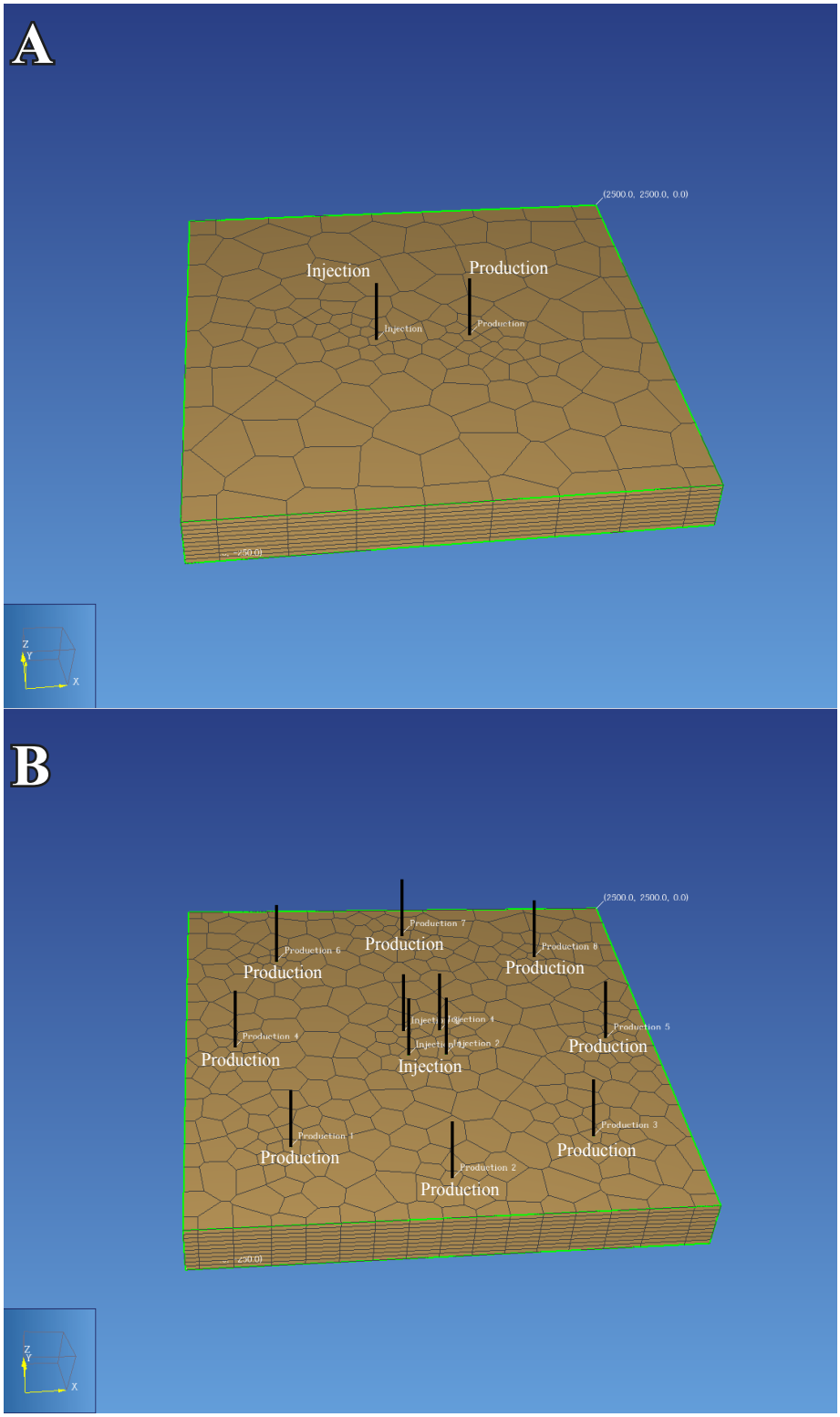

Figure 2.2: (A) The doublet well configuration. (B) The well configuration using four injection wells and eight production wells.

Well ID	DST Number	DST Bottom Hole Temp. (degC)	Maximum Shut-in Pressure (kPa)
200c050K094J0900	1	87.8	19822.4
200c050K094J0900	3	99.4	19705.2
200c050K094J0900	4		19739.7
200c050K094J0900	5		19781.1
200c056L094J0900	1	87.8	19684.5
200c056L094J0900	2	53.3	19753.5
200b072L094J0900	1		18498.6
200b073L094J0900	1	116.7	15761.4
200a077L094J0900	1	103.3	17064.5
200a077L094J0900	3	121.1	17085.2
202d088L094J0900	2	71.1	20256.8
202d088L094J0900	3	91.1	19843.1
200d091L094J0900	3	90	
200c092L094J0900	1	105.6	17209.3
200c052F094J1000	1	101.1	18443.5
200c052F094J1000	2		18347
200c054F094J1000	1	98.9	19684.5
200c054F094J1000	2	108.9	16871.5
200c054F094J1000	3	53.3	17636.8
200a061F094J1000	1	106.7	
200a061F094J1000	2	106.7	18871
200a061F094J1000	3	107.2	18643.4
200a061F094J1000	4	108.9	19622.5
200d066G094J1000	1	108.9	17000
200d072G094J1000	1	123.3	19739.7
200a081G094J1000	1	88.7	
200a081G094J1000	2	97.2	16378
200b018I094J1000	1	151.7	19650.1
200c020I094J1000	1	127.8	19705.2
200c069I094J1002	1	87.8	18967.5
200c069I094J1002	2	101.7	18843.4
200c078I094J1000	4	100.6	19829.3
200c085I094J1000	1	148.9	17767.8
200c085I094J1000	2	121.1	19326
200a094I094J1000	1	118.9	16905.9
200c043J094J1000	1	80	19264
200c043J094J1000	2	57.2	19222.6
200b046J094J1000	1	78.9	19553.5
200b046J094J1000	2	95.6	19353.6
200c008D094J1600	1	74.4	19526
200c008D094J1600	2	75.6	20822.2
200c008D094J1600	3	77.8	20256.8
200c008D094J1600	4	96.1	18526.2

Table 2.1: Well ID showing the DST number and the corresponding temperature and maximum shut-in pressure recorded.

Facies Association	Facies	Rock Type(s)	Bioclasts	Depositional Environment	Average Porosity (frac)	Average Permeability (m^2)
Facies Association 1	1A	Wackestone, packstone, grainstone	*Stachyodes* , nodular stromatoporoids, corals, *Amphipora*	Reef flat	0.073	6.80E-14
	1B	Wackestone, packstone, grainstone	Amphipora, nodular stromatoporoids, minor *Stachyodes*	Lagoon	0.076	2.87E-14
	1C	Mudstone	Minor *Amphipora*	Tidal flats	0.06	2.94E-15
	1D	Wackestone, packstone	*Stachyodes* , lamellar stromatoporoids, coral, crinoids	Open platform	N/A	N/A
Facies Association 2	2A	Boundstone	Massive, hemispherical stromatoporoids	Reef margin	0.064	5.49E-14
	2B	Wackestone, packstone, grainstone	*Stachyodes* , nodular and tabular stromatoporoids , corals, *Amphipora* , crinoids	Reef margin	0.064	5.49E-14
	2C	Wackestone, grainstone	Tabular stromatoporoids, *Stachyodes* , crinoids, gastropods	Reef foreslope	N/A	N/A
Facies Association 3	3A	Wackestone, mudstone	Crinoid ossicles, brachipod shell fragments	Basinal/deep interior	0.105	7.09E-14
	3B	Mudstone	Crinoid ossicles, brachipod shell fragments	Basinal/deep interior	0.105	7.09E-14
Facies Association 4	4A	N/A	N/A	N/A	0.05	2.01E-13
	4B	N/A	N/A	N/A	0.503	5.59E-14

Table 2.2: Described facies and their respective rock types, bioclasts, depositional environments, average porosity and average permeability.

Point Formation in Figure 2.3. Vertical variograms are modeled to represent the spatial variability in porosity. A horizontal variogram is assumed to be proportional to the vertical variogram, an assumption commonly made where there is a lack of horizontal data pairs available to calculate a stable experimental horizontal variogram. Porosity realizations are then simulated using the sequential Gaussian method (Deutsch & Journel, 1999). A bivariate distribution is fit between the porosity and permeability data so that a permeability value can be associated with the simulated

porosity by drawing from the conditional distributions. We used these simulated realizations as inputs into flow models.

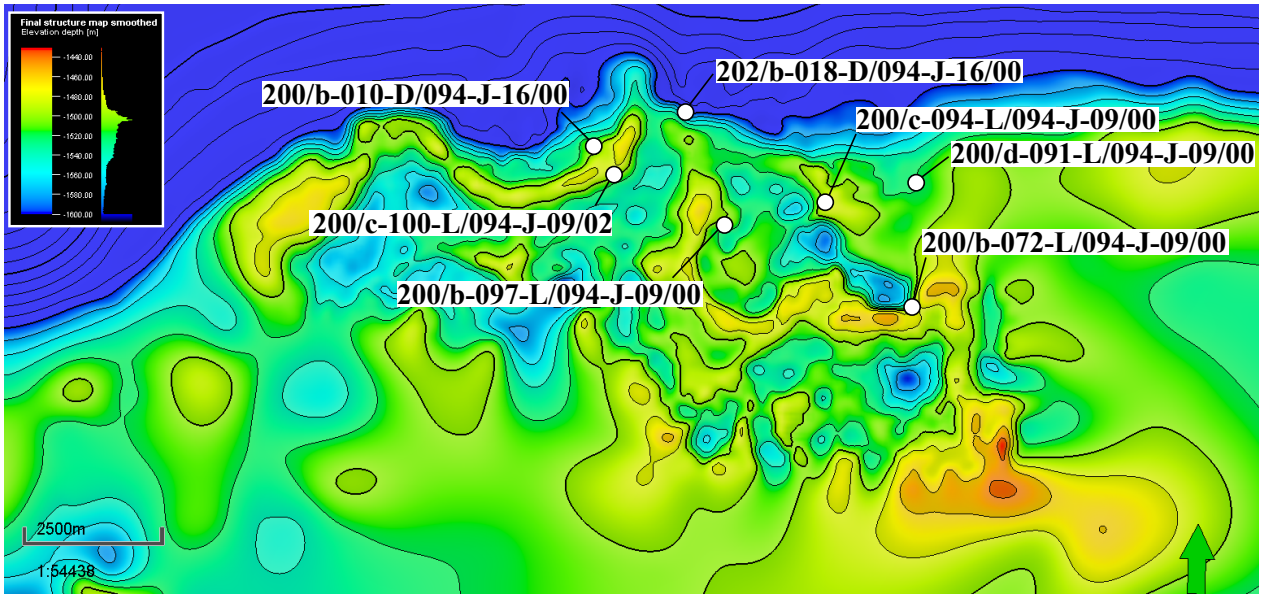

Figure 2.3: The location of wells where porosity from core plugs and well logs were used to construct the geostatistical analysis for simulation inputs.

2.2.3 Flow Simulations

Facies 1A simulations

For the first set of simulations, fourteen 25-year flow simulation cases were conducted within a 2500 x 2500 x -250 polygonal mesh representing Facies 1A, which consists of nodular stromatoporoid coral wackestone to packstone and is characterized by relatively high mean porosity and permeability. It represents a significant proportion of Slave Point Formation sediments. A polygonal mesh was used to provide a refined cell structure around the production and injection wells. Completion zones were set to a thickness of 50 m. Twelve of the fourteen simulations are doublet configurations. Both the injection and production water circulation rates were 25 kg/s. The last two of these simulations were based on the four injection-eight production well configuration (Figure 2.2), where injection was set to 50 kg/s and production wells produced at 25 kg/s, for a total flow rate of 200 kg/s. For each simulation, we assumed uniform horizontal permeability, vertical permeability and porosity. We tested the maximum, minimum, mean, median, Q1 (first quartile) and Q3 (third quartile) values of Facies 1A porosity, horizontal permeability and

vertical permeability. For doublet configurations, each value was populated throughout the grid and was tested twice, using 2.8 x 10^7 Pa and 1.8 x 10^7 Pa as initial pressure conditions. The four injection-eight production well model was tested using mean porosity and permeability twice, using the same pressure initial conditions. Facies 1A porosity and permeability inputs are shown in Table 2.3.

Statistical input	Horizontal permeability (m^2)	Horizontal permeability (md)	Vertical permeability (m^2)	Vertical permeability (md)	Porosity (frac)
Max	1.03E-12	1044	6.91E-15	7	0.17
Min	2.07E-16	0.21	9.87E-18	0.01	0.01
Mean	9.18E-14	93	6.81E-15	6.9	0.08
Median	9.18E-15	9.3	5.13E-17	0.05	0.07
Q1	1.48E-15	1.5	1.78E-16	0.18	0.05
Q3	5.72E-14	58	2.76E-15	2.8	0.1

Table 2.3: Facies 1A inputs of horizontal, vertical permeability and porosity

Monte-Carlo simulations using cloud transformed data

The second set of Monte-Carlo simulations were run 200 times using different probabilistic inputs of porosity and permeability to populate 100 x 100 x 10 m reservoir cells within a 2000 x 2000 x -250 m regular mesh. This set attempted to better simulate the natural heterogeneity of flow patterns within the hydrothermal dolomite reservoir. The model was populated with porosity and a cloud transformation was run to assign appropriate permeability values using a conditional bivariate distribution that was fit between the collocated data. The cloud transformation uses the location of a randomly drawn porosity value to select a distribution from which a random value of permeability is drawn. Doublet configurations with 25 kg/s flow rates and 50 m completions were used. The final temperatures within production well cells were averaged and reviewed to provide a distribution of the final temperature at the production well after a 25-year simulation period. Initial pressure conditions were set to 2.1 x 10^7 Pa.

Varying flow rates and completion lengths using cloud transformed data

A third set of simulations was conducted on a 20 x 20 x 25 cell (100 x 100 x 10 m cell size) grid using a doublet configuration to test the effects of differing completion lengths and flow rates. The model was tested using flow rates of 10 kg/s, 25 kg/s and 50 kg/s using a 50 m completion length. The model also used a 100 m completion length as an input with a 25 kg/s flow rate. Each parameter was simulated 25 times using different realizations of porosity and permeability,

derived from the previously described cloud transformation, in which porosity and permeability values are selected using a conditional bivariate distribution. Initial pressure conditions were set with a value of 2.1 x 10^7 Pa.

Varying grid size using cloud transformed data

The fourth set of simulations was completed with grids of varying cell sizes to identify how cell size and number affects the modeled temperature-drop at the production well after a 25-year simulation. The grid sizes used were 20 x 20 x 25 (100 x 100 x 10 m cell size), 40 x 40 x 25 (50 x 50 x 10 m cell size), 50 x 50 x 25 (40 x 40 x 10 m) and 80 x 80 x 25 (25 x 25 x 10 m). The different grids with their associated porosity are shown in Figure 2.4 Flow through each grid was simulated 5 times using a doublet configuration, using different realizations sourced from the cloud transformation previously described, in which porosity and permeability values were selected using a conditional bivariate distribution. We also tested the fine grid (80 x 80 x 25) at a flow rate of 50 kg/s to compare with the 50 kg/s coarse grid simulations (in section 2.3.3).These simulations used 2.1 x 10^7 Pa as an initial pressure condition, 25 kg/s flow rates and 50 m completions.

2.2.4 Power potential calculations

We estimate the electrical power (kWe) and the electrical power loss as a result of thermal breakthrough for the doublet and four injection-eight production well configurations by using a thermal power equation:

$$kWe = (\dot{m})(Cp)(dT)(\eta) \quad (1)$$

Where $\dot{m}$ represents mass flow rate (kg/s), Cp is fluid heat capacity (kJ/kgK), dT is change in temperature (K) and η is the electrical utilization factor (the ratio of the time an engine is in use to the total time it could be in use). Mass flow rates of 10 kg/s, 25 kg/s and 50 kg/s were used for the doublet well configuration and 200 kg/s was used for the four injection-eight production well configuration. We assume a fluid heat capacity of 4.19 kJ/kgK for water (Chase, 1998). The parameter dT is the difference between the inlet temperature and the outlet temperature of an organic rankine cycle engine, a system in which low-enthalpy geothermal heat can be converted

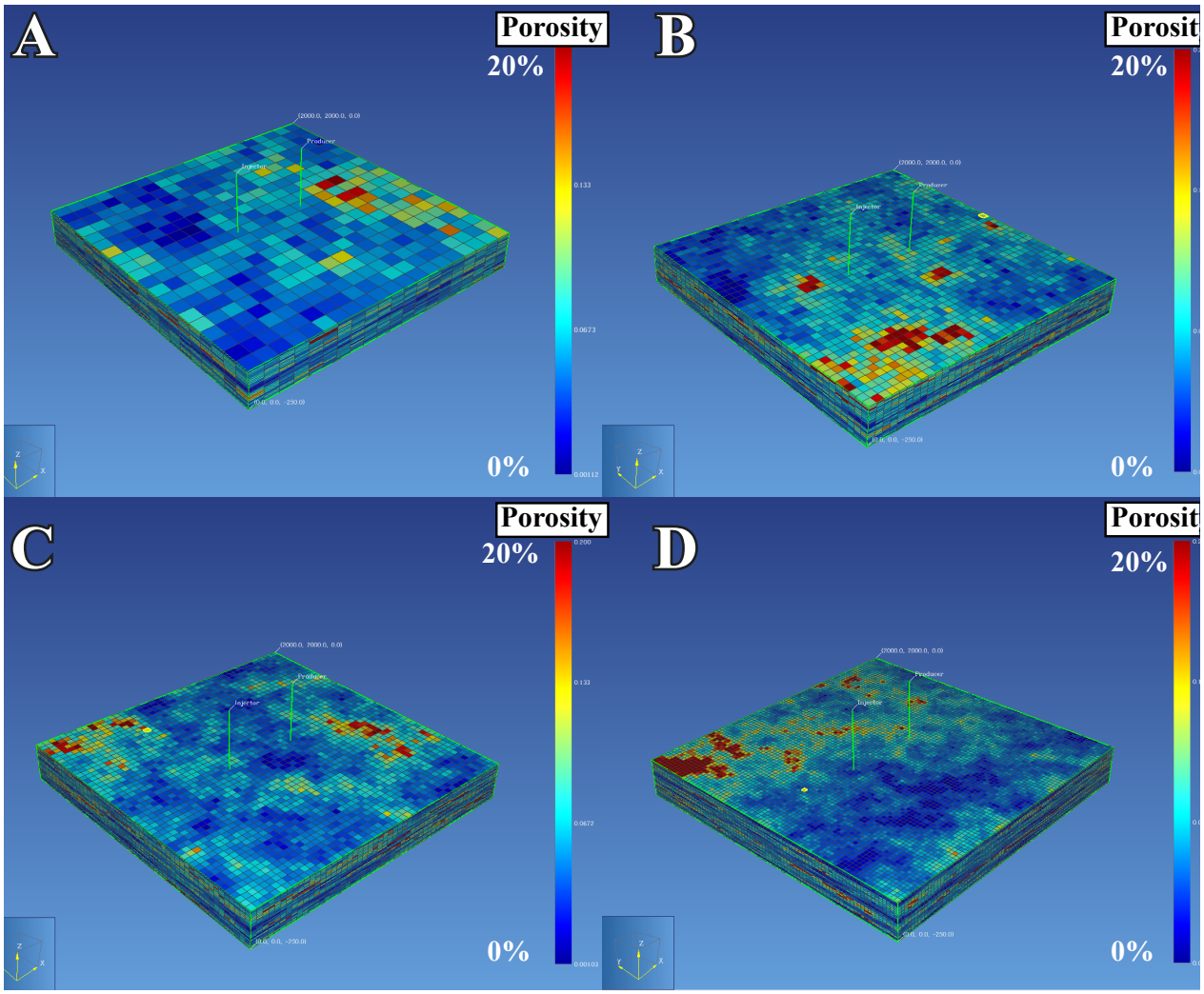

Figure 2.4: Varying grid sizes representing a 2000m x 2000m portion of Clarke Lake with cloud transformed porosity and permeability data. (A) 20 x 20 x 25 cell grid. (B) 40 x 40 x 25 grid. (C) 50 x 50 x 25 grid. (D) 80 x 80 x 25 grid.

to electricity (Yamamoto et al., 2001). We assume an inlet temperature of 100°C corresponding to produced Slave Point Formation reservoir fluids and an outlet temperature of 70°C, which corresponds to the temperature of fluid reinjected into the formation. For the electrical utilization factor we assume a value based on a linear relationship between the inlet temperature (Tr) and the utilization factor. The utilization factor is defined as (Augustine et al., 2009):

$$\eta = [(0.3083(Tr))-98.794]/100 \quad (2)$$

2.3 Results

2.3.1 Facies 1A simulations

The results of the simulations are shown in Table 2.4. Using the maximum, mean, median and third quartile (Q3) values of porosity and permeability for Facies 1A with doublet configurations, the temperature of produced fluid after 25 years of production ranged from 97.42 to 98.46 °C, a 1.54 to 2.58 °C temperature drop. The four injection-eight production well configuration showed a relatively large temperature drop (4.62 °C) when using high pressure as an initial condition; however, when using low pressure as an initial condition the temperature drop was small (0.32 °C). Using minimum and Q1 values of porosity and permeability caused the simulations to halt prematurely due to the calculated pressure at the injection well exceeding the software's limit. In these cases, pressure reached a near zero value. An example of a doublet simulation run is shown in Figure 2.5, which depicts four representative stages in the simulation: 4.76 $x10^{-5}$, 0.208, 5 and 25 years (referred to as time steps). The cold water temperature plume around the injection well grows at each time step as cold, 70°C water is re-injected into the reservoir. At the 25-year time step, the plume reaches the production well, and the final temperature of the produced water is 97.89°C. Figure 2.6 shows the temperature and pressure at the production and injection wells through simulation time (in years). Pressure decay is linear in both the injection and production wells. Pressure at the injection well initially decreases due to a cold, less dense fluid being inject-

Well model	XY Perm/Z Perm/Pororsity Inputs	Pressure	Average final temperature at producer (degrees C)
Doublet	1.03E-12 m^2/ 6.91E-15 m^2/ 17 %	2.8 x 10^7 Pa	97.89
Doublet	1.03E-12 m^2/ 6.91E-15 m^2/ 17 %	1.8 x 10^7 Pa	97.99
Doublet	9.18E-14 m^2/ 6.81E-15 m^2/ 8 %	2.8 x 10^7 Pa	97.82
Doublet	9.18E-14 m^2/ 6.81E-15 m^2/ 8 %	1.8 x 10^7 Pa	97.92
Doublet	9.18E-15 m^2/ 5.13E-17 m^2/ 7 %	2.8 x 10^7 Pa	98.35
Doublet	9.18E-15 m^2/ 5.13E-17 m^2/ 7 %	1.8 x 10^7 Pa	98.46
Doublet	2.07E-16 m^2/ 9.87E-18 m^2/ 1 %	2.8 x 10^7 Pa	N/A
Doublet	2.07E-16 m^2/ 9.87E-18 m^2/ 1 %	1.8 x 10^7 Pa	N/A
Doublet	1.48E-15 m^2/ 1.78E-16 m^2/ 5 %	2.8 x 10^7 Pa	N/A
Doublet	1.48E-15 m^2/ 1.78E-16 m^2/ 5 %	1.8 x 10^7 Pa	N/A
Doublet	5.72E-14 m^2/ 2.76E-15 m^2/ 1 %	2.8 x 10^7 Pa	97.42
Doublet	5.72E-14 m^2/ 2.76E-15 m^2/ 1 %	1.8 x 10^7 Pa	97.55
4 injector 8 producer	9.18E-14 m^2/ 6.81E-15 m^2/ 8%	2.8 x 10^7 Pa	95.38
4 injector 8 producer	9.18E-14 m^2/ 6.81E-15 m^2/ 8%	1.8 x 10^7 Pa	99.68

Table 2.4: Results of simulations using varying porosity and permeability inputs for Facies 1A.

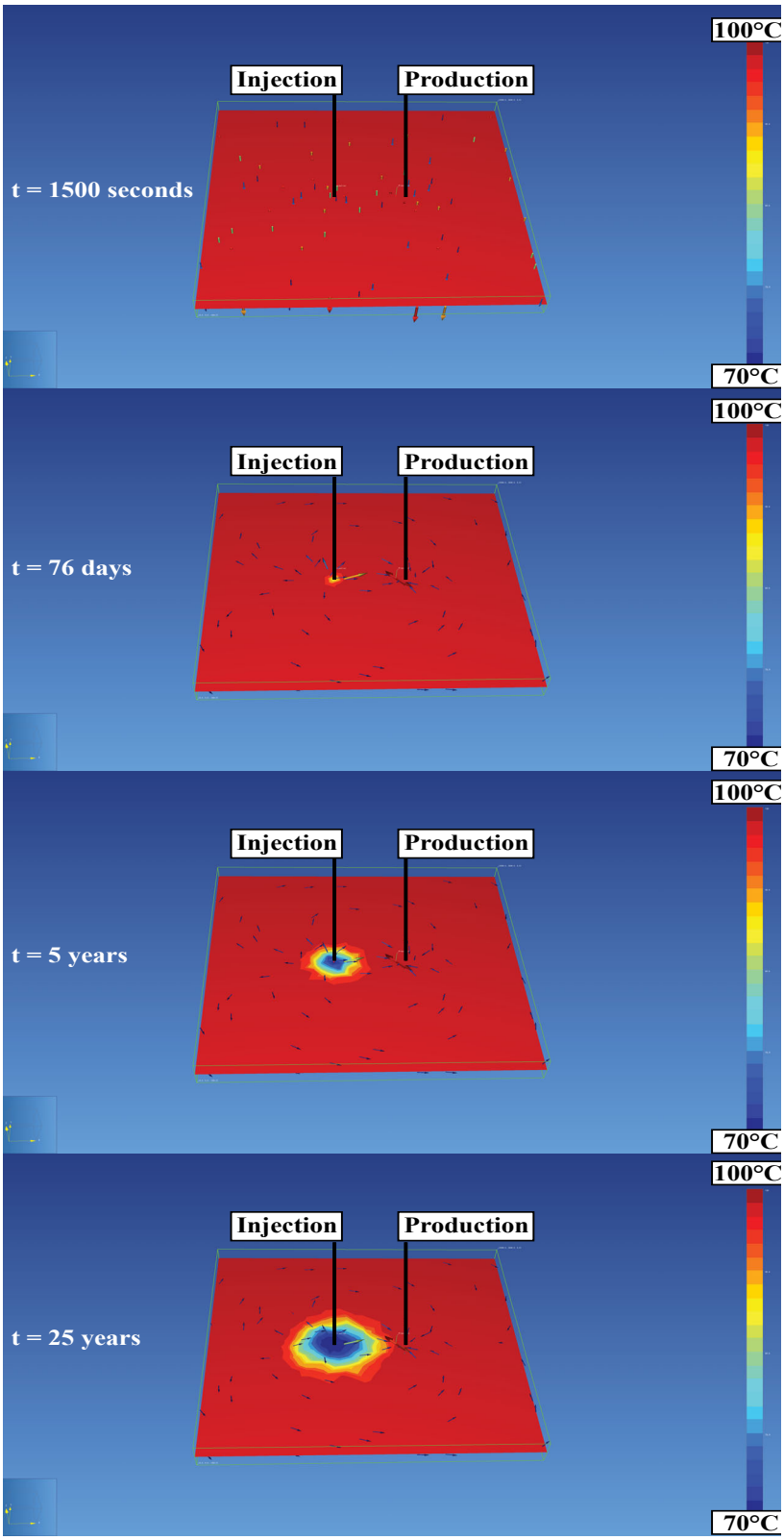

Figure 2.5: Four time steps through the first set of simulations showing the movement of the cold reinjection plume when using max values of porosity and permeability for Facies 1A at high reservoir pressure.

ed, but then stabilizes at the start of the linear decay once the temperature around the injection well stabilizes to 70°C.

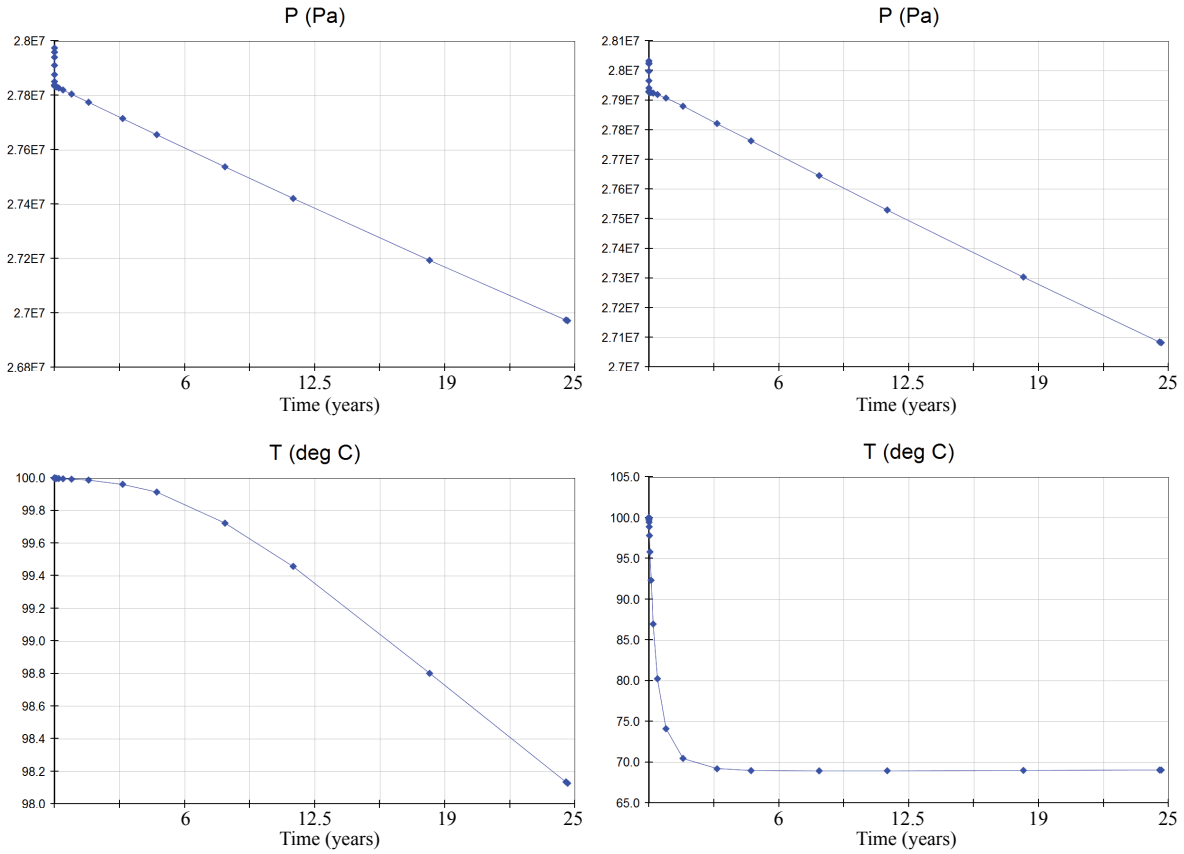

Figure 2.6: Production well pressure and temperature through the 25-year simulation (left) and the injection well pressure and temperature through the 25-year simulation (right) for the maximum porosity and permeability and high pressure Facies 1A simulation case.

2.3.2 Monte-Carlo simulations using cloud transformed data

The results of a series of Monte-Carlo simulations of production well temperatures after 25 years represent a left-skewed distribution, as shown in Figure 2.7. The mean final temperature of produced fluid from the 200 simulations is 97.31°C ± 1.38°C. The maximum temperature recorded at the production well is 99.64°C and the minimum is 92.61°C. Figure 2.8 shows time steps through one of the simulations. The left column shows cross-sections through the 3D simulation and the temperature of each cell, whereas the right column shows the expansion of the 95°C isotherm.

2.3.3 Varying flow rates and completion lengths using cloud transformed data

The results of this set of simulations are shown in Table 2.5. Increasing the circulation rates shows an inversely proportional relationship with the final temperature at the production well. The temperature decreases after 25 years associated with 10 kg/s and 25 kg/s flow rates are 0.47°C and 2.54°C, respectively. These are relatively small drops in temperature compared to the

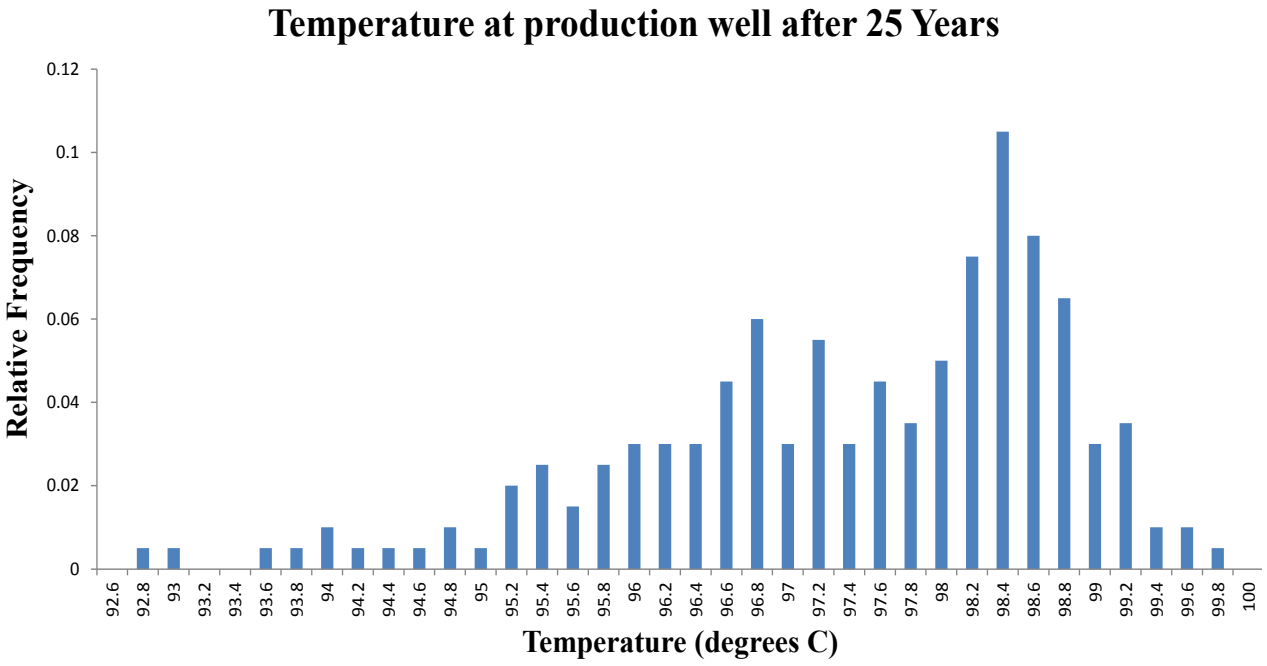

Figure 2.7: A histogram representing the results of the Monte-Carlo analysis showing the final temperature of at the production well from 200 simulations. Temperature for each bin is rounded to the nearest 0.2°C.

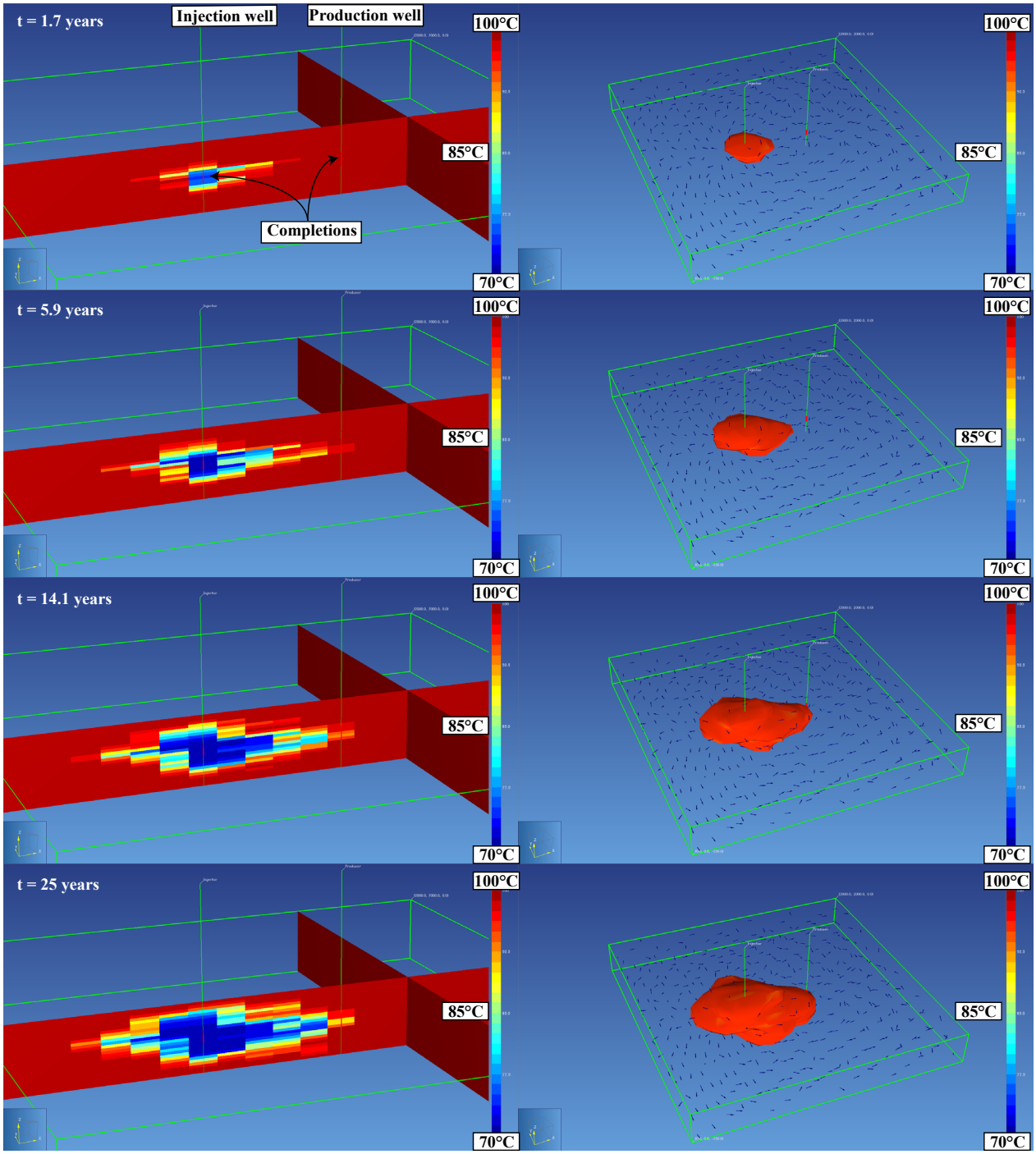

Figure 2.8: Example from one Monte-Carlo simulation using a realization for porosity and permeability. The left column shows time steps through the simulation and how temperature permeates each cell. The right column shows the 95°C isotherm through the same time steps in the simulation.

Flow rate	Completions length	Average final temperature at producer (degrees C)
10 kg/s	50 m	99.53
25 kg/s	50 m	97.46
50 kg/s	50 m	94.45
25 kg/s	100 m	97.71

Table 2.5: The final temperature results of simulations when varying the flow rates and completion lengths.

50 kg/s flow rate simulations, which saw an average temperature drop of 5.55°C. Doubling the completion length from 50 m to 100 m did not have a significant impact on the final temperature at the production well. The temperature drop (2.29°C) is relatively similar to that of the 25 kg/s and 50 m completion simulation case, although the range of data within the 100 m completion simulations is smaller (Figure 2.9).

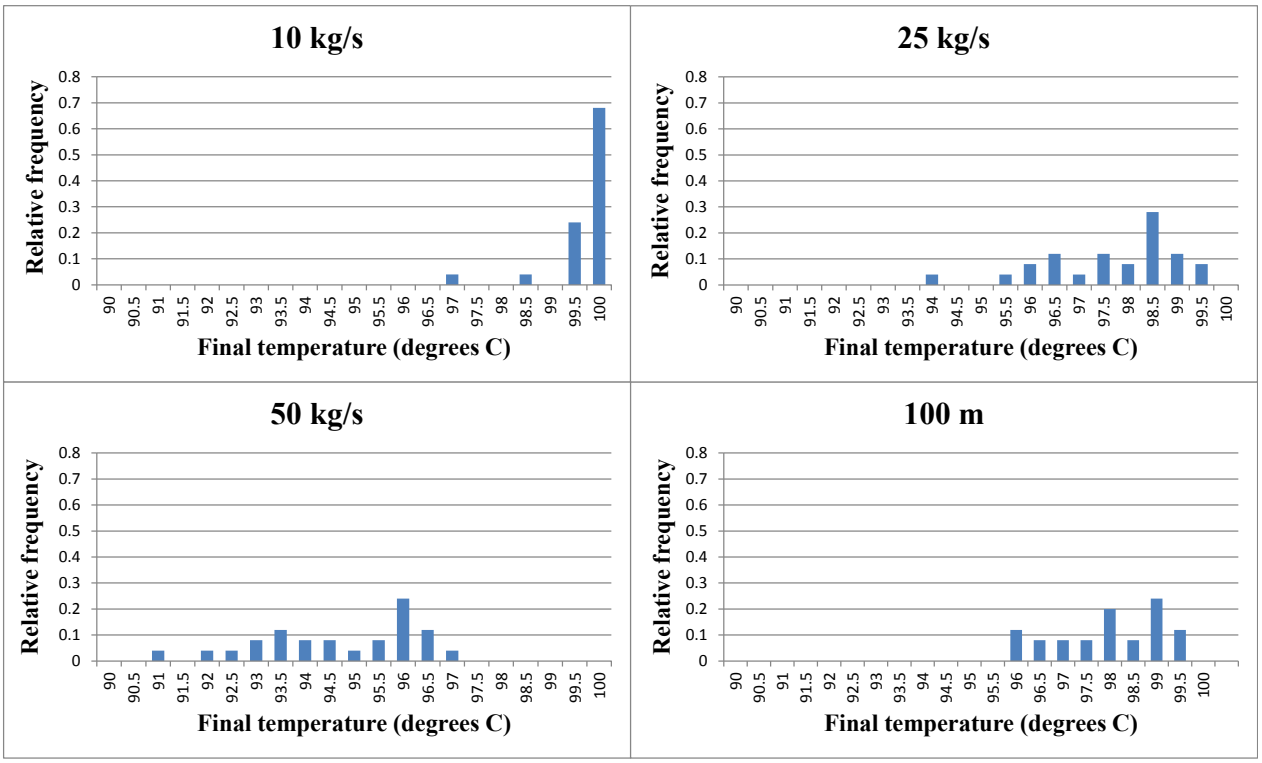

Figure 2.9: Histograms showing the results of the simulations that varied the flow rate (top right, top left and bottom left) and completion lengths (bottom right). Temperature for each bin is rounded to the nearest 0.5°C.

2.3.4 - Varying grid size using cloud transformed data

The results of these simulations are shown in Table 2.6. Progressively finer grids result in smaller temperature drops at the production well. The difference between the average final temperature of the five simulations using the coarsest grid (20 x 20 x 25 cells) and the finest grid (80 x 80 x 25 cells) is 1.88 °C. The 40 x 40 x 25 and the 50 x 50 x 25 grids show a difference in the average final temperature of 0.15 °C. The difference between the average final temperatures of the 50 x 50 x 25 and the 80 x 80 x 25 grids is 0.31 °C. A similar relationship is found using a 50 kg/s flow rate. The finest grid showed a final average temperature drop of 2.43 °C compared to 5.55 °C using the coarsest grid.

Grid size (cells)	Flow rate (kg/s)	Cell resolution (meters)	Average final temperature at producer (degrees C)
20 x 20 x 25	25	100 x 100 x 10	97.79
40 x 40 x 25	25	50 x 50 x 10	98.88
50 x 50 x 25	25	40 x 40 x 10	99.18
80 x 80 x 25	25	25 x 25 x 10	99.46
80 x 80 x 25	50	25 x 25 x 10	97.57

Table 2.6: The final temperature results of simulations varying the grid size and flow rates.

2.3.5 Power output estimates

We quantified the decrease in power potential as a result of temperature decrease at the production well using the thermal power equation (1) and applying the mean temperature drop of the produced formation fluids from probabilistic simulations. With no temperature change at the production well (produced fluids remain at 100 °C) and a 25 kg/s flow rate, we estimate a base case of power potential at 511 kWe. Using the mean value of temperature drop (2.7 °C) from probabilistic simulations, this estimate is reduced to 465 kWe, which amounts to a ~ 10% reduction in power due to thermal breakthrough. Similarly, a base case using 50 kg/s flow rates has a power potential of 1036 kWe compared with a power potential of 930 kWe resulting from 5.6 °C temperature drop, a 10 % reduction in power. The four injection-eight production well configuration, with a flow rate total of 200 kg/s has a base case power potential of 4085 kWe. A mean temperature drop of 4.6 °C (from the high pressure simulation case), results in a 3456 kWe estimate of power, or a ~ 15% reduction in power due to the effects of thermal breakthrough. Using 10 kg/s flow rates produced a negligible effect on the power potential, reducing the estimate assuming no

thermal breakthrough of 204 kWe to 203 kWe.

2.4 Discussion

2.4.1 Thermal breakthrough

All sets of simulations show temperature drops at the production well(s), assuming a realistic range of values for porosity and permeability. The most significant control on temperature change at the production well is flow rate. The average temperature drop of 5.6 °C associated with a 50 kg/s flow rate indicates an upper limit to possible flow rates for doublet well configurations. When power reduction is calculated as a percentage of the base case (no thermal breakthrough), the 25 kg/s and 50 kg/s flow rate scenarios show a similar power reduction of ~ 10 %. Although the temperature drop associated with 50 kg/s flow rates is larger than the 25 kg/s scenario, more overall power can be produced with the same efficiency using 50 kg/s flow rates. The power reduction increases to ~ 15 % using the four injection-eight production well configuration, suggesting that more wells or more complex well configurations reduce the overall efficiency of power production. Using 10 kg/s flow rates for well doublet models showed a negligible effect on thermal breakthrough.

Because produced water temperatures decline to their 25 year values over time, sometimes quite late in the time span, average power reduction over 25 years is less than that seen at the end of the period. The efficiency of power production decreases linearly with temperature at the first instance of reinjection fluids reaching the production well. To quantify the difference in power, we compare the average power output over the period from the first moment of thermal breakthrough to the end of the 25 year period and the power output assuming production from the final temperature over the 25 year period. The difference between these estimated power outputs is ~ 6%. Providing estimates based on the linear decrease of power production requires calculating the average power output on a simulation-by-simulation basis, which is out of the scope of this study. Instead, we offer conservative estimates based on average temperature drops observed within the several simulations undertaken herein.

Varying the grid size in simulations affects the estimation of thermal breakthrough. Coarser grid

sizes (20 x 20 x 25 cells) slightly underestimate the final temperature compared to finer grids (80 x 80 x 25). The difference in temperatures between fine grid sizes and coarse grids is small (1.7 °C difference in the mean final temperature). Similar results were obtained using 50 kg/s flow rates, the average final temperature of the 80 x 80 x 25 grid being 2.4 °C, lower than the average temperature drop (5.6 °C) using the 20 x 20 x 25 grid. Using coarser grids tend to overestimate the average temperature drop at the production well, the dT value in the thermal power equation and the overall power reduction due to thermal breakthrough. The discrepancy in final temperatures between fine and coarse grid sizes is most likely due to numerical discretization error, wherein error is accumulated with each iteration of the simulation. The error in each step is large with the coarse grid, compared to a finer grid, which produces smaller error (positive or negative) with more iterations, and generally the more reliable result. Completion lengths affect the final temperature much less than varying flow rates, since the average temperature drop from simulations using 100 m completions is 2.3 °C compared to a 2.5 °C average temperature drop using 50 m completions.

2.4.2 Geothermal potential at Clarke Lake field

We compare the calculated power potentials of the different well configurations in this study to previous estimates of Clarke Lake's geothermal power potential to estimate the number of geothermal installations necessary to achieve the power potential estimated in previous studies of Clarke Lake (34.8 MW ± 10.8 MW and 63.2 MW; Walsh, 2013; Palmer-Wilson et al., 2018). A total of 136 well doublets using a 25 kg/s flow rate would need to be installed to achieve the highest estimate of 63.2 MW, whereas 52 well doublets would achieve the lowest estimate of 24 MW (lower end of the 34.8 ±10.8 MW. Sixty eight well doublets flowing at 50 kg/s would achieve 63.2 MW and 26 well doublets would be needed to achieve 24 MW. The four injection-eight production well configuration would require 19 installations to achieve 63.2 MW and 7 installations to achieve 24 MW. However, the four injection-eight production well configuration requires a specific arrangement of injection and production wells that current gas wells at Clarke Lake field do not have. The irregular nature of the reservoir body also complicates the use of the doublet and four injection-eight production well configurations. In certain locations of the reservoir, the four

injection-eight production well configuration would not fit within the reservoir extent (assuming a circle with a radius of 1.9 km to account for interference between four injection-eight production well models; Fig. 2.10). Given the area of the dolomite alteration body and assuming a circle with a diameter of 0.75 km to account for interference between doublets, the field could roughly fit 63 doublets (Fig. 2.10). Based on these limits, the estimate for total power of 63.2 MW is unreasonable when using the 25 kg/s flow rates for the doublet model. Using 50 kg/s flow rates, 63.2 MW would not be achievable given the constraint of the reservoir area, which would not be able to fit 68 well doublets. Achieving power production within the lower range of estimates is feasible for all scenarios except when using a flow rate of 10 kg/s. To achieve the lowest estimate, 24 MW, using 10 kg/s, a total of 118 doublets would be needed.

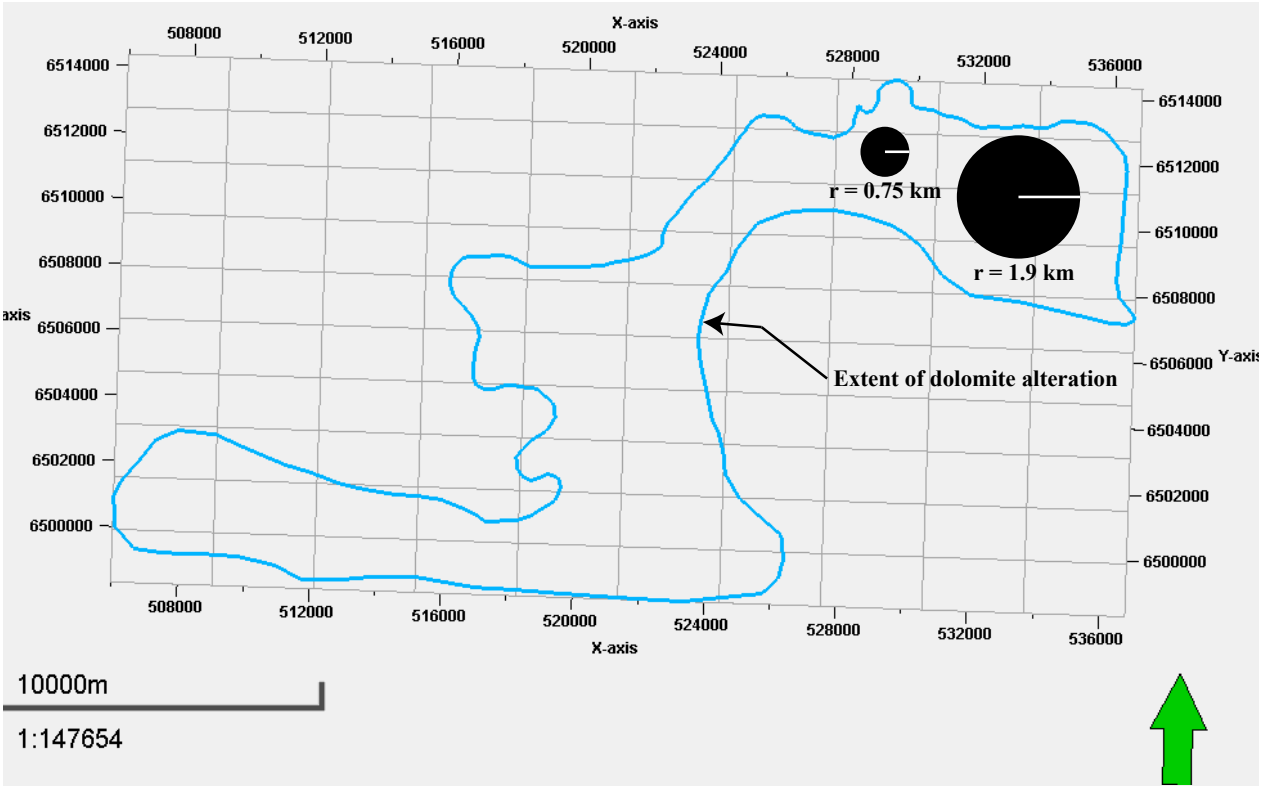

Figure 2.10: Boundary of the reservoir body at the Clarke Lake field with circles representing the area needed for a doublet (r = 0.75 km) and four injection-eight production (r = 1.9 km) well model.

Reservoir permeability generally increases from the reef interior toward the reef margin, because hydrothermal alteration was most intense in high primary porosity and permeability sediments that were stratigraphically trapped by shale. Increased hydrothermal alteration coincides

with increased development of natural fracture networks, resulting in the highest average permeabilities even where porosity is relatively low. Areas of intense hydrothermal alteration are also associated with collapse synclines, identifiable with seismic data (Gorecki et al., 2010). These locations are viable locations for geothermal doublets because of the natural high permeability associated with fault and fracture networks. However, faults and fractures provide fast migration paths for reinjected fluids, which can cause early thermal breakthrough, like in the Ahuachapan, Palinpinon, and Svartsengi fields (Stefansson, 1997). Faults and fractures must be accounted for a successful geothermal production and injection scenario, and tracer analysis between pre-existing wells at Clarke Lake could provide insight into early breakthrough. The integration of models of natural and artificial fractures (assuming Clarke Lake wells undergo hydraulic fracturing) could provide additional insights into well-pair productivity and the timing of thermal breakthrough (Blöcher et al., 2010; Shaik et al., 2011).

2.4.3 Applicability to other sedimentary reservoirs

Major reservoir bodies around the world, including Devonian, Mississippian, Ordovician, Permian, Triassic, Jurassic and Cretaceous carbonate deposits in Canada, the United States, Spain, the Arabian Gulf and elsewhere, contain reservoir facies and hydrothermal dolomite bodies similar to Clarke Lake (Davies & Smith, 2006). With rich histories in oil and gas exploration and production, these reservoirs host large oil and gas data sets that can be used to investigate the suitability of repurposing the fields into sources of geothermal power. As these fields become depleted of oil and gas, retrofitting the infrastructure with geothermal facilities offers further economic utility and a source of renewable power.

Proven and prospective geothermal resources are hosted in sedimentary formations across the world, but geological uncertainty is a crucial factor in the exploration and production phases of geothermal energy development (Mathiesen et al., 2010; Schellschmidt et al., 2010; Banks & Harris, 2018; Gluyas et al., 2018; Limberger et al., 2018). The Paris Basin has produced geothermal power for over 40 years from the 14,000 km^2. Dogger carbonate aquifer and will continue to provide heating for the region in the future (Lopez et al., 2010). Carbonate units within the Dogger aquifer display high degrees of lateral and vertical heterogeneity in hydrogeological prop-

erties, which poses difficulties in accurate reservoir modelling. Commonly, 3 and 20 individual producing layers constitute only 10 % of the total aquifer thickness. Using a conditional bivariate distribution to draw porosity and permeability for model inputs provides a useful methodology that can aid in 3D modelling the highly compartmentalized units, such as those of the Dogger aquifer.

Similarly, Upper Jurassic geothermal reservoirs hosted in carbonate sediments within the German Molasse Basin show complex heterogeneity associated with facies differentiation, karstification, dolomitization, fractures and faults (Homuth et al., 2014). Increases in permeability on the order of 2 - 3 magnitudes are observed within dolomite bodies altered from original limestone facies. These dolomitized bodies, which are associated with dissolution along major fault zones, offer hydraulic conditions suitable for high flow rates, which are needed for a sustainable geothermal reservoir. Highly permeable dolomite zones associated with collapse synclines observed at the Clarke Lake field are similar to the reservoir elements of the Upper Jurassic in the Molasse Basin. A better understanding of heterogeneity in dolomite reservoirs can further improve 3D models, resulting in accurate reservoir simulations and more successful geothermal operations. Using variograms with cloud transformed data to model the spatial continuity of porosity and permeability can help predict thermal breakthrough not just for carbonate reservoirs, but for geothermal systems hosted in sedimentary reservoirs as a whole.

2.5 Conclusions

This study has applied porosity and permeability data from the Clarke Lake field to test the potential for thermal breakthrough in geothermal production / injection well pairs. A comprehensive suite of simulations shows that the heterogeneous reservoir properties in the Clarke Lake reservoir are conducive to 25-years of geothermal production, but thermal breakthrough does pose a minor risk to the power potential of the Clarke Lake resource. Further geothermal development of the field must account for the possibility of reinjected fluids reaching the production well.

Monte-Carlo simulations using porosity and permeability inputs drawn from a conditional bivariate distribution show an average temperature drop at the production well of 2.7 °C after a

25-year simulation. Similar values of the temperature drop were shown using both porosity and permeability inputs from reef flat facies and using conditional bivariate distribution inputs for the 100 m completion, 10 kg/s and 25 kg/s simulation cases. The 50 kg/s flow rate simulations resulted in the most significant temperature change at the production well, with an average temperature drop of 5.6 °C at the end of the 25-year simulation. Using coarser grids and decreasing the total cell count resulted in larger temperature drops, whereas finer grids showed smaller, more realistic temperature drops.

We apply the thermal power equation to estimate reduced power potentials as a result of thermal breakthrough. The base case scenarios for power potential, assuming no thermal breakthrough, are 511 kWe, 1036 kWe, and 4085 kWe for the doublet well configuration at 25 kg/s, 50 kg/s and the four injection-eight production configuration at 25 kg/s, respectively. With thermal breakthrough, these estimates are reduced to 465 kWe, 930 kWe, and 3456 kWe. The 25 kg/s and 50 kg/s doublet scenarios show similar values of reduced efficiency at ~ 10%, while the more complex four injection-eight production configuration shows a reduced efficiency of ~ 15% at the end of the 25 year production period. This implies that doublet well configurations are more practical than complex well configurations in terms of power production efficiency. The area of reservoir viable rock at Clarke Lake field supports doublet placements for the lower end of previously established power estimates at 24 MW. Also, the irregular nature and area of the reservoir body does not support the highest estimate of 63.2 MW. Based on the reservoir area and our estimates of power potential from a 50 kg/s doublet, Clarke Lake field has a total power potential of 58 MW.

Drilling of geothermal wells should target the reef margin, or areas with evidence of collapse synclines, due to the high permeability associated with fractures and faults. Variogram modelling and the use of a conditional bivariate distribution provides a strong tool in understanding the natural heterogeneity of hydrogeological characteristics and the effect of thermal breakthrough in geothermal injection-production scenarios hosted in sedimentary reservoirs.

Chapter 3: Conclusions

3.1 Characterization of the Slave Point Formation

Deposition of Slave Point Formation sediments occurred on a rimmed carbonate platform located on the northern edge of the Middle Devonian Presqu'ile Barrier in northeastern British Columbia. During episodes of relative sea level rise, open marine conditions existed across the platform top, depositing cylindrical stromatoporoid shoals. As accommodation space decreased, a difference in energy levels developed across the platform top due to a well-defined reef margin. This resulted in facies differentiation, deposition of tidal flat, lagoonal and reef flat facies occurring in the platform interior and homogeneous foreslope facies at the platform margin. Further south of Clarke Lake field, deposition more closely resembles a platform depositional model, containing open and deepwater platform facies.

High-frequency or composite sequences identified in this study correspond to either fourth or third order sequences deposited during transgressive and highstand system tracts. A comparison of stratigraphic relationships and relative thicknesses of Beaverhill Lake Group strata from the Clarke Lake area to the Swan Hills platform in Alberta shows that the Slave Point Formation at Clarke Lake may be equivalent to three third order depositional sequences, Beaverhill Lake 1, 2 and 3.

The most significant control on reservoir properties is hydrothermal alteration of limestone to dolomite. Primary porosity within limestone is generally poor and cemented by calcite. In dolomite, stromatoporoid bioclasts have been dissolved, resulting in mouldic and vuggy pores and porosity values ranging from 5 to 17 %. Permeability ranges from a few md up to 4000 md where fractures are present. Reef margin deposits tend to show the most hydrothermal alteration due to their high primary porosity and permeability, which allowed dolomitizing brines to preferentially alter the rock. High hydrothermal alteration can also result in lower porosity as pores are cemented by saddle dolomite, fluorite and sulphides. Collapse synclines identified on seismic data represent hydrothermally altered zones that have been highly productive within fields in Alberta. These areas represent interesting targets for production and injection wells due to associated high

permeabilities, a requirement to achieve high flow rates for a successful geothermal operation.

3.2 Numerical modelling of thermal breakthrough at Clarke Lake field

Thermal breakthrough, the impingement of a cold reinjected water plume on a production well, poses a risk to the power potential of geothermal production and injection at Clarke Lake. Future field development will need to account for this risk and mitigate it by choosing appropriate well spacing, well configurations, and flow rates. The base case scenarios for power potential, assuming no thermal breakthrough, are 511 kWe, 1036 kWe, and 4085 kWe for the doublet configuration at 25 kg/s, the doublet configuration at 50 kg/s and the four injection-eight production configuration, respectively. With thermal breakthrough, these estimates are reduced to 465 kWe, 930 kWe, and 3456 kWe. The doublet configurations show reduced efficiencies of ~ 10 %, compared to ~ 15 % with the more complex four injection-eight production configuration. This suggests that using doublet configurations for the well field development may be the most optimal solution in terms of sustainable geothermal power production.

Flow rates had the greatest effect on the final temperature at the production well, high flow rates (50 kg/s in our simulations) resulting in the greatest average temperature drop of 5.6 °C at the end of 25-years of production. Using a lower rate of 25 kg/s resulted in a modeled average of 2.7 °C, and a negligible temperature drop was associated with a 10 kg/s flow rate. Changing the total cell count of models affected estimates of temperature drop at the production well. Using coarser grids resulted in larger temperature drops compared to finer grids, which showed smaller, more realistic temperature drops.

The irregular area of the reservoir constrains the number of idealized well configurations that can be placed at Clarke Lake and whether the previously established estimates of total power production can be achieved. If we account for interference between wells, the four injection-eight production configuration is not an ideal well layout for the Clarke Lake reservoir. If the field is developed with doublets, the Clarke Lake reservoir could accommodate roughly 63 doublets (using a 0.75 km diameter circle to account for interference between doublet models). The power potential of Clarke Lake has been estimated to be between 24 – 63.2 MW. The spatial limitation

of 63 doublets makes the 63.2 MW estimate unreasonable, since 136 doublets flowing at 25 kg/s would be needed to achieve it. Similarly, the highest estimate could not be achieved using 50 kg/s flow rates, since 68 doublets would be needed to achieve 63.2 MW. The lower range of estimates is more feasible except when using 10 kg/s flow rates, which would require 118 doublets to achieve 24 MW. Based on the reservoir area and our estimates of power potential from a 50 kg/s doublet, Clarke Lake field has a total power potential of 58 MW.

References

Arianpoo, N. (2009). The geothermal potential of Clarke Lake and Milo gas fields in northeast British Columbia (Doctoral dissertation, University of British Columbia).

Augustine, C., Field, R., DiPippo, R., Gigliucci, G., Fastelli, I., & Tester, J. (2009). Modeling and analysis of sub-and supercritical binary Rankine cycles for low-to mid-temperature geothermal resources. GRC Transactions, 33, 689-693.

Banks, J., & Harris, N. B. (2018). Geothermal potential of Foreland Basins: a case study from the Western Canadian Sedimentary Basin. Geothermics, 76, 74-92.

Blöcher, M. G., Zimmermann, G., Moeck, I., Brandt, W., Hassanzadegan, A., & Magri, F. (2010). 3D numerical modeling of hydrothermal processes during the lifetime of a deep geothermal reservoir. Geofluids, 10(3), 406-421.

British Columbia Oil and Gas Commission (2019). [Production Data for all wells in B.C.csv]. The BC Oil and Gas Commission. Retrieved from https://www.bcogc.ca/online-services.

Bernstein, L., and Stoakes, F. (1996). Controls on Reservoir Distribution and Quality in the Devonian Slave Point Formation, Cranberry Field, Northwest Alberta: A Geologic Overview.

Boreen, T., and Colquhoun, K. (2001). Ladyfern, NEBC: major gas discovery in the Devonian Slave Point Formation.

Brook, C. A., Mariner, R. H., Mabey, D. R., Swanson, J. R., Guffanti, M., and Muffler, L. J. P. (1978). Hydrothermal convection systems with reservoir temperatures≥ 90° C. Muffler LPJ, Assessment of Geothermal Resources of the United States–1978, Circular, 790, 18-85.

Catuneanu, Octavian, Vitor Abreu, J. P. Bhattacharya, M. D. Blum, R. W. Dalrymple, P. G. Eriksson, Christopher R. Fielding et al. “Towards the standardization of sequence stratigraphy.” Earth-Science Reviews 92, no. 1-2 (2009): 1-33.

Chase, M.W., Jr. (1998). NIST-JANAF Themochemical Tables, Fourth Edition, J. Phys. Chem. Ref. Data, Monograph 9, 1-1951.

Craig, J. H. (1987). Depositional environments of the Slave Point Formation, Beaverhill Lake Group, Peace River Arch.

Crooijmans, R. A., Willems, C. J. L., Nick, H. M., & Bruhn, D. F. (2016). The influence of facies heterogeneity on the doublet performance in low-enthalpy geothermal sedimentary reservoirs. Geothermics, 64, 209-219.

Cutler, W. G. (1983). Stratigraphy and sedimentology of the Upper Devonian Grosmont Formation, northern Alberta. Bulletin of Canadian Petroleum Geology, 31(4), 282-325.

Davies, G. R., 1999, Clarke Lake Slave Point – Keg River reservoir project, northwestern British Columbia: Proprietary report prepared for Petro-Canada Oil and Gas, 70 p.

Davies, G. R., and Smith Jr, L. B. (2006). Structurally controlled hydrothermal dolomite reservoir

facies: An overview. AAPG bulletin, 90(11), 1641-1690.

Deutsch, C. V., & Journel, A. G. (1992). Geostatistical software library and user's guide. New York, 119, 147.

Dunham, R. J. (1962). Classification of carbonate rocks according to depositional textures.

Dunham, R. J. (1970). Stratigraphic reefs versus ecologic reefs. AAPG Bulletin, 54(10), 1931-1932.

Dunham, J. B., Crawford, G. A., and Panasiuk, W. (1983). Sedimentology of the Slave Point Formation (Devonian) at Slave Field Lubicon Lake, Alberta.

Fowler, M. G., Stasiuk, L. D., Hearn, M., and Obermajer, M. (2001). Devonian hydrocarbon source rocks and their derived oils in the Western Canada Sedimentary Basin. Bulletin of Canadian Petroleum Geology, 49(1), 117-148.

Franco, A., & Villani, M. (2009). Optimal design of binary cycle power plants for water-dominated, medium-temperature geothermal fields. Geothermics, 38(4), 379-391.

Franco, A., & Vaccaro, M. (2014). Numerical simulation of geothermal reservoirs for the sustainable design of energy plants: a review. Renewable and Sustainable Energy Reviews, 30, 987-1002.

Geological Survey of Canada, Reinson, G. E., Lee, P. J., Dallaire, S. M., and Waghmare, R. R. (1993). Devonian gas resources of the Western Canada sedimentary basin. Geological Survey of Canada.

Gluyas, J. G., Adams, C. A., Busby, J. P., Craig, J., Hirst, C., Manning, D. A. C., ... & Westaway, R. (2018). Keeping warm: a review of deep geothermal potential of the UK. Proceedings of the Institution of Mechanical Engineers, Part A: Journal of Power and Energy, 232(1), 115-126.

Gorecki, C., Sorensen, J., Steadman, E. (2014). Fort Nelson Test Site – Site Characterization Report (Plains CO2 Reduction (PCOR) Partnership Phase III). Retrieved from the Energy and Environmental Research Center (EERC) website: https://undeerc.org/pcor/technicalpublications/pdf/TR-2014-Fort-Nelson-Test-Site-Characterization-Report.pdf

Gosselin, E. G., Smith, L., and Mundy, D. J. (1988). The Golden and Evi reef complexes, Middle Devonian, Slave Point Formation, northwestern Alberta.

Gray, F. F., and Kassube, J. R. (1963). Geology and stratigraphy of Clarke Lake gas field, British Columbia. AAPG Bulletin, 47(3), 467-483.

Gregg, J. M., and Sibley, D. F. (1984). Epigenetic dolomitization and the origin of xenotopic dolomite texture. Journal of Sedimentary Research, 54(3), 908-931.

Hamm, V., & Lopez, S. (2012, January). Impact of fluvial sedimentary heterogeneities on heat transfer at a geothermal doublet scale.

Homuth, S., Götz, A. E., & Sass, I. (2014). Lithofacies and depth dependency of thermo-and petrophysical rock parameters of the Upper Jurassic geothermal carbonate reservoirs of the Molasse Basin. Zeitschrift der Deutschen Gesellschaft für Geowissenschaften, 165(3), 469-486.

Hriskevich, M. E. (1967, January). Middle Devonian reefs of the Rainbow region of northwestern Canada exploration and exploitation. In 7th World Petroleum Congress. World Petroleum Congress.

Hutton, A. N. (1994). Textural Evidence for the Origin of Dolomitization in the Slave Point Hamburg to Clarke Lake.

Johnstone, M.C. 1982. Study on the feasibility of using Middle Devonian formation water from Clarke Lake gas field, N.E. British Columbia, as a geothermal energy resource, No. 11698. Ministry of Energy and Mines.

Kerans, C. (1991). Geologic characterization of San Andres reservoirs: outcrop-analog mapping, Algerita Escarpment, Guadalupe Mountains and Seminole San Andres unit, northern Central Basin Platform. In Characterization of Reservoir Heterogeneity in Carbonate-ramp Systems, San Andres/Grayburg, Permian Basin (pp. 3-46). The University of Texas at Austin, Bureau of Economic Geology.

Kerans, C., & Kempter, K. A. (2002). Hierarchical stratigraphic analysis of a carbonate platform, Permian of the Guadalupe Mountains.

Kershaw, S., 1998, The application of stromatoporoid palaeobiology in palaeoenvironmental analysis, Palaeontology, vol. 41, pp. 509-544.

Limberger, J., Boxem, T., Pluymaekers, M., Bruhn, D., Manzella, A., Calcagno, P., ... and van Wees, J. D. (2018). Geothermal energy in deep aquifers: A global assessment of the resource base for direct heat utilization. Renewable and Sustainable Energy Reviews, 82, 961-975.

Lonnee, J., and Al-Aasm, I. S. (2000). Dolomitization and fluid evolution in the Middle Devonian sulphur Point Formation, Rainbow South Field, Alberta: petrographic and geochemical evidence. Bulletin of Canadian Petroleum Geology, 48(3), 262-283.

Lonnee, J., and Machel, H. G. (2006). Pervasive dolomitization with subsequent hydrothermal alteration in the Clarke Lake gas field, Middle Devonian Slave Point Formation, British Columbia, Canada. AAPG bulletin, 90(11), 1739-1761.

Lopez, S., Hamm, V., Le Brun, M., Schaper, L., Boissier, F., Cotiche, C., & Giuglaris, E. (2010). 40 years of Dogger aquifer management in Ile-de-France, Paris Basin, France. Geothermics, 39(4), 339-356.

Mathiesen, A., Nielsen, L. H., & Bidstrup, T. (2010). Identifying potential geothermal reservoirs in Denmark. Geological Survey of Denmark and Greenland Bulletin, 20(1), 19-22.

Meijer Drees, N. M. (1988). The Middle Devonian sub-Watt Mountain unconformity across the Tathlina Uplift; District of Mackenzie and northern Alberta, Canada.

Meijer Drees, N. C. (1994). Devonian Elk Point Group of the Western Canada Sedimentary Basin. Geological Atlas of the Western Canada Sedimentary Basin, 129-138.

Morrow, D. W., Zhao, M., and Stasiuk, L. D. (2002). The gas-bearing Devonian Presqu'ile Dolomite of the Cordova embayment region of British Columbia, Canada: Dolomitization and the stratigraphic template. AAPG bulletin, 86(9), 1609-1638.

Muir, I., Wendte, J., and Wong, P. (1985). Devonian Hare Indian-Ramparts (Kee Scarp) evolution, Mackenzie Mountains and subsurface Norman Wells, NWT: basin-fill and platform reef development.

Muir, I. D., & Dravis, J. J. (1992). Burial porosity development in middle Devonian Keg River reservoirs. In Lithoprobe Alberta Basement Transects Workshop, Report (Vol. 28, pp. 102-103).

Nadjiwon, L., Morrow, D. W., and Coniglio, M. (2001). Brecciation and hydrothermal dolomitization of the Middle Devonian Dunedin, Keg River, and Slave Point formations of northeastern British Columbia.

O'Connell, S. C., Dix, G. R., and Barclay, J. E. (1990). The origin, history, and regional structural development of the Peace River Arch, Western Canada. Bulletin of Canadian Petroleum Geology, 38(1), 4-24.

Park, D. G., and Jones, B. (1985). Nature and genesis of breccia bodies in Devonian strata, Peace Point area, Wood Buffalo park, Northeast Alberta. Bulletin of Canadian Petroleum Geology, 33(3), 275-294.

Peters, K. E., & Nelson, P. H. (2012). Criteria to determine borehole formation temperatures for calibration of basin and petroleum system models. SEPM Special Publication, 103, 5-15.

Petro-Canada Oil and Gas (2009). Clarke Lake Experimental Scheme (Annual Report #4).

Phillips, W. J. (1972). Hydraulic fracturing and mineralization. Journal of the Geological Society, 128(4), 337-359.

Potma, K., Weissenberger, J. A., Wong, P. K., and Gilhooly, M. G. (2001). Toward a sequence stratigraphic framework for the Frasnian of the Western Canada Basin. Bulletin of Canadian Petroleum Geology, 49(1), 37-85.

Pruess, K., Oldenburg, C. M., & Moridis, G. J. (1999). TOUGH2 user's guide version 2 (No. LBNL-43134). Lawrence Berkeley National Lab.(LBNL), Berkeley, CA (United States).

Qing, H., and Mountjoy, E. W. (1994). Formation of coarsely crystalline, hydrothermal dolomite reservoirs in the Presqu'ile barrier, Western Canada sedimentary basin. AAPG bulletin, 78(1), 55-77.

Russell, W. L. (1944). The total gamma ray activity of sedimentary rocks as indicated by Geiger counter determinations. Geophysics, 9(2), 180-216.

Sack, L. A. (2000). Sedimentology and dolomitization of the Middle Devonian (Givetian) Slave Point Formation, Cranberry Field, northwestern Alberta, Canada.

SB Geological Associates, 1988, Slave Point and Elk Point facies and stratigraphic study: Fort Nelson area, B.C. NTS 94-J: Proprietary report, 104 p.

Schellschmidt, R., Sanner, B., Pester, S., & Schulz, R. (2010, April). Geothermal energy use in Germany. In Proceedings World geothermal congress (Vol. 152, p. 19).

Shaik, A. R., Rahman, S. S., Tran, N. H., & Tran, T. (2011). Numerical simulation of fluid-rock coupling heat transfer in naturally fractured geothermal system. Applied thermal engineering, 31(10), 1600-1606.

Shook, G. M. (2001). Predicting thermal breakthrough in heterogeneous media from tracer tests. Geothermics, 30(6), 573-589.

Sibley, D. F., and Gregg, J. M. (1987). Classification of dolomite rock textures. Journal of Sedimentary Research, 57(6), 967-975.

Stefansson, V. Đ. (1997). Geothermal reinjection experience. Geothermics, 26(1), 99-139.

Sun, S. Q. (1995). Dolomite reservoirs: porosity evolution and reservoir characteristics. AAPG bulletin, 79(2), 186-204.

Tooth, J. W., and Davies, G. R. (1988). Gift Lake Slave Point Reef, Middle Devonian, Alberta.

Turner, W. A., and Gal, L. P. (2003). Regional structural data from the Hay River area, Northwest Territories, with emphasis on the Pine Point mining camp. Natural Resources Canada, Geological Survey of Canada.

Turner, W. A., Laamrani, A., and Rivard, B. (2003). Laboratory reflectance spectra of hydrothermally altered carbonate facies, Pine Point mining camp, NWT, Canada. Geochemistry: Exploration, Environment, Analysis, 3(4), 369-379.

Walsh, W., and Grasby, S. (2013). Geothermal resource assessment of the Clarke Lake Gas Field, Fort Nelson, British Columbia. Bulletin of canadian petroleum geology, 61(3), 241-251.

Warren, J. (2000). Dolomite: occurrence, evolution and economically important associations. Earth-Science Reviews, 52(1-3), 1-81.

Weides, S., and Majorowicz, J. (2014). Implications of spatial variability in heat flow for geothermal resource evaluation in large foreland basins: the case of the Western Canada Sedimentary Basin. Energies, 7(4), 2573-2594.

Weissenberger, J. A., and Potma, K. (2001). The Devonian of western Canada—Aspects of a petroleum system: Introduction. Bulletin of Canadian Petroleum Geology, 49(1), 1-6.

Wendte, J. C. (1992). Evolution of the Judy Creek complex, a Late Middle Devonian isolate platform-reef complex in west-central Alberta.

Wendte, J., Brynes, A., Sargent, D., and Al-Aasm, I., 2009, Depositional facies framework, evolution, and reservoir architecture of the Upper Devonian Jean Marie Member (Redknife Formation) in the July Lake area of northeastern British Columbia, Bulletin of Canadian Petroleum Geology, vol. 57, pp. 209-250.

White, K. E. (1995). A petrophysical evaluation of the Slave Point Formation, Cranberry field, Alberta.

Willems, C. J. L., Goense, T., Nick, H. M., & Bruhn, D. F. (2016, February). The relation between well spacing and Net Present Value in fluvial Hot Sedimentary Aquifer geothermal doublets; a West Netherlands Basin case study. In 41st Workshop on geothermal aquifer engineering Stanford University.

Witzke, B. J., and Heckel, P. H. (1988). Paleoclimatic indicators and inferred Devonian paleolatitudes of Euramerica.

Wong, P. K., and Oldershaw, A. E. (1980). Causes of cyclicity in reef interior sediments, Kaybob Reef, Alberta. Bulletin of Canadian Petroleum Geology, 28(3), 411-424.

Yamamoto, T., Furuhata, T., Arai, N., & Mori, K. (2001). Design and testing of the organic Rankine cycle. Energy, 26(3), 239-251.

Yose, L. A., Brown, S., Davis, T. L., Eiben, T., Kompanik, G. S., and Maxwell, S. R. (2001). 3-D geologic model of a fractured carbonate reservoir, Norman Wells Field, NWT, Canada. Bulletin of Canadian Petroleum Geology, 49(1), 86-116.

Zhang, Y., Doughty, C., Pan, L., Kneafsey, T., & EC Team. (2018). What Could We See at The Production Well Before The Thermal Breakthrough?. In PROCEEDINGS, 44th Workshop on Geothermal Reservoir Engineering.

Appendix A: Thin Section Descriptions and Photos

Batch 1

WA# 397

#1 6361.17 ft: Minor vuggy porosity partially infilled by saddle dolomite and planar-c crystals. Pyrobitumen occludes intercrystalline porosity. Fluorite occludes vuggy porosity, and shows up as a replacement and alteration product of dolomite crystals. Minor fracture porosity exists. Matrix is composed of nonplanar-a dolomite crystals. Φ= 0.03 K= 8.079

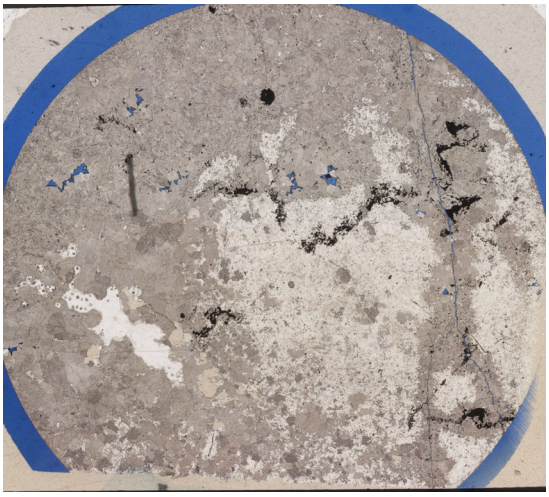

#2 6462.42 ft: Minor fracture porosity that is partially infilled by fluorite. Several laminated mudstone clasts occur that are penetrated and brecciated by veins filled by dolomite. Some mudstone clasts are close to being fully dolomitized, with small mudstone fragments existing as remnants. Pyrobitumen occludes intercrystalline pores. Minor fluorite occludes intercrystalline pores. Matrix is composed of nonplanar-a dolomite crystals. Φ= 0.04 K= 0.022

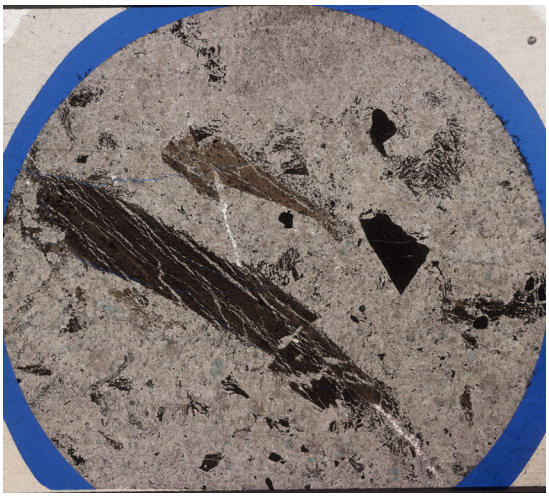

#3 6464.84 ft: Minor fracture porosity partially cemented by dolomite. Minor intercrystalline porosity is partially infilled by planar-c cement. A large quantity of fluorite mineralization occludes porosity and shows up as a replacement and alteration product of dolomite crystals. Minor amounts of pyrobitumen occluding intercrystalline porosity. Matrix is composed of nonplanar-a to coarser planar-s/nonplanar-a transitional dolomite crystals. Φ= 0.03 K= 0.097

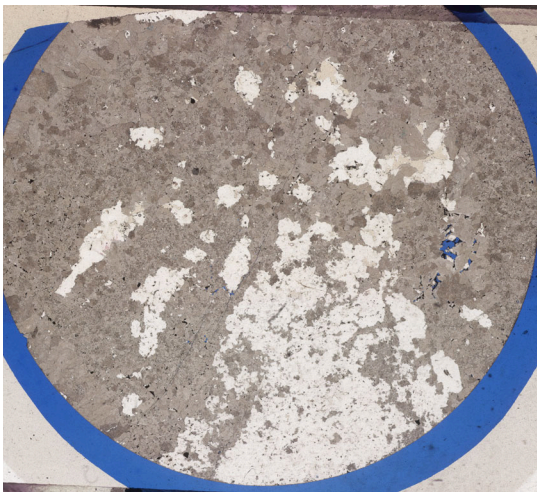

#4 6424.75 ft: No visible porosity due to fluorite occluding intercrystalline and vuggy pores. Matrix is composed of relatively large (10mm) planar-s/nonplanar-a transitional dolomite crystals. Minor amounts of pyrobitumen infilling intercrystalline pores. Φ= 0.04 K= 0.031

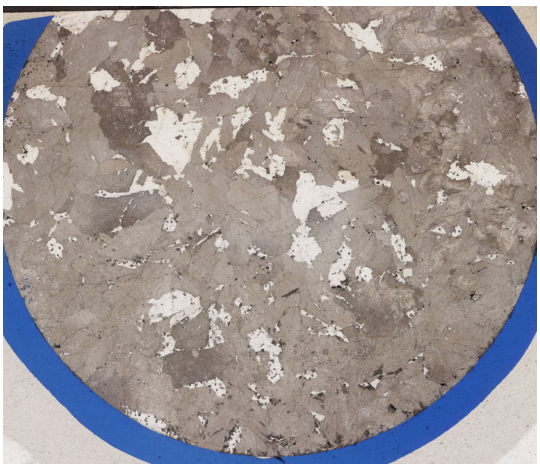

#5 6425.25 ft: Relatively large (0.5 cm) vuggy pores partially infilled by saddle dolomite crystals. Minor amounts of fluorite and saddle dolomite crystals occluding intercrystalline porosity. Matrix composed of planar-s/nonplanar-a transitional dolomite crystals. Φ= 0.03 K= 0.026

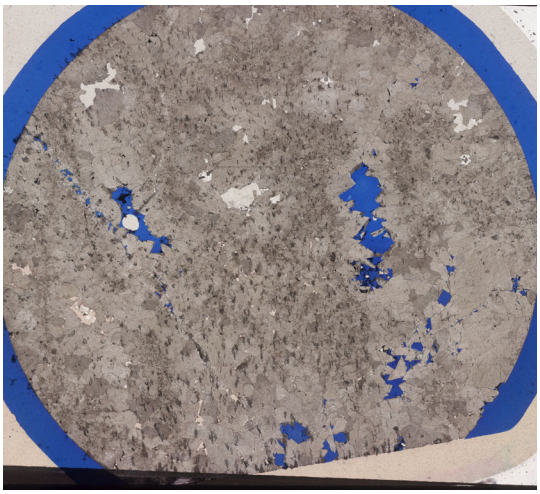

#6 6426.375 ft: Small vuggy pores partially infilled by planar-c dolomite crystals. Fracture porosity occluded by dolomite. Minor intercrystalline porosity occluded by fluorite. Large (0.75 cm) pore with floating planar-e dolomite crystals. Pore is partially infilled by relatively large (20 mm) saddle dolomite crystals. Matrix is composed of planar-s/nonplanar-a transitional dolomite crystals. Φ= 0.02 K= 0.026

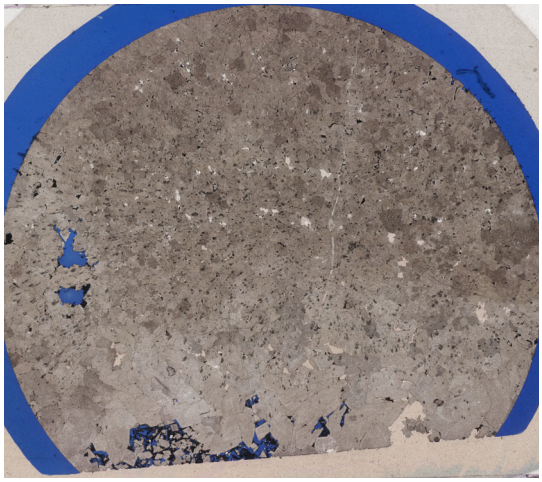

#7 6483.83 ft: 90% of thin section is composed of fluorite. No visible porosity. Edge of thin section is composed of nonplanar-a dolomite crystals. Fluorite also shows as an alteration product of dolomite. Φ= 0.03 K= 0.016

#8 6484.83 ft: Very similar to thin section #7 in that it is 80% is composed of fluorite. Minor fracture porosity that is partially to fully infilled by planar-c dolomite crystals, which seem to have been altered to fluorite in some cases. Pyrobitumen occludes intercrystalline porosity. Matrix is composed of planar-s/nonplanar-a transitional dolomite crystals.¬ Φ= 0.04 K= 0.227

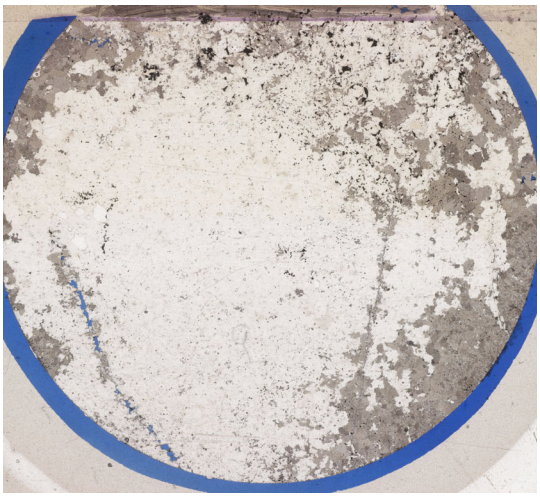

WA# 1833

#9 6427.25 ft: Large (~ 1 - 2 cm) stromatoporoid and coral fragments with intragranular porosity occluded by calcite. Some intragranular calcite is opaque in XPL. Fracture porosity occluded by calcite cementation. Matrix is composed of micrite, peloids, calcispheres and small carbonate fragments. Φ= 0.03 K= 0.002

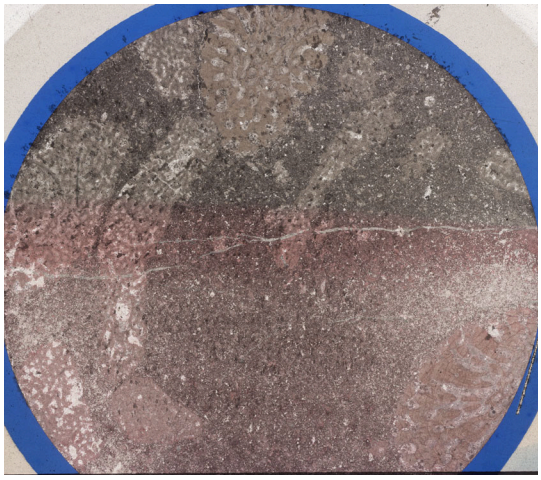

#10 6427.75 ft: Several stromatoporoid fragments varying in size from 0.5 - 2 cm. Few intragranular pores and fracture porosity is occluded by calcite cementation. Matrix is a wackestone that is generally coarser than thin section #9, and includes ostracod shells, micrite, peloids and calcispheres. Φ= 0.03 K= 0.002

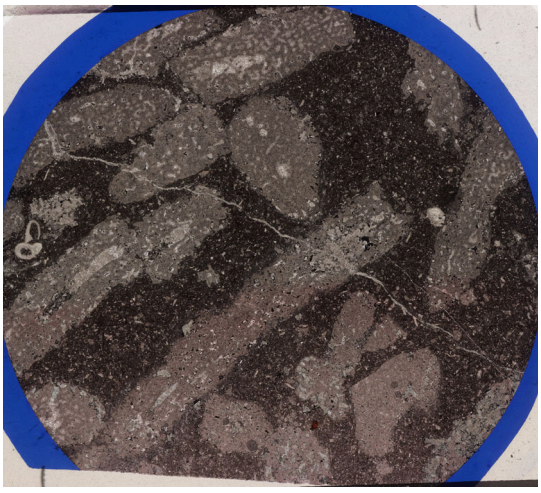

#11 6428.17 ft: Large (up to 2.4 cm) stromatoporoid fragments showing very minor amounts of intragranular porosity that is occluded by calcite cementation. Matrix is a wackestone that includes micrite, peloids and calcispheres. Φ= 0.03 K= 0.002

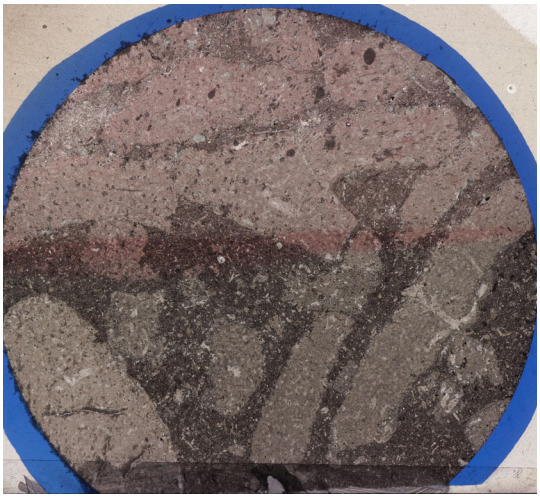

#12 6429 ft: Stromatoporoid fragments (0.5 -1.5 cm) with central canals showing large calcite crystals. Fractures oriented perpendicular to each other are occluded by calcite cementation. Matrix is a wackestone composed of micrite, peloids and carbonate fragments Φ= 0.02 K= 0.002

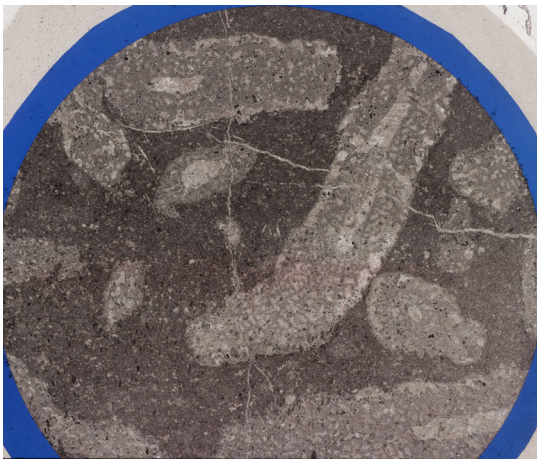

#13 6474 ft: Thin section is dominantly composed of 0.5 – 1.5 cm stromatoporoid and coral fragments that show relatively more intragranular porosity occluded by calcite cementation. Intergranular porosity present, but occluded by calcite cementation. An unfilled fracture is likely the result of thin section preparation. Matrix is a packstone dominantly composed of peloids with micrite and carbonate fragments. Φ= 0.01 K= 7.678

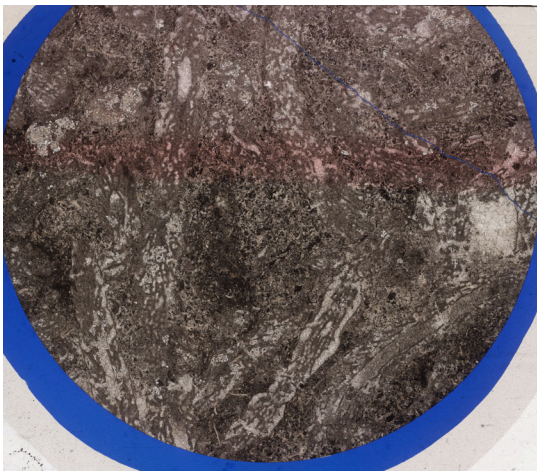

#14 6494.13 ft: Stromatoporoid fragments (~ 1 cm) showing intragranular porosity (including the central canals) that is occluded by calcite cementation. Matrix is a wackestone mainly composed of micrite with peloids, calcispheres and carbonate fragments. Φ= 0.01 K= 0.002

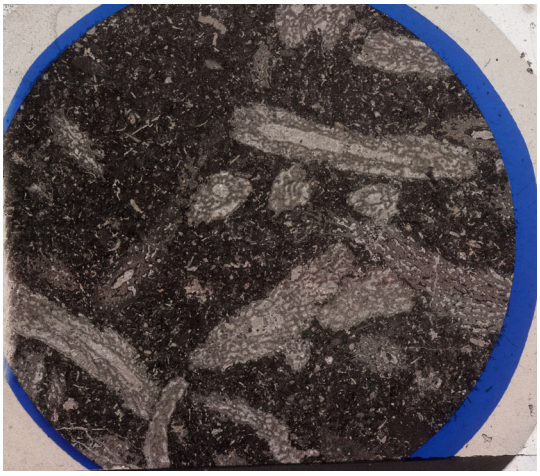

WA# 2176

#15 6430.79 ft: Thin section is almost completely composed of very fine (sub-mm) nonplanar-a dolomite crystals. A fracture propagates through the thin section and is infilled by dolomite crystals that are slightly coarser and lighter in colour compared to matrix dolomite crystals. A minor amount of intercrystalline porosity is occluded by pyrobitumen. Φ= 0.02 K= 0.027

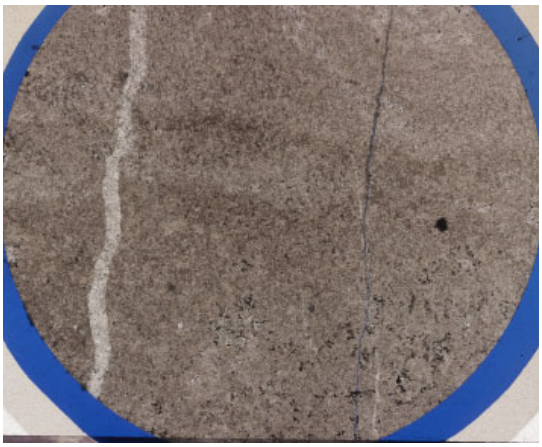

#16 6431 ft: Small (2 mm) vuggy porosity exists and is partially infilled by saddle and planar-c dolomite crystals. Small fractures are partially infilled by planar-s/nonplanar-a transitional dolomite crystals. Minor amounts of intercrystalline porosity exists, but sometimes is occluded by fluorite or pyrobitumen. The matrix is composed of planar-s/nonplanar-a transitional dolomite crystals. Φ= 0.08 K= 1.411

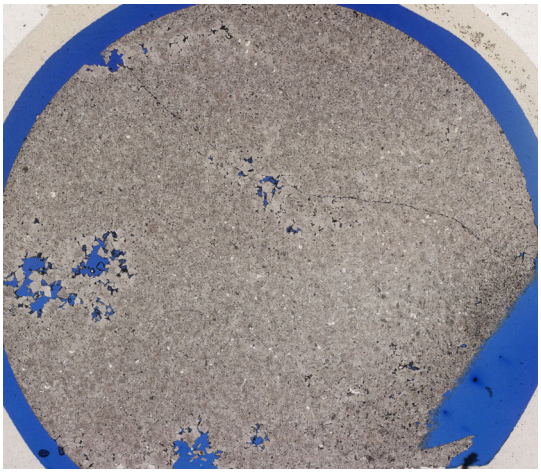

WA# 458

#17 6440.04 ft: Thin section is dominantly a mudstone composed of peloids and micrite. Minor amounts of calcispheres, carbonate fragments and small (2 mm) stromatoporoid fragments also exist. In some locations the matrix has been recrystallized to very fine calcite crystals. Fractures propagating across thin section are occluded by relatively coarse calcite cementation. No visible porosity. Φ= 0.01 K= 0.002

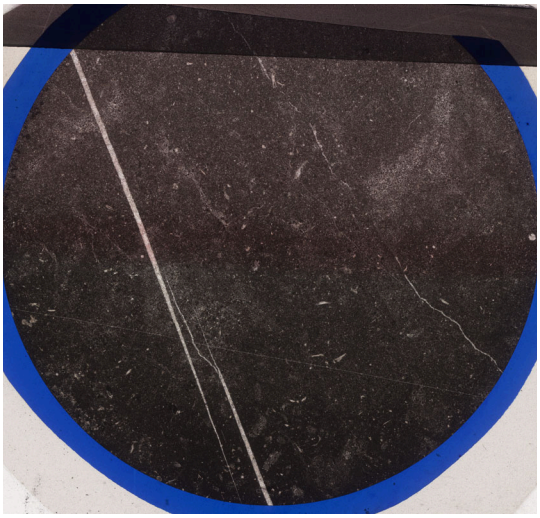

#18 6440.46 ft: Similar to thin section #17, the thin section is dominantly a mudstone that is composed of peloids and micrite. Brachiopod shell fragments and crinoid ossicle fragments form a minor component of the bioclast assemblage. Fractures propagating across the thin section are occluded by calcite cementation. Φ=0.004 K= 0.002

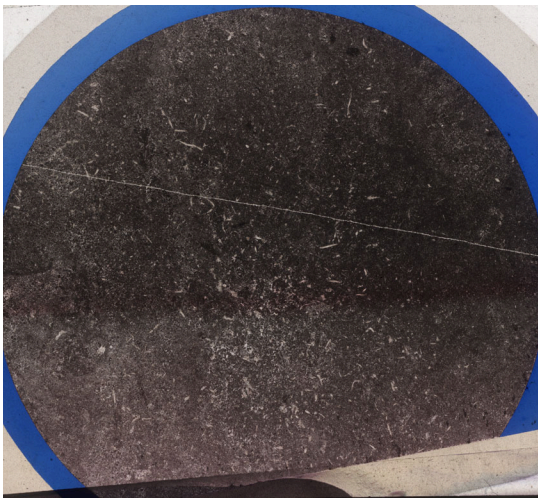

WA# 1866

#19 6558.5 ft: Small (1 – 2 mm) mouldic pores are partially infilled by saddle dolomite or completely occluded by fluorite mineralization. Relict bioclasts are completely replaced by coarse nonplanar-a dolomite crystals, while the matrix is composed of finer nonplanar-a dolomite crystals. Small amounts of intercrystalline porosity are occluded by pyrobitumen and fluorite. Φ= 0.11 K= 0.092

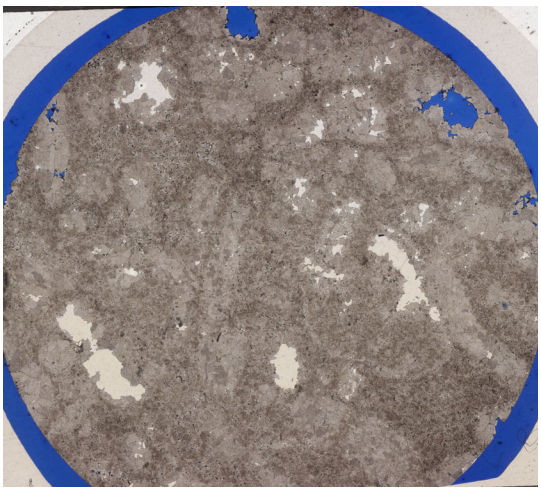

#20 6558.75 ft: Small (0.5 mm) vuggy pores are partially infilled by saddle and planar-c dolomite crystals and completely infilled by fluorite mineralization. Relatively large (2 mm) planar-s dolomite crystals completely replace bioclasts, while the matrix is composed of fine nonplanar-a dolomite crystals. Pyrobitumen and fluorite mineralization occlude intercrystalline porosity. Φ= 0.02 K= 0.074

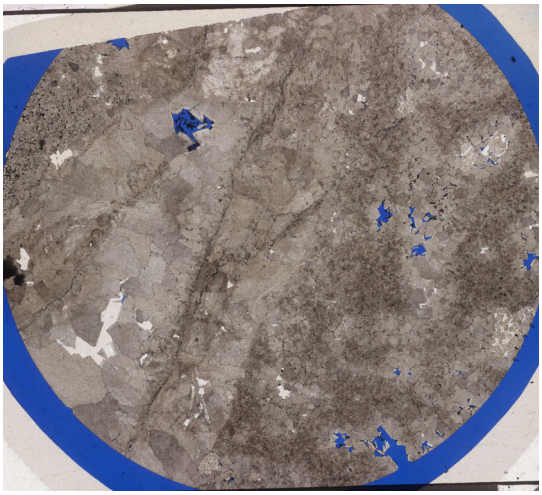

WA# 1875

#21 6766.58 ft: Small vuggy pores partially infilled by saddle and planar-c dolomite crystals. Relatively large planar-s/nonplanar-a transitional dolomite crystals replace bioclasts, while the matrix is composed of nonplanar-a dolomite crystals. Fluorite occludes intercrystalline porosity and shows as an alteration product of dolomite. Minor amounts of pyrobitumen occlude intercrystalline porosity. Φ= 0.01 K= 0.002

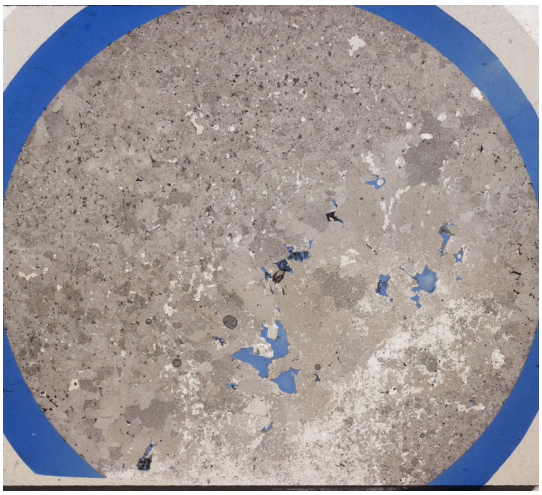

#22 6767.58 ft: Large (~ 2 cm) laminated mudstone clasts are penetrated by fractures that are unfilled, filled by fluorite or filled by dolomite. Some clasts have been partially digested by dolomitization. Opaque minerals are visible at the bottom of the thin section are likely sulphide minerals (as seen in core). Pyrobitumen occludes intercrystalline porosity. The matrix is composed of nonplanar-a dolomite crystals. Very minor amount of porosity restricted to fractures. Φ= 0.02 K= 6.128

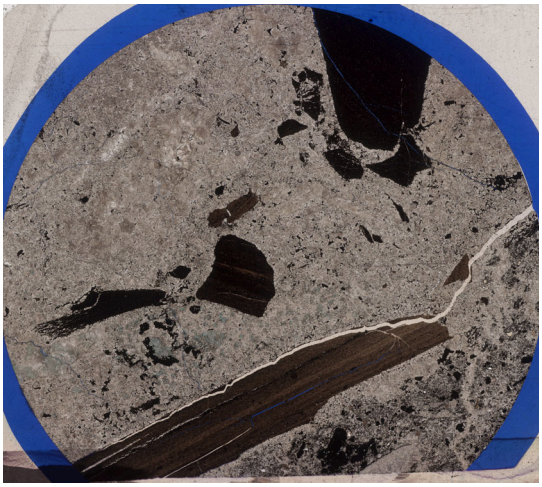

#23 6768.58 ft: No visible porosity. Thin section is composed of relatively coarse planar-s/non-planar-a dolomite crystals where bioclasts have been replaced. The matrix is composed of fine nonplanar-a dolomite crystals. Minor amounts of intercrystalline porosity are occluded by pyrobitumen. Φ= 0.01 K= 0.017

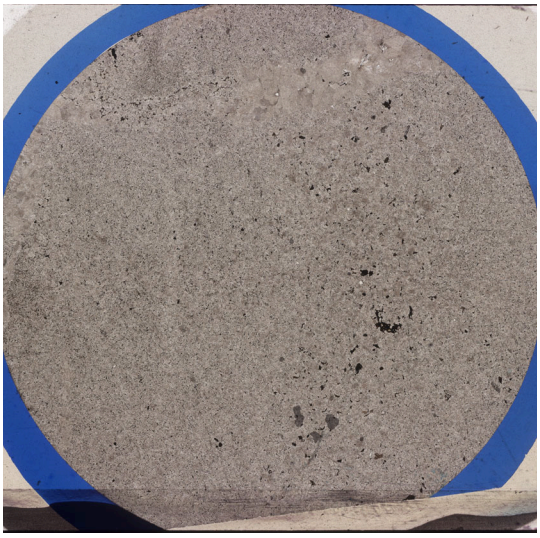

#24 6769.25 ft: Porosity restricted to very small fractures that seem to terminate part way through the thin section. One large, circular section of dolomite is composed of very fine nonplanar-a crystals, and is rimmed by intercrystalline porosity that is occluded by pyrobitumen. Small amounts of fluorite occur directly next to fractures, and within intercrystalline pores with pyrobitumen. Opaque minerals are present and are likely sulphide minerals (as seen in core). Φ= 0.01 K= 0.094

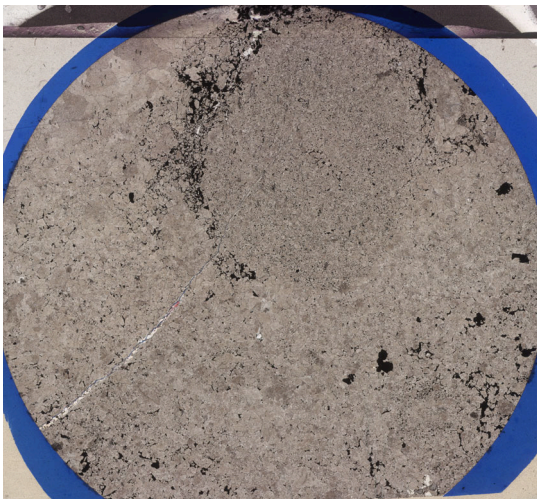

Batch 2

WA# 2509

#1 6263.58 ft: Large (1 cm) vuggy pores that are cemented by planar-c dolomite crystals that show preferential alteration to fluorite. Fluorite has altered matrix dolomite and occluded porosity. A dark fine grained material occludes fracture porosity. The matrix is composed of fine grained nonplanar-a dolomite crystals, while infilled pores are composed of coarser planar-s/nonplanar-a transitional dolomite crystals. Φ= 0.13 K= 0.05

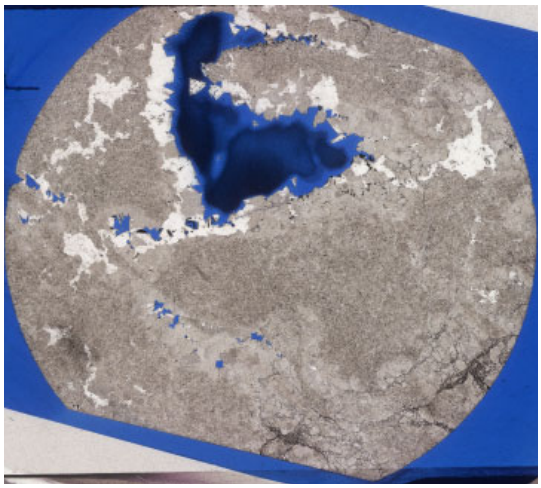

#2 6264.08 ft: Large (0.5 – 1 cm) vuggy pores partially cemented by saddle and planar-c dolomite crystals. Minor amounts of intercrystalline porosity that is sometimes occluded by pyrobitumen. Around 60% of the dolomite in this thin section has been replaced to fluorite (either showing an alteration texture with dolomite, or the dolomite crystals are completely replaced by fluorite). Matrix dolomite crystal sizes vary but are either planar-s/nonplanar-a transitional to

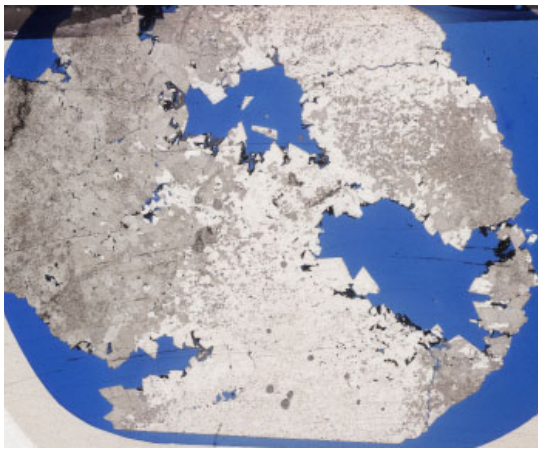

nonplanar-a in crystal shape. Φ= 0.06 K= 1.00

#3 6288.25 ft: Mouldic pores are 1 cm in diameter and are partially cemented by saddle dolomite crystals which are preferentially altered to fluorite. Fracture porosity is partially infilled by saddle dolomite crystals. Replaced bioclasts are shown by relatively coarser planar-s/nonplanar-a dolomite crystals compared to finer, nonplanar-a dolomite crystals in the matrix. Φ= 0.05 K= 0.02

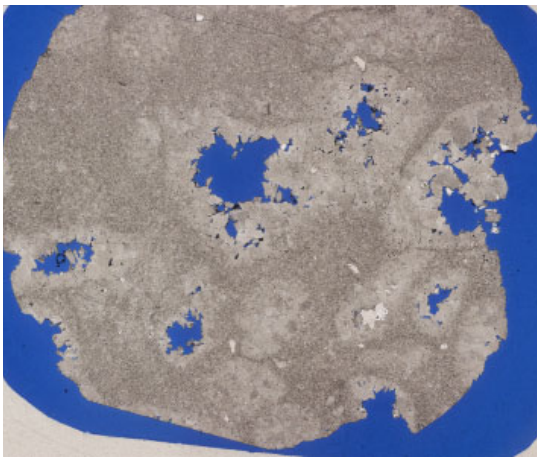

#4 6291.04 ft: Small (0.25 cm) mouldic pores partially infilled by saddle dolomite crystals. Some bioclasts have been completely replaced by relatively coarser, planar-s/nonplanar-a transitional dolomite crystals which contrast with nonplanar-a dolomite crystals in the matrix. Minor amounts of fluorite as an alteration product of dolomite and as a cement occluding mouldic porosity. Φ= 0.17 K= 0.08

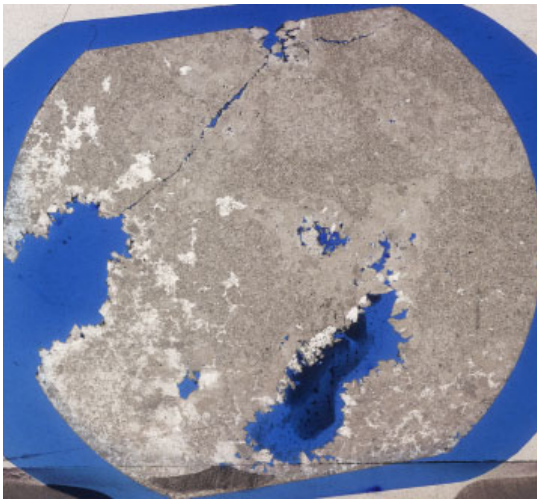

#5 6296.96 ft: Vuggy porosity partially infilled by saddle dolomite crystals and pyrobitumen. Fracture porosity is partially infilled by small, nonplanar-a dolomite crystals. Fluorite occludes smaller vuggy pores. Fractures are lined by pyrobitumen and are also infilled by a fine grained dark material. The matrix is composed of nonplanar-a dolomite crystals. Φ= 0.06 K= 10.05

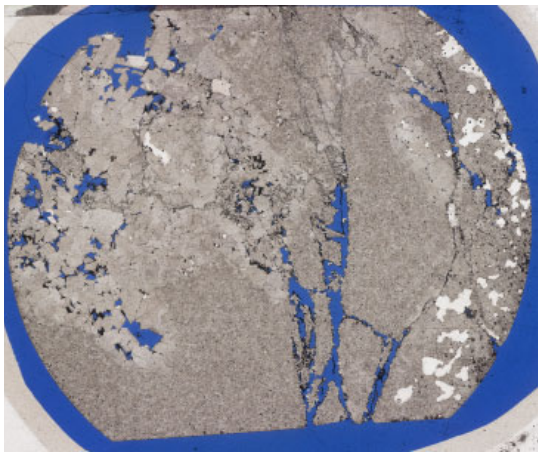

#6 6297.63 ft: Mouldic pores (0.5 cm) are partially cemented by relatively coarse saddle dolomite. Fluorite occludes mouldic porosity and is an alteration product of dolomite. Pyrobitumen lines pores and occludes intercrystalline porosity. Some bioclasts have been completely replaced by relatively coarser, planar-s/nonplanar-a transitional and saddle dolomite crystals. The matrix is composed of nonplanar-a dolomite crystals. Φ= 0.06 K= 0.03

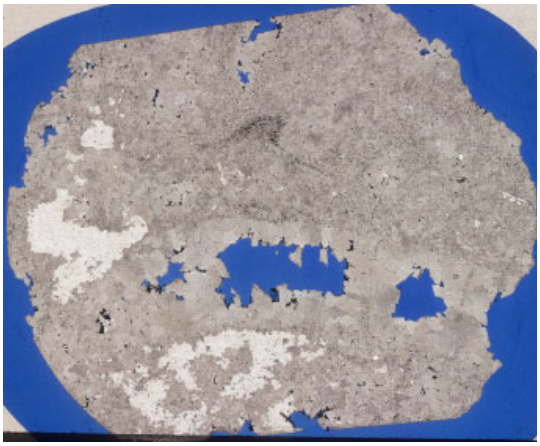

WA# 2176

#7 6414.67 ft: Vuggy porosity that is partially infilled by large (0.5 cm) saddle dolomite crystals that have been completely replaced by fluorite. The thin section is 85% fluorite, with minor amounts of dolomite that is partially altered to fluorite. The dolomite crystals are nonplanar-a in crystal shape. Φ= 0.05 K= 0.01

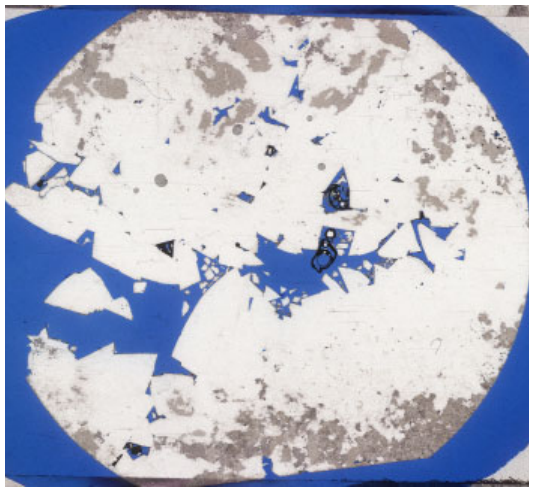

#8 6418.59 ft: Fracture and intercrystalline porosity exist and are partially infilled by saddle dolomite and fluorite. Around 60% of the thin section has been altered to fluorite. The matrix is composed of nonplanar-a dolomite crystals but crystals close to pores are relatively coarser and are planar-s/nonplanar-a transitional in shape. Φ= 0.07 K= 0.12

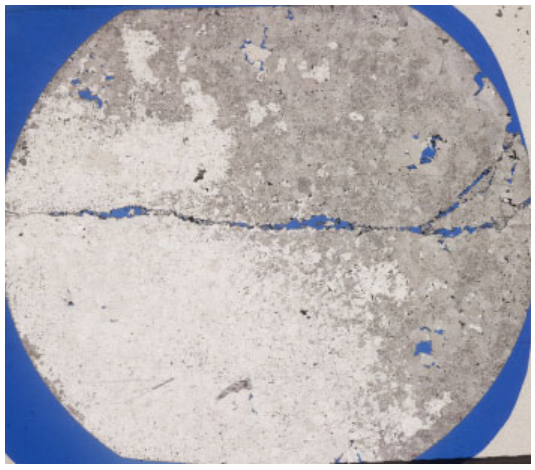

#9 6418.76 ft: Intercrystalline and vuggy porosity partially infilled by saddle dolomite and occluded by fluorite. Dolomite crystals within vugs show preferential alteration to fluorite. Intercrystalline porosity is occluded by pyrobitumen. The matrix is composed of nonplanar-a dolomite crystals but crystals close to pores are relatively coarser saddle dolomite crystals. Φ= 0.06 K= 0.05

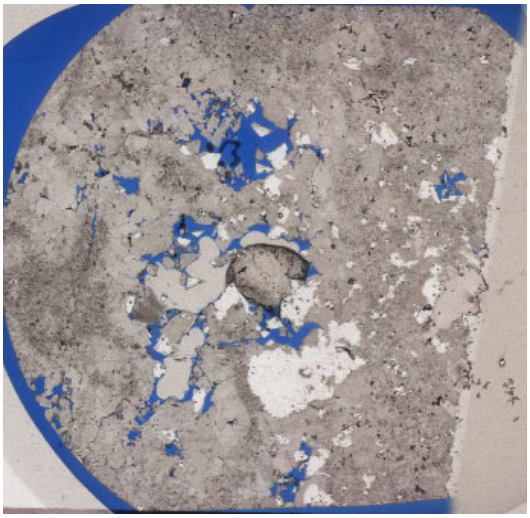

#10 6428.5 ft: One mouldic pore (0.5 cm) partially infilled by saddle dolomite crystals. Minor amounts of uncemented intercrystalline porosity exist; however, most of the intercrystalline pores are cemented by fluorite. One fracture that is filled with fluorite terminates at the mouldic pore. Nonplanar-a dolomite crystals get coarser towards the mouldic pore and finer away from it. Φ= 0.05 K= 0.04

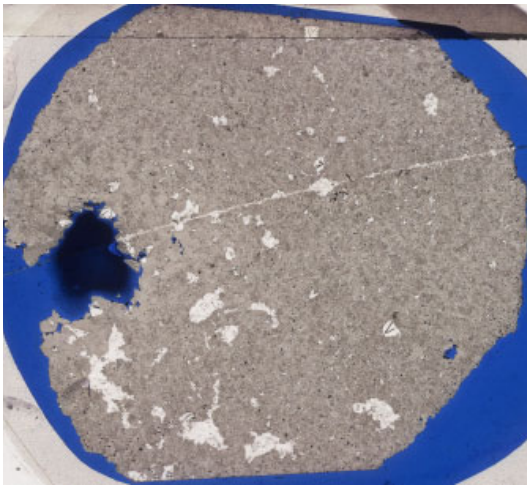

#11 6430.58 ft: Minor amounts of intercrystalline porosity exist between large saddle dolomite crystals. Vuggy porosity exists in the matrix dolomite. Fluorite occludes intercrystalline porosity and partially infills vuggy porosity. Fracture porosity is partially infilled by dolomite. The matrix is composed of nonplanar-a dolomite crystals. Φ= 0.04 K= 0.09

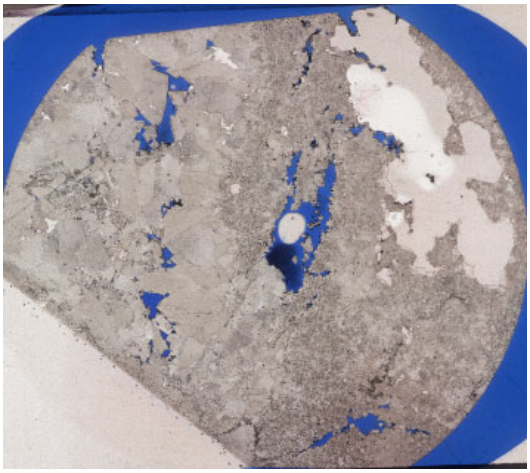

WA# 2540

#12 6242.17 ft: Two mouldic pores (~ 0.5 cm) show partial saddle dolomite cementation along the edge of the pore. One pore shows saddle and planar-c dolomite crystals floating in the pore. Minor fractures occluded by fluorite mineralization. The thin section is dominantly composed of fine, nonplanar-a dolomite crystals. Replaced bioclasts show relatively larger dolomite crystals. Φ= 0.06 K= 0.02

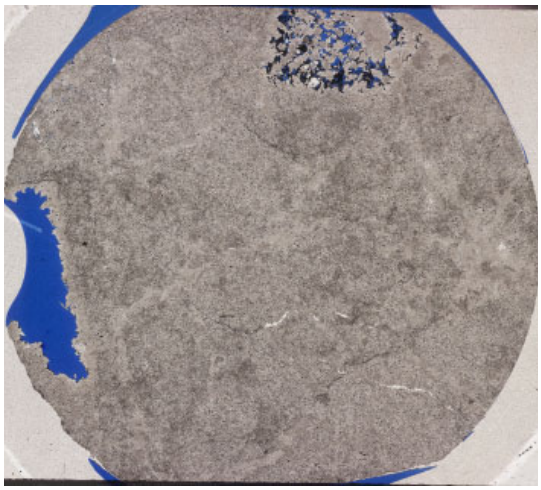

#13 6243.8 ft: A minor amount of intercrystalline porosity exists, but is mostly occluded by pyrobitumen. One unfilled fracture occurs that terminates halfway through the thin section. Fluorite exists as a minor component, and is occurs as an alteration product of dolomite. The thin section is dominantly composed of dolomite with relatively similar crystal sizes and are planar-s to planar-s/nonplanar-a in crystal shape. Φ= 0.07 K= 4.56

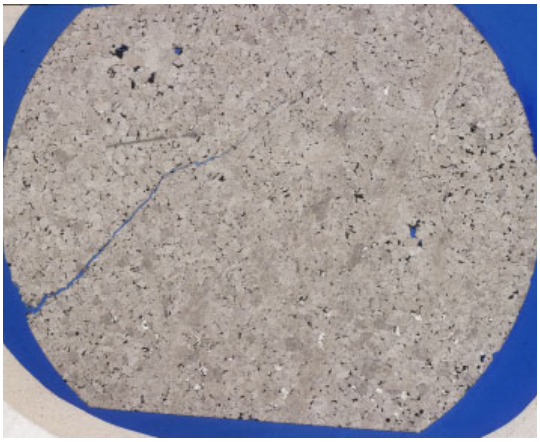

#14 6245.92 ft: Several vuggy and mouldic pores that are either partially infilled by planar-c or saddle dolomite crystals or completely occluded by fluorite. Minor amounts of intercrystalline porosity that is sometimes occluded by pyrobitumen. Fluorite also shows up as an alteration product of dolomite. Matrix dolomite crystal sizes vary but are either planar-s/nonplanar-a to nonplanar-a in crystal shape. Φ= 0.10 K= 0.15

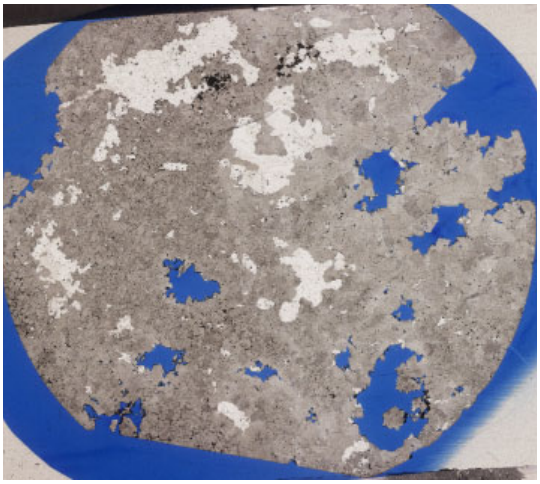

#15 6248.58 ft: Large (1 cm) mouldic pores that show very limited amount of infilling by planar-c dolomite crystals. Some bioclasts are completed replaced by coarser planar-s/nonplanar-a transitional dolomite crystals. A fracture propagating through the thin section is completely filled by fluorite. The matrix is composed of dolomite fine, nonplanar-a dolomite crystals. Φ= 0.11 K= 0.08

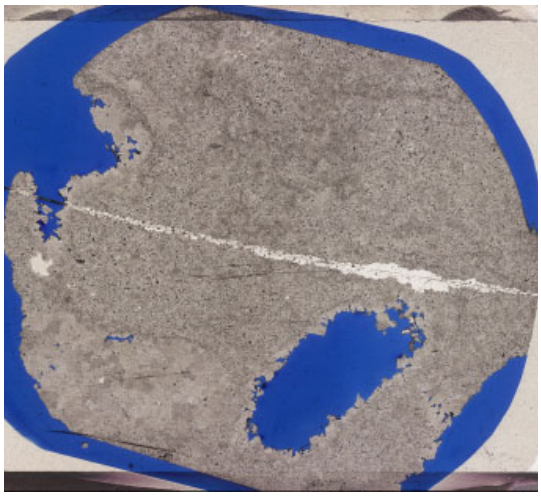

#16 6249.66 ft: Large (~ 1 cm) vuggy pores with planar-c dolomite crystals floating inside of the pores and occurring on the rim of the pores. Saddle dolomite also partially infills vuggy porosity. Some of the dolomite crystals have been completely replaced by fluorite mineralization. This is especially apparent around the edge of the pores. Fluorite also shows as large (50 mm) blotchy textured areas with dolomite crystals occurring inside. Minor intercrystalline porosity is present, with much of it being occluded by pyrobitumen. The matrix is composed of finer nonplanar-a dolomite crystals and coarser planar-s/nonplanar-a transitional dolomite crystals. Φ= 0.04 K= 0.12

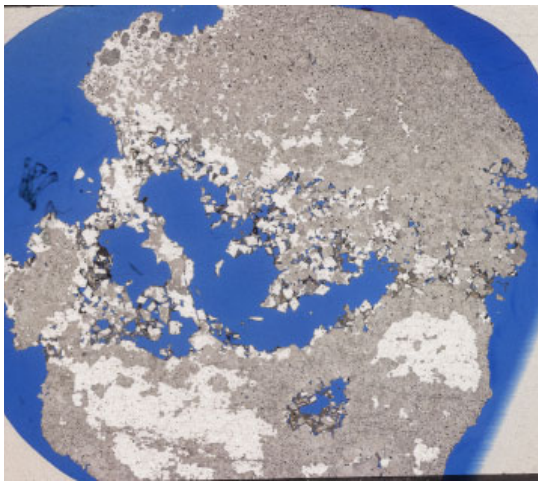

WA# 9732

#17 6222.6 ft: Stromatoporoid fragment packstone with minor amounts of corals, gastropods, brachiopod fragments, ostracods and varying carbonate fragments. The matrix is composed of peloids with intergranular porosity that is cemented by calcite. Intragranular porosity exists in coral bioclasts and is cemented by calcite. Thin section is composed entirely of calcite. Φ= 0.01 K= 0.005

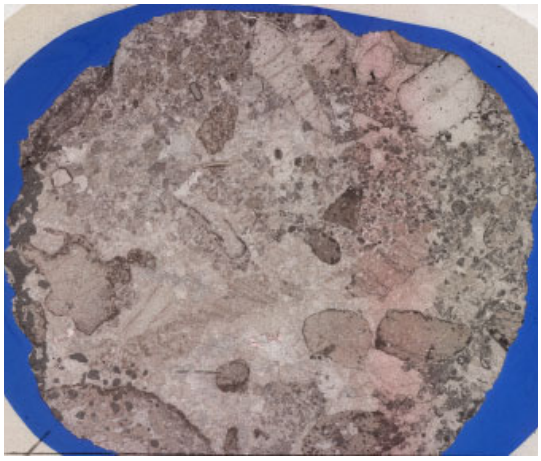

WA# 1578

#18 6708.13 ft: Minor intercrystalline porosity exists between relatively coarse saddle dolomite crystals that show some alteration to fluorite. Pyrobitumen occludes intercrystalline porosity. Thin fractures propagating through the thin section exist and are unfilled to partially infilled by saddle dolomite crystals. The matrix is composed of relatively coarse planar-s/nonplanar-a dolomite crystals with smaller nonplanar-a dolomite crystals. Φ= 0.07 K= 3.93

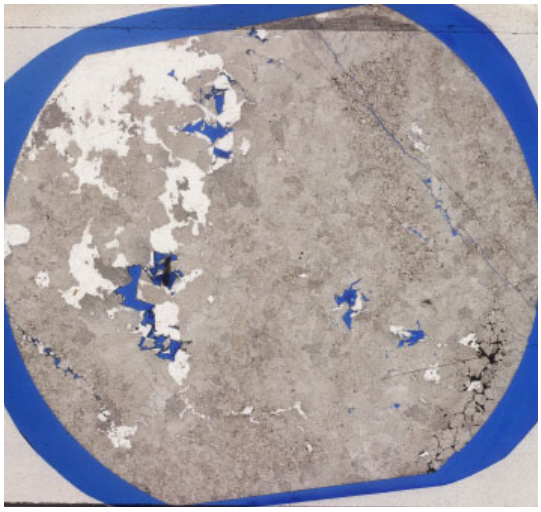

#19 6711.42 ft: Vuggy pores (~ 1 cm) partially infilled by saddle dolomite crystals that have been partially altered to fluorite. Fracture porosity is unfilled, and forms a minor amount of porosity. Fluorite occurs as blotchy patches, possibly occluding mouldic pores. The matrix is composed of relatively coarse planar-s/nonplanar-a dolomite crystals with smaller nonplanar-a dolomite crystals. Φ= 0.03 K= 0.12

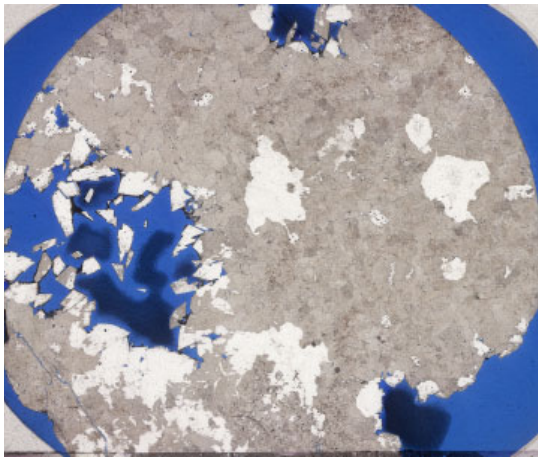

#20 6715.75 ft: Mouldic pores (1 cm) with minor amounts of intercrystalline porosity that are partially to completely occluded by fluorite. Fracture porosity is also present, but is nearly occluded by saddle dolomite crystals. Minor amounts of pyrobitumen occlude intercrystalline porosity. The matrix is composed of relatively coarse planar-s/nonplanar-a dolomite crystals. Φ= 0.03 K= 0.13

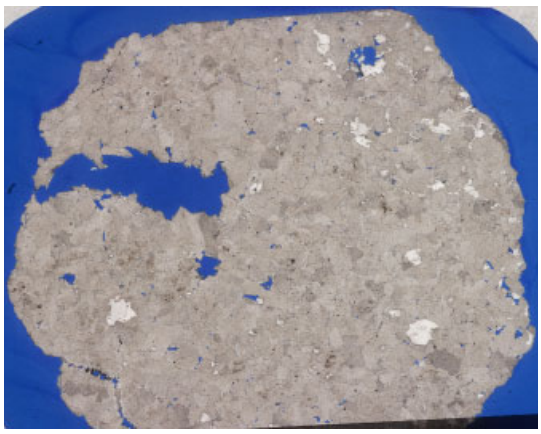

#21 6718.42 ft: Small (0.2 cm) vuggy pores are partially cemented by saddle dolomite crystals. Fractures propagating throughout the thin section are unfilled and lined with pyrobitumen. Fluorite occludes porosity, and occurs as an alteration product of dolomite preferentially around the mouldic pores. The matrix is composed of relatively coarse planar-s/nonplanar-a dolomite crystals with smaller nonplanar-a dolomite crystals. Φ= 0.11 K= 18.66

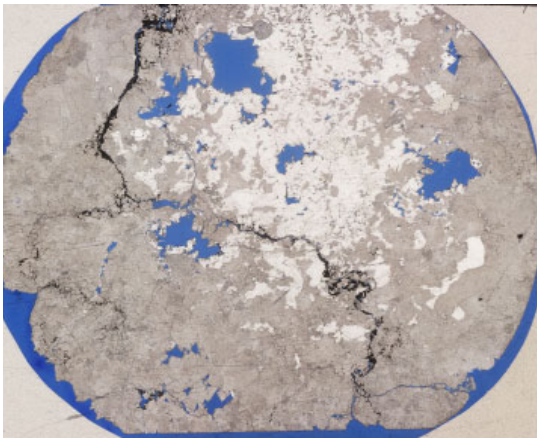

#22 6718.84 ft: Vuggy and mouldic pores (0.5 – 1 cm) partially infilled by saddle and planar-c dolomite crystals. Fractures are open and lined by pyrobitumen in some cases. There is a substantial amount of fluorite that has mineralized or has occurred as an alteration product of dolomite. The matrix is dominantly composed of relatively coarse planar-s/nonplanar-a transitional dolomite crystals. Minor amounts of fluorite occlude porosity. Φ= 0.07 K= 0.17

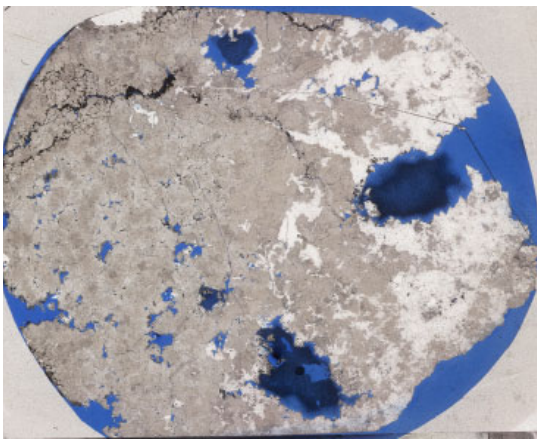

WA# 585

#23 6462.25 ft: Minor intercrystalline and vuggy porosity that is partially infilled by saddle dolomite. Fluorite composes 30% of the thin section and is a result of alteration of dolomite. Fluorite preferentially alters saddle dolomite crystals occurring within pores and it also occludes intercrystalline porosity. Matrix dolomite crystals are usually nonplanar-a in crystal shape. Φ= 0.06 K= 0.02

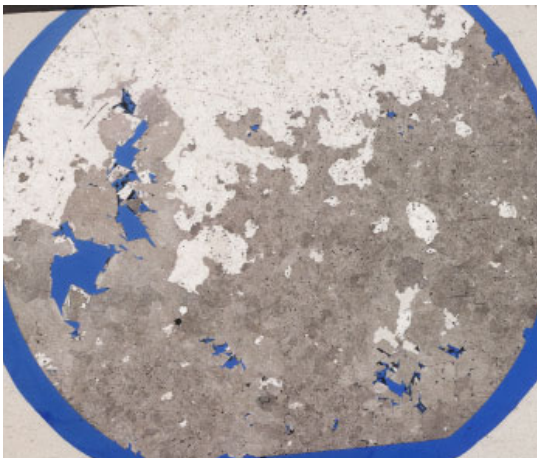

#24 6464.08 ft: Intercrystalline porosity and vuggy porosity partially infilled by saddle dolomite crystals. Calcite makes up less than 10% of the total grains. Minor amounts of pyrobitumen occlude intercrystalline porosity. Dolomite crystals are predominantly similar in size and are relatively coarse planar-s/nonplanar-a transitional dolomite crystals. Φ= 0.07 K= 0.08

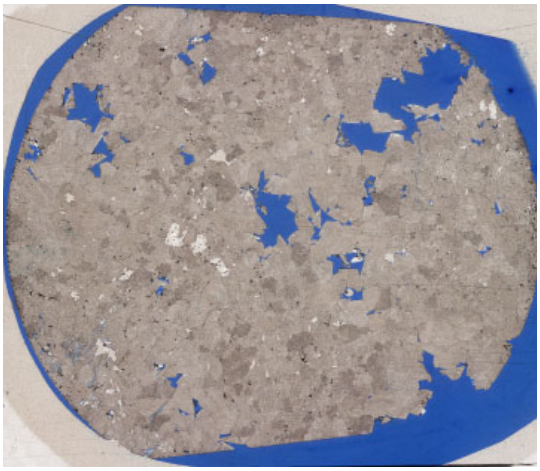

#25 6467.58 ft: Saddle dolomite partially infills porosity. The most prominent feature in this thin section is a fracture swarm that is partially infilled by dolomite and calcite. Calcite grains show twinning and make up less than 10% of the total grains. Pyrobitumen and fluorite occlude intercrystalline porosity between dolomite and calcite grains. Matrix dolomite crystals are usually nonplanar-a in crystal shape. Φ= 0.07 K= 14.17

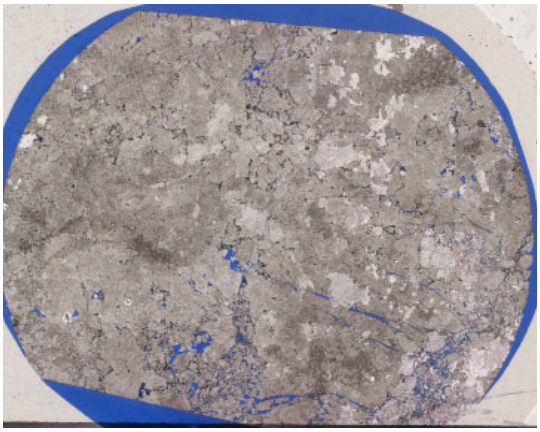

#26 6472 ft: Thin section is predominantly composed of large (0.5 cm) saddle dolomite crystals, which are sometimes floating in vuggy pores. Fluorite occludes porosity and alters saddle dolomite crystals within vugs but also within the matrix. Where present, matrix dolomite crystals are nonplanar-a in shape. Calcite makes up less than 5% of the total grains. Φ= 0.07 K= 13.04

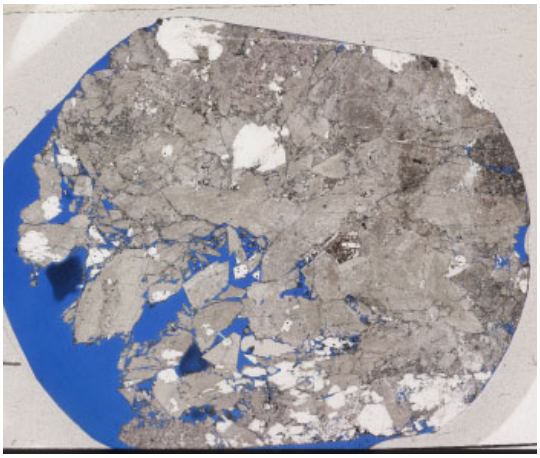

Appendix B: Core Descriptions

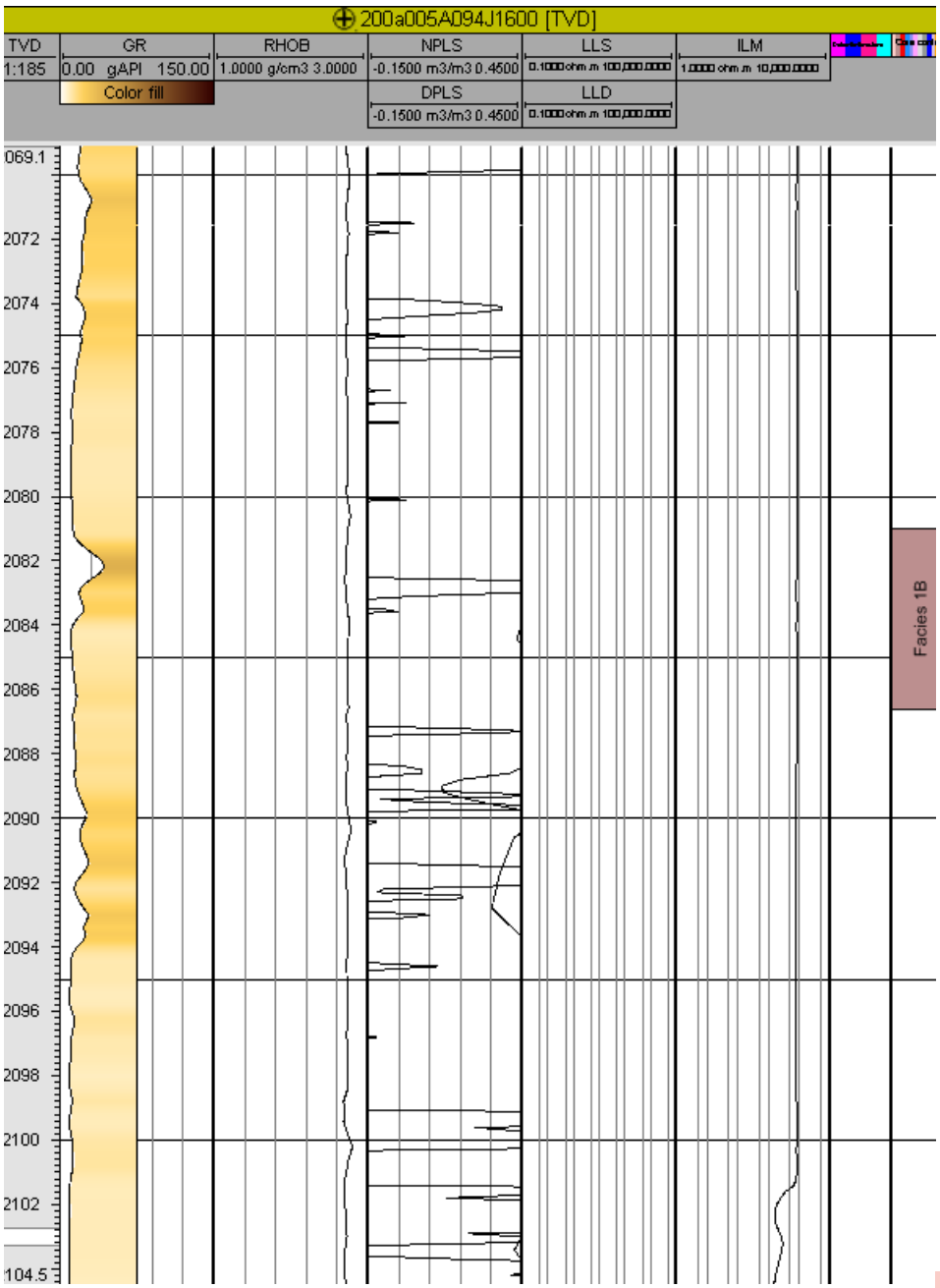

Facies 1A
Facies 1B
Facies 1C
Facies 1D
Facies 2A
Facies 2B
Facies 2C
Facies 3A
Facies 3B
Facies 4A
Facies 4B

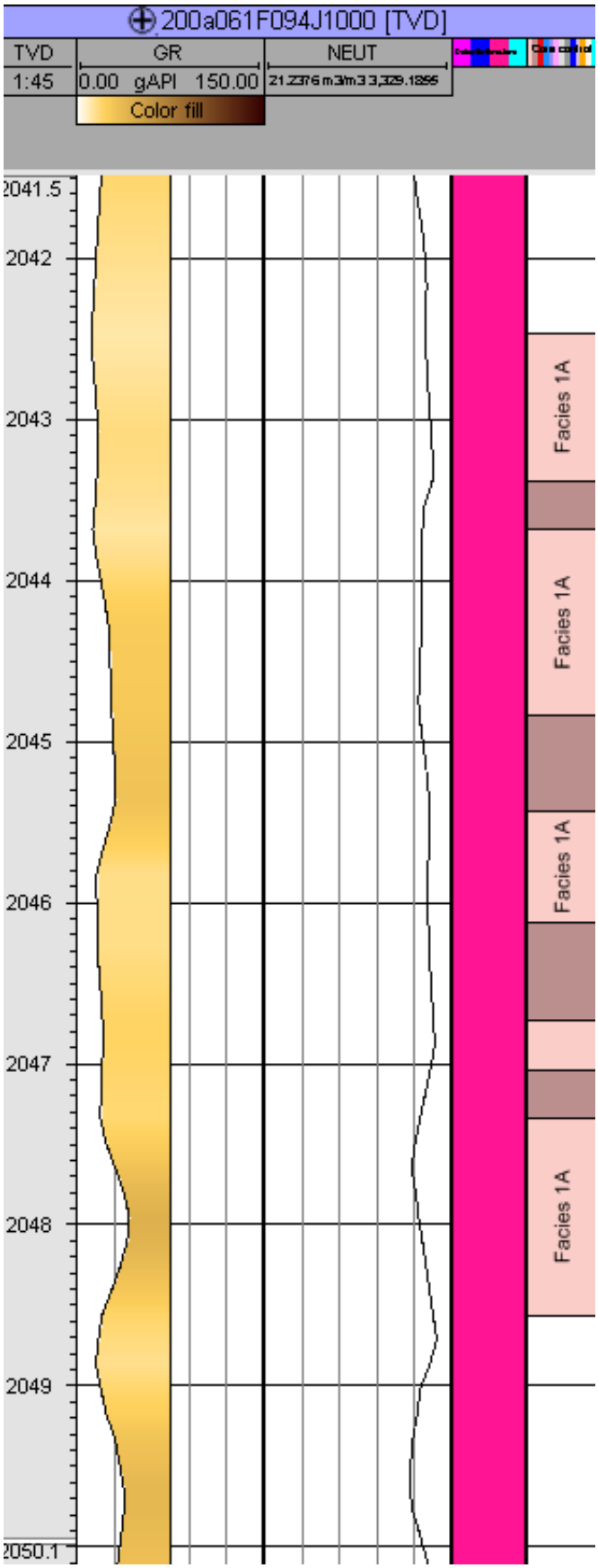
200a061F094J1000 [TVD]
TVD
1:45
GR
0.00 gAPI 150.00
NEUT
Color fill
2041.5
2042
2043
2044
2045
2046
2047
2048
2049
2050.1
Facies 1A
Facies 1A
Facies 1A
Facies 1A


Facies 1A
Facies 1B
Facies 1C
Facies 1D
Facies 2A
Facies 2B
Facies 2C
Facies 3A
Facies 3B
Facies 4A
Facies 4B

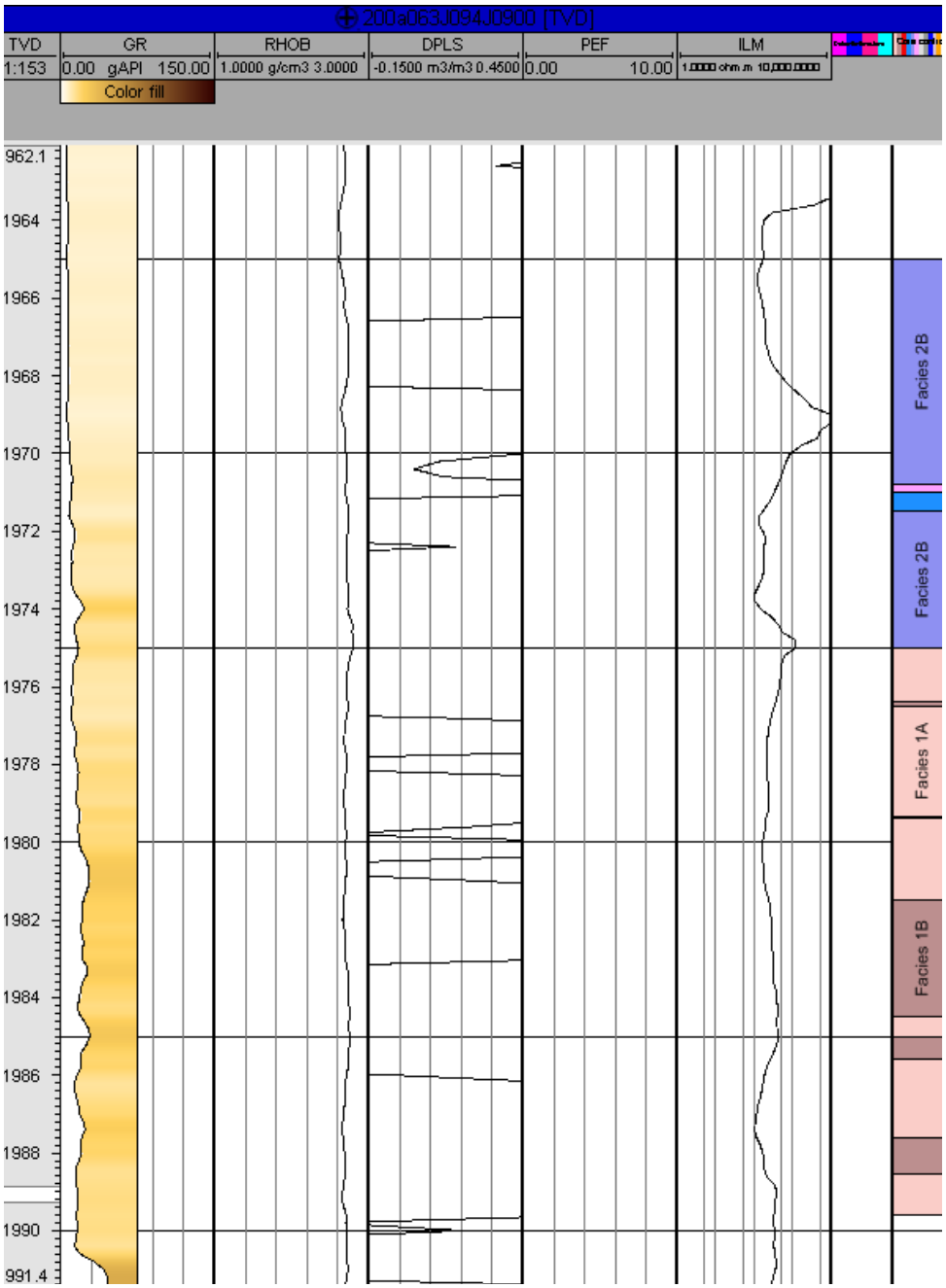

Facies 1A
Facies 1B
Facies 1C
Facies 1D
Facies 2A
Facies 2B
Facies 2C
Facies 3A
Facies 3B
Facies 4A
Facies 4B

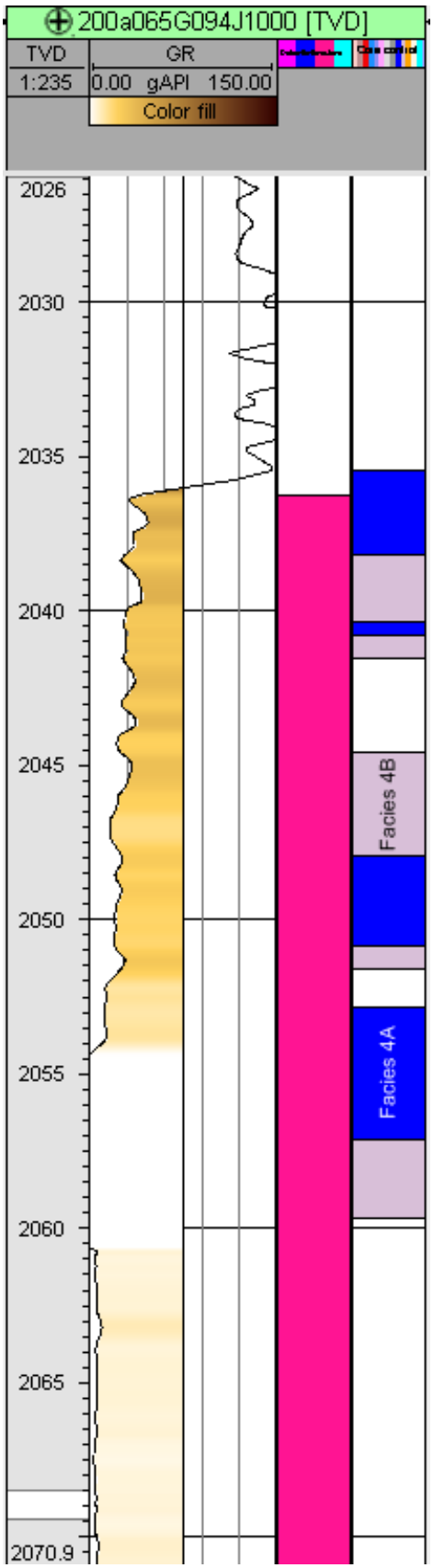

Facies 1A
Facies 1B
Facies 1C
Facies 1D
Facies 2A
Facies 2B
Facies 2C
Facies 3A
Facies 3B
Facies 4A
Facies 4B

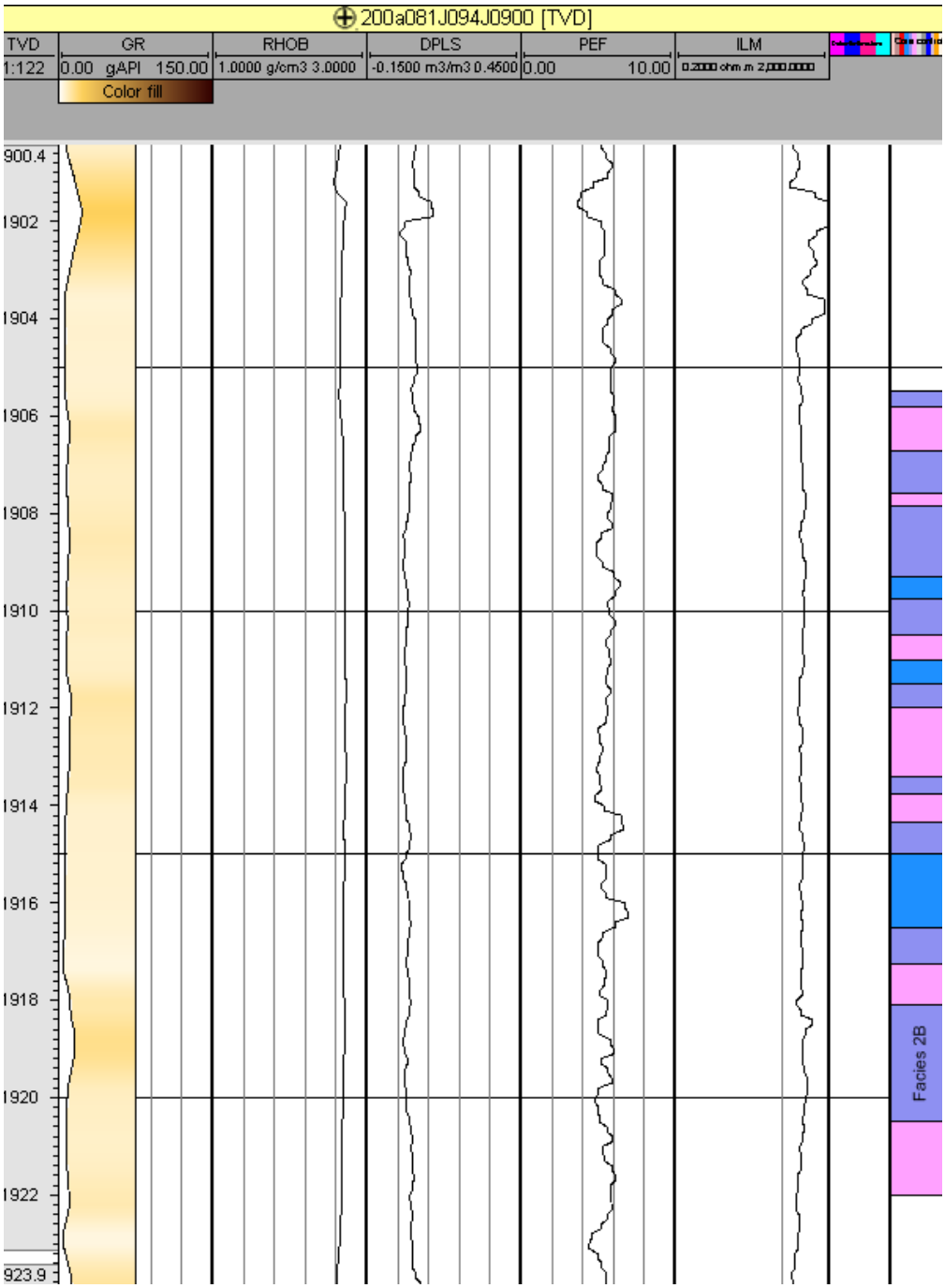

Facies 1A
Facies 1B
Facies 1C
Facies 1D
Facies 2A
Facies 2B
Facies 2C
Facies 3A
Facies 3B
Facies 4A
Facies 4B

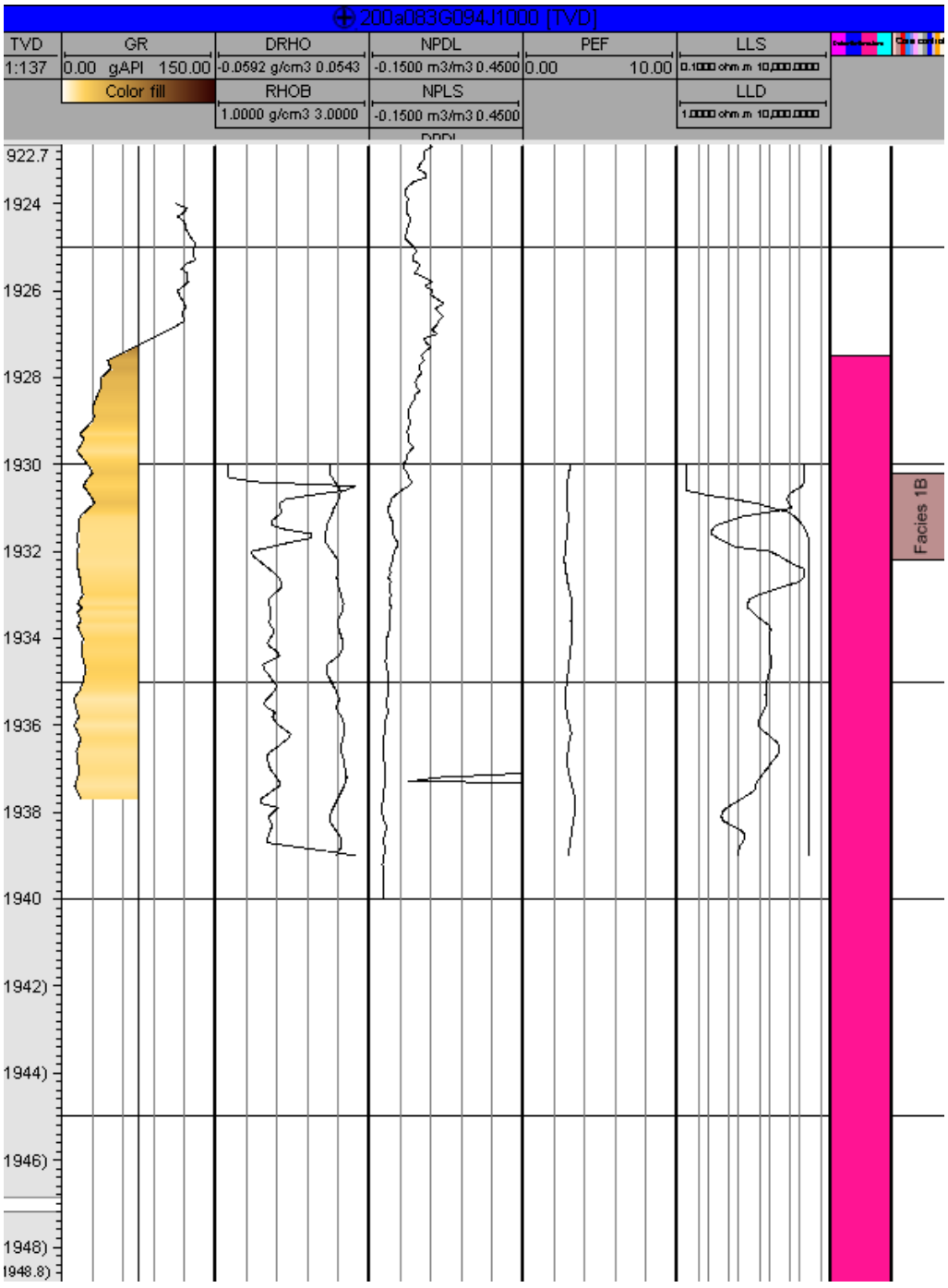

Facies 1A
Facies 1B
Facies 1C
Facies 1D
Facies 2A
Facies 2B
Facies 2C
Facies 3A
Facies 3B
Facies 4A
Facies 4B

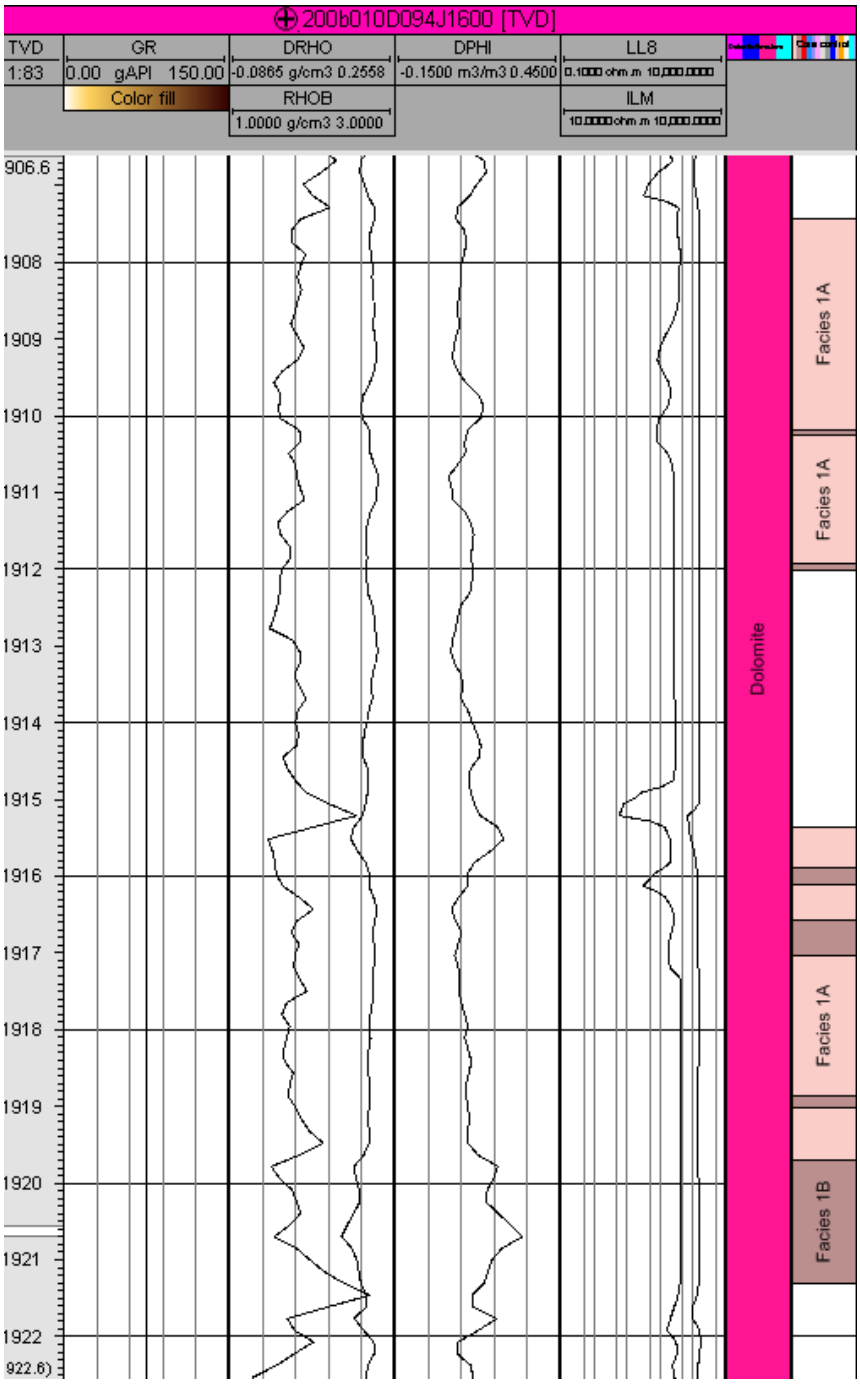

Facies 1A
Facies 1B
Facies 1C
Facies 1D
Facies 2A
Facies 2B
Facies 2C
Facies 3A
Facies 3B
Facies 4A
Facies 4B

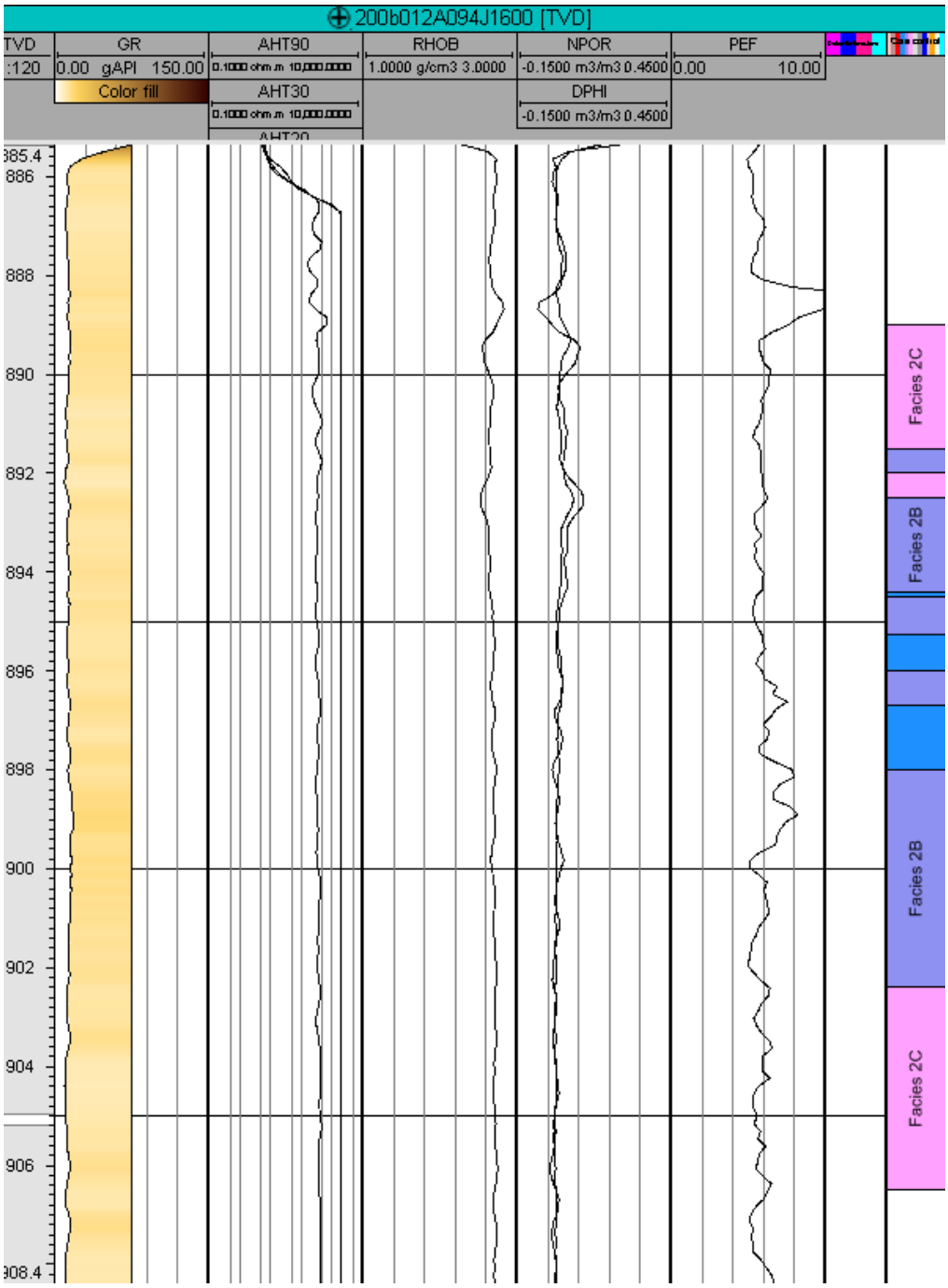

Facies 1A
Facies 1B
Facies 1C
Facies 1D
Facies 2A
Facies 2B
Facies 2C
Facies 3A
Facies 3B
Facies 4A
Facies 4B

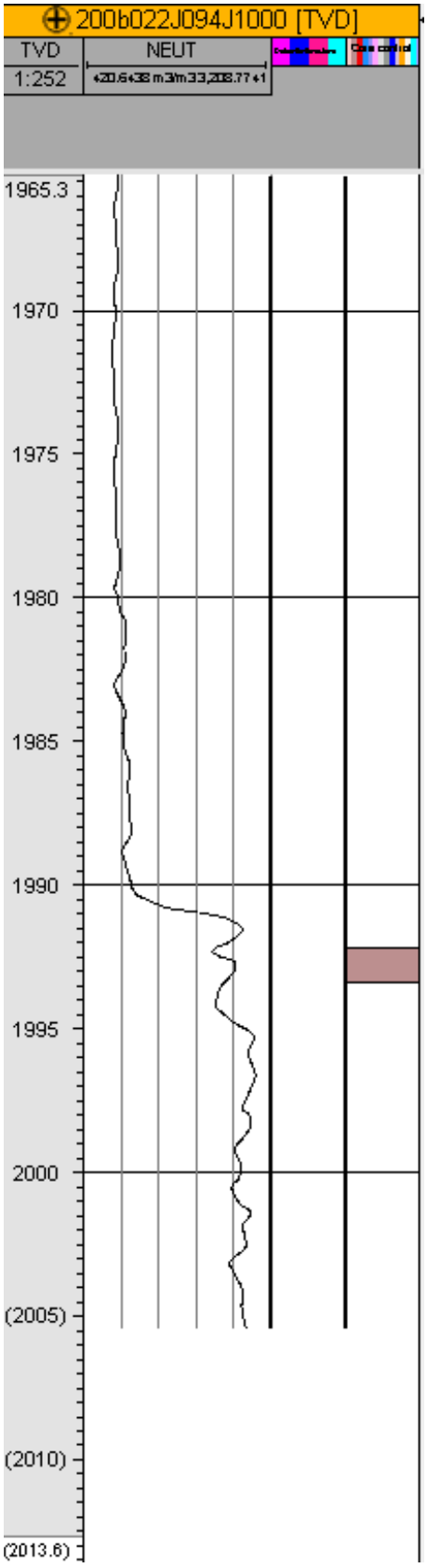

Facies 1A
Facies 1B
Facies 1C
Facies 1D
Facies 2A
Facies 2B
Facies 2C
Facies 3A
Facies 3B
Facies 4A
Facies 4B

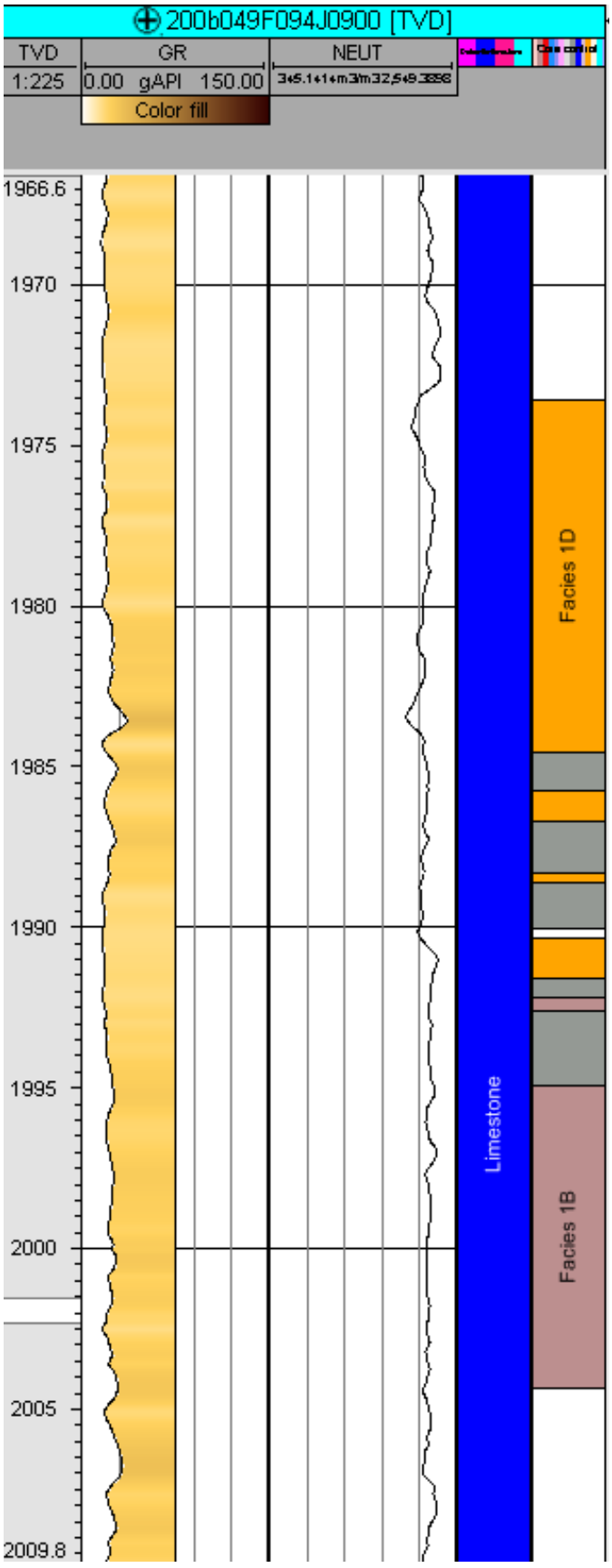

Facies 1A
Facies 1B
Facies 1C
Facies 1D
Facies 2A
Facies 2B
Facies 2C
Facies 3A
Facies 3B
Facies 4A
Facies 4B

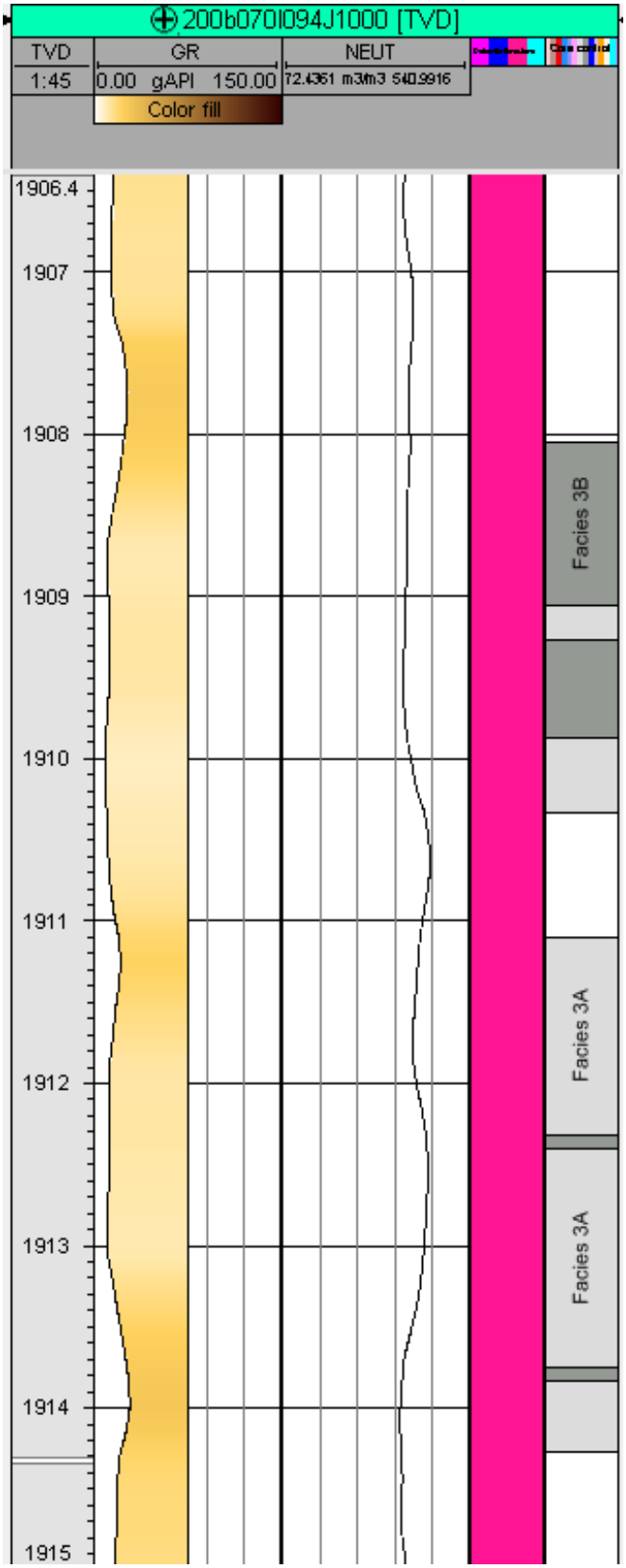
200b070l094J1000 [TVD]
TVD
1:45
GR
0.00 gAPI 150.00
Color fill
NEUT
72.4361 m3/m3 540.9916
1906.4
1907
1908
1909
1910
1911
1912
1913
1914
1915
Facies 3B
Facies 3A
Facies 3A


Facies 1A
Facies 1B
Facies 1C
Facies 1D
Facies 2A
Facies 2B
Facies 2C
Facies 3A
Facies 3B
Facies 4A
Facies 4B

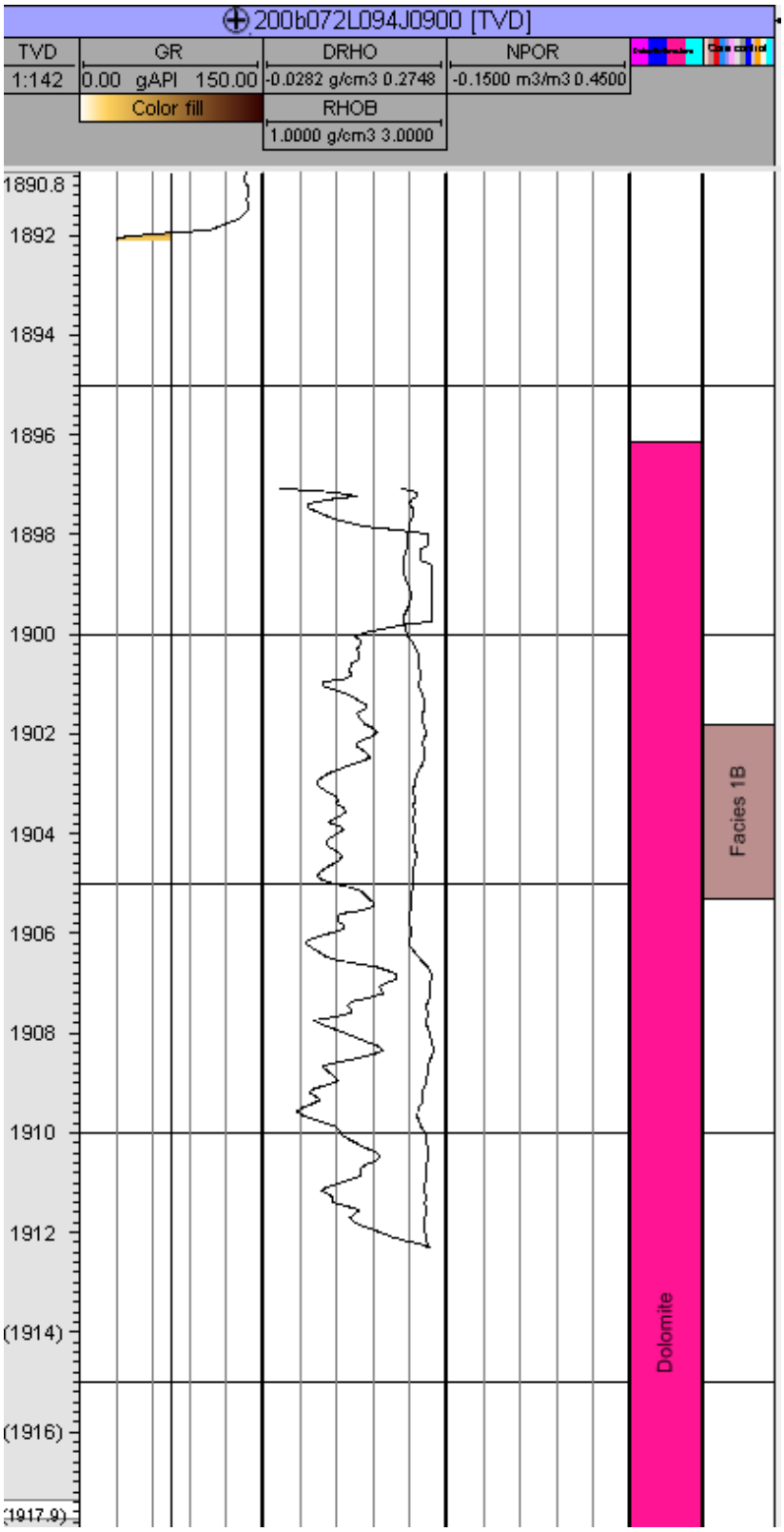
200b072L094J0900 [TVD]
TVD
1:142
GR
0.00 gAPI 150.00
Color fill
DRHO
-0.0282 g/cm3 0.2748
RHOB
1.0000 g/cm3 3.0000
NPOR
-0.1500 m3/m3 0.4500
1890.8
1892
1894
1896
1898
1900
1902
1904
1906
1908
1910
1912
(1914)
(1916)
(1917.9)
Facies 1B
Dolomite


Facies 1A
Facies 1B
Facies 1C
Facies 1D
Facies 2A
Facies 2B
Facies 2C
Facies 3A
Facies 3B
Facies 4A
Facies 4B

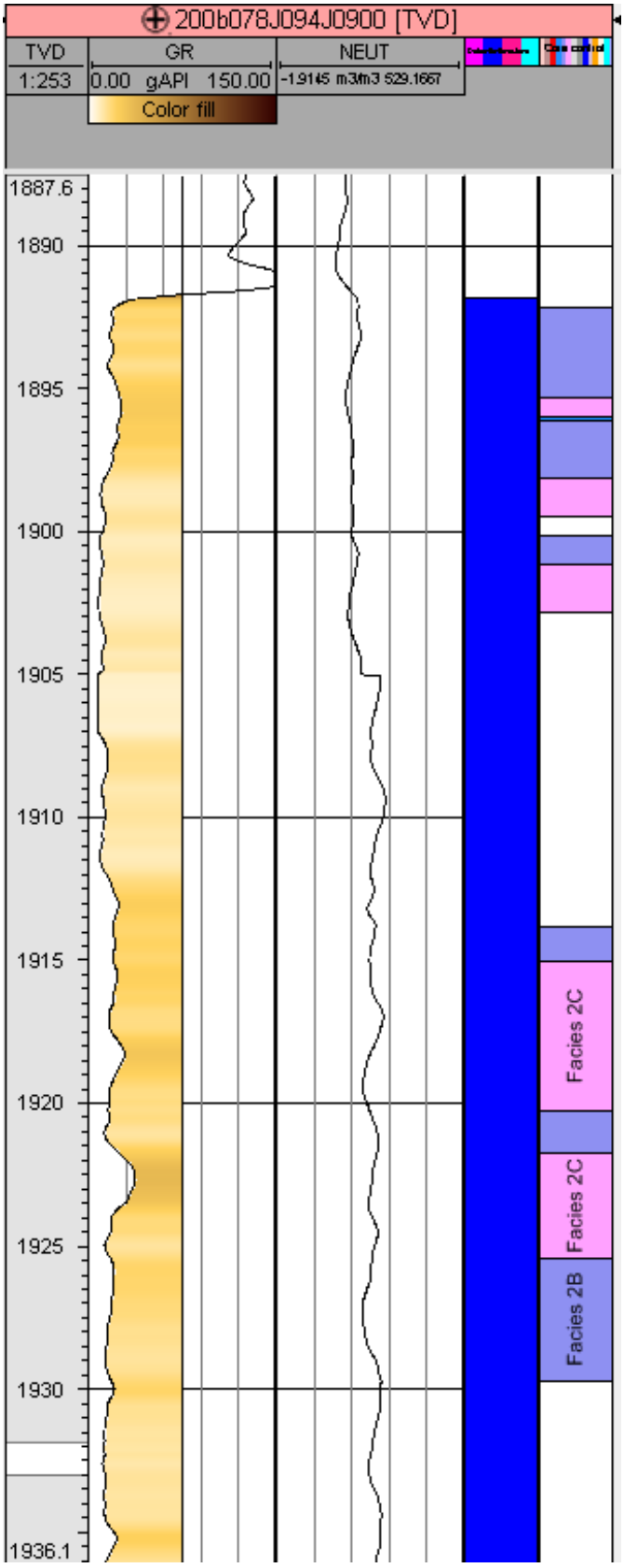
200b078J094J0900 [TVD]
TVD
1:253
GR
0.00 gAPI 150.00
NEUT
-1.9145 m3/m3 529.1667
Color fill
1887.6
1890
1895
1900
1905
1910
1915
1920
1925
1930
1936.1
Facies 2C
Facies 2C
Facies 2B


Facies 1A
Facies 1B
Facies 1C
Facies 1D
Facies 2A
Facies 2B
Facies 2C
Facies 3A
Facies 3B
Facies 4A
Facies 4B

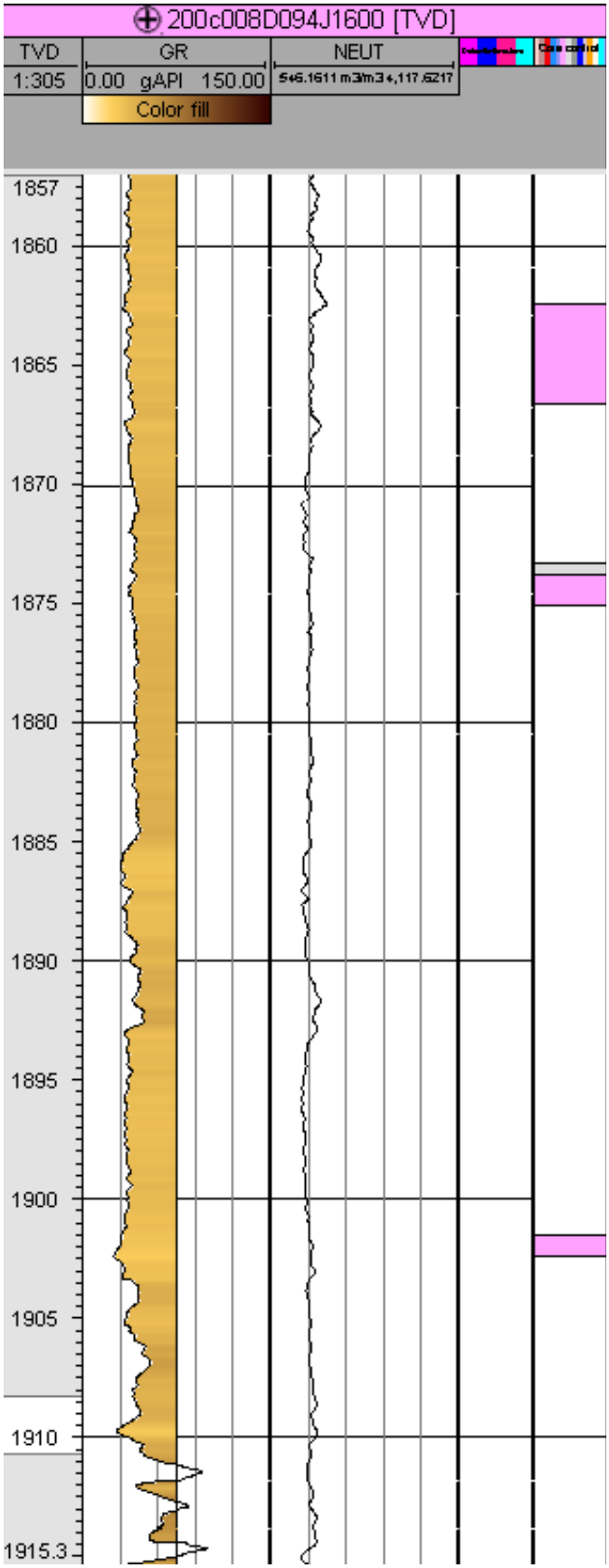

Facies 1A
Facies 1B
Facies 1C
Facies 1D
Facies 2A
Facies 2B
Facies 2C
Facies 3A
Facies 3B
Facies 4A
Facies 4B

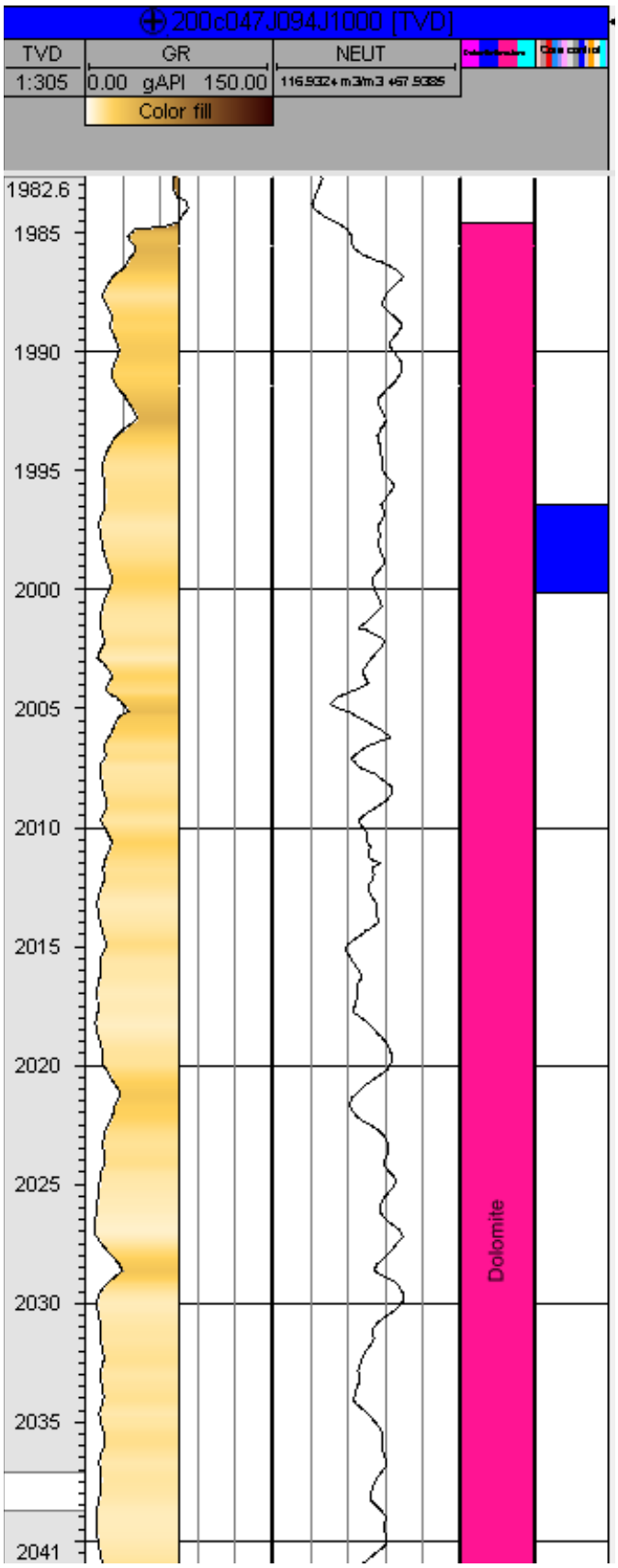

Facies 1A
Facies 1B
Facies 1C
Facies 1D
Facies 2A
Facies 2B
Facies 2C
Facies 3A
Facies 3B
Facies 4A
Facies 4B

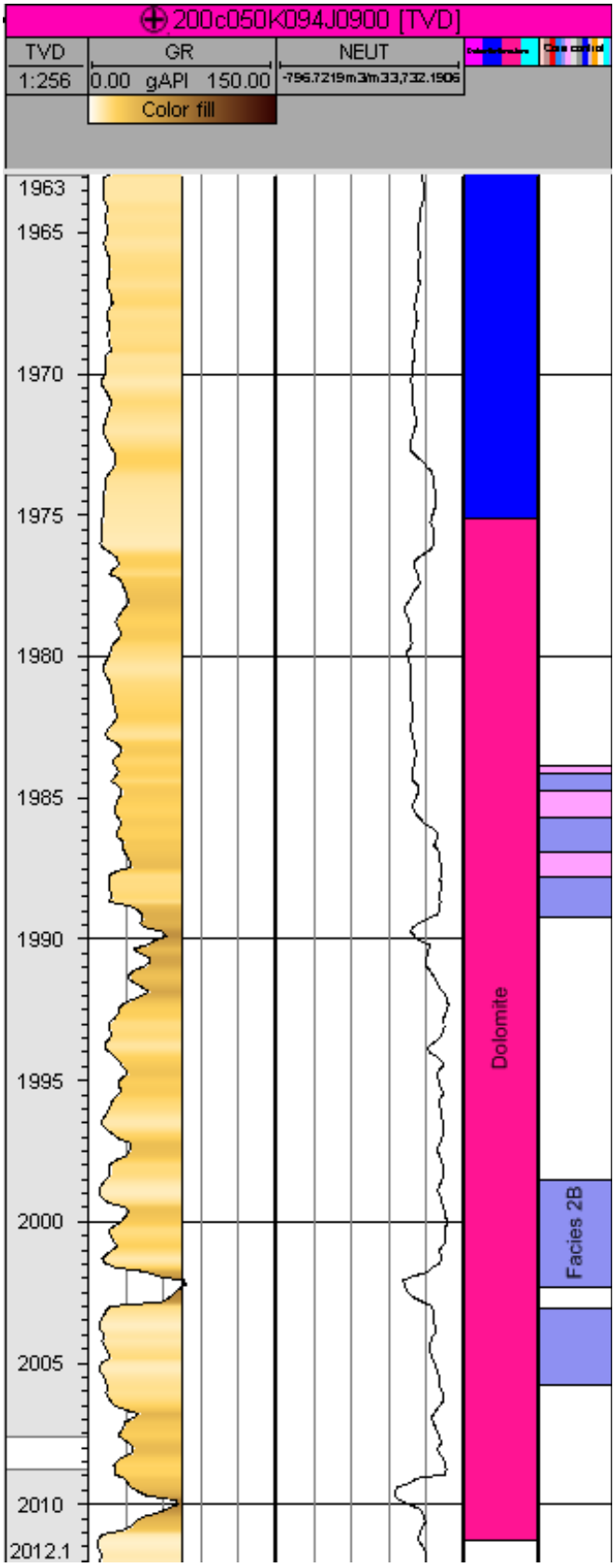

Facies 1A
Facies 1B
Facies 1C
Facies 1D
Facies 2A
Facies 2B
Facies 2C
Facies 3A
Facies 3B
Facies 4A
Facies 4B

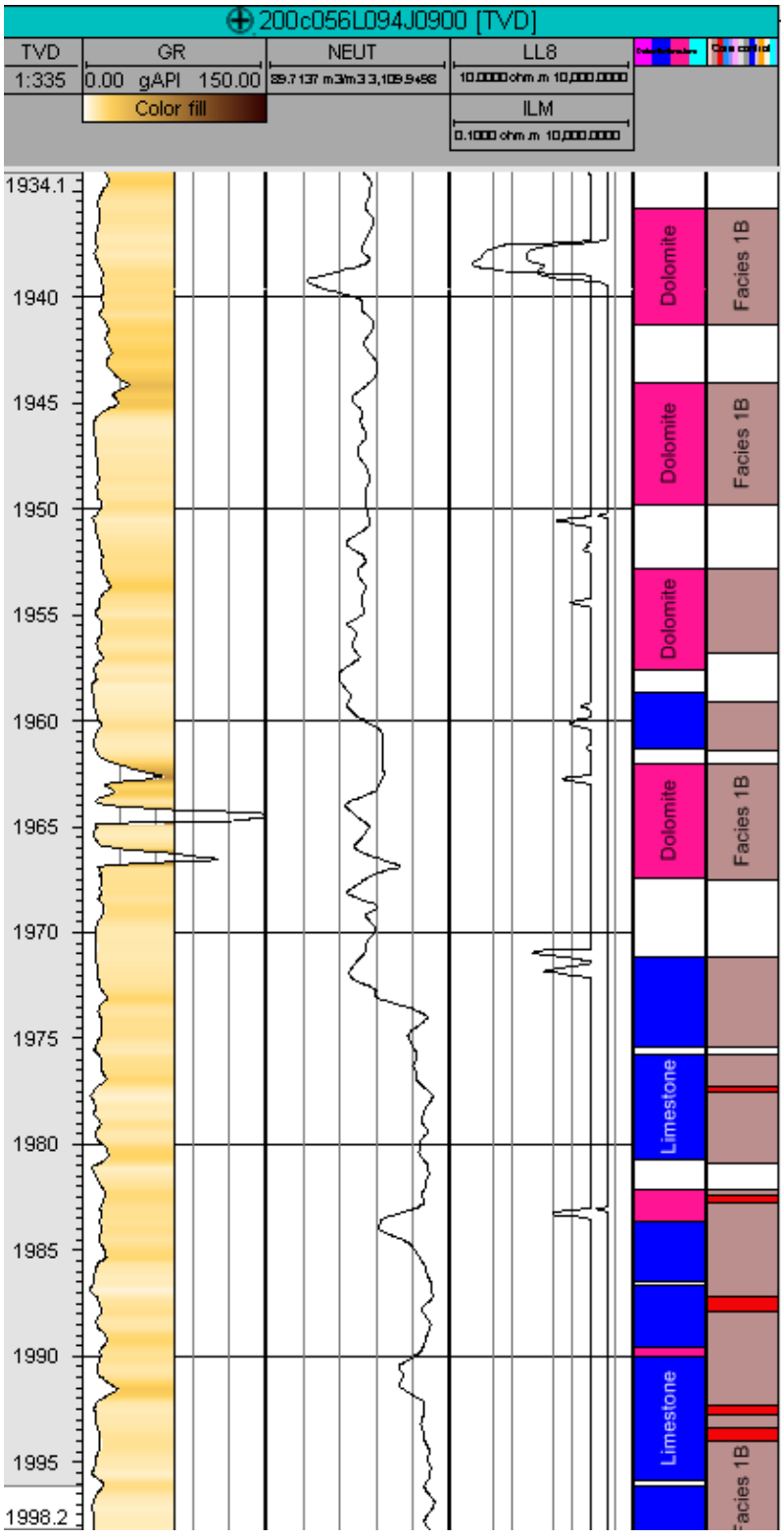
200c056L094J0900 [TVD]
TVD
1:335
GR
0.00 gAPI 150.00
Color fill
NEUT
LL8
ILM
1934.1
1940
1945
1950
1955
1960
1965
1970
1975
1980
1985
1990
1995
1998.2
Dolomite
Dolomite
Dolomite
Dolomite
Limestone
Limestone
Facies 1B
Facies 1B
Facies 1B
Facies 1B
Facies 1B


Facies 1A
Facies 1B
Facies 1C
Facies 1D
Facies 2A
Facies 2B
Facies 2C
Facies 3A
Facies 3B
Facies 4A
Facies 4B

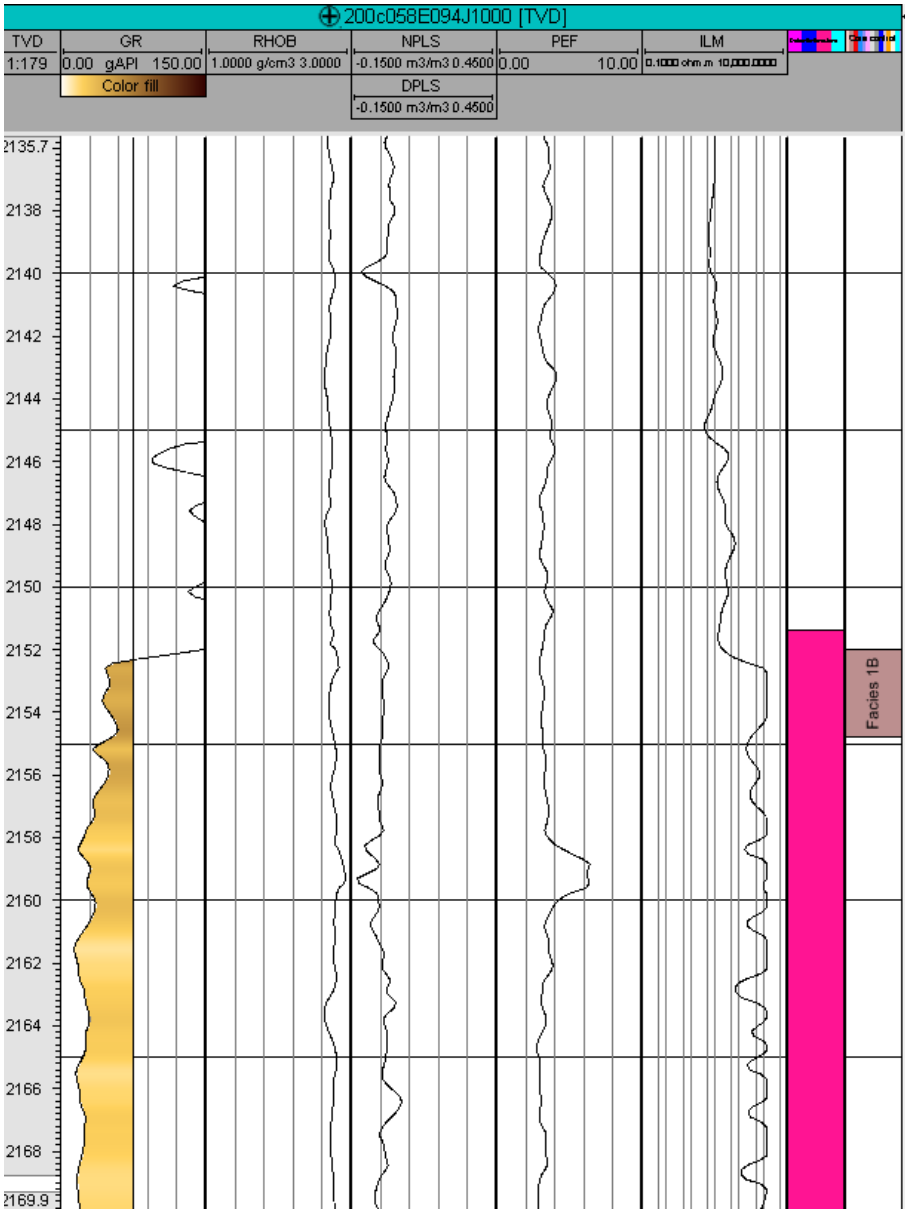

Facies 1A
Facies 1B
Facies 1C
Facies 1D
Facies 2A
Facies 2B
Facies 2C
Facies 3A
Facies 3B
Facies 4A
Facies 4B

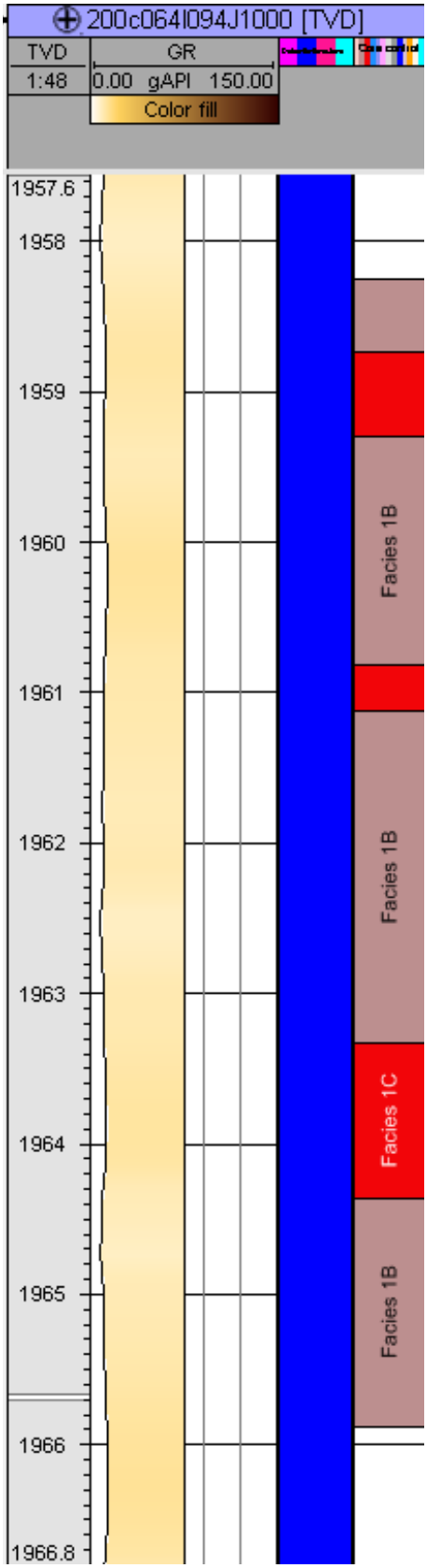
200c064l094J1000 [TVD]
TVD
1:48
GR
0.00 gAPI 150.00
Color fill
1957.6
1958
1959
1960
1961
1962
1963
1964
1965
1966
1966.8
Facies 1B
Facies 1B
Facies 1C
Facies 1B


Facies 1A
Facies 1B
Facies 1C
Facies 1D
Facies 2A
Facies 2B
Facies 2C
Facies 3A
Facies 3B
Facies 4A
Facies 4B

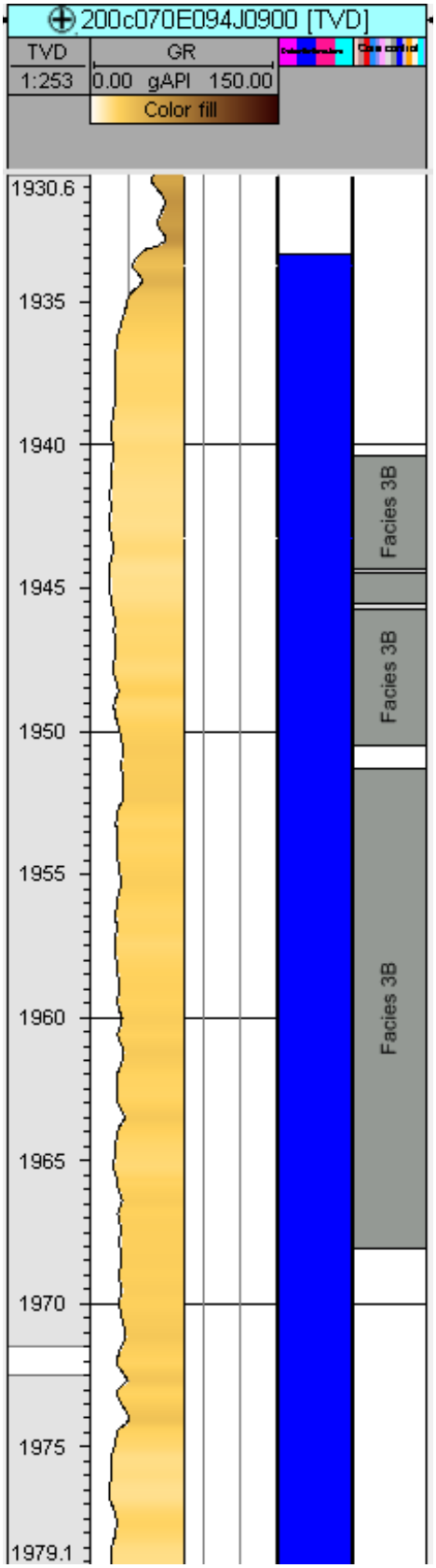
200c070E094J0900 [TVD]
TVD
1:253
GR
0.00 gAPI 150.00
Color fill
1930.6
1935
1940
1945
1950
1955
1960
1965
1970
1975
1979.1
Facies 3B
Facies 3B
Facies 3B


Facies 1A
Facies 1B
Facies 1C
Facies 1D
Facies 2A
Facies 2B
Facies 2C
Facies 3A
Facies 3B
Facies 4A
Facies 4B

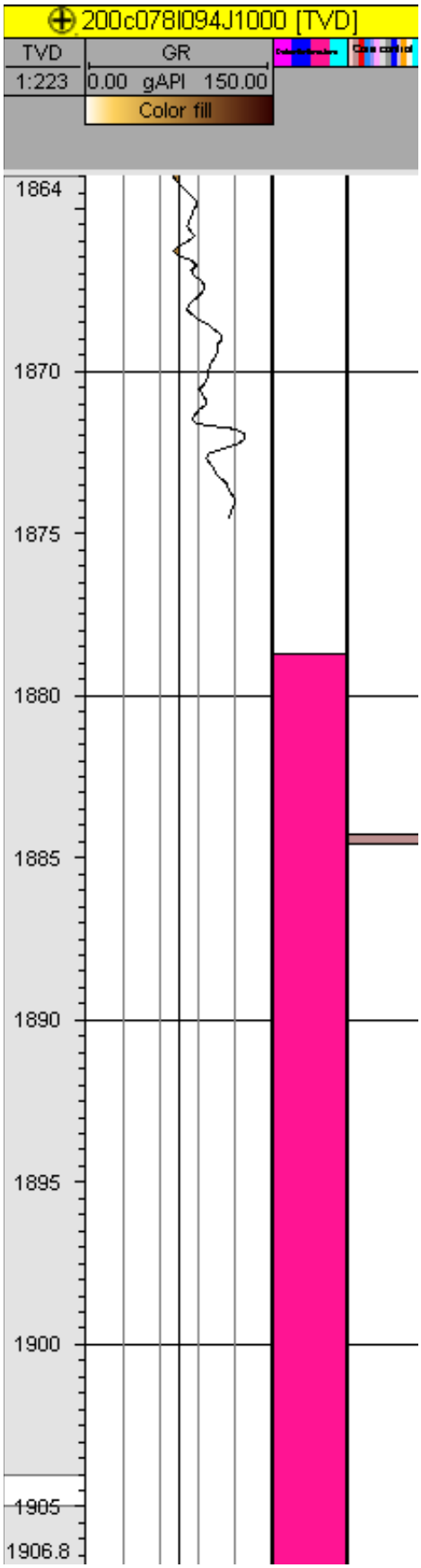

Facies 1A
Facies 1B
Facies 1C
Facies 1D
Facies 2A
Facies 2B
Facies 2C
Facies 3A
Facies 3B
Facies 4A
Facies 4B

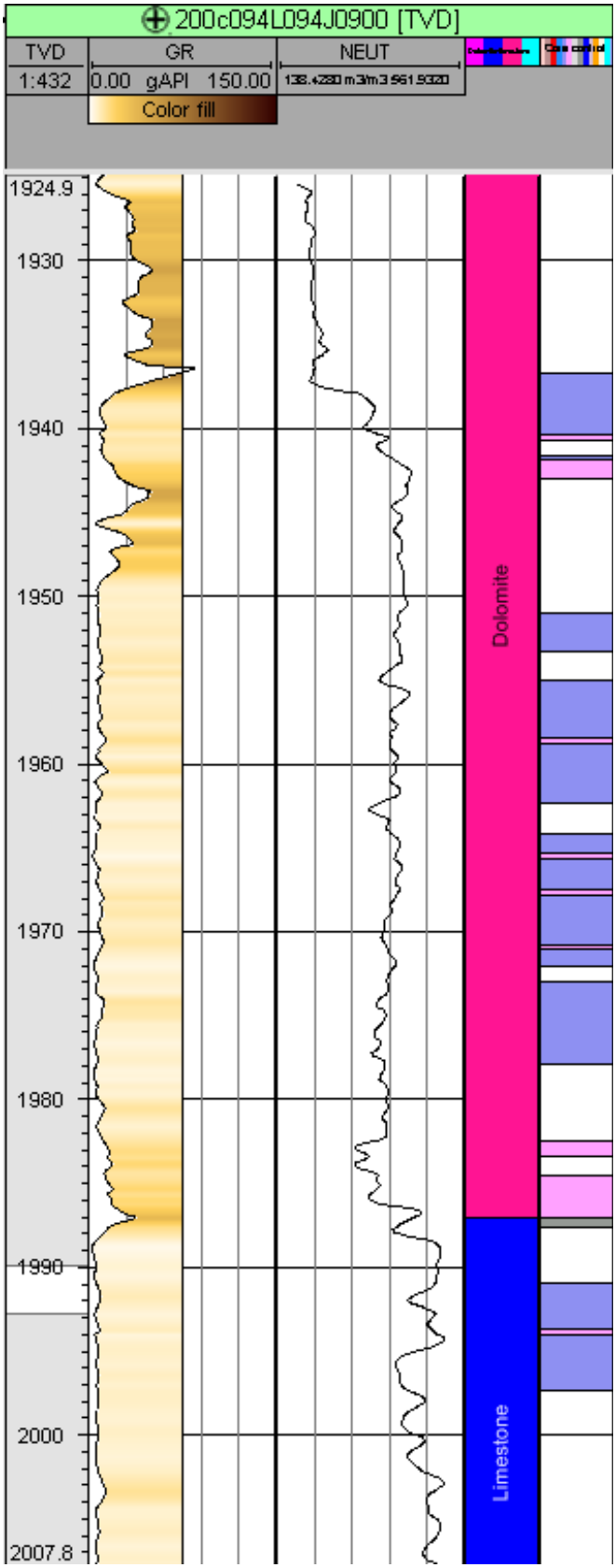

Facies 1A
Facies 1B
Facies 1C
Facies 1D
Facies 2A
Facies 2B
Facies 2C
Facies 3A
Facies 3B
Facies 4A
Facies 4B

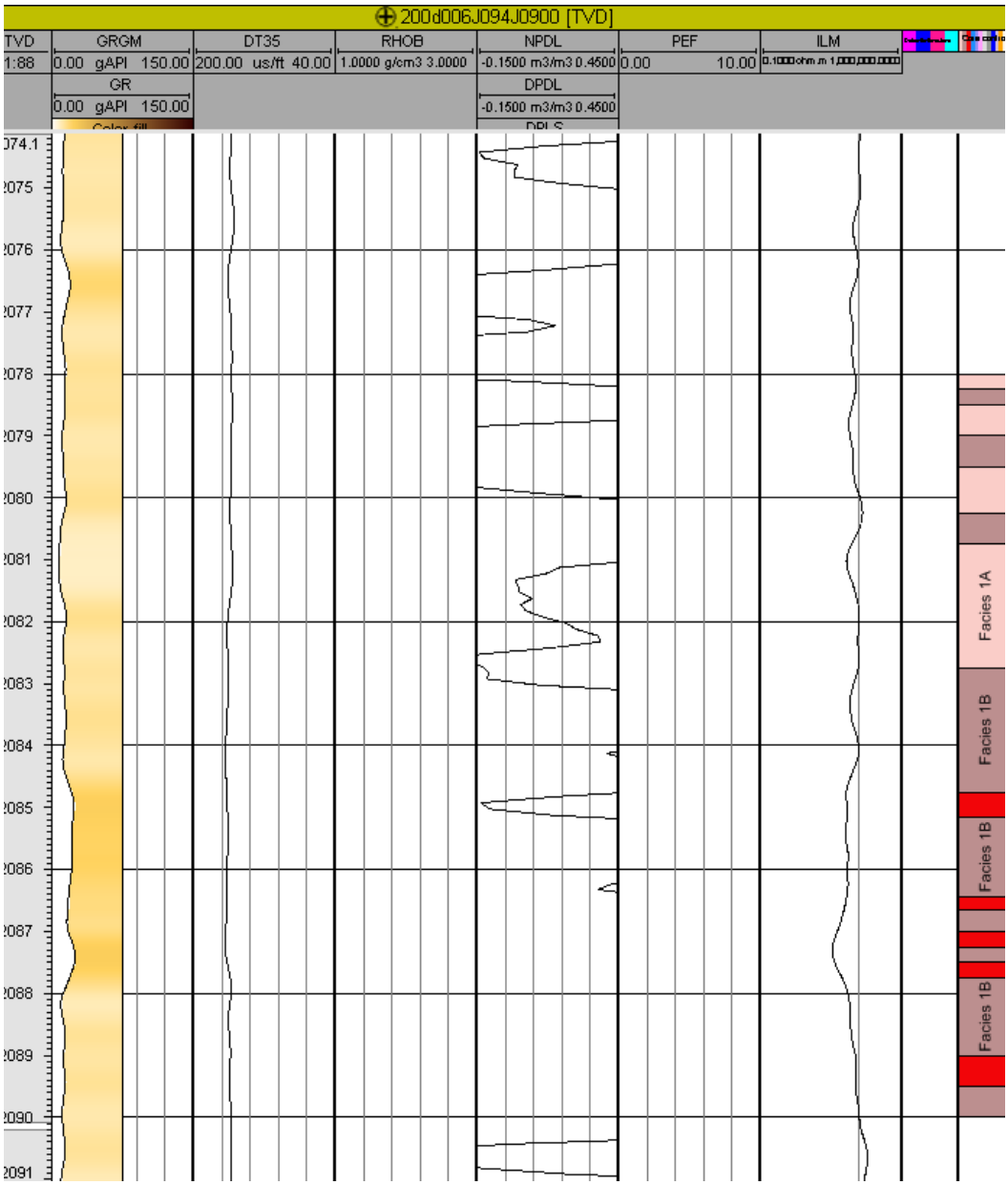

Facies 1A
Facies 1B
Facies 1C
Facies 1D
Facies 2A
Facies 2B
Facies 2C
Facies 3A
Facies 3B
Facies 4A
Facies 4B

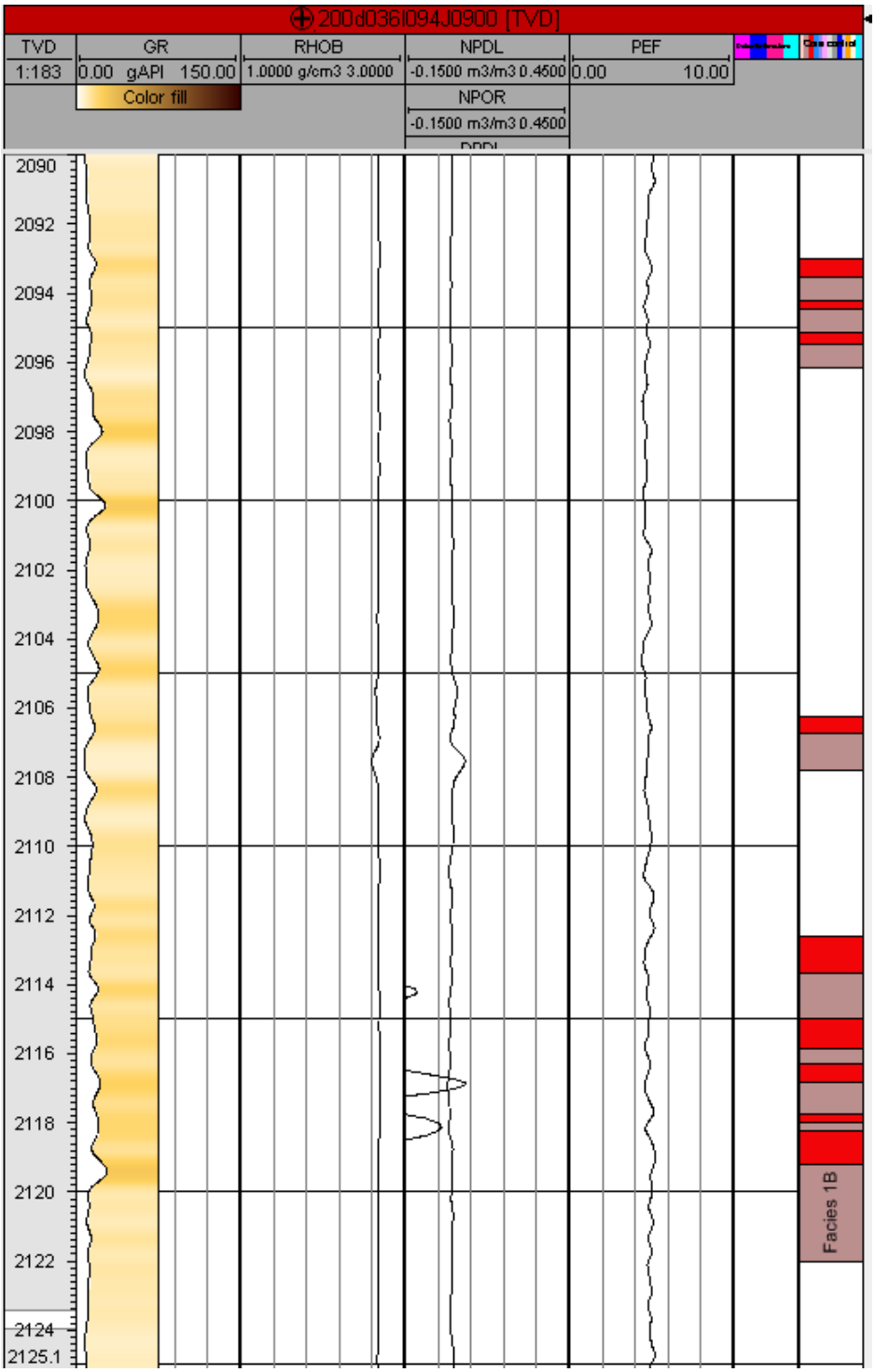

Facies 1A
Facies 1B
Facies 1C
Facies 1D
Facies 2A
Facies 2B
Facies 2C
Facies 3A
Facies 3B
Facies 4A
Facies 4B

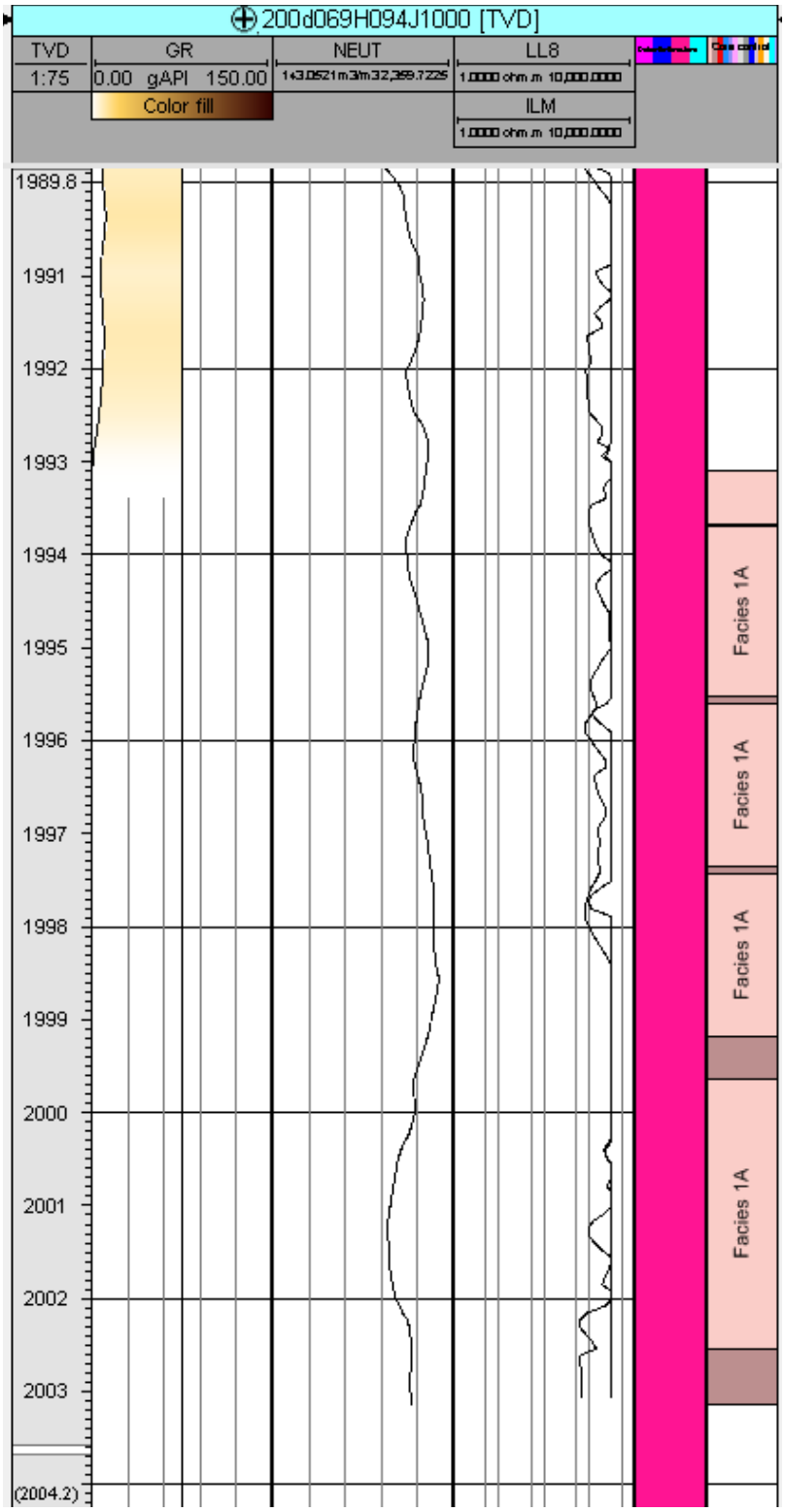

Facies 1A
Facies 1B
Facies 1C
Facies 1D
Facies 2A
Facies 2B
Facies 2C
Facies 3A
Facies 3B
Facies 4A
Facies 4B

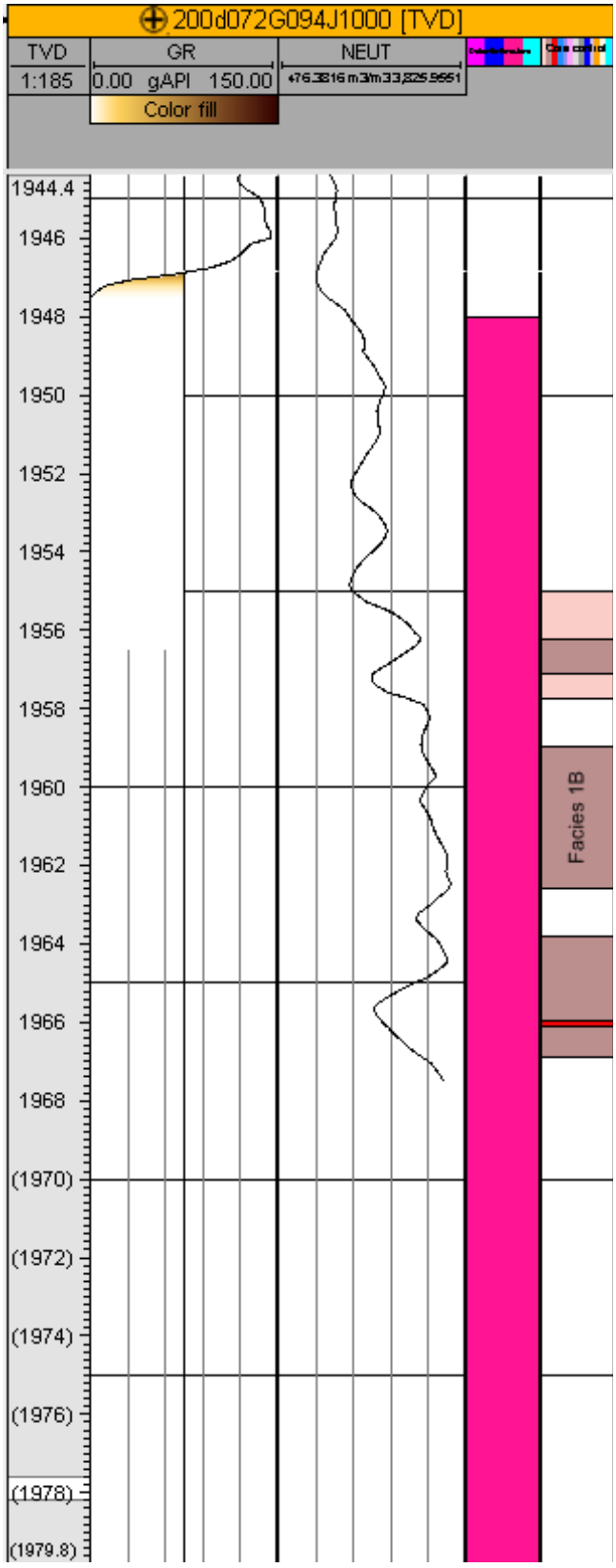

Facies 1A
Facies 1B
Facies 1C
Facies 1D
Facies 2A
Facies 2B
Facies 2C
Facies 3A
Facies 3B
Facies 4A
Facies 4B

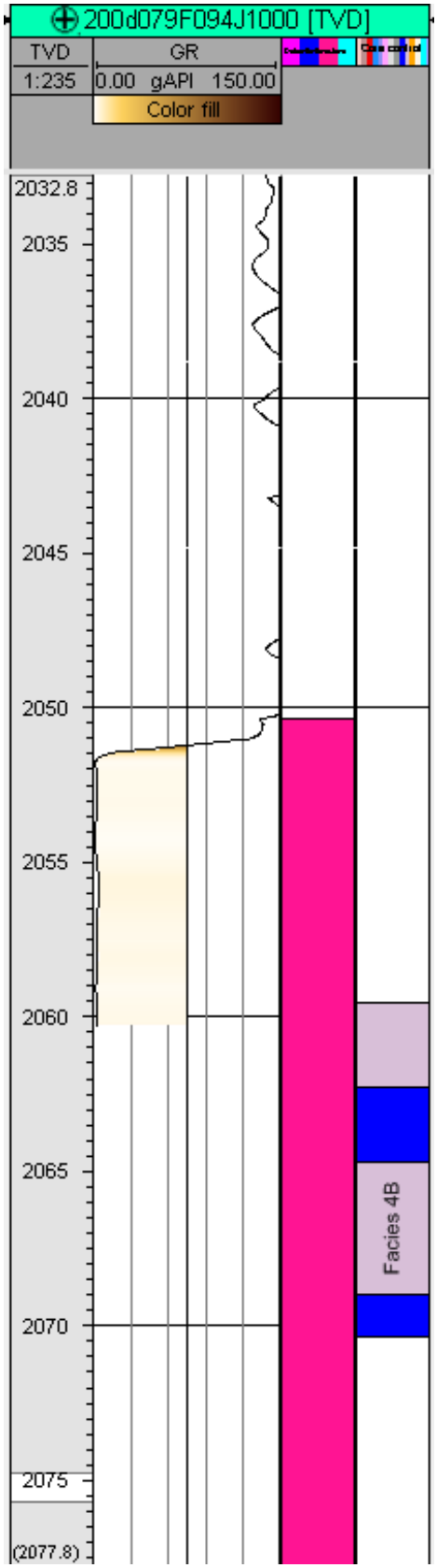

Facies 1A
Facies 1B
Facies 1C
Facies 1D
Facies 2A
Facies 2B
Facies 2C
Facies 3A
Facies 3B
Facies 4A
Facies 4B

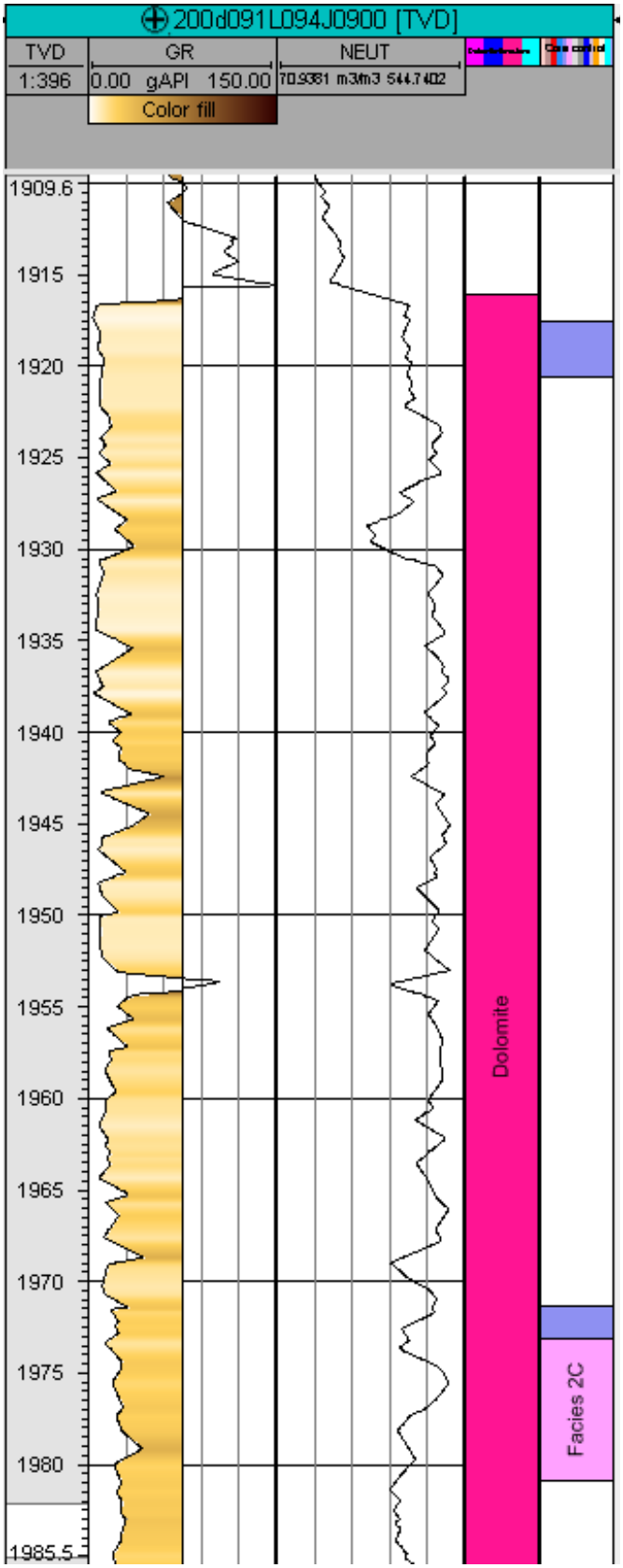
200d091L094J0900 [TVD]
TVD
1:396
GR
0.00 gAPI 150.00
NEUT
Color fill
1909.6
1915
1920
1925
1930
1935
1940
1945
1950
1955
1960
1965
1970
1975
1980
1985.5
Dolomite
Facies 2C


Facies 1A
Facies 1B
Facies 1C
Facies 1D
Facies 2A
Facies 2B
Facies 2C
Facies 3A
Facies 3B
Facies 4A
Facies 4B

Appendix C: Flow Simulations

200kg/s Temperature Model - Facies 1A - High Reservoir Pressure	
Time = 1500 seconds	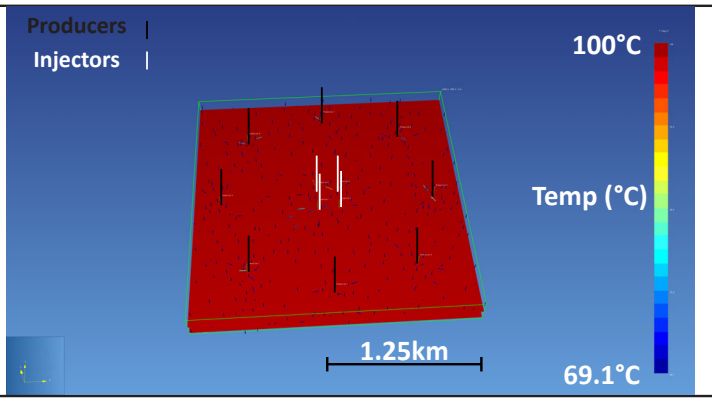
Time = ~76 days	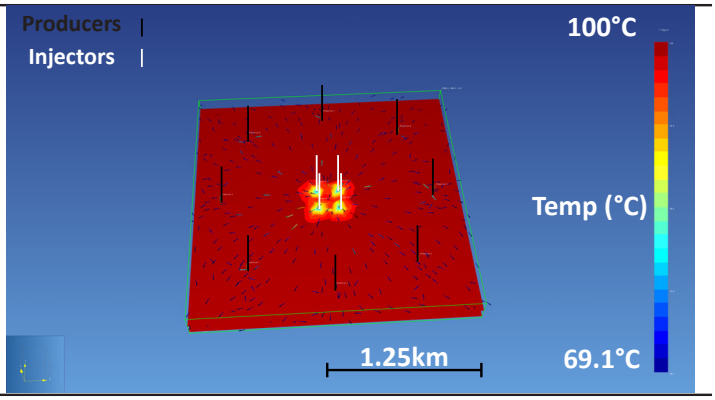
Time = ~5 years	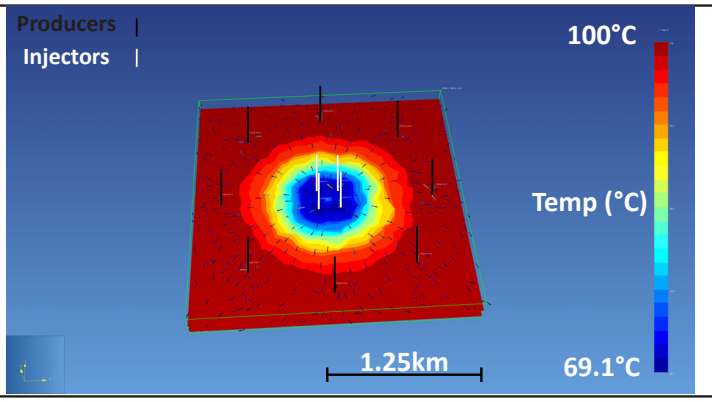
Time = 25 years	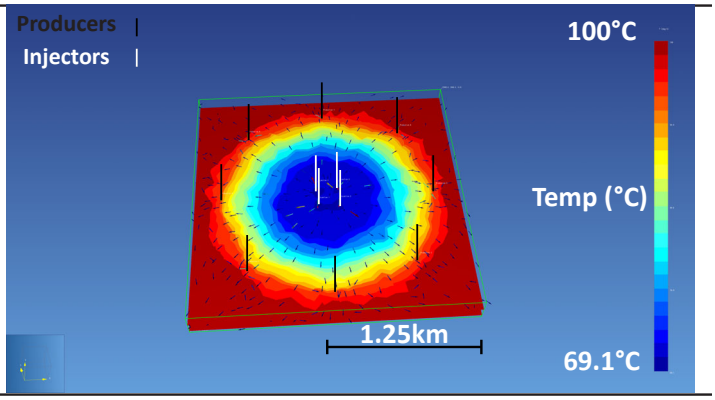

200kg/s Temperature Model - Facies 1A - Low Reservoir Pressure

Time = 1500 seconds	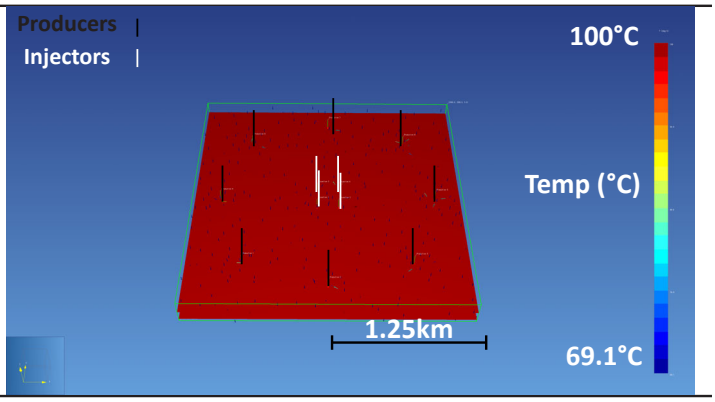
Time = ~76 days	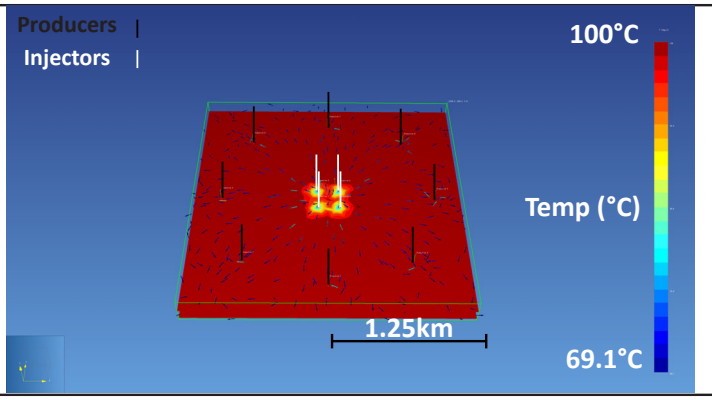
Time = ~5 years	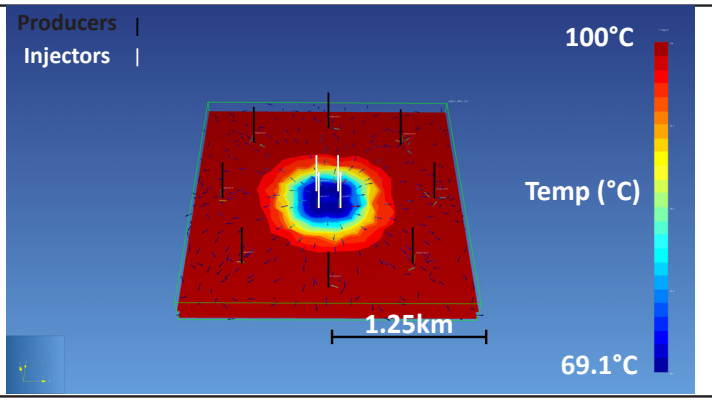
Time = 25 years	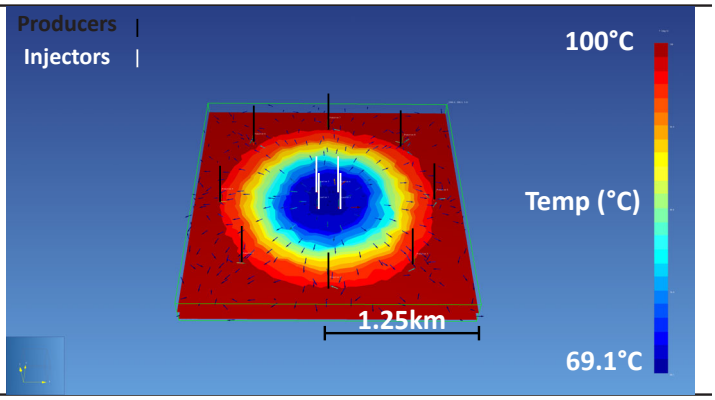

Doublet Model - Facies 1A - Max High Reservoir Pressure

Time = 1500 seconds	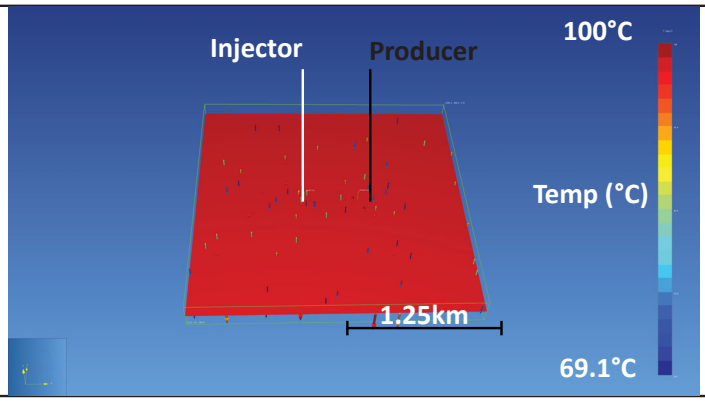
Time = ~76 days	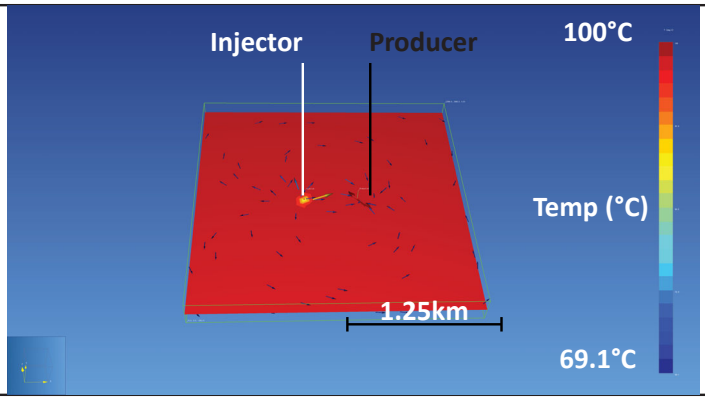
Time = ~5 years	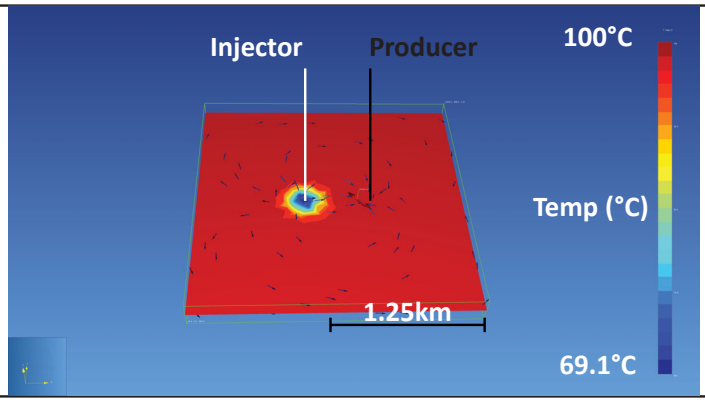
Time = 25 years	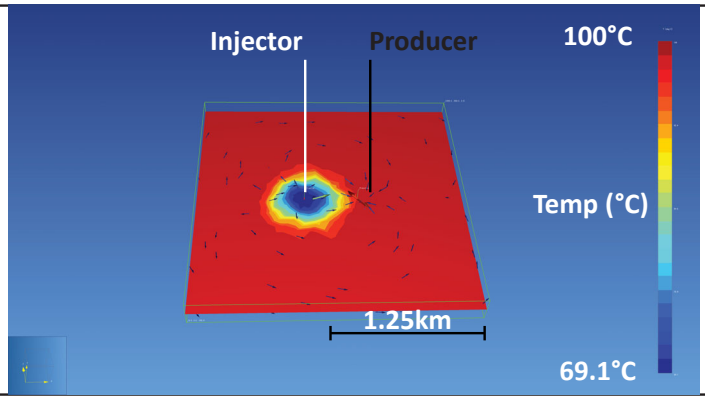

Doublet Model - Facies 1A - Max Low Reservoir Pressure	
Time = 1500 seconds	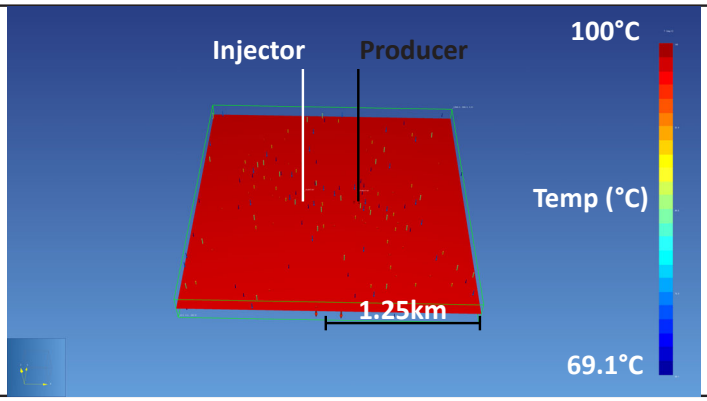
Time = ~76 days	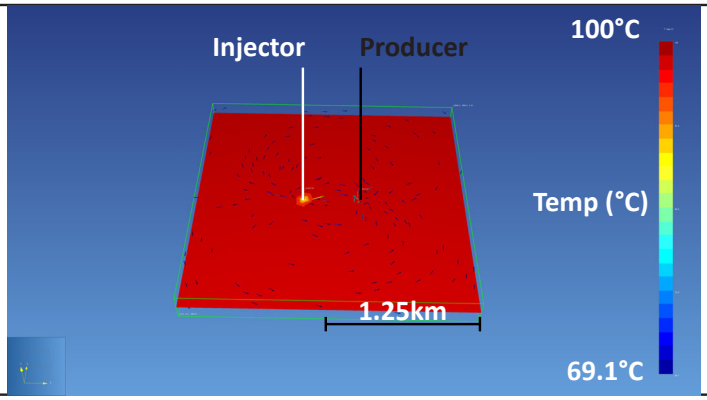
Time = ~5 years	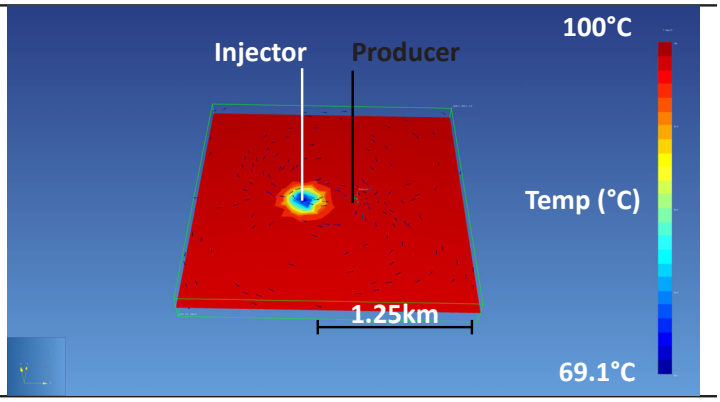
Time = 25 years	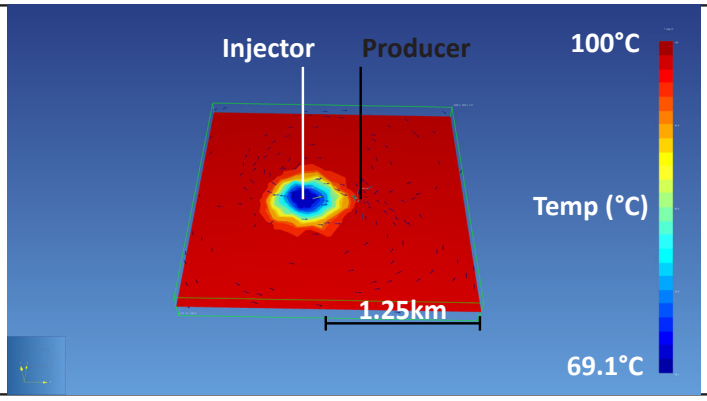

Doublet Model - Facies 1A - Mean High Reservoir Pressure

Time = 1500 seconds	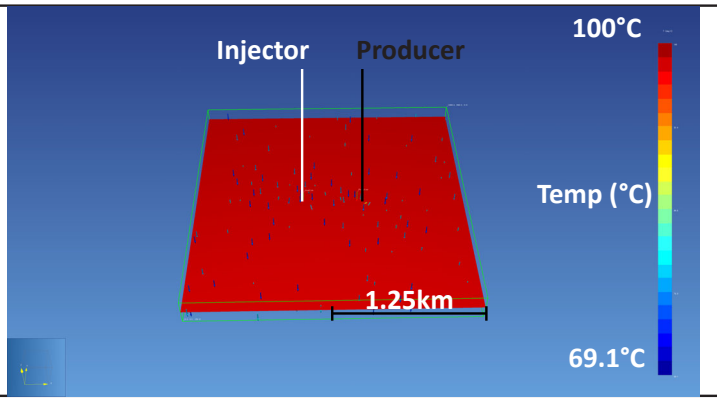
Time = ~76 days	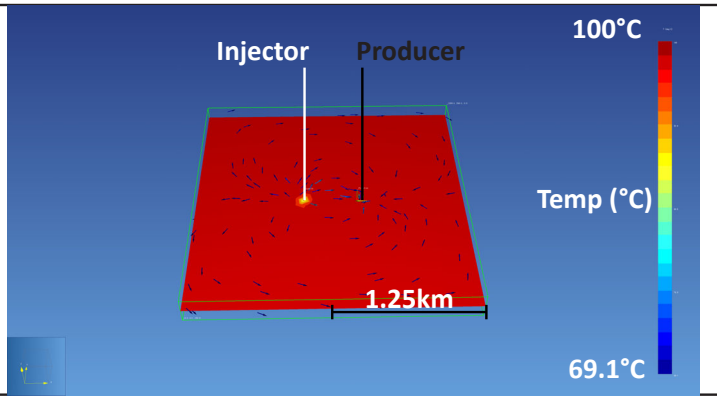
Time = ~5 years	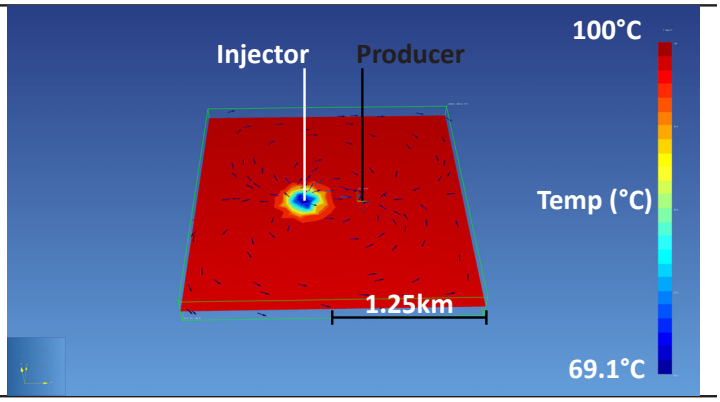
Time = 25 years	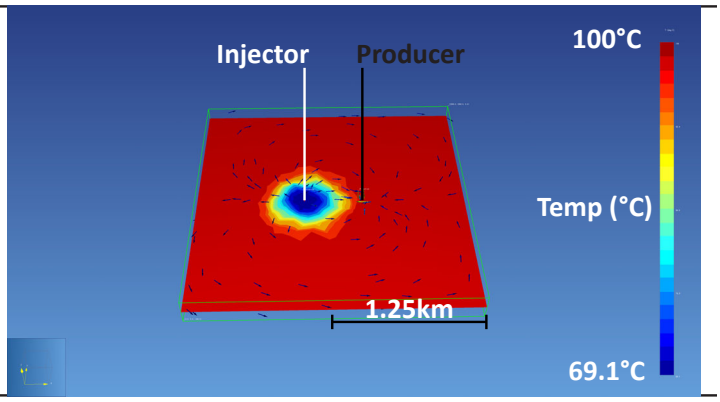

Doublet Model - Facies 1A - Mean Low Reservoir Pressure	
Time = 1500 seconds	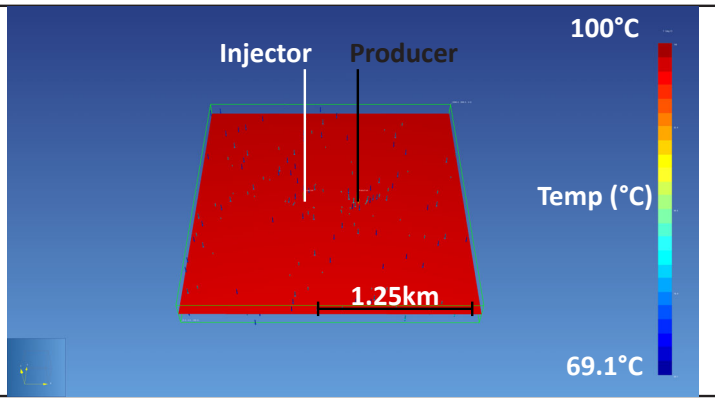
Time = ~76 days	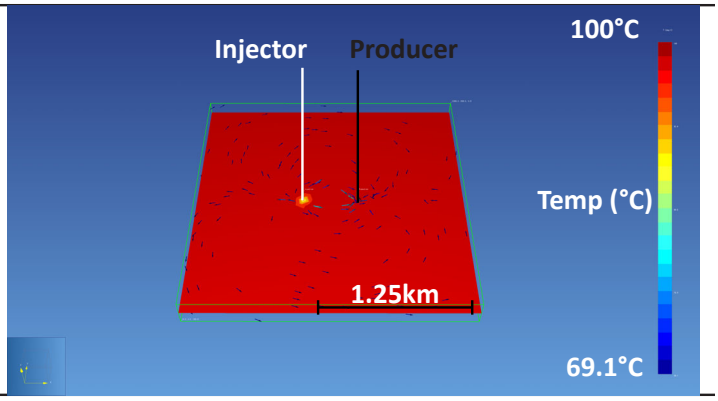
Time = ~5 years	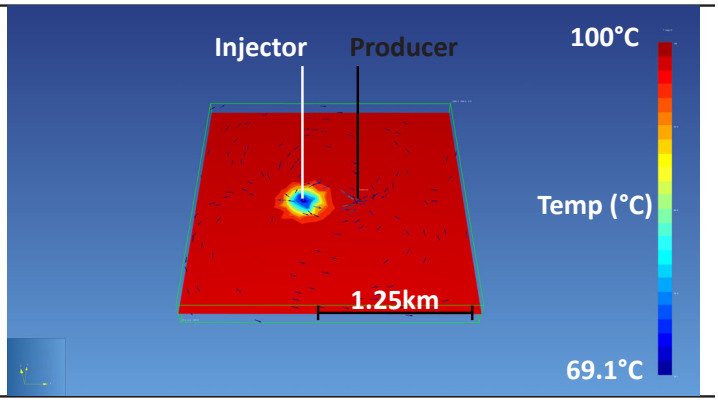
Time = 25 years	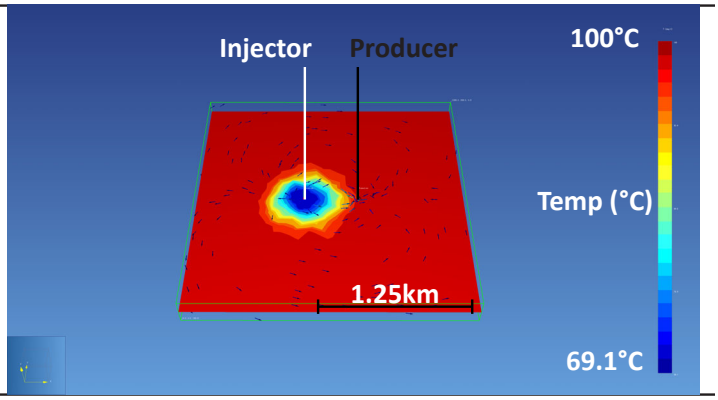

Doublet Model - Facies 1A - Median High Reservoir Pressure	
Time = 1500 seconds	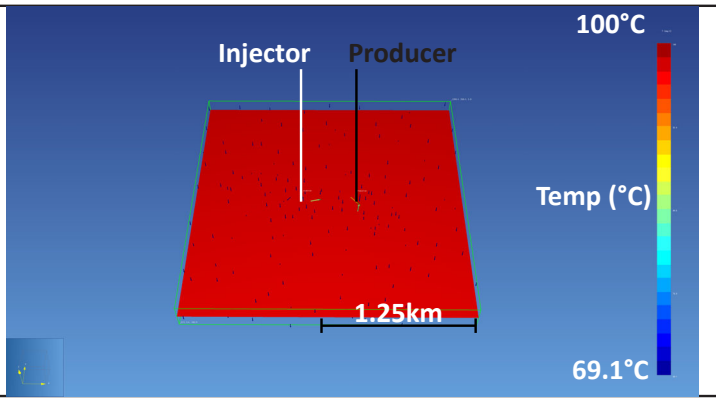
Time = ~76 days	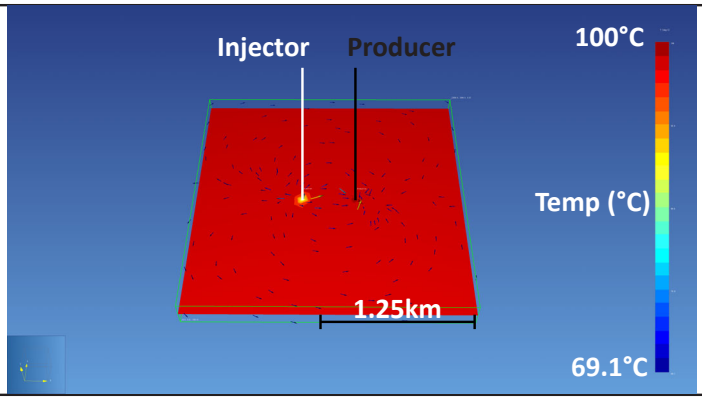
Time = ~5 years	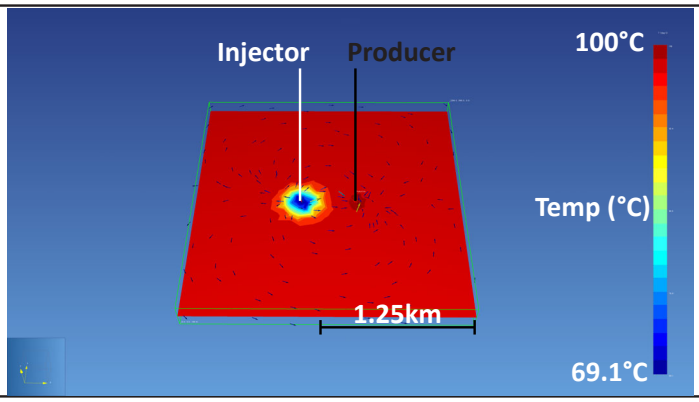
Time = 25 years	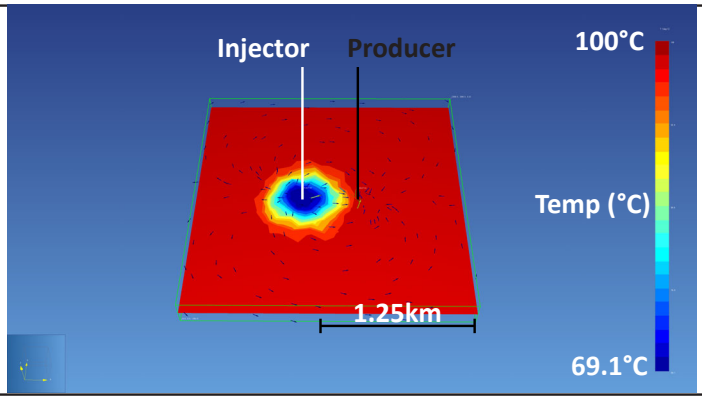

Doublet Model - Facies 1A - Median Low Reservoir Pressure

Time = 1500 seconds	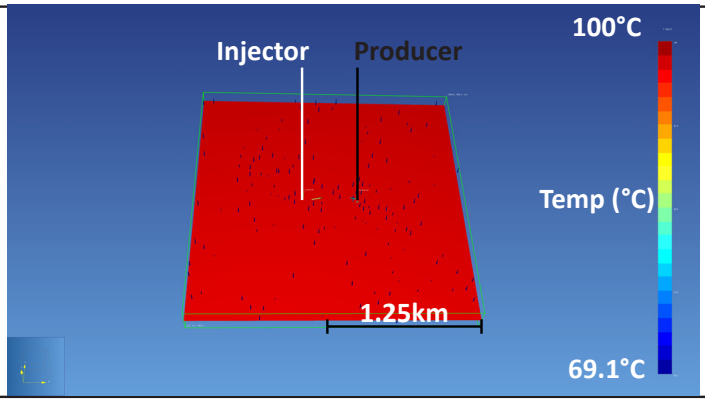
Time = ~76 days	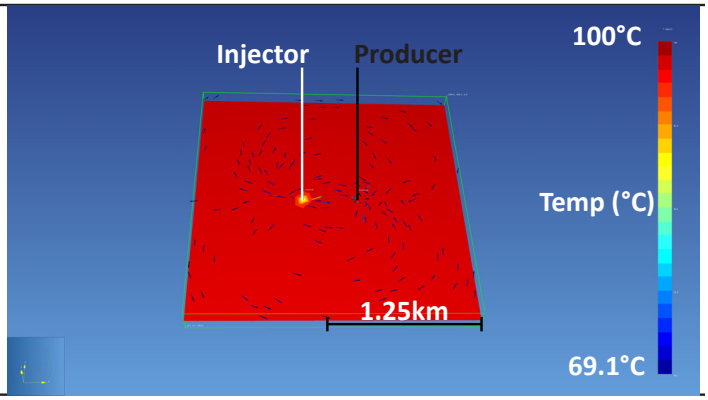
Time = ~5 years	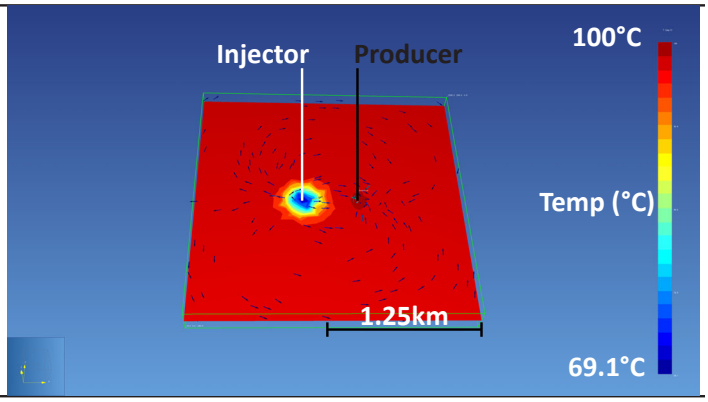
Time = 25 years	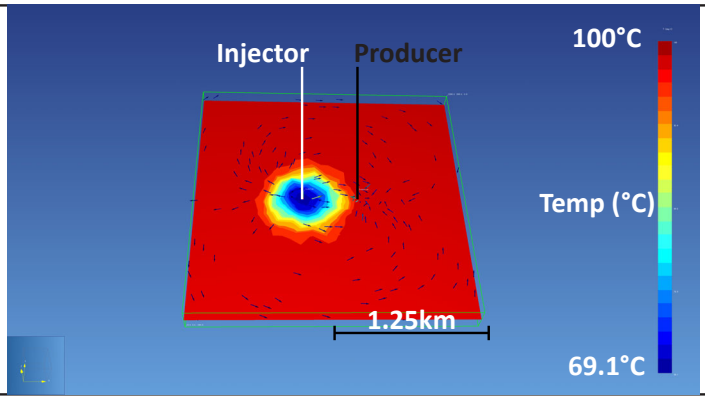

Doublet Pressure Model - Facies 1A - Minimum High Reservoir Pressure	
Time = 1500 seconds	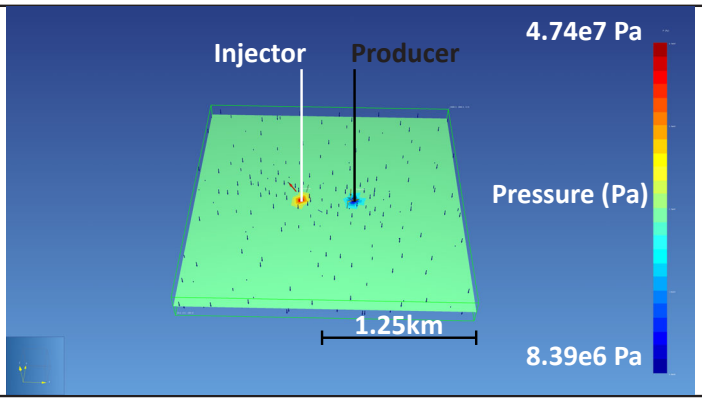
Time = 8606 seconds	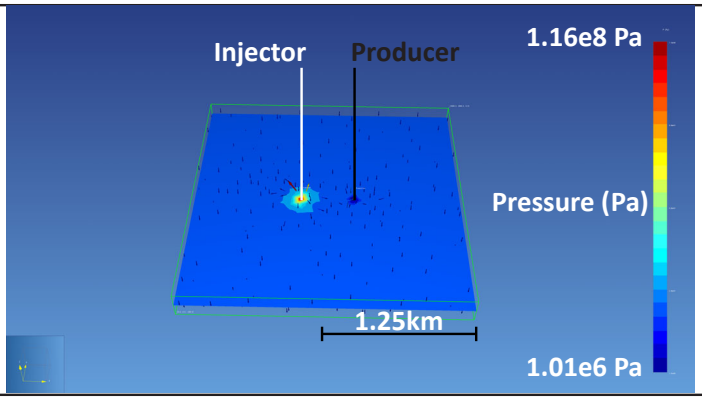
Time = ~7.7 hours	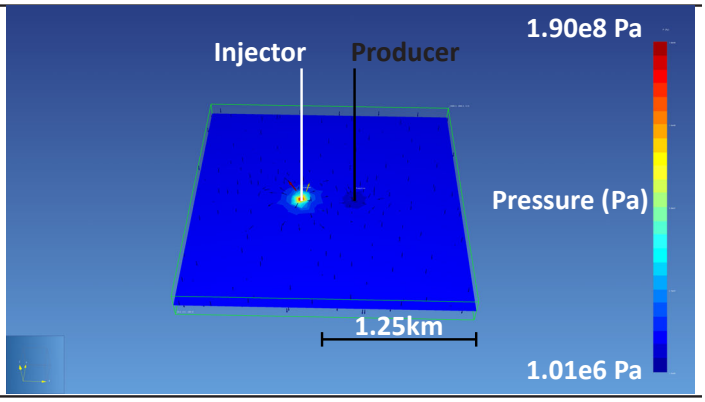
Time = ~48 hours	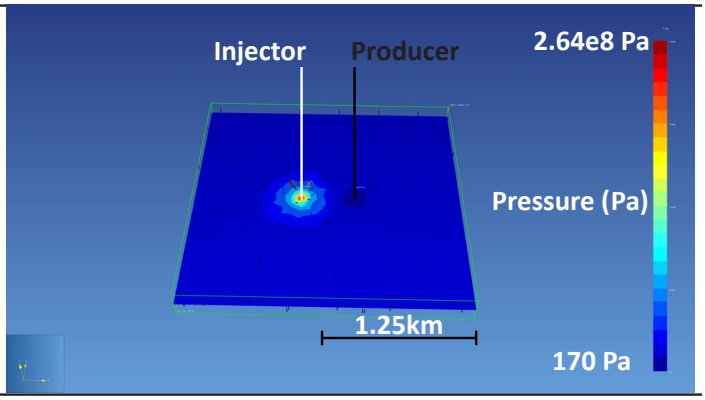

Doublet Pressure Model - Facies 1A - Minimum Low Reservoir Pressure	
Time = 1518 seconds	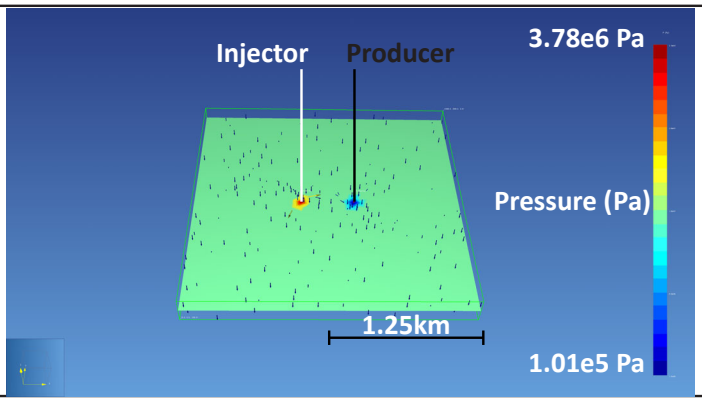
Time = 7818 seconds	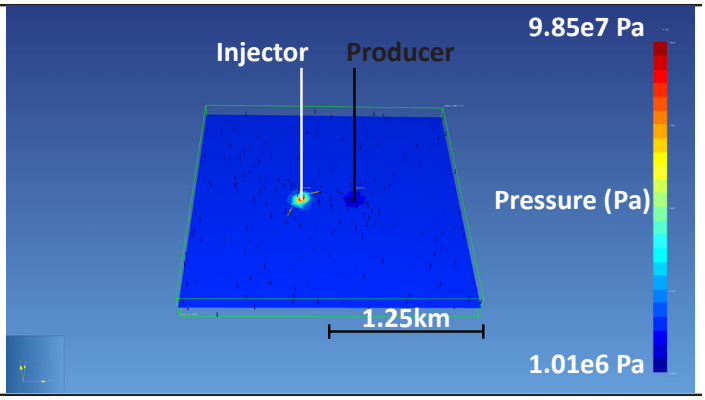
Time = ~29 hours	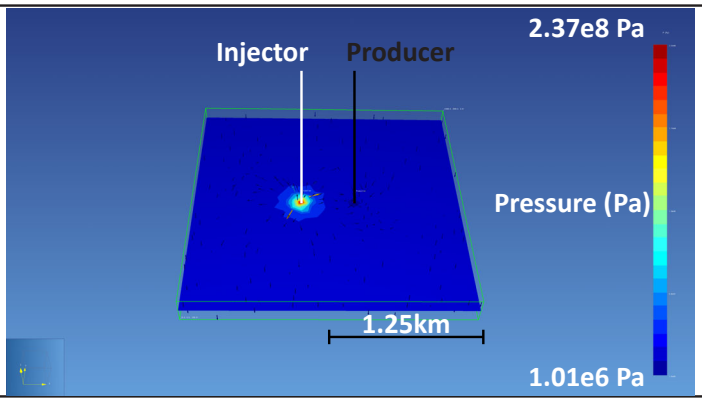
Time = ~45 hours	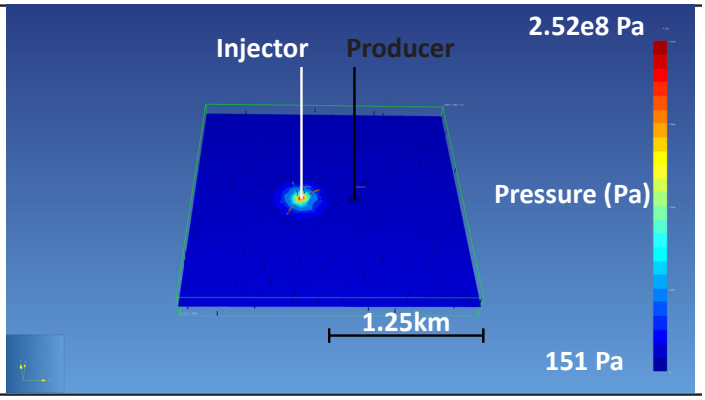

Doublet Pressure Model - Facies 1A - Q1 High Reservoir Pressure	
Time = 1500 seconds	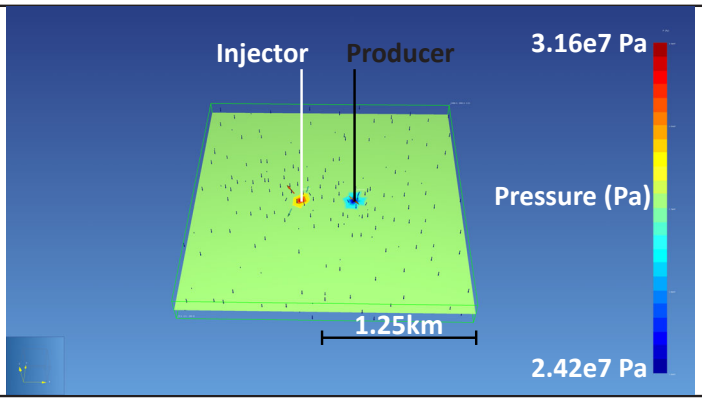
Time = ~83 days	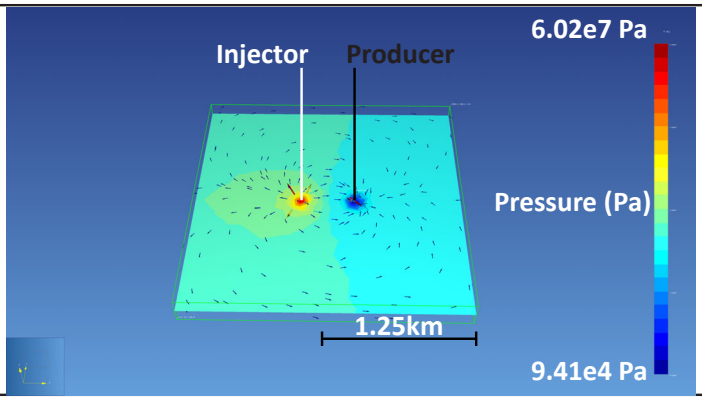
Time = ~158 days	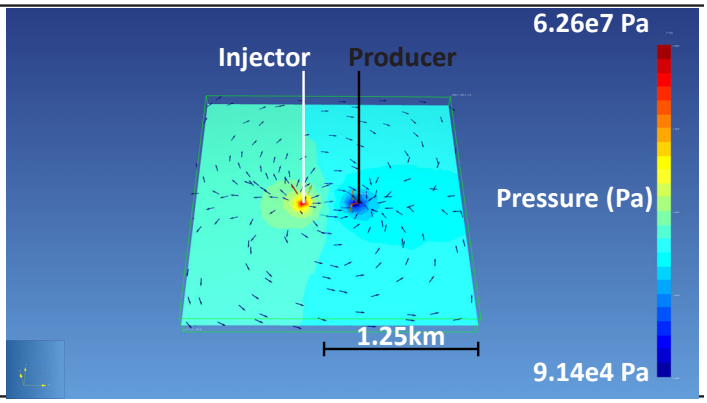
Time = ~265 days	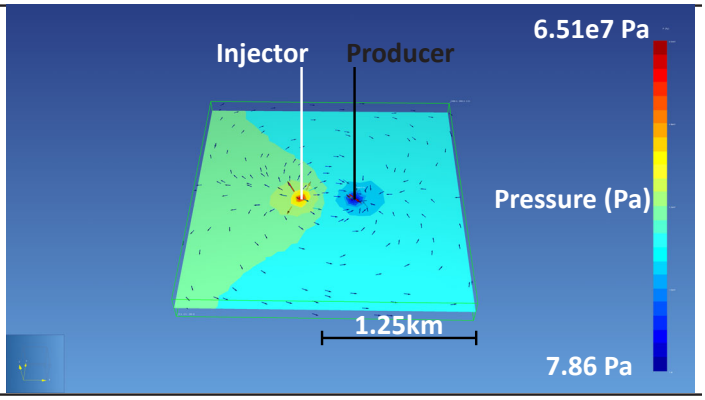

Doublet Pressure Model - Facies 1A - Q1 Low Reservoir Pressure

Time = 1500 seconds	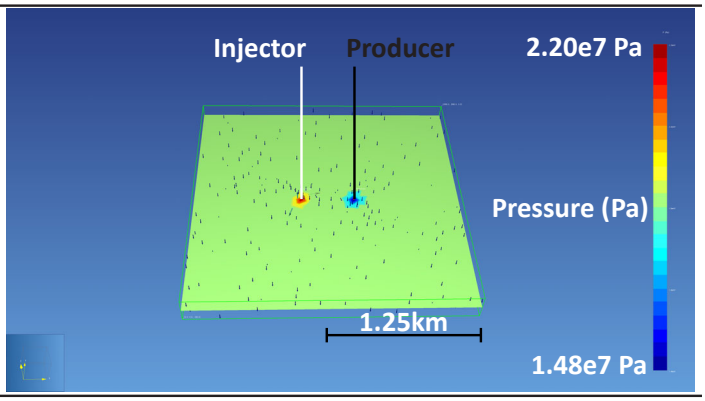
Time = 1270 seconds	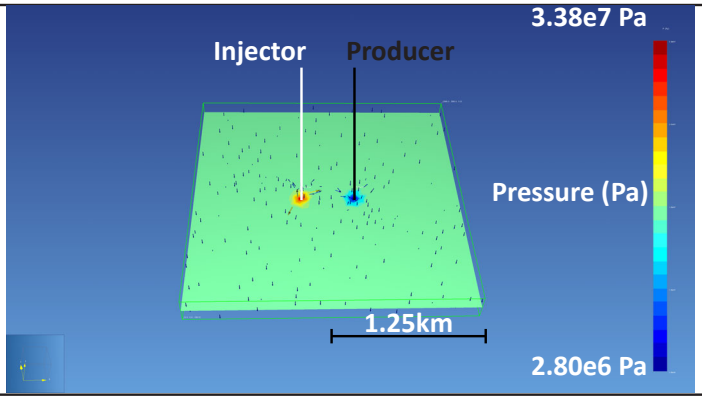
Time = ~2.6 days	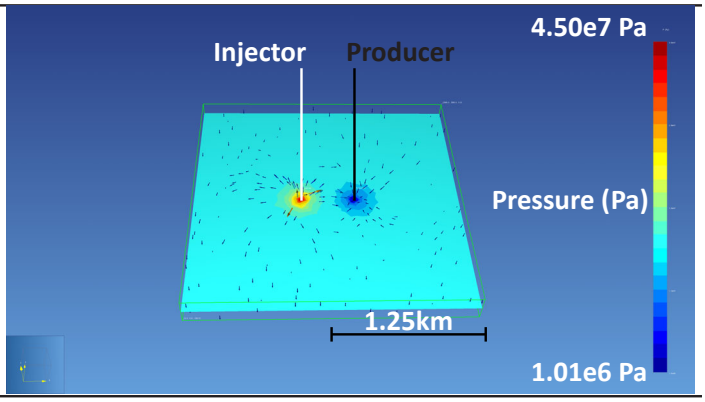
Time = ~26 days	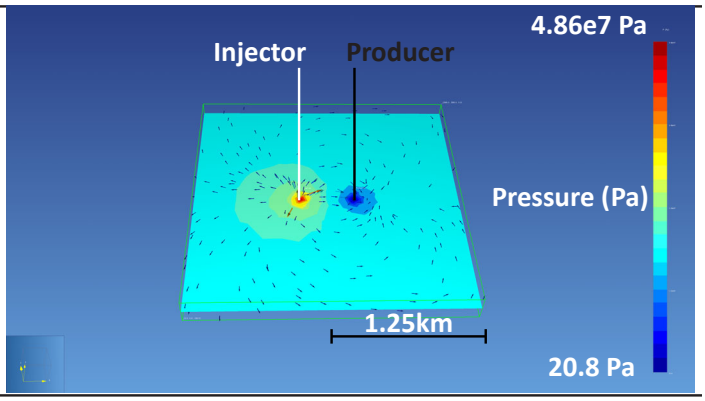

Doublet Temperature Model - Facies 1A - Q3 High Reservoir Pressure	
Time = 1500 seconds	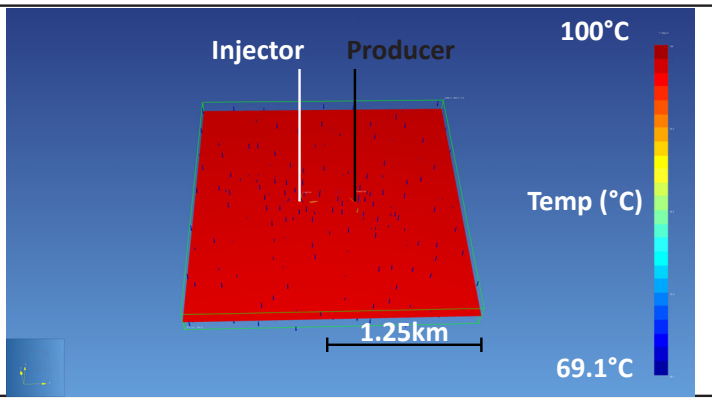
Time = ~76 days	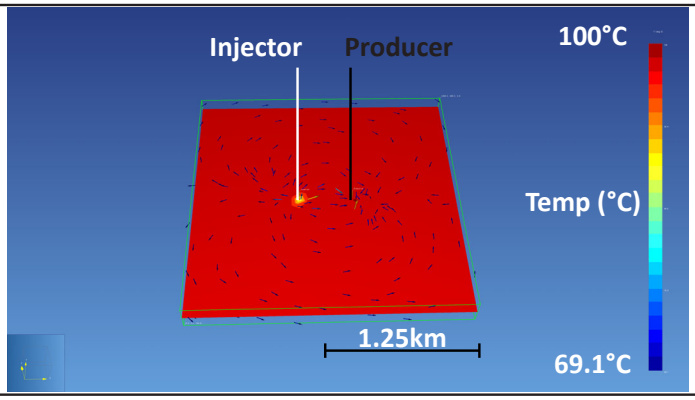
Time = ~5 years	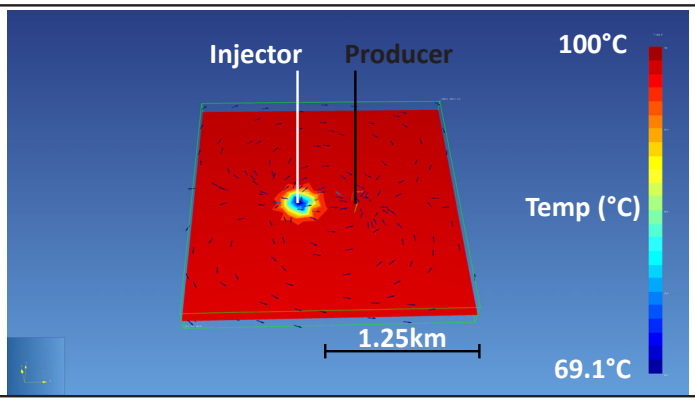
Time = 25 years	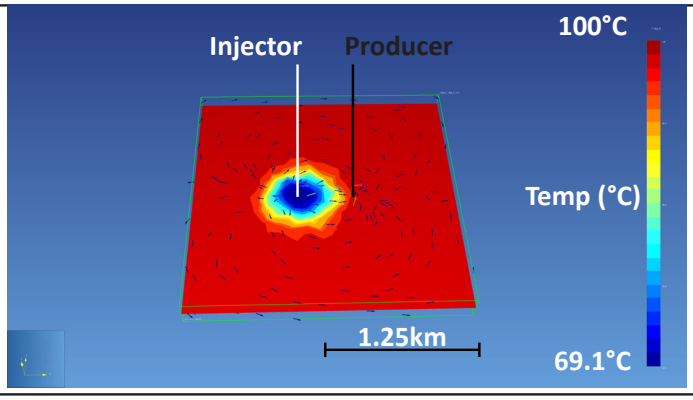

Doublet Temperature Model - Facies 1A - Q3 Low Reservoir Pressure

Time = 1500 seconds	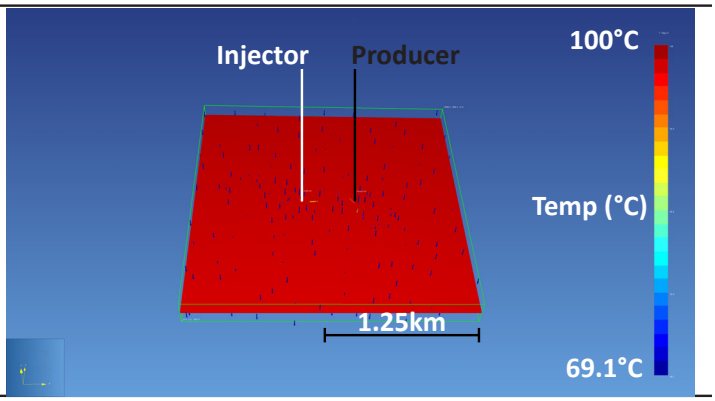
Time = ~76 days	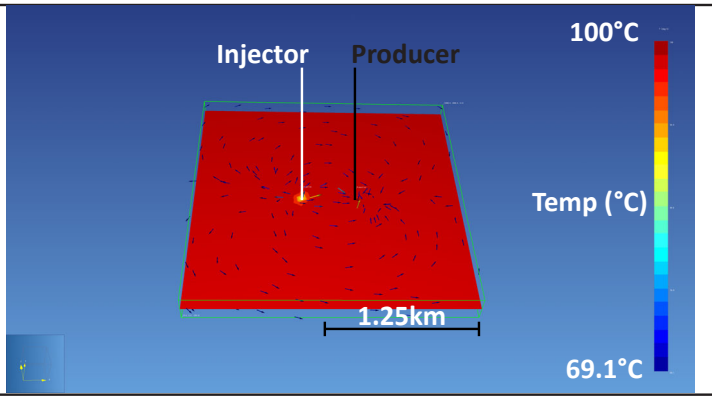
Time = ~5 years	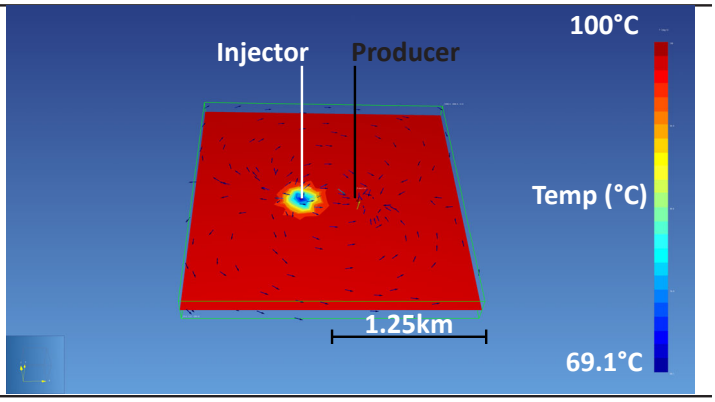
Time = 25 years